APERIODIC STRUCTURES IN OPTICS AND INTEGRATED OPTICS

AND

THE TRANSVERSE BRAGG REFLECTOR LASER

Thesis by

Jeffrey B. Shellan

In Partial Fulfillment of the Requirements

for the Degree of

Doctor of Philosophy

California Institute of Technology

Pasadena, California

1978

(Submitted February 28, 1978)

This work is dedicated to the memory of my mother, who, after all, started me on "my numbers."

ACKNOWLEDGMENT

I would like to express my sincere appreciation for the fine guidance I received from my thesis advisor, Professor Amnon Yariv. His support, counseling and expertise helped make the last three years at Caltech enjoyable for me. His fine instruction in quantum electronics, which I received as a senior, was a major factor in my choosing his group to work in two years later.

During my three years as a graduate student, I have had the privilege of working with a large number of people in our group. I would especially like to thank C. S. Hong, Pochi Yeh, Willie Ng and Pinchas Agmon for their cooperation and guidance during various phases of my work. The advice of Alexis Livanos of Hughes Research Center and Al Cho of Bell Labs was also invaluable.

It is a pleasure to acknowledge the skillful technical assistance of Desmond Armstrong, as well as the fine typing job of Ruth Stratton and Verona Carpenter in preparing the manuscript.

Generous financial support from the John and Fannie Hertz Foundation is especially appreciated, and allowed me total freedom in completing my Ph.D.

Finally, I wish to thank my parents for their financial support during my undergraduate years at the California Institute of Technology. More important than financial support, however, was the constant moral support and encouragement I received from my father over the last seven years. His character and example will always be admired.

ABSTRACT

The first part of this work describes the uses of aperiodic structures in optics and integrated optics. In particular, devices are designed, fabricated, tested and analyzed which make use of a chirped grating corrugation on the surface of a dielectric waveguide. These structures can be used as input-output couplers, multiplexers and demultiplexers, and broad band filters.

Next, a theoretical analysis is made of the effects of a random statistical variation in the thicknesses of layers in a dielectric mirror on its reflectivity properties. Unlike the intentional aperiodicity introduced in the chirped gratings, the aperiodicity in the Bragg reflector mirrors is unintentional and is present to some extent in all devices made. The analysis involved in studying these problems relies heavily on the coupled mode formalism. The results are compared with computer experiments, as well as tests of actual mirrors.

The second part of this work describes a novel method for confining light in the transverse direction in an injection laser. These so-called transverse Bragg reflector lasers confine light normal to the junction plane in the active region, through reflection from an adjacent layered medium. Thus, in principle, it is possible to guide light in a dielectric layer whose index is lower than that of the surrounding material. The design, theory and testing of these diode lasers are discussed.

TABLE OF CONTENTS

Part I

APERIODIC STRUCTURES IN OPTICS AND INTEGRATED OPTICS

PART I

APERIODIC STRUCTURES IN OPTICS AND INTEGRATED OPTICS

Chapter 1

GENERAL INTRODUCTION

1.1 Integrated Optics and Optical Communication--Introduction

The invention of the laser almost twenty years ago brought with it the possibility of optical communication. There were, however, many problems to overcome. The optical communication systems, as envisioned at that time, consisted of bulky, heavy components requiring careful alignment and protection from temperature fluctuations and vibrations. The most difficult problem to overcome was that of the high attenuation of light propagating in the atmosphere or in existing glass fibers. The major breakthrough came with the chemical vapor deposition techniques that enabled Corning to produce fibers with losses as low as 1 or 2 dB/km. The alignment and vibration problems have been largely overcome by the technique of integrated optics; that is, fabricating optical components on a small chip where light is waveguided in a thin film from one fixed optical component to the next.

There are a number of advantages in optical communication. There are large savings in size, weight, power consumption and cost; silicon is much lighter and cheaper than copper. Furthermore, no ground loop problem exists and the system is free from electromagnetic interference. These advantages are important for applications ranging from aeronautics and avionics to the telephone industry.

The greatest advantage of optical communication, however, is the extremely large bandwidth and high data rates possible. The evolution of increasing carrier frequency started with AM radio in the kHz range, proceeded to FM transmission in the MHz range, and on to microwaves in the GHz range. The carrier frequency available if optical methods are

used is almost one million GHz. That is, if methods can be found to modulate, transmit and process the optical signals, a factor of almost one million can be gained in the data rate over that of microwave communication.

There are many problems to be overcome if such high data rates are to be realized. One of the principal problems is that of pulse spreading or broadening in a fiber, which is a result of multimode group delay or material dispersion. Figure 1.1 shows three kinds of fibers which can be used.[1] Figure 1.1b is a multimode fiber and a pulse will typically spread at a rate of 50 nsec/km as a result of multimode group delay. This sets an upper limit of about 20 MHz in pulse rate for a one kilometer long fiber. If the index of the multimode fiber is graded as in Figure 1.1c, the pulse rate can be increased to about 2 GHz. For maximum data rates, however, a single mode fiber as in Figure 1.1a must be used. The main source of pulse spreading in this fiber is material dispersion, and for a single mode injection laser with a frequency width of 1Å, 100 GHz data rates should be possible over a one kilometer long fiber.

The light source for the system should have adequate output power, long lifetime, high efficiency, ease of modulation, low cost and fiber compatibility. The double heterostructure diode laser is superior to the LED and solid state laser in these requirements. The rise time of the injection laser is a fraction of a nanosecond (due to the finite carrier recombination time), thus making direct modulation of up to several hundred megahertz possible. This may be sufficient for multimode fibers, but in order to take advantage of the small pulse spread in single mode fibers, external modulators may be employed.

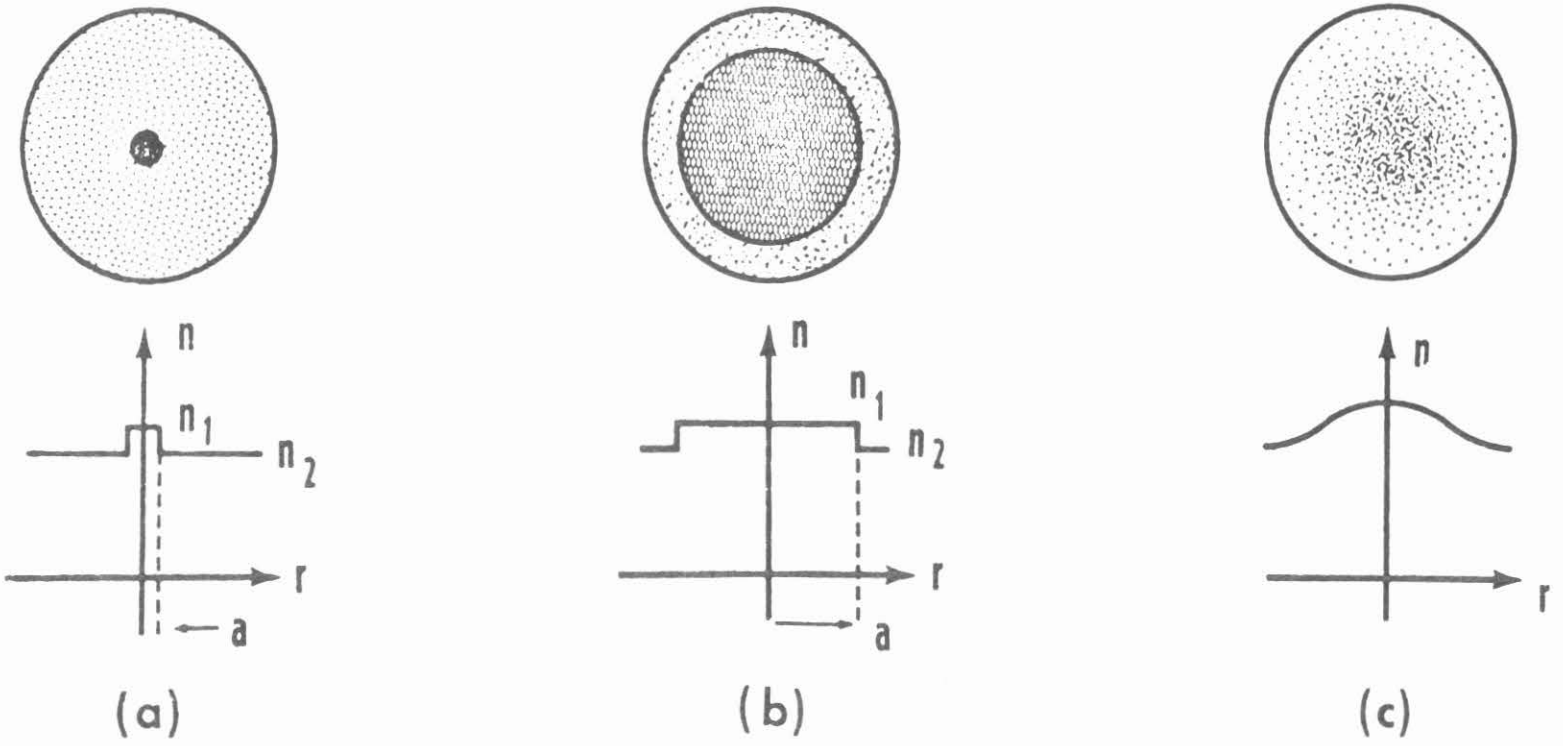

Fig. 1.1 Cross-sectional sketches of principal fiber types and their refractive index profiles for (a) single-mode step index fiber, (b) multimode step index fiber, and (c) multimode graded index fiber.

One of the best materials to use for modulation, switching and guiding of light is $LiNbO_3$. It has a high electrooptic coefficient, and directional couplers can be used to efficiently switch light from one channel to another. Guides operating near cutoff can be made to guide light or radiate light, depending on whether an external voltage is applied. Lens, prisms, beam splitters and gratings can all be fabricated on the $LiNbO_3$ processing chip. A large part of this thesis investigates the uses of gratings and in particular chirped gratings in the processing of optical signals.

1.2 Periodic Structures

The study of periodic structures in nature, as well as man-made structures, has occupied scientists since before the time of Lord Rayleigh in the 19th century.[2] The interaction of various kinds of waves, from sound to electromagnetic to quantum mechanical, with periodic structures plays an important part in our understanding of nature. The special properties of periodically stratified media have been used to make devices ranging from electric filters to linear accelerators to distributed feedback lasers.

Our study and understanding of crystals are largely based on the interaction of these crystals with x-rays. In 1928 Bloch[3] generalized the results of Floquet and formulated the basis of a theory of electrons in crystals.

The mechanical and structural engineer must understand the properties of periodic structures if he is to understand the interaction of a bridge or skyscraper with its surroundings.[4,5] Even the biologist

encounters layered media when he studies nature. The cornea of a horsefly eye is coated with a periodic set of layers and the rhabdom of a Buckeye butterfly eye or the rhabdom of a skipper eye has reflecting filters.[6]

However, it is the man-made device or technological application of periodic structures which most interests an applied physicist or engineer. The material scientist may work with zeolite crystals and superlattices which can now be grown with molecular beam epitaxy.[7-11] The high energy physicist will corrugate a linear accelerator in order to slow the microwave to a velocity comparable to that of the particle being accelerated.[12] In order to perform the complementary function and remove energy from a beam of particles and convert it to electrical energy, the electrical engineer uses the traveling wave tube.[13] Electrical filters, pulse compressors, and antenna arrays are further applications of periodic structures in electrical engineering.

Perhaps no other field makes greater use of layered media than optics where reflectors, filters, antireflection coatings, polarizers, pulse compressors and beam splitters are used extensively.[14] In integrated optics and integrated surface acoustics the distributed feedback laser (DFB),[15-17] distributed Bragg reflector laser (DBR),[18,19] second harmonic generator, mode converter,[20,21] grating coupler,[22,23] deflector,[24,25] transducer and modulator[21,26] are all familiar devices.

There are several methods of analysis available for the propagation of waves in periodically stratified media. They include the use of the Floquet theorem,[27] Hill and Mathieu functions and differential equations,[6,28] the transfer matrix and matrix multiplication,[14,29] and the coupled mode formalism.[30,31]

Because of the ease and versatility of the coupled mode equations, these equations will be used extensively in this work. They are easily adaptable to the study of aperiodic structures and, although they do not give exact solutions as do other methods, they give accurate closed form solutions in many cases of practical interest. An outline of this important method is given in Appendix 1-B.

1.3 Aperiodic Structures and Outline of Thesis Part I

As can be seen from the previous survey, the field of periodic structures has been studied extensively for over one hundred years, and thousands of articles, books and theses have dealt with the topic. By contrast, aperiodic structures, or almost periodic structures, have been largely ignored until quite recently. One of the main reasons for the lack of literature on the subject is due to the mathematical difficulty in solving problems involving aperiodic devices. Most of the previously mentioned methods cannot be used, except perhaps if perturbation techniques are employed. It is the purpose of Part I of this thesis to study practical aperiodic devices in optics and integrated optics. Aperiodicity in a device can be of two varieties; intentional or unintentional. In the class of intentional aperiodicity, we will describe the use of chirped gratings on the surface of dielectric waveguides. A chirp is simply a monotonic variation in the period of a grating. The concept of chirping is familiar to electrical engineers who have studied radar. It was used in Great Britain during World War II to measure weak reflected radar signals reflected from distant targets.

In Figure 1.2a,b,c a chirped pulse is emitted, reflected from a distant target and enters a dispersive element. If the lower frequency

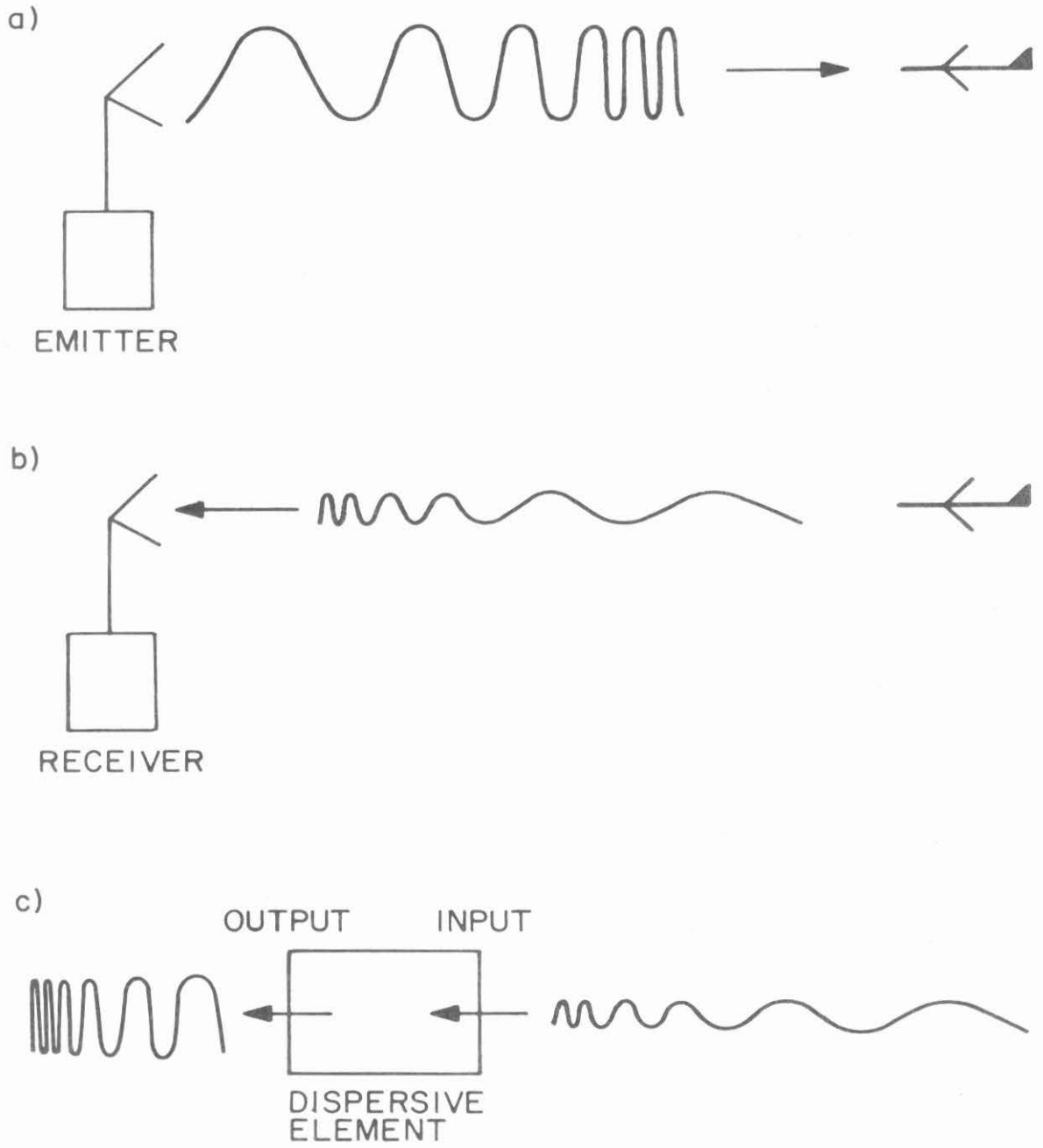

Fig. 1.2 a) Chirped radar pulse being emitted. b) Pulse after reflection from target. c) Pulse amplitude is increased after propagation through a dispersive element.

longer wavelength part of the signal travels faster in the dispersive element than the shorter wavelength, then the pulse is compressed and the increased amplitude can be detected more easily.

Figure 1.3a shows light guided in a dielectric waveguide. The light is confined inside the guiding layer by total internal reflection from the dielectric interfaces. A summary of the analysis of this guiding is presented in Appendix 1-A. Figure 1.3b shows a chirped grating which has been etched on the air-guide interface of the structure. The possible effects of such a corrugation are shown in Figures 1.4 and 1.5. In Figure 1.4a the light is coupled out of the guide and focused along a line normal to the plane of the paper.[32] In Figure 1.4b the light is reflected straight back and remains inside the guide.[33,34] It should be noted that an output coupler similar to that in Figure 1.4a, but with uniform grating, couples out a plane wave rather than a focused wave. Similarly a reflector such as that shown in Figure 1.4b, but with uniform corrugation, will also reflect light, but over a much narrower bandwidth; that is, the use of chirped grating produces a broad band filter and will reflect light over a wide frequency range, while the uniform grating will only reflect a tiny frequency range proportional to the reciprocal of the length of the corrugated region. The design, fabrication, and analysis of these two devices is presented in Chapters 2 and 3.

Figure 1.5 indicates a third use of such a device. Here the normal to the grating makes an angle α ($\alpha \simeq 45°$) with respect to the sides of the waveguide. When light is coupled into the guide parallel to the edge it is reflected in the plane of the guide as shown in the figure. Since the grating is chirped, different wavelengths of

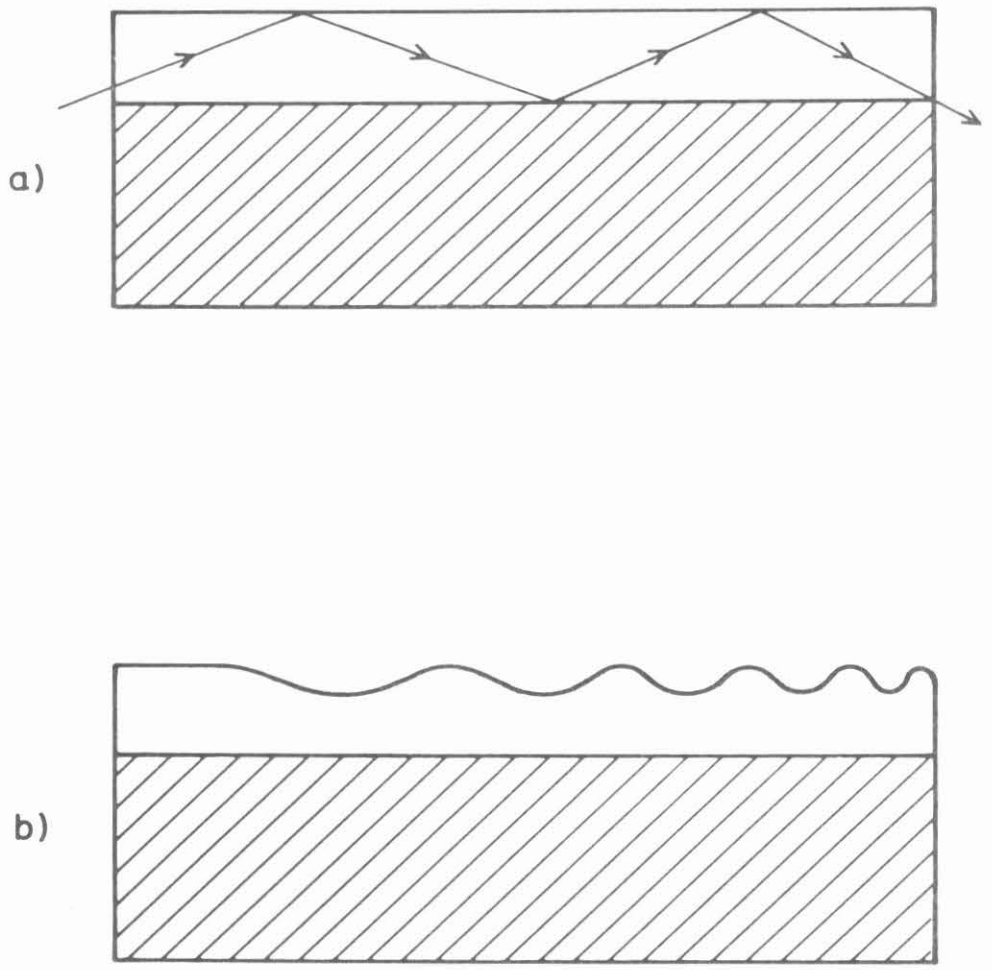

Fig. 1.3 a) Light guided inside a dielectric waveguide.
b) Chirped grating etched on the surface of a dielectric waveguide.

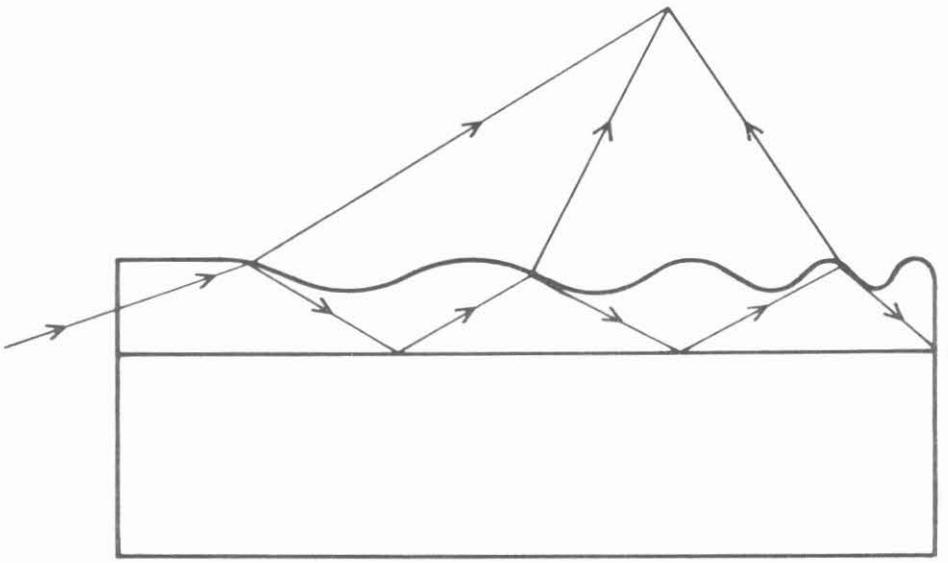

a) Output Coupler

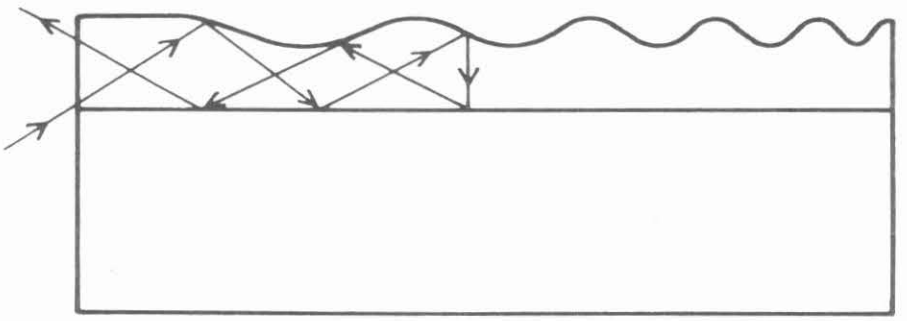

b) Reflector or Broad Band Filter

Fig. 1.4 a) Chirped grating used as an output coupler.
b) Chirped grating of smaller period being used as a broad band filter.

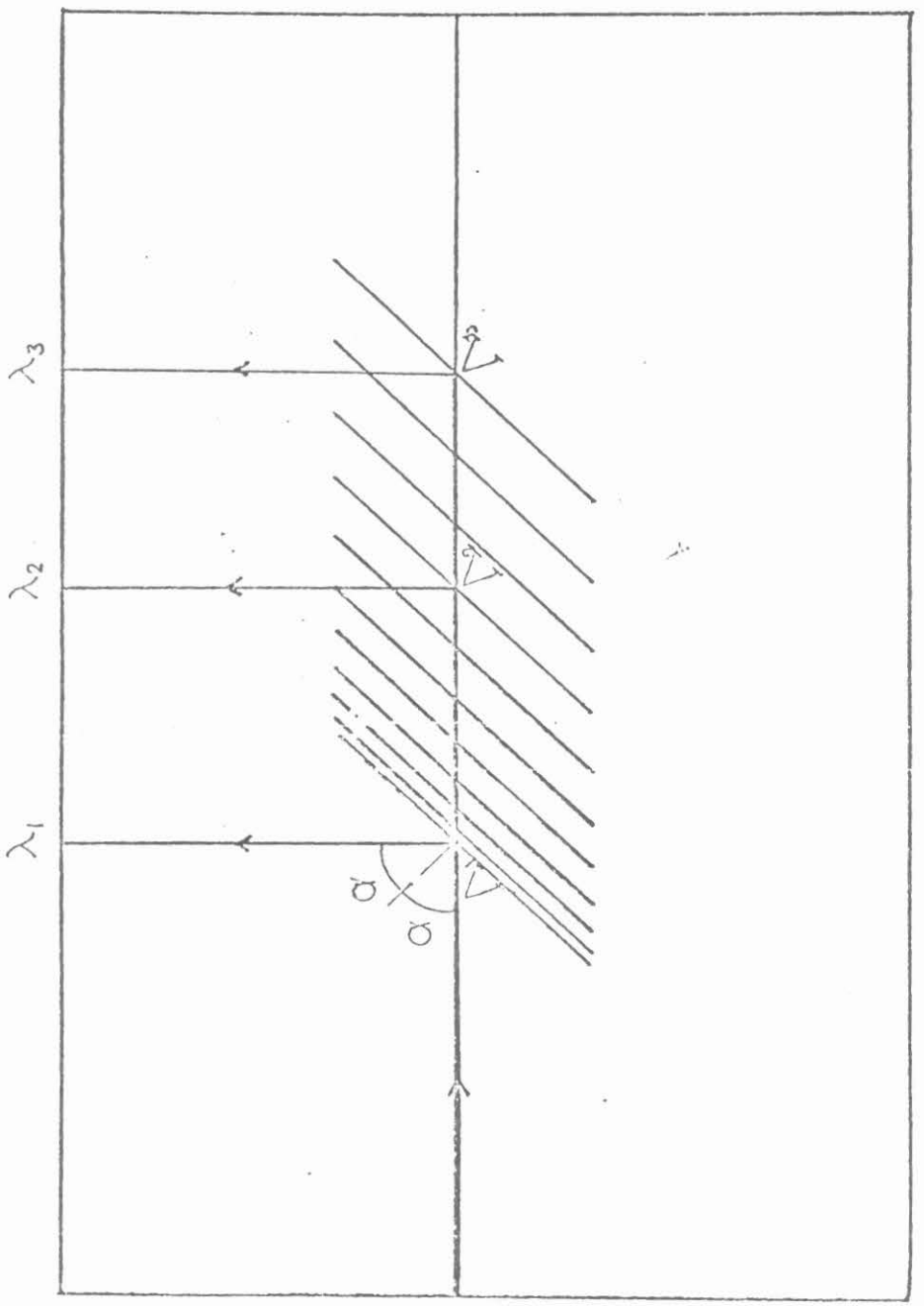

Fig. 1.5 Wavelength Multiplexer and Demultiplexer

light will be reflected from different locations along the grating; short wavelengths are reflected from the left side where the grating period is small, while longer wavelengths are reflected from the right side where the grating period is longer.[35] The condition $\lambda = 2n_{eff} \Lambda \cos \alpha$ is simply the Bragg condition and is familiar to those who have studied x-ray diffraction. The device thus acts as a multiplexer or demultiplexer. If a multiplexed signal is coupled into the left side of the guide, the various components, λ_1, λ_2, λ_3, will separate. Conversely, if several frequencies are coupled into the guide from above at various positions, they can be combined and coupled into one optical fiber joined to the left edge of the guide.

In Chapter 5 additional aperiodic structures are presented, including a review of the work of others, notably Streifer and co-workers, Kogelnik, Kock, Cross and Apfel. Topics covered are the effects on the gain in distributed feedback lasers of chirped grating or, what is equivalent, the tapering of the thickness of the guiding layer. Also considered are the effects of tapering grating depth (constant period) and period variation in dielectric mirrors so as to reduce the electric field intensity inside high power laser mirrors.

The second class of aperiodic structures consists of "unintentional" period variations. For example, <u>any</u> dielectric layered medium made by man is aperiodic. It is not possible to manufacture perfect structures, and the effect of these imperfections is analyzed in Chapter 4 . The coupled mode equations are used in this statistical analysis of Bragg reflectors and the results compared with a computer experiment in which

1500 different mirrors are analyzed and average properties determined. As expected, the peak reflectivity decreases and the bandwidth widens for these imperfect structures.[36]

Chapter 1 References

1. H. Hodara, Fiber and Integrated Optics (Crane, Russak and Co., Inc., New York, 1977).
2. L. Rayleigh, Phil. Mag. 24, 145 (1887).
3. F. Bloch, Z. Phys. 52, 555 (1928).
4. M. A. Heckel, J. Acoust. Soc. Amer. 36, 1335 (1964).
5. D. J. Mead, Shock Vibr. Bull. 35, 45 (1966).
6. An excellent and comprehensive review article on periodic structures is found in the work of Charles Elachi: C. Elachi, IEEE Proc. 64, 1666 (1976).
7. L. Esaki and L. L. Chang, Phys. Rev. Lett. 33, 495 (1974).
8. R. Dingle, A. C. Gossard and W. Wiegmann, Phys. Rev. Lett. 34, 1327 (1975).
9. J. P. Van der Ziel et al, Appl. Phys. Lett. 26, 463 (1975).
10. K. Fischer and W. M. Meier, Fortschr. Mineral 42, 50 (1965).
11. W. M. Meier, SCI Monograph on Molecular Sieves 10 (1968).
12. P. M. Lapostolle, Linear Accelerators (North Holland Pub. Co., Amsterdam, 1970).
13. J. R. Pierce, Traveling-Wave Tubes (Van Nostrand, New York, 1950).
14. M. Born and E. Wolf, Principles of Optics 4th ed. (Pergamon Press, New York, 1970).
15. H. Kogelnik and C. V. Shank, Appl. Phys. Lett. 18, 152 (1971).
16. C. V. Shank, J. E. Bjorkholm and H. Kogelnik, Appl. Phys. Lett. 18, 395 (1971).
17. J. F. Bjorkholm and C. V. Shank, Appl. Phys. Lett. 20, 306 (1972).
18. F. K. Reinhart, R. A. Logan and C. V. Shank, Appl. Phys. Lett. 27, 45 (1975).

19. H. C. Casey, S. Somekh and M. Ilegems, Appl. Phys. Lett. 27, 142 (1975).

20. L. Kuhn, P. F. Heidrich and E. G. Lean, Appl. Phys. Lett. 19, 428 (1971).

21. Y. Ohmachi, Electron. Lett. 9, 539 (1973).

22. T. Tamir and H. L. Bertoni, J. Opt. Soc. Am. 61, 1397 (1971).

23. S. T. Peng, T. Tamir and H. L. Bertoni, Electron. Lett. 9, 150 (1973).

24. L. Kuhn, M. L. Dakss, P. F. Heidrich and B. A. Scott, Appl. Phys. Lett. 17, 265 (1970).

25. M. Lurikkala and P. Merilainen, Electron. Lett. 10, 80 (1974).

26. J. N. Polky and J. H. Harris, Appl. Phys. Lett. 21, 307 (1972).

27. C. Kittel, Introduction to Solid State Physics 5th ed. (Wiley, New York, 1976).

28. P. M. Morse and H. Feshbach, Methods of Theoretical Physics (McGraw-Hill, New York, 1953).

29. P. Yeh, A. Yariv and C. S. Hong, J. Opt. Soc. Am. 67, 423 (1977).

30. D. Marcuse, Theory of Dielectric Optical Waveguides (Academic Press, New York, 1974).

31. A. Yariv, Quantum Electronics 2d ed. (John Wiley & Sons, New York, 1975).

32. A. Katzir, A. C. Livanos, J. B. Shellan and A. Yariv, IEEE J. Quantum Electron. 13, 296 (1977).

33. J. B. Shellan, C. S. Hong and A. Yariv, Opt. Comm. 23, 398 (1977).

34. C. S. Hong, J. B. Shellan, A. C. Livanos, A. Yariv and A. Katzir, Appl. Phys. Lett. 31, 276 (1977).

35. A. C. Livanos, A. Katzir, A. Yariv and C. S. Hong, Appl. Phys. Lett. 30, 519 (1977).

36. J. B. Shellan, P. Agmon, P. Yeh and A. Yariv, J. Opt. Soc. Am., to be published January 1978.

Appendix 1-A

In this appendix we outline the solution for the electric field and propagation constant inside a dielectric slab waveguide. We consider only the case of TE waves ($E_x = E_z = 0$) for confined modes and air radiation modes, since these solutions will be used elsewhere in this thesis. The case of TM waves, as well as substrate radiation modes and leaky waves are solved by A. Yariv and D. Marcuse.[1,2]

Consider the slab structure shown in Figure 1-A.1. The field must satisfy the wave equation

$$\nabla^2 E - \frac{n^2}{c^2} E = 0 \qquad (1\text{-A.1})$$

We assume it has the form

$$E(x,z,t) = E(x)\, e^{i\beta z}\, e^{-i\omega t} \qquad (1\text{-A.2})$$

Combining equations (1-A.1) and (1-A.2) we find

$$\frac{d^2E(x)}{dx^2} + (n^2k^2 - \beta^2)\, E(x) = 0 \qquad (1\text{-A.3})$$

$$k \equiv \frac{\omega}{c} \quad , \quad n_1 > n_2 > n_3$$

This equation must hold in all three regions of the guide. If we first consider the case of a confined wave we get

$$E(x) = A\, e^{-\delta x} \qquad \text{for } x \geq 0 \qquad (1\text{-A.4})$$

$$= A\left[\cos \kappa x - \frac{\delta}{\kappa} \sin \kappa x\right] \qquad \text{for } 0 \geq x \geq -d \qquad (1\text{-A.5})$$

$$= A\left[\cos \kappa d + \frac{\delta}{\kappa} \sin \kappa d\right] e^{\gamma(x+d)} \qquad \text{for } x \leq -d \qquad (1\text{-A.6})$$

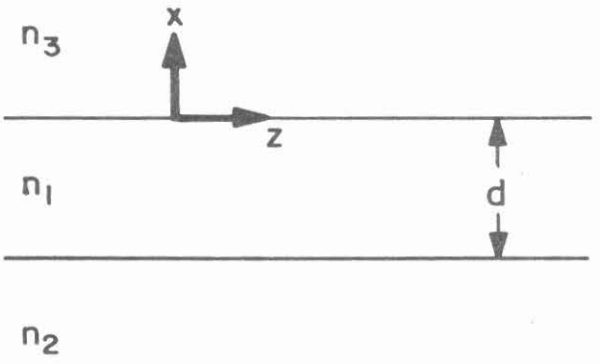

$$n_1 > n_2 > n_3$$

Fig. 1-A.1 Geometry of dielectric slab waveguide

where

$$\kappa = (n_1^2 k^2 - \beta^2)^{1/2} \tag{1-A.7}$$

$$\gamma = (\beta^2 - n_2^2 k^2)^{1/2} \tag{1-A.8}$$

$$\delta = (\beta^2 - n_3^2 k^2)^{1/2} \tag{1-A.9}$$

It is easily verified that these equations satisfy equation (1-A.3) for the three regions and the form was chosen so that E(x) is continuous across x = 0 and x = -d, and $\partial E/\partial x$ is continuous across x = 0. Requiring that $\partial E/\partial x$ also be continuous across x = -d, we can combine equations (5) and (6) and find an eigenvalue equation for the propagation constant β ,

$$\tan \kappa d = \frac{\kappa(\gamma+\delta)}{\kappa^2 - \gamma\delta} \tag{1-A.10}$$

For a guide which carries a total power P, where

$$P = \int_{-\infty}^{\infty} (\vec{E} \times \vec{H})_z \, dx \tag{1-A.11}$$

$$= \frac{\beta}{2\omega\mu_o} \int_{-\infty}^{\infty} |E_y(x)|^2 \, dx \tag{1-A.11}$$

we find a value for the remaining constant A

$$A^2 = \frac{4\kappa^2 \omega\mu_o P}{|\beta|[d + \frac{1}{\gamma} + \frac{1}{\delta}][\kappa^2 + \delta^2]} \tag{1-A.12}$$

Upon examining equations (1-A.4) through (1-A.9) we see that in order to have confined modes we require

$$kn_1 > |\beta| > kn_2, \; kn_3 \tag{1-A.13}$$

If $kn_3 < |\beta| < kn_2$, substrate radiation modes exist; that is, the light is not confined but radiates into the substrate. For the case

$$0 < |\beta| < kn_3 \tag{1-A.14}$$

air radiation modes will exist for which light will radiate both into the substrate and superstrate (air).

We again use the Helmholtz equation given in equation (1-A.3) with β in the range given in equation (1-A.14). The solution is

$$E(x) = G \cos \Delta x + H \sin \Delta x \qquad \text{for } x \geq 0 \tag{1-A.15}$$

$$= L \cos \sigma x + M \sin \sigma x \qquad \text{for } 0 \geq x \geq -d \tag{1-A.16}$$

$$= N \cos \rho(x+d) + P \sin \rho(x+d) \qquad \text{for } x \leq -d \tag{1-A.17}$$

$$\Delta = (n_3^2 k^2 - \beta^2)^{1/2} \tag{1-A.18}$$

$$\sigma = (n_1^2 k^2 - \beta^2)^{1/2} \tag{1-A.19}$$

$$\rho = (n_2^2 k^2 - \beta^2)^{1/2} \tag{1-A.20}$$

Again we match boundary conditions at $x = 0$ and $x = -d$ and are able to eliminate four of the coefficients in equations (15), (16) and (17). We find

$$E(x) = C_r[\cos \Delta x + (\tfrac{\sigma}{\Delta})F_i \sin \Delta x] \qquad \text{for } x \geq 0 \tag{1-A.21}$$

$$= C_r(\cos \sigma x + F_i \sin \sigma x) \qquad \text{for } 0 \geq x \geq -d \tag{1-A.22}$$

$$= C_r[(\cos \sigma d - F_i \sin \sigma d)\cos \rho(x+d) \qquad \text{for } x \leq -d \tag{1-A.23}$$

$$+ \tfrac{\sigma}{\rho} (\sin \sigma d + F_i \cos \sigma d)\sin \rho(x+d)$$

where C_r is again determined by the power carried by the mode, just as in the guided mode case, and F_i can be chosen arbitrarily. Expressions for C_r are given in the main body of the thesis.

References for Appendix 1-A

1. A. Yariv, Quantum Electronics, 2nd ed. (John Wiley and Sons, New York, 1975).

2. D. Marcuse, Theory of Dielectric Optical Waveguides (Academic Press, New York, 1974).

Appendix 1-B

In this appendix we introduce the coupled mode equations in their general form which will be used extensively in this thesis. We start with Maxwell's equations for a non-magnetic bulk material with no external charges or currents.

$$\nabla \times \vec{E} = -\mu_o \frac{\partial \vec{H}}{\partial t} \tag{1-B.1}$$

$$\nabla \times \vec{H} = \frac{\partial}{\partial t} (\varepsilon \vec{E}) \tag{1-B.2}$$

$$\nabla \cdot \vec{H} = 0 \tag{1-B.3}$$

$$\nabla \cdot (\varepsilon \vec{E}) = 0 \tag{1-B.4}$$

where

$\vec{E}$ = electric field

$\vec{H}$ = magnetic field

μ_o = free space magnetic permeability

ε = permittivity of dielectric

After taking the curl of equation (1-B.1) and using equation (1-B.2) we find

$$-\nabla^2 \vec{E} + \nabla(\nabla \cdot \vec{E}) = +\mu_o \varepsilon \omega^2 E \tag{1-B.5}$$

In arriving at (1-B.5) we have assumed ε is constant in time and the time dependence of the electric field is $e^{-i\omega t}$. If we next use equation (1-B.4) we find

$$\nabla^2 \vec{E} + \nabla \left[E \cdot \frac{\vec{\nabla} \varepsilon}{\varepsilon} \right] + n^2 k^2 \vec{E} = 0 \tag{1-B.6}$$

where $n^2k^2 \equiv \mu_o \varepsilon \omega^2$, $k = \frac{\omega}{c}$.

Finally, we will consider, for simplicity, the case of the TE wave, that is $\vec{E} = E \hat{y}$ and an $\varepsilon = \varepsilon(x)$ dependence. The geometry is shown in figures (1-B.2a) and (1-B.2b). With these restrictions eq. (1-B.6) reduces to the familiar Helmholtz equation.

$$\nabla^2 E + k^2 n^2 E = 0 \tag{1-B.7}$$

$$k = \frac{\omega}{c}$$

$$n = n(x) = \text{index of refraction}$$

Next we take the electric field and index of refraction to have the following form

$$E(x,z) = R(x)e^{i\beta z}\, e^{i(\pi/\Lambda_o)x} + S(x)e^{i\beta z}\, e^{-i(\pi/\Lambda_o)x} \tag{1-B.8}$$

$$n^2(x) = n_o^2 + n_1^2 \cos\left(\frac{2\pi}{\Lambda_o} x + \phi(x)\right) \tag{1-B.9}$$

$$\frac{d\phi}{dx} < \frac{2\pi}{\Lambda_o}\ ,\ n_1^2 << n_o^2$$

Since in this derivation we have taken a time dependence $e^{-i\omega t}$, R(x) represents the amplitude of the forward traveling wave, while S(x) is the amplitude of a wave traveling in the backward direction. The form of the index of refraction indicates a stratified media with variation in the x direction. For $\phi = 0$, we have a periodic structure.

Before proceding, a further comment is due regarding the assumed form of the solution taken in equation (1-B.8). From the Floquet theorem

we expect an E field of the following form for $\phi(x) = 0$.

$$E = \sum_{p=-\infty}^{\infty} E_p e^{i\beta z} e^{i(2\pi p/\Lambda_o + \kappa)x} \qquad (1\text{-B.10})$$

If this is substituted into the Helmholtz equation (1-B.7) and terms of similar x dependence are equated we find

$$\left\{\left(\frac{2\pi p}{\Lambda_o} + \kappa\right)^2 + \beta^2 - k^2 n_o^2\right\} E_p = \frac{k^2 n_1^2}{2}\left[E_{p-1} + E_{p+1}\right] \qquad (1\text{-B.11})$$

Furthermore, we are free to restrict $-\frac{\pi}{\Lambda_o} \leq \kappa \leq \frac{\pi}{\Lambda_o}$ in order to obtain a unique solution for (1-B.10). The sum in (1-B.10) represents an infinite sum of forward and backward traveling waves (space harmonics) and equation (1-B.11) indicates that E_p is only coupled to E_{p-1} and E_{p+1} to first order in (n_1^2). The coupling between E_p and E_{p-2} and E_{p+2} is proportional to $(n_1^2)^2$ and so on. Thus to first order in n_1^2, we need only consider a single interaction; that is, E_p interacts with E_{p+q} and E_{p-q} only for q=1. For coupling between a forward and reverse traveling wave, this requires interaction between the smallest positive value of $(\frac{2\pi}{\Lambda_o} p + \kappa)$ and the largest negative value of $(\frac{2\pi}{\Lambda_o}(p-1) + \kappa)$. For κ positive and thus p=0, interaction between the forward traveling space harmonic $e^{i\kappa x}$ and the reverse traveling harmonic $e^{i(\kappa - 2\pi/\Lambda_o)x}$ is dominant. This is the only interaction between a forward and reverse traveling wave to first order in (n_1^2).

Using equation (1-B.11), taking p = -1 and ignoring the non-interacting E_{-2} term, we find

$$E_{-1} = \frac{k^2 n_1^2}{2} \frac{E_o}{(-2\pi/\Lambda_o + \kappa)^2 + \beta^2 - k^2 n_o^2} \qquad (1\text{-B.12})$$

Similarly for p = o equation (1-B.11) becomes

$$E_o = \frac{k^2 n_1^2}{2} \frac{E_{-1}}{\left[\kappa^2 + \beta^2 - k^2 n_o^2\right]} \qquad (1\text{-B.13})$$

For maximum coupling, the denominators in equations (1-B.12) and (1-B.13) should both approach zero. This can only happen when

$$\left(\kappa - \frac{2\pi}{\Lambda_o}\right)^2 \sim \kappa^2 \quad \text{or} \quad \kappa \approx \frac{\pi}{\Lambda_o} \quad .$$

This condition results in maximum interaction between the forward traveling wave $\sim e^{i\pi x/\Lambda_o}$ and the reverse traveling wave $\sim e^{-i\pi x/\Lambda_o}$ and is the reason for the assumed form of equation (1-B.8).

After combining equations (1-B.7) and (1-B.8) we find

$$(k^2 n_o^2 - \frac{\pi^2}{\Lambda_o^2} - \beta^2)(R(x)\, e^{i\beta z}\, e^{i(\pi x/\Lambda_o)} + S(x)\, e^{i\beta z}\, e^{-i(\pi x/\Lambda_o)})$$

$$+2i\,\frac{\pi}{\Lambda_o}\,(\frac{dR(x)}{dx}\, e^{i\beta z}\, e^{i(\pi x/\Lambda_o)} - \frac{dS(x)}{dx}\, e^{i\beta z}\, e^{-i(\pi x/\Lambda_o)})$$

$$+\frac{k^2 n_1^2}{2}\,(e^{i(2\pi/\Lambda_o)x + \phi(x))} + e^{-i(2\pi x/\Lambda_o) + \phi(x))})(R(x)e^{i\beta z}\, e^{i(\pi/\Lambda_o)x}$$

$$+ S(x)e^{i\beta z}\, e^{-i(\pi/\Lambda_o)x}) = 0 \qquad \text{(1-B.14)}$$

We have assumed $\left|\frac{d^2R}{dx^2}\right| << \left|2\,(\pi/\Lambda_o)\,\frac{dR}{dx}\right|$ and $\left|\frac{d^2S}{dx^2}\right| << \left|2\,(\pi/\Lambda_o)\frac{dS}{dx}\right|$ and thus neglected these terms in equation (1-B.4). An inspection of equation (1-B.14) indicates terms with x dependence $e^{i(\pi x/\Lambda_o)}$ and $e^{-i(\pi x/\Lambda_o)}$. We can thus separate equation (1-B.14) into two equations, each equation containing only coherent terms. This is the coupled mode approximation.

$$\frac{dR}{dx} - i\,\delta\,R = -\,\eta\,S\,e^{i\phi}$$

$$\frac{dS}{dx} + i\,\delta\,S = -\,\eta^*\,Re^{-i\phi} \qquad \text{(1-B.15)}$$

with $$\delta \equiv \frac{(k^2 n_o^2 - \frac{\pi^2}{\Lambda_o^2} - \beta^2)}{2\pi/\Lambda_o} \qquad (1\text{-B.16})$$

$$\eta \equiv -i\,\kappa = \frac{-ik^2 n_1^2\,\Lambda_o}{4\pi} \qquad (1\text{-B.17})$$

These are the coupled mode equations. The term δ is often referred to as the phase mismatch term and must be near zero for effective interaction between the forward and backward traveling waves. The quantity η is the coupling constant and depends on the amplitude of the modulation of the refractive index.

If we make the substitution

$$R(x) \equiv R'(x)\, e^{i\delta x}$$
$$S(x) \equiv S'(x)\, e^{-i\delta x} \qquad (1\text{-B.18})$$

the equations can be put in a more compact form which is often easier to use

$$\frac{dR'}{dx} = -\eta\, S'\, e^{i(\phi - 2\delta x)}$$
$$\frac{dS'}{dx} = -\eta^*\, R'\, e^{-i(\phi - 2\delta x)} \qquad (1\text{-B.19})$$

This form also provides an obvious physical interpretation of $|n|$

$$|n| = \left|\frac{dS'/dx}{R'}\right| = \left|\frac{\text{amplitude reflected/unit length}}{\text{amplitude incident}}\right| \quad (1\text{-B.20})$$

From equation (1-B.13) we have for $n_1^2 << n_o^2$ and $\phi = 0$

$$n(x) \approx n_o + \frac{n_1^2}{2n_o} \cos\left(\frac{2\pi}{\Lambda_o} x\right) \quad (1\text{-B.21})$$

It is well known that light incident with electric field parallel to the dielectric discontinuity is reflected with the amplitude

$$\frac{n_L \cos\theta_L - n_R \cos\theta_R}{n_L \cos\theta_L + n_R \cos\theta_R} \quad (1\text{-B.22})$$

Where θ is the angle of incidence and quantities with L and R subscripts refer to regions on the left and right side of the discontinuity. For small discontinuities equation (1-B.22) can be replaced with

$$\frac{\Delta(n \cos\theta)}{2n \cos\theta} = \frac{\Delta n}{2n \cos^2\theta} \quad (1\text{-B.23})$$

Snell's law ($n \sin\theta$ = constant) was used for the right side of equation (1-B.23) and

$$\Delta n = n_L - n_R \ , \ n = \frac{n_L + n_R}{2} \ .$$

Thus for the continuous case being considered, an amplitude $\frac{\frac{dn(x)}{dx}\,dx}{n(x)\cos^2\theta}$ is reflected from a slab of thickness dx. If this is summed over one period, with the phase factor included, we find an expression for the amplitude of light reflected per unit length.

$$\left|\frac{\text{amplitude reflected/unit length}}{\text{amplitude incident}}\right| = \frac{1}{\Lambda_o}\left|\int_0^{\Lambda_o} \frac{\frac{dn}{dx}\, e^{2ik_x x}}{2n\cos^2\theta}\, dx\right|$$

$$= \frac{\pi n_1^2}{2 n_o^2 \Lambda_o^2 \cos^2\theta}\left|\int_0^{\Lambda} \sin\frac{2\pi}{\Lambda_o}\, x\, e^{i(2\pi/\Lambda_o)x}\right| = \frac{\pi n_1^2}{4 n_o^2 \Lambda_o \cos^2\theta}$$

In arriving at equation (1-B.24) we have taken the x component of the wave-vector $k(k_x)$ as being equal to π/Λ_o, and have considered only the case of the incident electric field being parallel to the slab layers (TE modes). That is, the device is a "quarter wave stack" ($k_x^2 \equiv k^2 n_o^2 - \beta^2$). Referring to Figure 1-B.1, we see $k \simeq \frac{\pi}{n_o \Lambda_o \cos\theta}$ and the expression in equation (1-B.24) reduces to $(k^2 n_1^2 \Lambda_o)/4\pi$ which is in agreement with equation (1-B.17) for

$$|n| = \frac{k^2 n_1^2 \Lambda_o}{4\pi}$$

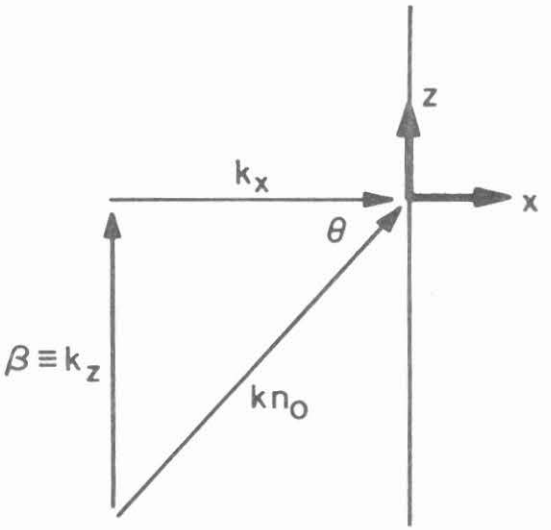

$$\cos\theta = \frac{k_x}{kn_o}$$

$$k^2 n_o^2 - \beta^2 = k_x^2$$

$$\delta = \left(k_x^2 - \frac{\pi^2}{\Lambda_o^2}\right) \frac{\Lambda_o}{2\pi}$$

$$k_x \approx \frac{\pi}{\Lambda_o}$$

Fig. 1-B.1 Wavevector geometry and relationships

The case of finding $|\eta|$ for a slab structure with actual dielectric discontinuities is straightforward. (See Figure 1-B.2b.) If the reflection from each dielectric interface is r_1, then

$$|\eta| = \frac{r_1}{\Lambda_{o/2}} \approx \frac{2(n_L - n_R)}{\Lambda_o(n_L + n_R)\cos^2\theta} \qquad (1\text{-B.25})$$

If we take $n_L = n_o + \frac{n_1^2}{2n_o}$ and $n_R = n_o - \frac{n_1^2}{2n_o}$ equation (1-B.15) becomes

$$|\eta| \approx \frac{2n_1^2}{n_o^2 \Lambda \cos^2\theta} \qquad (1\text{-B.26})$$

Taking the ratio of $|\eta|$ given in equation (1-B.24) and (1-B.26) gives

$$\frac{\eta(14)}{\eta(16)} = \frac{\pi}{4} \qquad (1\text{-B.27})$$

This was to be expected, since the slab structure can be Fourier decomposed into a series of sinusoidal variations and the amplitude of the first harmonic is $\frac{4}{\pi}$.

A final important case to consider, after the previous cases of slab structures, is that of waveguiding in a thin film with a periodic perturbation on a surface, leaking to the transfer of power from one mode to another (Figs. 1-B.2c,d). Note that now, in order to follow convention the coordinate system has been changed with the periodicity in the z direction. Again the coupled mode equations provide an excellent means of analyzing the phenomenon. Expressions for the coupling

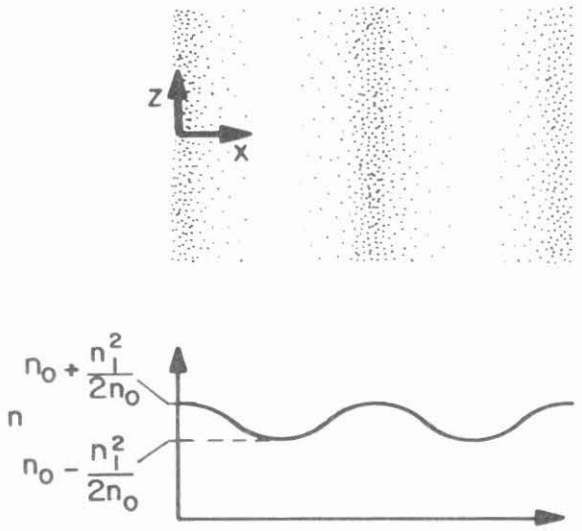

a) Index profile for a sinusoidal slab reflector (Note coordinate system used for slab structure)

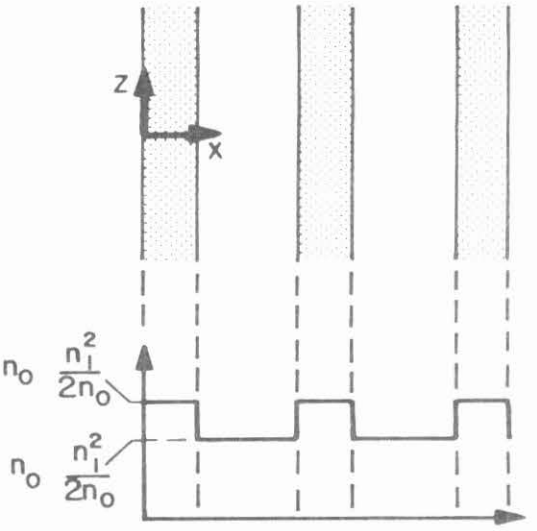

b) Index profile for a discontinuous slab reflector

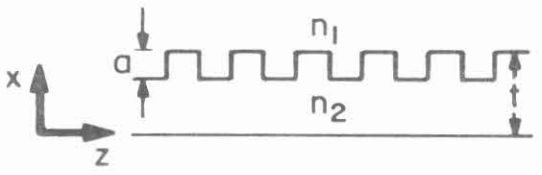

c) Cross section of a dielectric waveguide with square wave perturbation (Note coordinate system used for waveguide structure)

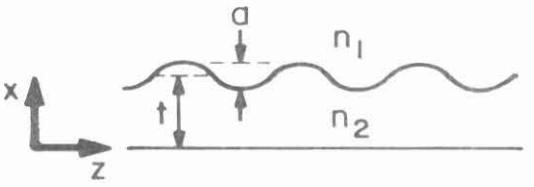

d) Cross section of a dielectric waveguide with sinusoidal surface perturbation

Fig. 1-B.2 Slab and guiding structures for which the coupled mode equations are applicable.

constant η have been given by several authors. A. Yariv [1] has found that for well confined modes and a "square wave" surface corrugation between a guide of index n_2 and a superstrate of index n_1, the coupling constant for contradirectional coupling is given by

$$|\eta| = \frac{2\pi^2 m^2}{3\ell\lambda} \frac{(n_2^2 - n_1^2)}{n_2} \left(\frac{a}{t}\right)^3 \left[1 + \frac{3}{2\pi} \frac{\lambda/a}{(n_2^2 - n_1^2)^{1/2}}\right.$$

$$\left. + \frac{3}{4\pi^2} \frac{(\lambda/a)^2}{n_2^2 - n_1^2)}\right] \qquad (1\text{-B.28})$$

where

a = height of square wave perturbation

t = waveguide thickness

ℓ is an integer given by $\beta_m = \frac{\ell\pi}{\Lambda_o}$ with β_m the propagation constant of the $m^{\underline{th}}$ order mode ($m = 1,2,\ldots$)

λ = wavelength of light

In a slightly different analysis Yen [2] has arrived at the following equation for the contradirectional coupling constant for the $m^{\underline{th}}$ mode for a square wave surface perturbation.

$$|\eta| = \frac{\omega\varepsilon_o \sin\frac{\ell\pi}{2}}{4\pi\ell} \int_{-a}^{0} (n_2^2 - n_1^2)\left|E_y^m(x)\right|^2 dx$$

$$= \frac{\sin\frac{\pi\ell}{2}}{\pi\ell\ \beta_m\ t_{eff}} \left\{ \frac{a}{2}(n_2^2 - n_1^2)k^2 + \frac{\sin(2\kappa_m a)}{4\kappa_m}(\kappa_m^2 - \delta_m^2) + \frac{\delta_m}{2}(1 - \cos(2\kappa_m a)) \right\} \qquad (1\text{-B.29})$$

where t_{eff} is the effective width of the guide

$$= t + \frac{1}{\gamma_m} + \frac{1}{\delta_m}$$

κ_m, δ_m, γ_m defined in Appendix 1-A.

m subscript denotes the m^{th} mode

ℓ defined through $\beta_m = \frac{\ell\pi}{\Lambda_o}$

If $a << t$ we can find an approximate expression for $|\eta|$ to first order in a as

$$|\eta| = \frac{\kappa_m^2 a}{\pi\ell\ \beta_m\ t_{eff}} \qquad \ell = 1,3,5 \qquad (1\text{-B.30})$$

In a similar manner, for a sinusoidal corrugation (Figure 1-B.2d), Flanders [3] has shown

$$|\eta| = \frac{a\ \kappa_m^2}{4\ \beta\ t_{eff}} \qquad (1\text{-B.31})$$

Once again, if we take the ratio of $\eta_{sinusoidal}$ to η_{square} we find the same result as for slab structures; again because the square well can be Fourier decomposed into sinusoidal functions with the amplitude of the first Fourier harmonic being $\frac{4}{\pi}$.

$$\left|\frac{\eta_{sinusoidal}}{\eta_{square}}\right| = \frac{\pi}{4} \tag{1-B.32}$$

Streifer et al.[4] have worked out the calculation of $|\eta|$ for an arbitrary corrugation, including blazed gratings.

We now proceed to give the solution to the coupled mode equation, equation (1-B.19). The boundary conditions on equation (1-B.19) for a stratified structure extending from x = 0 to x = L are

$$\begin{aligned} R'(0) &= 1 \\ S'(L) &= 0 \end{aligned} \tag{1-B.33}$$

The solutions to the equations for the case $\phi(x) = 0$ are

$$S'(x) = \frac{-i\eta^* e^{+i\delta x} \sinh[T(x - L)]}{\delta \sinh(TL) + i T \cosh(TL)} \tag{1-B.34}$$

$$R'(x) = \frac{e^{-i\delta x}}{\delta \sinh(TL) + i T \cosh(TL)} \{ - \delta \sinh[T(x - L)] + i T \cosh[T(x - L)]\} \tag{1-B.35}$$

where $T \equiv \sqrt{\kappa^2 - \delta^2}$

$\kappa \equiv - i\eta$ = real number

For waveguide structures with the periodicity along the length of the guide, it is customary to define the direction along the length of the guide as the z axis (see Fig. 1-B.2). In this case $S'(x) \rightarrow S'(z)$ and $R'(x) \rightarrow R'(z)$ in equation (1-B.34) and (1-B.35).

Figure 1-B.3[2] is a plot of the incident field $R(z) = E_i(z)$ and reflected field $S(z) = E_r(z)$ for $\kappa L = 1.0$ and $\kappa L = 4.0$ indicating the effect of increasing coupling.

Except for special cases, such as $\phi(x)$ being quadratic in x[5] or $\phi(x)$ being a very small perturbation,[6] equations (1-B.15) cannot be solved exactly. They can, however, be transformed into a first order nonlinear Riccati equation[7] which can easily be solved by numerical means. We first make a change in variables

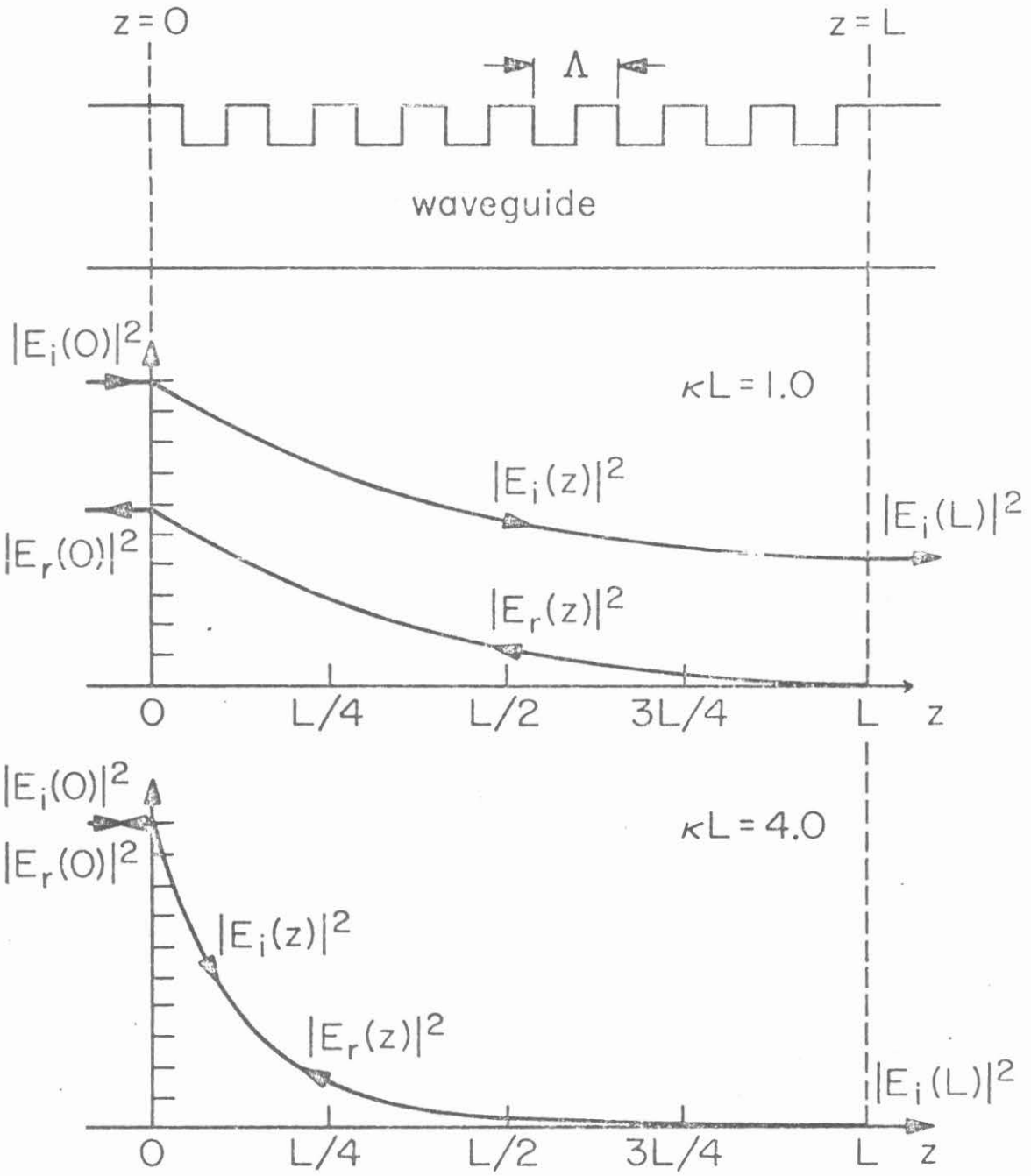

Fig. 1-B.3 The behavior of $|E_i(z)|^2$ and $|E_r(z)|^2$ in a periodic waveguide with $\kappa L = 1.0$ and 4.0 ($\Delta\beta = 0$). (From reference 2.)

$$\rho \equiv \frac{S}{R} e^{i\phi} \tag{1-B.36}$$

The x-derivative of this is

$$\frac{d\rho}{dx} = \left(\frac{dS/dx}{R} - \frac{S\frac{dR}{dx}}{R^2} + i\frac{d\phi}{dx}\frac{S}{R}\right)e^{i\phi} \tag{1-B.37}$$

After combining this with equation (1-B.5) we find

$$\frac{d\rho}{dx} = i\left(-2\delta + \frac{d\phi}{dx}\right)\rho + \eta(1 + \rho^2) \tag{1-B.38}$$

The boundary condition on equation (1-B.38) is $\rho(L) = 0$ and the reflection coefficient $\rho(0)$ is the quantity of interest. Some of the important numerical results are presented elsewhere in this thesis.

This appendix has merely been an outline of some features of the coupled mode formalism. Additional details can be found in the references.

References for Appendix I-B

(1) A. Yariv, Quantum Electronics, 2nd ed., (John Wiley and Sons, New York, 1975), p. 515.

(2) H. Yen, Ph.D. Thesis, California Institute of Technology, (1976), p. 23.

(3) D. Flanders, H. Kogelnik, R. V. Schmidt, and C. V. Shank, Appl. Phys. Lett. 24, 194 (1974).

(4) W. Streifer, D. Scifres, and R. D. Burnham, IEEE J. Quantum Electron. 11, 867 (1975).

(5) See appendix

(6) W. Streifer, D. R. Scifres, and R. D. Burnham, J. Opt. Soc. Am. 66, 1359 (1976).

(7) H. Kogelnik , Bell. Syst. Tech. J. 55, 109 (1976).

(8) A. Yariv, IEEE J. Quantum Electron. 9, 919 (1973).

(9) H. Kogelnik, Bell Syst Tech. J. 48, 2909 (1969).

(10) H. Kogelnik and C. V. Shank, J. Appl. Phys. 43, 2327 (1972).

(11) D. Marcuse, Bell Syst. Tech. J. 48, 3187 (1969).

(12) D. Marcuse, Theory of Dielectric Optical Waveguides (Academic Press, New York, 1974).

(13) J. B. Shellan, P. Agmon, P. Yeh, and A. Yariv, (to be published Jan. 1978 J. Opt. Soc. Am.).

(14) A. Katzir, A. C. Livanos, J. B. Shellan and A. Yariv, IEEE J. Quantum Electron. 13, 296 (1977).

Chapter 2

BROAD-BAND FILTERS

2.1 Introduction

In this chapter the properties of a dielectric waveguide with a chirped corrugation with periods approximately 2000Å are studied. The period of the grating is such that guided light is retroreflected in the guide; that is, a mode which propagates with a z dependence $e^{i\beta_o z}$ will interact with the grating and be converted into a mode which propagates as $e^{-i\beta_o z}$. Figure 1.4 of Chapter 1 illustrates this effect. The chirp in the grating has the effect of reflecting a broad band of frequencies. This tends also to decrease the amount of light reflected at any one frequency, thus allowing a simple analysis based on direct integration of the coupled mode equations and the use of the method of stationary phase. More exact results follow if asymptotic expansion of the parabolic cylinder functions are used.

The fabrication and testing of several broad-band filters is covered and the experimental results are found to be in excellent agreement with theory.

2.2 Theory of Broad-Band Filters

Following coupled mode theory, we assume the field in the guide can be represented by

$$E(z) = R(z)e^{-i(\pi/\Lambda(0))z} + S(z)e^{i(\pi/\Lambda(0))z} \qquad (2.1)$$

R and S are the complex amplitudes of the forward and backward traveling modes under consideration, and $\Lambda(0)$ is the grating period at z = 0. If

the guide is multimode we assume that the corrugation is such that the only interaction is between a particular forward and reverse traveling mode and that these do not couple to the other modes.

These amplitudes are related by the usual coupled mode equations which were presented in Appendix 1-B (eq. 1-B.5).

$$\frac{dR}{dz} - i\delta R = - \eta S e^{+i\gamma z^2} \tag{2.2}$$

$$\frac{dS}{dz} + i\delta S = - \eta^* R e^{-i\gamma z^2} \tag{2.3a}$$

$$\eta \equiv i\kappa, \ \kappa \text{ is real} \tag{2.3b}$$

η is the coupling constant which depends on the amplitude of the grating perturbation. The period of the grating can be approximated by

$$\frac{2\pi}{\Lambda(z)} = \frac{2\pi}{\Lambda(0)} - 2\gamma z \tag{2.4}$$

where Λ is the grating period and γ is the chirp factor of the grating. δ is the phase mismatch and $\delta = \frac{\pi}{\Lambda(0)} - \beta_o$. β_o is the propagation constant of the unperturbed guide. In uniform grating δ must be small if we are to have substantial interaction between the forward and backward traveling waves. This is not necessary for chirped gratings. For large chirps we expect the incident wave to be coupled into the backward running wave for a large range of wavelengths and for many cases the reflection may be small. Setting $S = 0$ in equation (2.2) gives

$R = e^{+i\delta z}$ (unit intensity). We now replace R on the right side of equation (3a) with $e^{+i\delta z}$ and let $S' \equiv Se^{i\delta z}$. This results in

$$\frac{dS'}{dz} = - \eta^* e^{+2i\delta z} \, e^{-i\gamma z^2} \tag{2.3b}$$

Before integrating this equation, we will modify it to include attenuation by replacing δ with $\delta_o + \frac{i\alpha}{2}$, where $\frac{\alpha}{2}$ is the attenuation factor for the wave amplitude.[1]

$$\frac{dS'}{dz} = \eta^* e^{+2i(\delta_o + i\frac{\alpha}{2})z} e^{-i\gamma z^2} \tag{2.3c}$$

We take our grating region between z = 0 and z = L and use the boundary condition S'(L) = 0

$$S'(0) = \int_0^L - \eta^*(z) e^{-i\gamma z^2} e^{+2i(\delta_o + i\frac{\alpha}{2})z} dz \tag{2.5}$$

$$\left|S'(0)\right| = \left| e^{-\alpha\frac{\delta_o}{\gamma}} \int_{-\frac{\delta_o}{\gamma}}^{L - \frac{\delta_o}{\gamma}} \eta(u + \frac{\delta_o}{\gamma}) e^{-\alpha u} e^{i\gamma u^2} du \right| \tag{2.6}$$

Most of the contribution will come from a region of width $\sim \frac{1}{\sqrt{\gamma}}$ centered about u = 0. We thus expand $e^{-\alpha u}$ as $1 - \alpha u + \frac{\alpha^2 u^2}{2}$ and then extend the limits of integration from minus infinity to positive infinity. The result is

$$\left|S'(0)\right|^2 \equiv \text{Reflectivity} = \frac{\pi\kappa^2}{\gamma}(z_B)\ e^{-2\alpha z_B}(1 + \frac{\alpha^4}{16\gamma^2}) \tag{2.7}$$

$$\text{for } 0 < z_B < L$$

$$= 0 \text{ otherwise}$$

where $z_B \equiv \frac{\delta_o}{\gamma}$ is the point where the Bragg condition is satisfied. In almost all cases of interest $\frac{\alpha^4}{\gamma^2} << 1$ and that factor can be dropped in equation (2.7). Alternatively we may write equation (2.7) as:

$$\text{Reflectivity} = \frac{\pi\kappa^2(z_B)}{\gamma} \; e^{-2\alpha z_o} \tag{2.8}$$

where

$$z_o = z_B - \frac{\alpha^3}{32\gamma^2}$$

Note that $z_o < z_B$ for the case of losses ($\alpha > o$) and $z_o > z_B$ for the case of gain ($\alpha < 0$).

If our reflection is not small, equations (2.2) and (2.3a) can be combined to give second order differential equations for R and S. The solutions of these equations are the parabolic cylinder functions,[2] and are presented in Appendix 2-A. By matching the boundary conditions for R and S and using the asymptotic expansions for the parabolic cylinder functions we get

$$\text{Reflectivity} = 1 - e^{-\frac{\pi\kappa^2}{\gamma}} \tag{2.9}$$

This asymptotic expression is good for cases when the Bragg point is far from the grating edges. That is, when $\frac{5\kappa}{\gamma} < z_B < L \; \frac{-5\kappa}{\gamma}$.[3] If losses are included, equation (2.9) must be modified by adding the factor $e^{-2\alpha z_B}$.

Next we will take a specific case corresponding to typical reflection grating made by the author. For small grating depth[4]

$$\kappa = \frac{\pi a}{\lambda_o} \; \frac{n_f^2 - N^2}{2W_{eff}\, N} \tag{2.10}$$

n_c = index of guide cover

n_s = index of substrate

n_f = index of film

$N = \frac{\beta_o}{k_o}$

$\lambda_o = \frac{2\pi}{k_o}$ = wavelength of light in vacuum

$W_{eff} = t + \frac{1}{q_o} + \frac{1}{p_o}$

t = guide thickness

a = grating depth

$q_o = (\beta_o{}^2 - n_c{}^2 k_o{}^2)^{1/2}$

$p_o = (\beta_o{}^2 - n_s{}^2 k_o{}^2)^{1/2}$

If we take the following values

$a = 350$ Å

$n_f = 1.540$

$n_s = 1.510$

$N = 1.524$

$\lambda_o = 6{,}000$ Å

$t = .75$ μ

we get $\kappa \approx 2300\ m^{-1}$.

If we take a chirp of Λ 1960 to 2060 Å over a 1.0 cm length $\gamma = 8 \times 10^7\ m^{-1}$

From equation (2.9), reflectivity = .19; equation (2.8) ($\alpha = 0$) gives reflectivity = .21. This agrees favorably with the experimental results for which the measured reflectivity was 18%.

Thus far we have assumed a linear chirp in $\frac{2\pi}{\Lambda(z)}$. If we do not make this linear approximation[5]

$$\frac{2\pi}{\Lambda(z)} = \frac{2\pi}{\lambda}\left[\sin\frac{\theta}{2} + \frac{z - z_f}{\sqrt{(z-z_f)^2 + x_f^2}}\right] \tag{2.11}$$

where

$$x_f = \frac{-L\cos(\phi + \frac{\theta}{2})}{\sin 2\phi}\cos(\phi - \frac{\theta}{2})$$

$$z_f = \frac{L\cos(\phi + \frac{\theta}{2})}{\sin 2\phi}\sin(\phi - \frac{\theta}{2})$$

$$\phi = \tan^{-1}(\frac{d}{2f})$$

Equation (2.11) follows from the well known result that the grating period formed by the interference of two plane waves with wavelength λ incident on a surface at angles θ_1 and θ_2 is given by $\frac{\lambda}{\sin\theta_1 + \sin\theta_2}$.

The quantities θ, x_f, z_f, d and f are all defined in Figure 2.1 For $(z - z_f)^2 << x_f^2$

$$\frac{2\pi}{\Lambda(z)} = \frac{2\pi}{\lambda}\left[\sin\frac{\theta}{2} + \frac{(z - z_f)}{x_f}\right] \tag{2.12}$$

which is the linear approximation.

For a general $\Lambda(z)$, the coupled mode equations can be written.

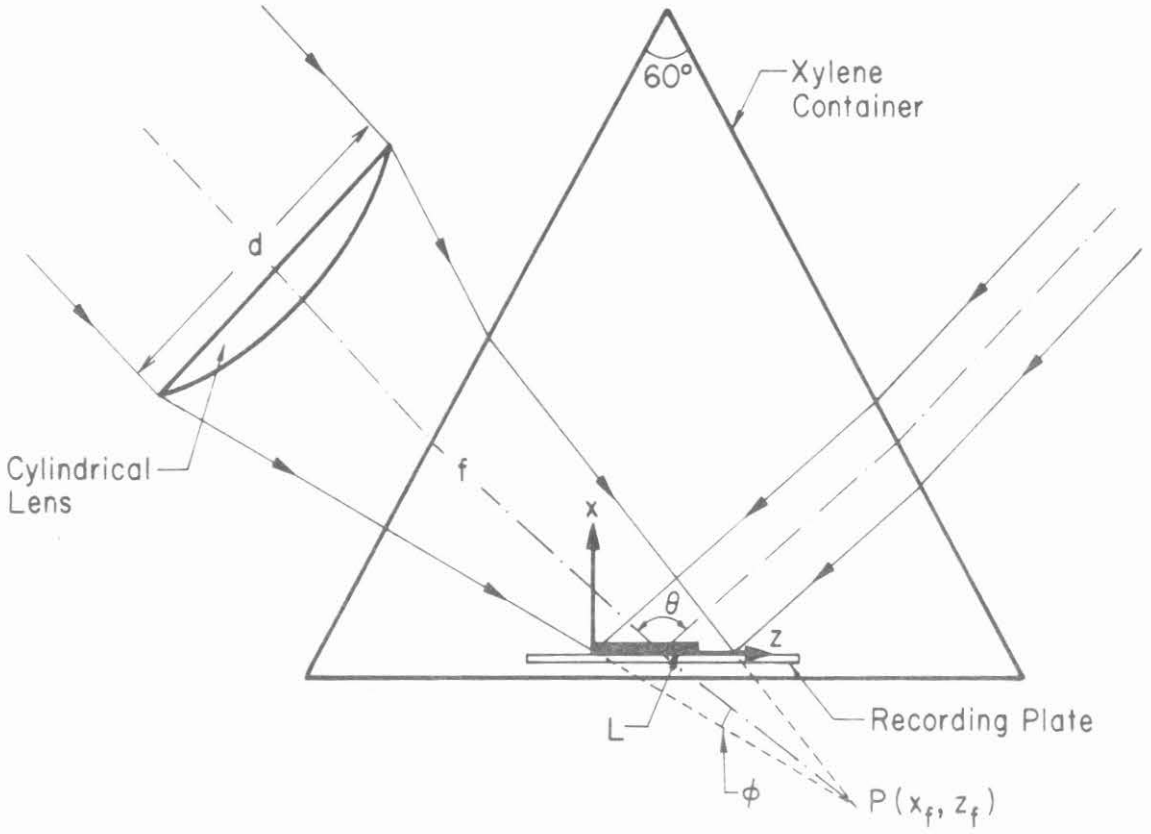

Fig. 2.1 Recording arrangement and geometry for the fabrication of chirped gratings. (After reference 13.)

$$\frac{dR'}{dz} = - \eta S' \, e^{-i\Psi} \tag{2.13}$$

$$\frac{dS'}{dz} = - \eta^* R' \, e^{+i\Psi} \tag{2.14}$$

$$\Psi(z) = \int^{z} \frac{2\pi}{\Lambda(z)} \, dz - 2\beta_o z$$

We will, for simplicity, neglect losses in the following derivation. Again, for large chirps the reflection may be small. After replacing R' with 1 in equation (2.14) we obtain

$$S'(0) = - \int_0^L \eta(z) \, e^{i\Psi(z)} \, dz \tag{2.15}$$

We can evaluate equation (2.15) by the method of stationary phase

$$\Psi(z) \approx \Psi(z_B') + \frac{(z - z_B')^2}{2} \frac{d^2\Psi(z_B')}{dz^2}$$

where

$$\frac{d\Psi(z_B')}{dz} = \frac{2\pi}{\Lambda(z_B')} - 2\beta_o = 0 \tag{2.16}$$

The quantity z_B' is the new Bragg point and from equations (2.11) and (2.14)

$$\frac{d^2\psi(z_B')}{dz^2} = \frac{2\pi}{\lambda x_f}\left[1 - \left(\frac{\lambda\beta_o}{\pi} - \sin\frac{\theta}{2}\right)^2\right]^{3/2} \qquad (2.17)$$

$$= \frac{2\pi}{\lambda x_f}\left[1 - \frac{(z_B' - z_f)^2}{(z_B' - z_f)^2 + x_f^2}\right]$$

After integrating equation (2.15) we get

$$\left|S'(0)\right|^2 = \text{Reflectivity} = \frac{2\pi\,\kappa^2(z_B')}{\left|\frac{d^2\psi(z_B')}{dz^2}\right|} = \frac{\pi\kappa^2(z_B')}{\gamma'\left[1 - \left(\frac{\lambda\beta_o}{\pi} - \sin\frac{\theta}{2}\right)^2\right]^{3/2}} \qquad (2.18)$$

for $0 < z_B' < L$

$= 0$ otherwise

where $\gamma' = \frac{\pi}{\lambda x_f}$.

As pointed out in the last section, for effective conversion of the forward traveling mode to backward traveling mode, the light had to be coupled into the end with smaller grating period. At the point

$$\frac{2\pi}{\Lambda(z_B)} = 2\beta_o \qquad (2.19)$$

we have the desired coupling, but at the points $\frac{2\pi}{\Lambda(z)} \lesssim \beta_o + kn_s$ we couple to the substrate radiation modes. If

$$\frac{2\pi}{\Lambda(z_s)} \equiv \beta_o + kn_s \quad , \tag{2.20}$$

then clearly $z_s > z_B$ for effective coupling, but if z_s is too close to z_B it will still interfere with the desired reflection.

Most of the light is reflected in a region of width $\sim \frac{1}{\sqrt{\gamma}}$ about the point z_B. In fact at the point $\frac{1}{2}\sqrt{\frac{\pi}{2}}\frac{1}{\sqrt{\gamma}}$ beyond z_B, the reflected intensity is down to 10% of the value, far to the left of the Bragg point.

Combining equations (2.19) and (2.20) we get

$$2\pi\left[\frac{1}{\Lambda(z_B)} - \frac{1}{\Lambda(z_s)}\right] = \beta_o - kn_s = k(N - n_s)$$

$$\Rightarrow z_s - z_B \approx \frac{\beta_o - kn_s}{2\gamma}$$

Thus the condition for the radiation modes not to interfere with the reflection is $z_s - z_B > \frac{1}{2}\sqrt{\frac{\pi}{2\gamma}}$

or

$$\gamma < \frac{2k^2}{\pi}(N - n_s)^2$$

This condition is easily satisfied by our gratings, but could present a problem in cases where $N \sim n_s$.

Finally for the lossless case and for small reflections we expand $\kappa(u + z_B)$ in equation (2.6) about $u = 0$, and integrate term by term. The result is

$$\text{Reflectivity} = \frac{\pi}{\gamma} \left| \sum_{p=0}^{\infty} \frac{\kappa^{(2p)}(z_B)}{2^{2p}\, p!\, (-i\gamma)^p} \right|^2 \tag{2.22}$$

Typically the ratio of two successive terms in the sum in (2.19) is

$$\sim \frac{1}{\gamma L^2} \sim 10^{-4}$$

where we have taken $\gamma \sim 10^{8}/_{m}2$ and $L \sim 10^{-2}$m as in our samples. Thus, equation (2.19) usually reduces to (2.7) for large chirps.

2.3 Fabrication of Broad-Band Filters

Glass waveguides were fabricated by sputter deposition of a layer of Corning 7059 glass on glass microscope slides. Two parts of Shipley AZ-1350 photoresist were diluted with one part thinner and spun-coated at 3600 rpm on the waveguide, resulting in a layer of resist 1700 Å thick. AZ-1350 resist was used because of extensive studies which the author had conducted previously on its properties. These are reported in Appendix 2-2 and have been published[6].

The chirped grating was recorded in the photoresist film by exposing the resist to the interference fringes of a plane wave and a cylindrically focused beam. An Ar^+ laser (4579 Å) was used, but in order to create the 2000 Å period grating it was also necessary to use a prism containing a Xylene solution as shown in Figure 2.1. Since the index of refraction of the Xylene is approximately 1.5, the interfering light which produced the grating had an effective wavelength of $\frac{4579}{1.5} \approx 3053$ Å.

The angle between the plane incident wave and the bisector of the converging beam was 102° and thus resulted in a grating whose period was 1950 Å in the central portion. Using the results of Appendix 2-B,[6] the samples were exposed for one minute and developed for ten seconds in AZ-303A, diluted 6-1 in deionized water.

The grating pattern was then transferred into the glass film by ion-beam etching[7-9] with argon ions of energy 2 keV. For maximum efficiency

in grating transfer, it is necessary that the etch rates of the resist not be substantially higher than the glass underneath it. This in fact occurs at low ion beam energies and it was found that the higher energies of 2 keV gave good results. Figures 2.2 are SEM photographs of a typical structure.

For convenience in later testing, only single mode waveguides were used and their thicknesses were measured with a Sloan-Dektak. The refractive index of the substrate was measured by the Brewster angle method and the index of refraction of the film was determined by the prism coupler method.[10-12]

2.4 Testing and Evaluation

Figure 2.3 is a schematic of the filter evaluation setup. Light from a tunable dye laser (linewidth $\sim$ 1 Å) is coupled through a high index prism into the waveguide, is reflected contradirectionally back through the prism, reflected by a beam-splitter and measured by a detector. By changing the frequency of the light output from the dye laser, the shifting Bragg point or point from which the light is reflected is readily evident. As mentioned earlier, in order to avoid excessive losses into the substrate, it was necessary to couple the light into the end of the grating with smaller period. Thus longer wavelengths penetrate further into the grating and undergo larger attenuation before being reflected. The loss factor α was determined

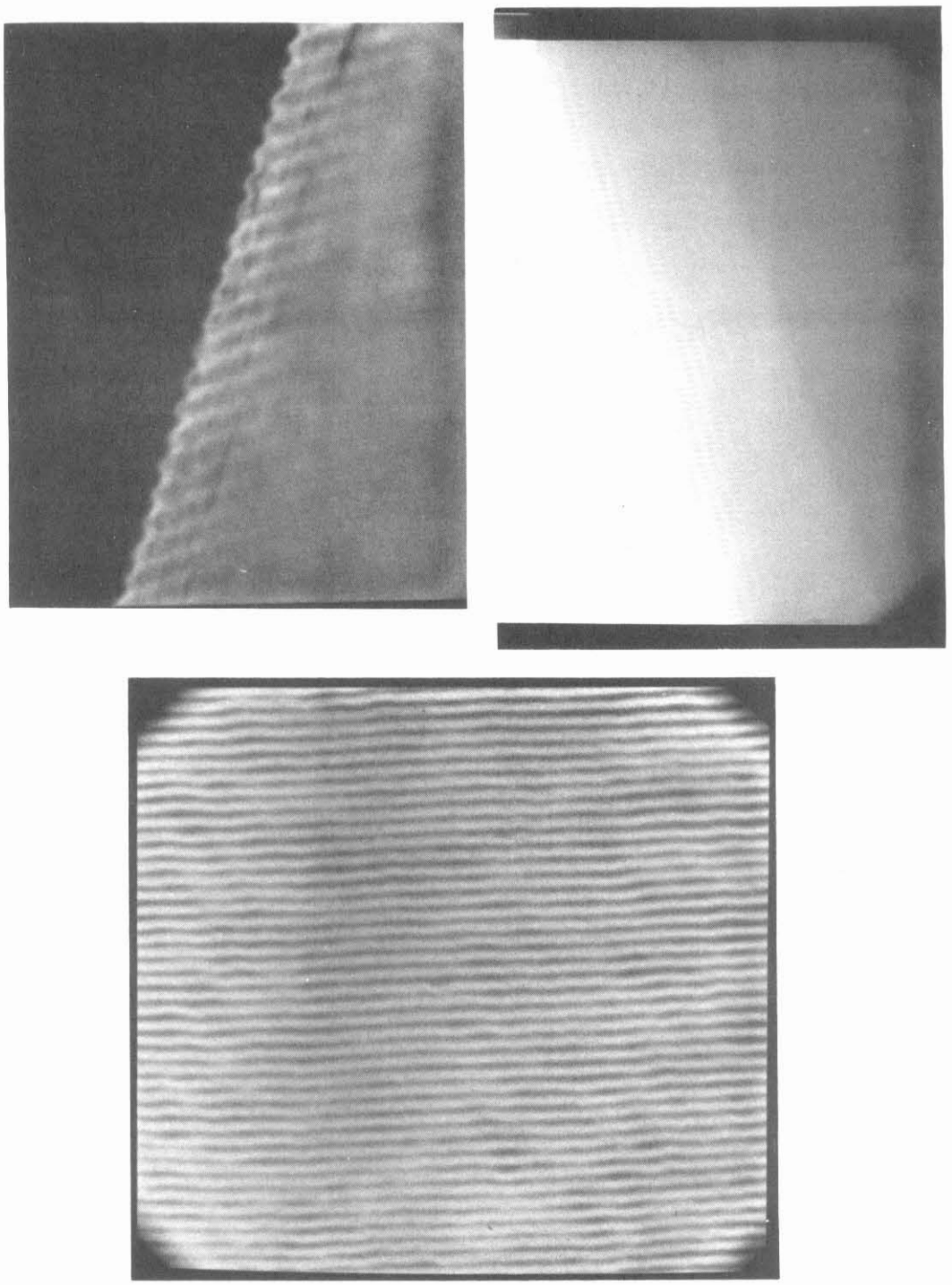

Fig. 2.2 SEM photograph of typical waveguide and surface corrugation. Guide thickness is .77 μ and corrugation depth is 350 Å.

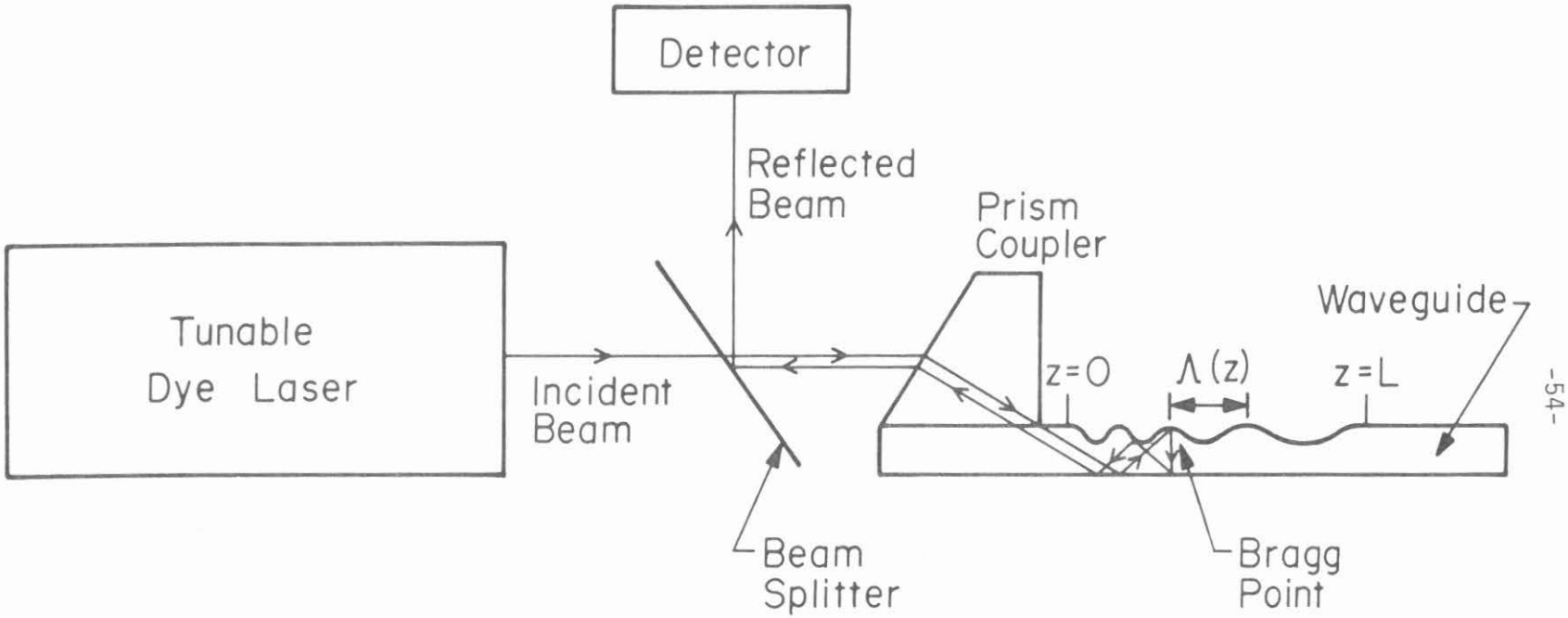

Fig. 2.3 Schematic of filter evaluation setup. (After reference 14.)

experimentally and the observed reflectivity at λ was multiplied by the factor $e^{2\alpha z_B(\lambda)}$ to obtain the intrinsic filter reflectivity.

Table 2.1 summarizes the properties of three tested filters. The measured reflectivities, after being corrected for waveguide losses, are in good agreement with theoretical predictions (within 10%), while the filter bandwidths are in excellent agreement with the values for which the devices were designed. The spectral response for the three filters are plotted in Figure 2.4 with the response of the one uniform-period filter shown in detail in the inset.

The author wishes to thank C. S. Hong for much of the experimental work as well as for his guidance during the fabrication process.

2.5 Conclusion:

The broad-band filters with a typical response of 300 Å have been fabricated and a simple theory based on a direct integration of the coupled mode equations gives results that are consistent with experiment. Both the general and linear chirped gratings are analyzed this way. For the case of the linear approximation, the results compare favorably with the more exact theory based on asymptotic expansions of the parabolic cylinder functions. For the case of a combination smooth taper and large chirp, the response depends strongly on the value of the coupling constant at the Bragg point and weakly on the derivatives of this constant at the Bragg point.

Losses have been included in some of the study and it is found that they lead to a response that decays as $e^{-2\alpha z_B}$. This corresponds to the attenuation due to the round trip distance to the Bragg point. If

		Period (Λ)	Length (L)	Corrugation depth (h)	Waveguide thickness (t)	Effective index of refraction at λ=5950Å[a]	Wavelength response	Bandwidth	Reflectivity
Filter 1	Chirped	1905 Å – 2005 Å	10 mm	350 Å	0.77 μm	1.524	5810 Å – 6110 Å	300 Å	18%
Filter 2	Chirped	1925 Å – 1975 Å	10 mm	400 Å	0.85 μm	1.524	5870 Å – 6020 Å	150 Å	40%
Filter 3	Uniform period	1955 Å	1 mm	250 Å	0.80 μm	1.519	5946 Å	4 Å	80%

a. $n_s \sim 1.51$, $n_f \sim 1.54$, $n_a \sim 1$

TABLE 2.1 Summary of data obtained from three grating filters. (After reference 14.)

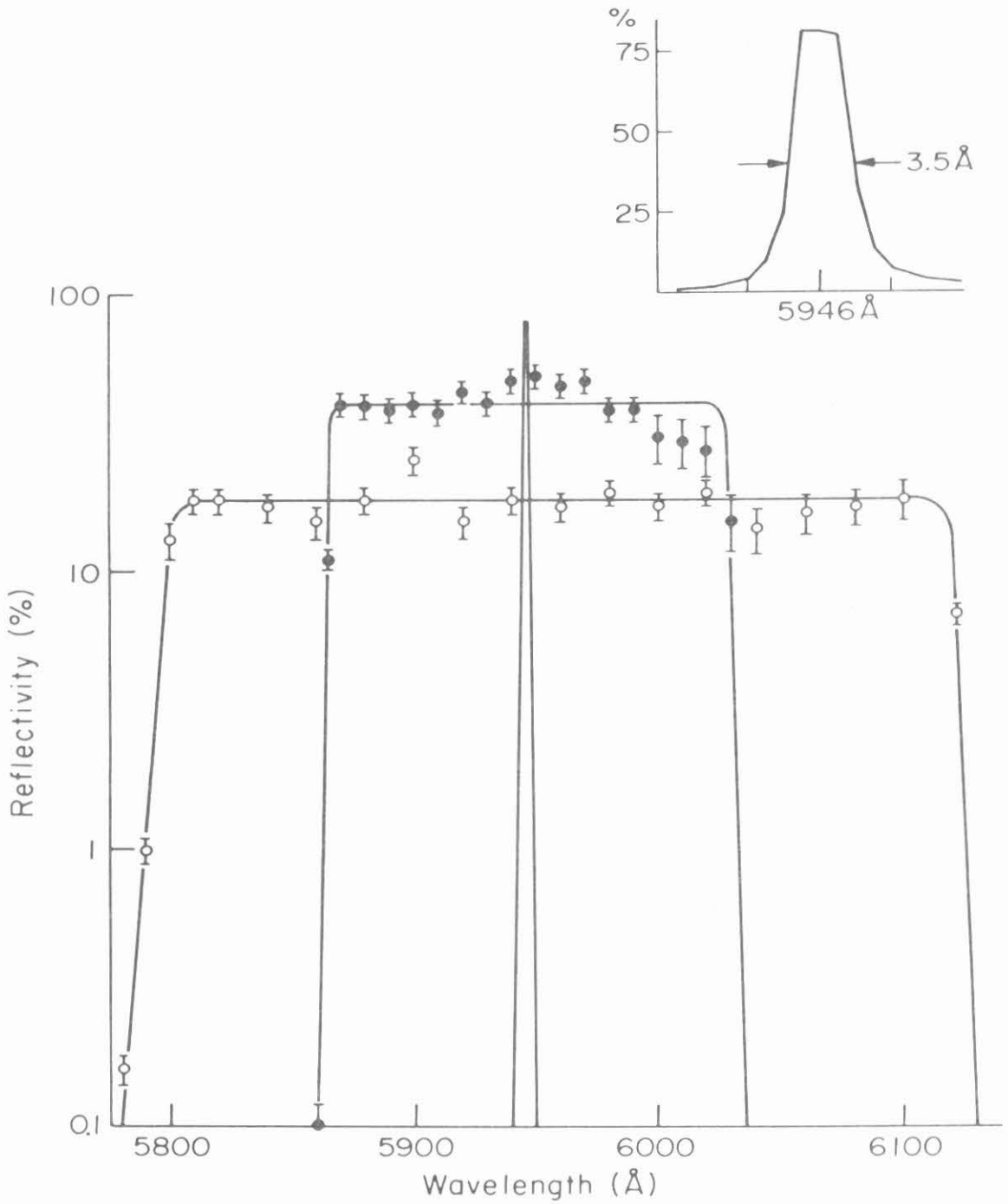

Fig. 2.4 Reflectivity vs wavelength for three grating filters. Circle represents filter 1, and dot represents filter 2. Details of the filter with uniform period are given in the inset. (After reference 14.)

higher order terms are kept in the loss, the effect can be interpreted as a new round trip distance, z_o, larger than z_B for gain and less than z_B for losses.

Chapter 2 References

1. A. Yariv, Quantum Electronics, 2nd ed. (John Wiley and Sons, Inc., N. Y., 1975), p. 526.
2. M. Matsuhara, K. O. Hill, and A. Watanabe, Opt. Soc. of Amer. 65, 804 (1975).
3. Robert B. Smith, J. Opt. Soc. Amer. 66, 882 (1976).
4. D. C. Flanders, H. Kogelnik, R. V. Schmidt, and C. V. Shank, Appl Phys. Lett. 24, 194 (1974).
5. A. Katzir, A. C. Livanos, J. B. Shellan, and A. Yariv, IEEE J. Quantum Electron. QE-13, 296 (1977).
6. A. C. Livanos, A. Katzir, J. B. Shellan, and A. Yariv, Appl. Optics 16, 1633 (1977).
7. H. Garvin, Solid State Tech ((c) Hughes Aircraft Co., 1972; paper presented at the Kodak Microelectronics Seminar, San Diego, Cal. Dec. 11-12, 1972.)
8. P. G. Glöersen, J. Vac. Sci. Technol. 12, 28 (1975).
9. W. Laznovsky, Research Development 47 (August, 1975).
10. R. Ulrich and R. Torge, Appl. Opt. 12, 2901 (1973).
11. R. Th. Kersten, Optica Acta 22, 503 (1975).
12. G. B. Brandt, Appl. Opt. 14, 946 (1975).
13. J. B. Shellan, C.S. Hong and A. Yariv, Opt. Com. 23, 398 (1977).
14. C. S. Hong, J. B. Shellan, A. C. Livanos, A. Yariv and A. Katzir, App. Phy. Lett. 31, 276 (1977).

Appendix 2-A

EXACT SOLUTION OF COUPLED MODE EQUATIONS FOR BROAD-BAND FILTER

We start with the coupled mode equations

$$\frac{dR}{dz} - i\delta R = - \eta S e^{i\gamma z^2} \tag{2-A.1}$$

$$\frac{dS}{dz} + i\delta S = -\eta^* R e^{-i\gamma z^2} \tag{2-A.2}$$

After making the substitution

$$R' \equiv R e^{-i\delta z} \tag{2-A.3}$$

$$S' = S e^{+i\delta z} \tag{2-A.4}$$

we find

$$\frac{dR'}{dz} = - \eta S' e^{(-2i\delta z + i\gamma z^2)} \tag{2-A.5}$$

$$\frac{dS'}{dz} = -\eta^* R' e^{(2i\delta z - i\gamma z^2)} \tag{2-A.6}$$

Equations (2-A.5) and (2-A.6) can then be combined, giving the defining equation for the parabolic cylinder functions

$$\frac{d^2R'}{dx^2} + 2i\gamma x \frac{dR'}{dx} - \kappa^2 R' = 0 \tag{2-A.7}$$

where $x \equiv z - z_B$

z_B = Bragg point $\equiv \frac{\delta}{\gamma}$

$\eta = i\kappa$ $\quad$ κ is real

The solution to equation (2-A.7) is

$$R'(x) = x^{-1/2} \exp(-i\frac{\gamma}{2} x^2) \left[G \cdot W_{K,\mu}(i\gamma x^2) + H \cdot W_{-K,\mu}(-i\gamma x^2)\right] \qquad (2\text{-A.8})$$

where $K = -\frac{1}{4} + i\frac{\kappa^2}{4\gamma}$, $\mu = 1/4$

In equation (2-A.8) $W_{K,\mu}(z)$ is the Whittaker function and G and H are constants of integration to be determined by the boundary conditions. After substituting equation (2-A.8) into equation (2-A.5), S' is found to be

$$S' = \frac{-1}{\kappa} e^{i(\gamma z_B^2 - 2\delta z_B)} x^{-3/2} e^{i\frac{\gamma}{2}x^2} \cdot$$

$$\left[G \cdot \{(-\frac{1}{2} - 2K) W_{K,\mu}(i\gamma x^2) - 2W_{K+1,\mu}(i\gamma x^2)\}\right.$$

$$+ H \cdot \{(-\frac{1}{2} - 2K) W_{-K,\mu}(-i\gamma x^2) - 2(\mu + K + \tfrac{1}{2})(\mu - K - \tfrac{1}{2}) \cdot$$

$$\left. W_{-K-1,\mu}(-i\gamma x^2)\}\right] \qquad (2\text{-A.9})$$

After using the approximation $\gamma x^2 \to \infty$ in equations (2-A.8) and (2-A.9) and using the asymptotic expansion for $W_{K;\frac{1}{2}}$, we find

$$R'(0) = P(x)\, R'(x) + Q^*(x)\, S'(x) \tag{2-A.10}$$

$$S'(0) = Q(x)\, R'(x) + P(x)^*\, S'(x) \tag{2-A.11}$$

where

$$P(x) = \left\{ e^{\pi \frac{\kappa^2}{8\gamma}} \; (\gamma x^2)^{i \frac{\kappa^2}{4\gamma}} \right\} \div \left\{ \frac{1}{\sqrt{\pi}} \cdot \Gamma\left(\frac{1}{2} + i \frac{\kappa^2}{4\gamma}\right) \right\} \tag{2-A.12}$$

$$Q(x) = \left\{ e^{\pi \frac{\kappa^2}{8\gamma}} \; (\gamma x^2)^{i \frac{\kappa^2}{4\gamma}} \right\} \; \div \tag{2-A.13}$$

$$\left\{ \frac{1}{\sqrt{\pi}} e^{i\gamma z_B^2} \left[\frac{\kappa}{2\sqrt{\gamma}} e^{i \frac{\pi}{4}} \right] \cdot \; \Gamma\left(i \frac{\kappa^2}{4\gamma}\right) \right\}$$

After using the initial conditions $R'(0) = 1$ and $S'(L) = 0$ together with equations (2-A.12) and (2-A.13) we finally derive the expressions

$$\left| R'(L) \right|^2 = e^{-\frac{\pi\kappa^2}{\gamma}} \tag{2-A.14}$$

$$|S'(0)| = \text{reflectivity} = 1 - e^{-\frac{\pi\kappa^2}{\gamma}} \tag{2-A.15}$$

It should be pointed out that in order to use the asymptotic expressions for the parabolic cylinder functions, the following must hold

$$\frac{5\kappa}{\gamma} < z_B < L - \frac{5\kappa}{\gamma} \qquad (2\text{-A.16})$$

In other words, the Bragg point or region of maximum interaction cannot be near the edge of the grating region. The key result is contained in equation (2-A.15). Figures 2-A.1, 2-A.2 and 2-A.3 are plots of the power reflected at various points along the guide for increasing values of κ^2/γ. The power reflected at the far right side ($z = L$) is zero from the boundary conditions, while the reflectivity at $z = 0$, which is the most important single parameter of the reflector, is given by equation (2-A.15) if equation (2-A.16) is satisfied. Because the parabolic cylinder functions are difficult to work with directly, except in certain asymptotic limits, the plots were made by directly solving equations (2.2) and (2.3a) of the main body of this chapter numerically. It should be noted from the figures that although the reflectivity (at $z = 0$) increases as κ increases, it is also necessary to increase the length of the grating as κ increases if a steady state non-oscillatory solution near $z = 0$ is desired.

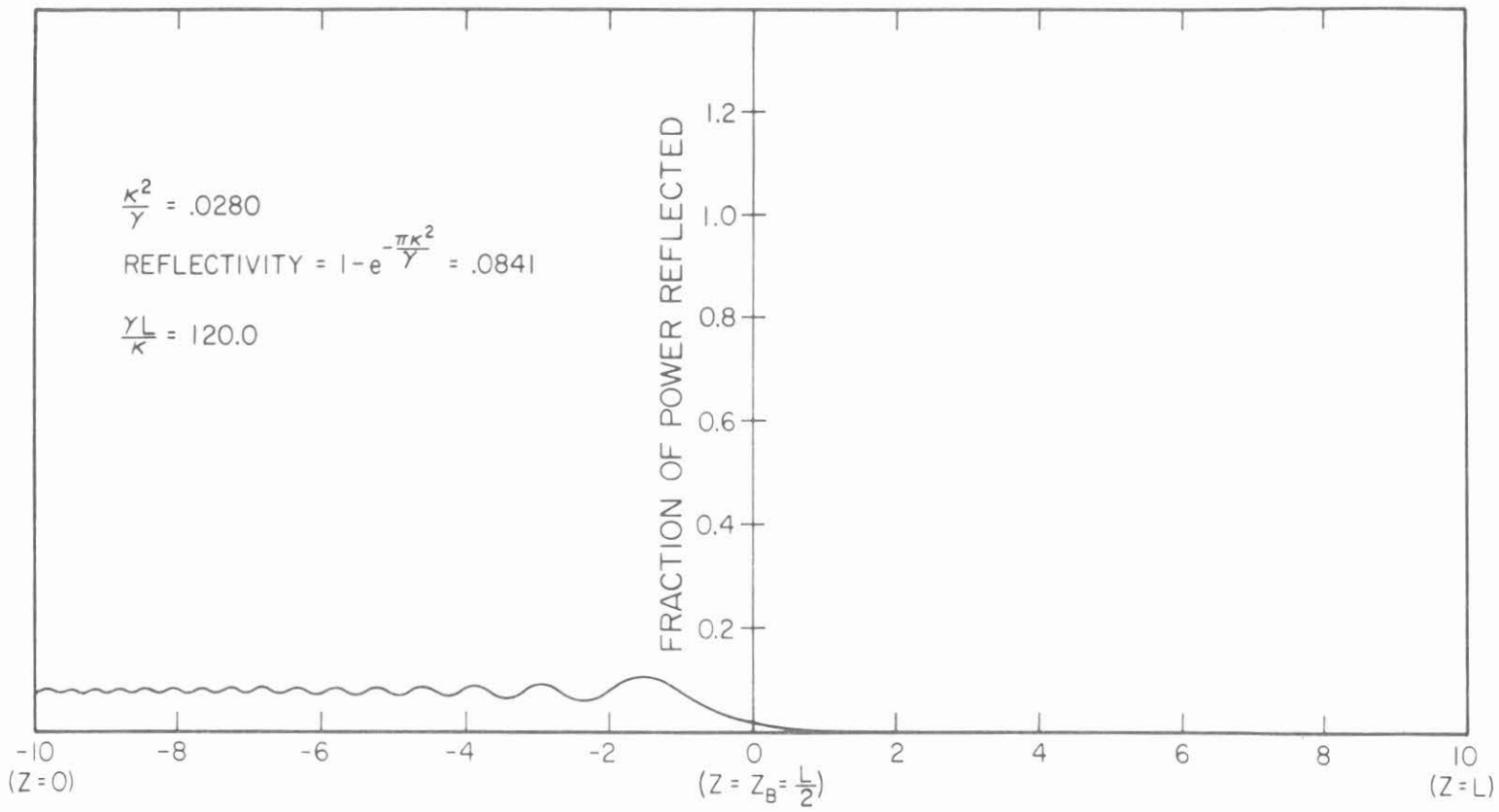

Fig. 2-A.1 Reflected power as a function of distance from Bragg point for a filter with small reflectivity.

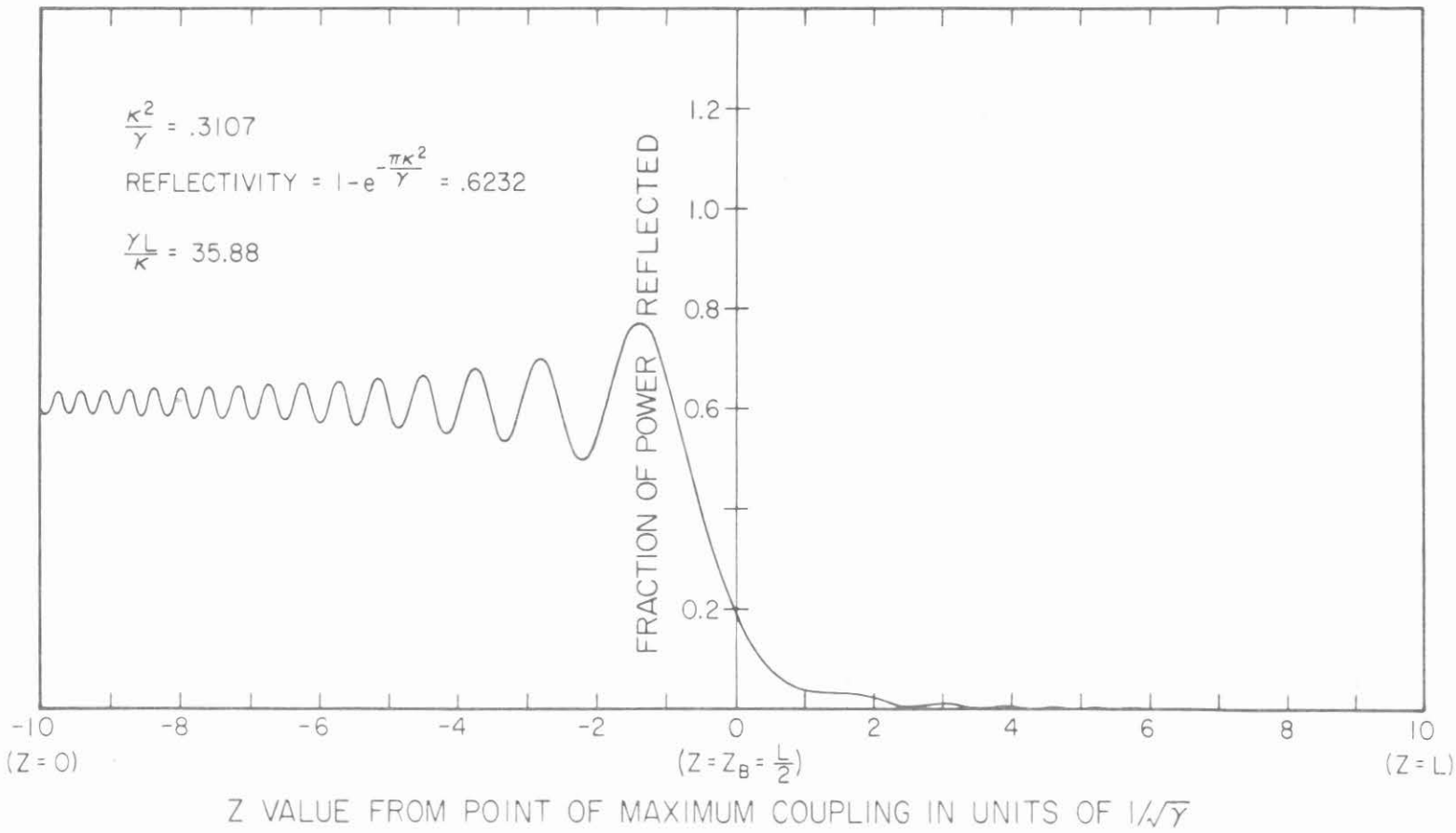

Fig. 2-A.2 Reflected power as a function of distance from Bragg point for a filter with moderate reflectivity.

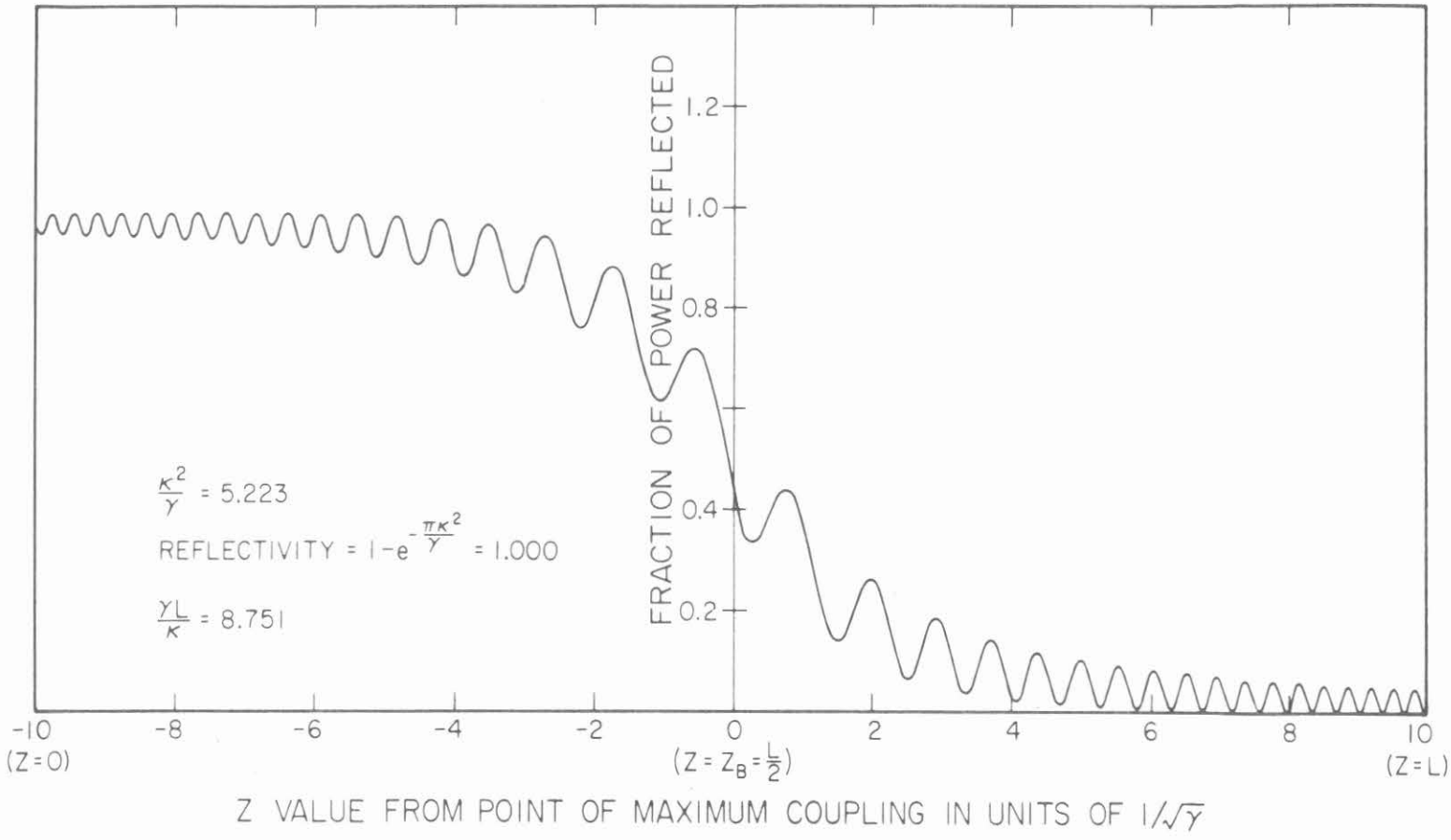

Fig. 2-A.3 Reflected power as a function of distance from Bragg point for a filter with large reflectivity.

Appendix 2-B

LINEARITY AND ENHANCED SENSITIVITY OF THE SHIPLEY AZ-1350B PHOTORESIST

Current work in integrated optics requires the fabrication of relief grating structures on photoresist and the subsequent chemical or ion beam etching through the photoresist.[1] If the period of the grating is to be less than .4μm the Shipley AZ-1350B photoresist is commonly used. The properties of this positive acting photoresist have been examined in detail[2,3] and it was found that the photoresist exhibits strong nonlinearity, especially for etch depth ranging from 0.05 to .2 μm. Bartolini[4,5] and others[6] have shown that a different developer, namely the AZ-303A, used with the AZ-1350J photoresist removes the nonlinearity and improves the sensitivity by a factor of two or three. Linearity and speed or sensitivity are always of practical interest.[7,8] The AZ-303A developer has not been used in conjunction with the AZ-1350B photoresist because of the unacceptable etch rate of unexposed AZ-1350J resist, namely 150-200Å per second. It is the purpose of this appendix to show that the AZ-303A developer can be used with the AZ-1350B photoresist, resulting in improved sensitivity and linearity.

Bartolini[5] has shown that for a positive acting photoresist the following relationship exists between etch depth Δd and exposure E (in units of energy per unit area):

$$\Delta d = T[r_1 - \Delta r \exp(-cE)] \qquad (2\text{-B}.1)$$

where T is the development time in seconds, c is the exposure constant characteristic of the photoresist, r_1 is the rate of etching of exposed molecules, and r_2 is the rate of etching of unexposed ones and $\Delta r = (r_1 - r_2)$. If the term cE is much less than 1, equation (2-B.1) can be linearized as follows:

$$\Delta \sim \Delta r \, TcE + r_2 T \qquad (2\text{-B.2})$$

In this work the parameters involved in equation (2-B.2) are determined for the Shipley AZ-1350B photoresist used with the AZ-303A developer. The samples used were NO-3010 microscope slides made by Clay Adams, which, cut in half, resulted in a size of 38 mm x 25 mm x 1 mm. The samples were cleaned according to the method presented in Ref. 6, and for some experiments the back surface was painted black with 3M Nextel 101-C10 velvet coating. The AZ-1350B photoresist was then deposited in a single layer, and after 30 seconds it was spun at 6000 rpm for 30 seconds. The samples were baked next for 30 min at 125°C.

The first experiment involved the determination of the etch rate of the unexposed resist as a function of development time, for various solutions of AZ-303A developer with distilled water. For this purpose the samples were half immersed in the developer for the required time, rinsed with deionized water for 2 minutes, and then baked under vacuum at 100°C for 30 min. The step size was measured using a Sloan Dektat instrument and the results are shown in Figure (2-B.1). The 4:1 solution (4 parts distilled water, 1 part AZ-303A developer) gave unacceptably high etch rates, and the 8:1 gave low and nonlinear ones. In all the experiments a 6:1 dilution was used, since it

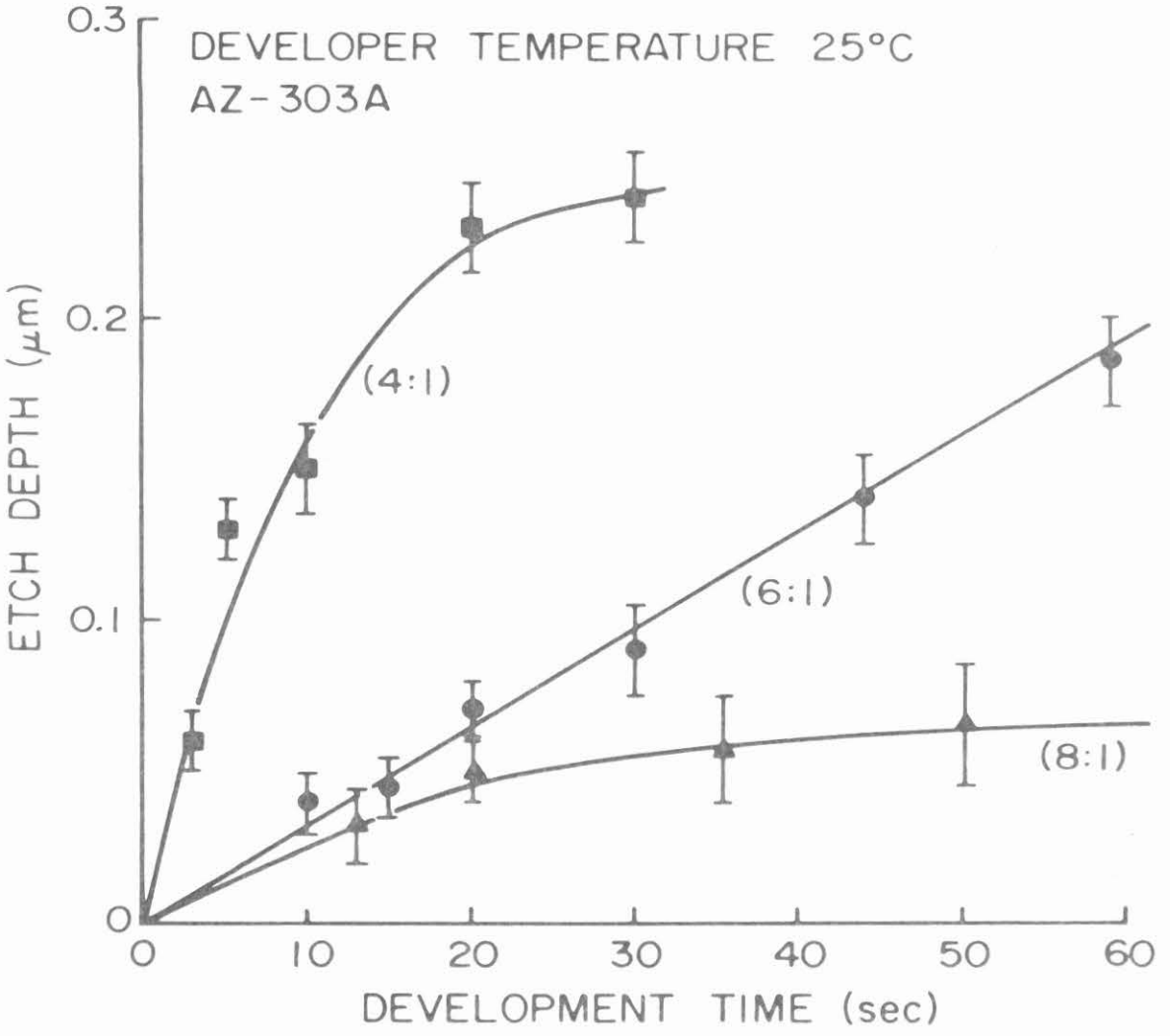

Fig. 2-B.1 Etch depths in μm of unexposed AZ-1350B photoresist as a function of development time in seconds, for various dilution ratios of AZ-303A developer. The slope of the curves determines r_2, which for the 6:1 dilution is 35Å ± 5Å.

exhibited a linear behavior and an acceptable etch rate of $r_2 = 35\text{Å} \pm 5\text{Å}$ per sec. The development time chosen for the subsequent experiment was 10 sec.

For comparison, the experiment was repeated using the Shipley MF-312 developer. This developer is free from trace-metallic elements and is commonly used in the fabrication of photoresist gratings in semiconductor substrates. Figure 2-B.2 shows the unexposed etch rate as a function of development time in minutes for the manufacturer's recommended dilution of 1:1. In this case r_2 is $5\text{Å} \pm 1\text{Å}$ per sec, which is a much lower etch rate than the one for AZ-303 developer. If resist thickness is small, if long exposure times are acceptable, and if linearity is unimportant, this may indeed be a better choice.

To demonstrate the thickness change as a function of exposure time, the .4416 μm line of a He-Cd laser was used to illuminate half of the sample. The back surface of the sample was coated with black paint to avoid interference fringes. The intensity distribution of the laser was better than 5% across the surface of the sample. The photoresist was exposed for a given time, and then developed for ten seconds in the AZ-303A developer 6:1 dilution. Figure 2-B.3 shows the thickness change as a function of exposure energy. It can be clearly seen that the behavior of the photoresist in the important range .1 μm to .2 μm is linear. In contrast, the MF-312 developer gave very small thickness changes for the same range of exposures. In order to verify that the stylus of the instrument was not scratching the surface, the same samples were aluminized and then tested.

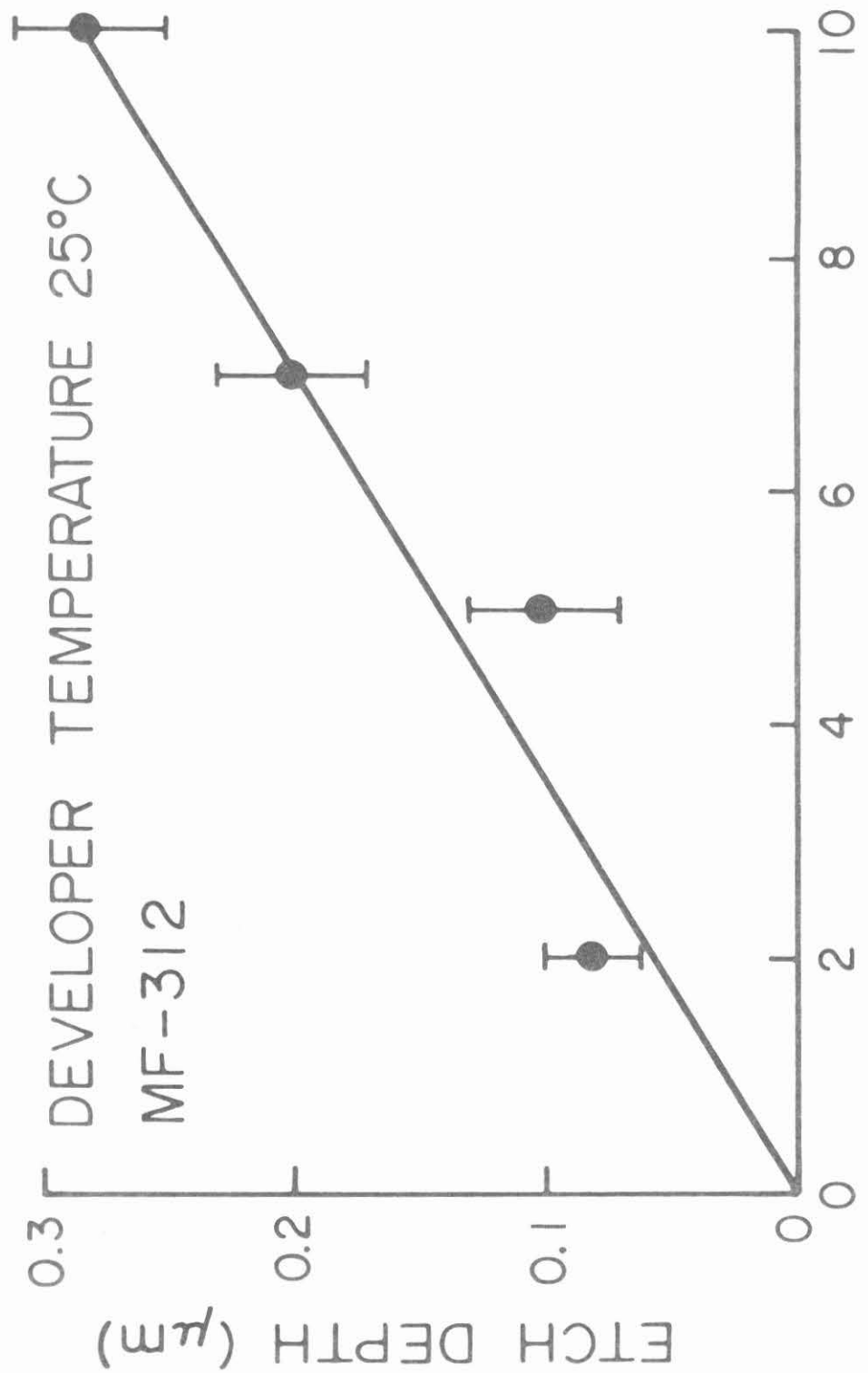

Fig. 2-B.2 Etch depth in μm of unexposed AZ-1350B photoresist as a function of development time in minutes for MF-312 developer. The 1:1 dilution results in $r_2 = 5\text{Å} \pm 1\text{Å}$.

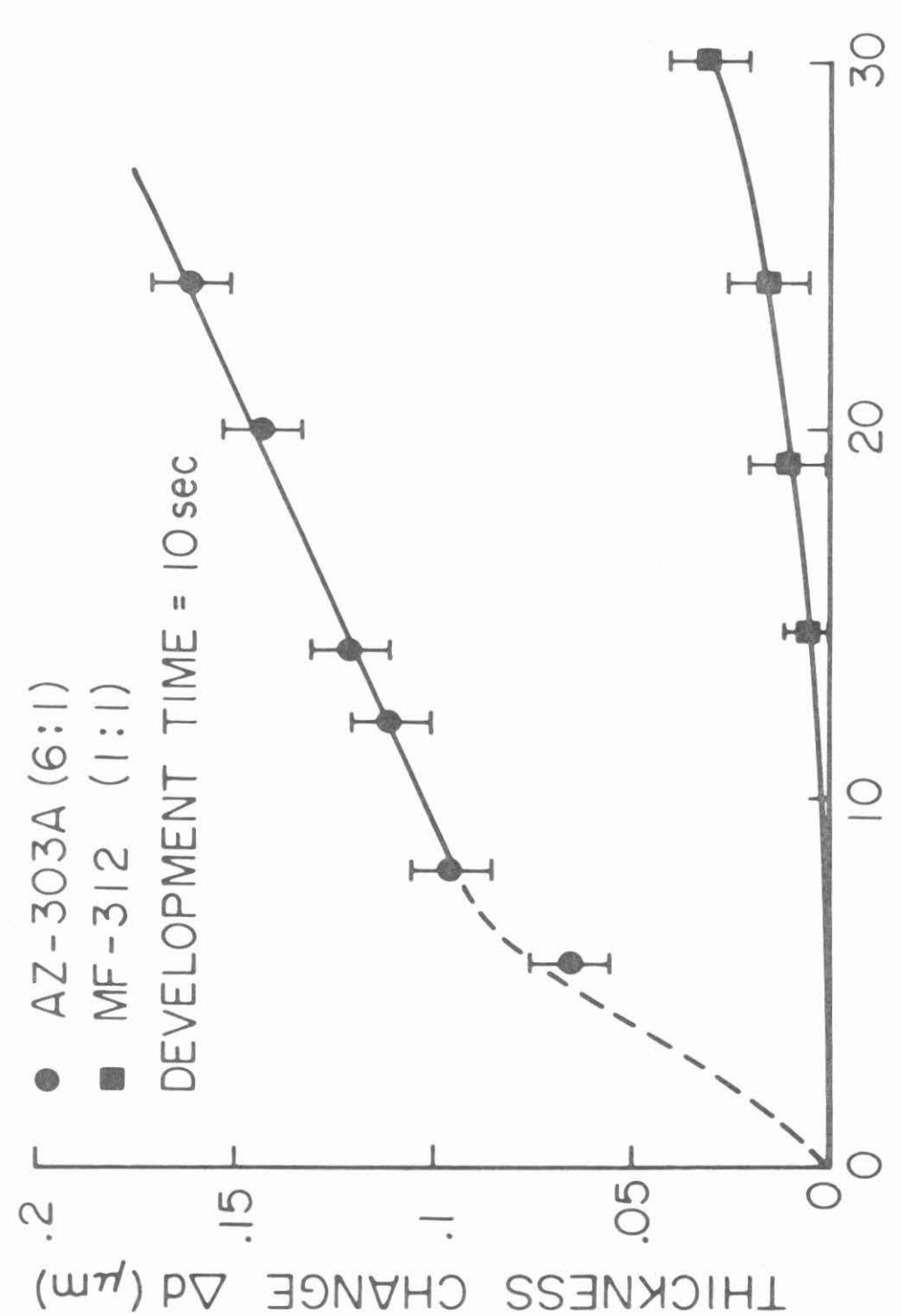

Fig. 2-B.3 Thickness change Δd in μm of AZ-1350B photoresist as a function of exposure E in mw/cm^2. The circles represent the AZ-303A developer and the squares represent the MF-312 developer.

To demonstrate the feasibility of using AZ-1350B photoresist with the AZ-303A developer in making high efficiency gratings, the following experiment was performed. Photoresist was spin-coated on samples at 3000 rpm, resulting in a resist thickness of about 3.1 μm. The gratings were generated by exposing the samples to the sinusoidal intensity distribution produced by the interference pattern of two collimated Ar^+ laser beams. The wavelength used was .4579 μm, the angle between the beams 94.5°, and the intensity per beam was .60 mw/cm^2. The exposed samples were developed in AZ-303A developer, baked under vacuum, and the efficiency of the gratings was measured. Figure 2-B.4 shows the absolute efficiency of the gratings as a function of exposure for two different development times. It is clear that high efficiency 23% resulted by developing the samples for 10 seconds. To verify the theoretically predicted period and the peak to trough height, a scanning electron microscope was used . The period was measured to be .31 μm, and the peak to trough height was .28 μm.

In conclusion, it has been found that the use of AZ-303A developer with the AZ-1350B photoresist results in an unexposed etch rate of $\sim$ 35Å/sec and significantly increases the sensitivity and linearity of the photoresist in the .05 to .2 μm range. Gratings with constant and variable period[9] have been made using this method, and they have been transferred to glass using ion beam etching techniques.

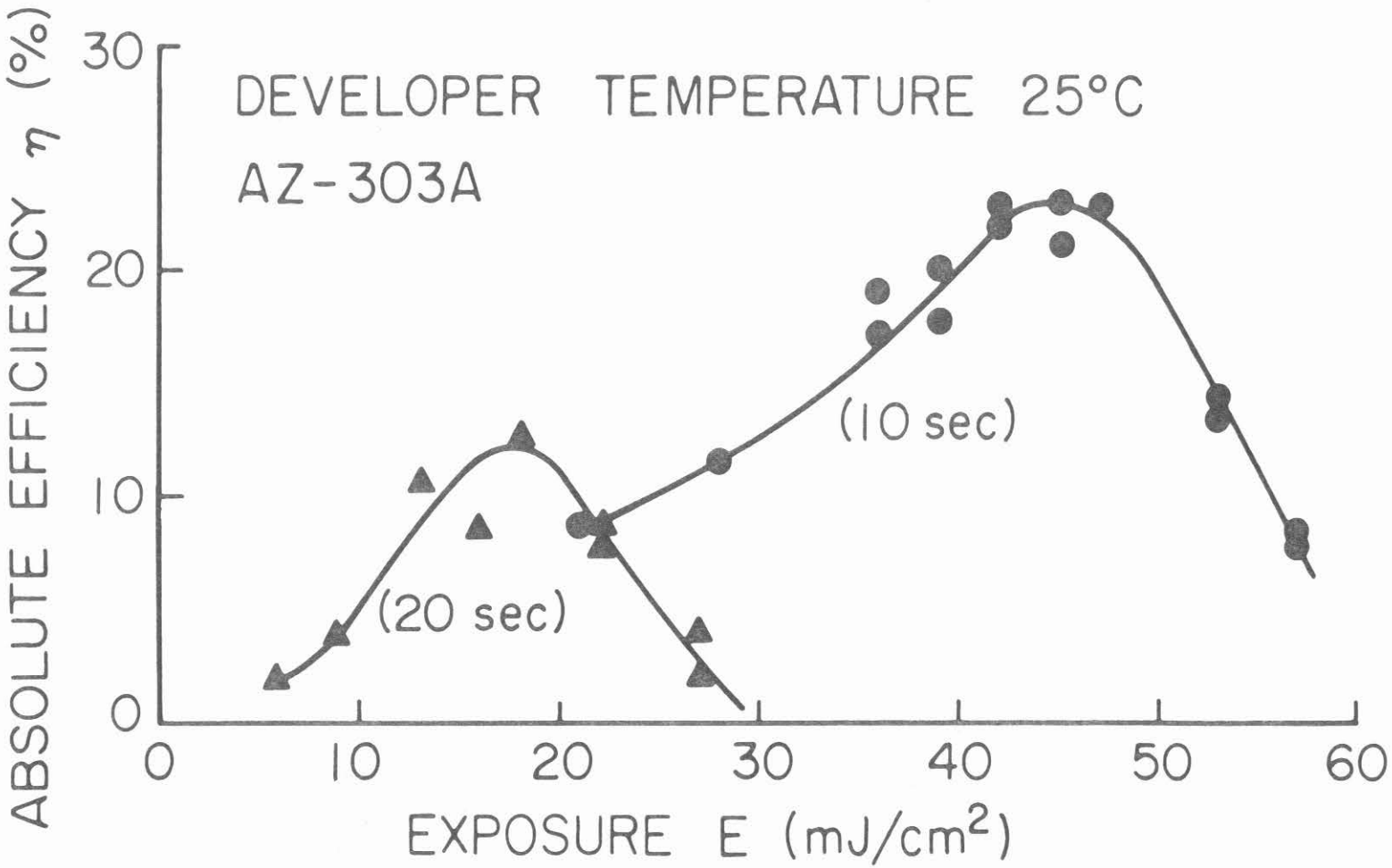

Fig. 2-B.4 Grating efficiency (absolute) as a function of exposure E in mw/cm^2 for 10 and 20 sec development times in AZ-303A developer. Initial resist thickness was 31 μm.

Appendix 2-B References

1. H. L. Garvin, E. Garmire, S. Somekh, H. Stoll and A. Yariv, Appl. Opt. 12, 455 (1973).
2. S. Austin, F. T. Stone, Appl. Opt. 15, 1071 (1976).
3. S. Austin, F. T. Stone, Appl. Opt. 15, 2126 (1976).
4. R. A. Bartolini, Appl. Opt. 11, 1275 (1972).
5. R. A. Bartolini, Appl. Opt. 13, 129 (1974).
6. S. L. Norman, M. P. Singh, Appl. Opt. 14, 818 (1975).
7. M. S. Htoo, Photogr. Sci. Eng. 12, 169 (1968).
8. F. J. Loprest, E. A. Fitzgerald, Photogr. Sci. Eng. 15, 260 (1971).
9. A. C. Livanos, A. Katzir and A. Yariv, accepted for publication in Opt. Commun.

Chapter 3

CHIRPED GRATINGS USED AS INPUT-OUTPUT COUPLERS

3.1 Introduction

In the last chapter we dealt with the topic of chirped gratings used as broad-band filters. The grating period had to be of the order of 2000Å for reflection. If, however, devices are made with longer periods, say 3000Å, light will be coupled out of the guide and into the air and the substrate. With conventional, uniform grating output couplers the light is coupled out as a plane wave. If chirped grating is used, however, the light is coupled out as a converging or diverging wave and can be focused to a line parallel to the guide and normal to the propagation direction, with different wavelengths focusing in different positions. Thus long grating regions can be used to efficiently couple out weak signals and focus them to a line where they can easily be detected. Conversely, external line or point sources of light may be coupled to waveguides more efficiently using chirped input couplers than uniform grating.

In this chapter we will consider in greater detail the design considerations involved in making chirped gratings. The relationships among key parameters such as period variations, F number of lens, length of grating region and recording geometry are established. Next, the coordinates of the point where light coupled out of the guide is focused is found and compared with experiment. Finally a comprehensive theory is presented which relates power output to grating and guide parameters.

3.2 Grating Fabrication Considerations

The grating is fabricated similarly to the broad band filter grating, except that now the xylene filled prism is not needed, since the

period is larger. Figure 3.1 is a schematic diagram of the setup used. The recording plate is located at the x = 0 plane, the angle of incidence of the plane wave is $\theta/2$, and the angle subtended by the collimated beam and the bisector of the converging beam angle is θ. The interference pattern is recorded over a distance L on the recording plate. The converging wave is generated by a cylindrical lens of focal length f and width d, and the focus is located at point $P(x_f, z_f)$.

Simple geometrical calculations relate the focal line coordinates with f, L, d and θ, namely [1]

$$x_f = \frac{-L \cos(\phi + \frac{\theta}{2})}{2 \sin 2\phi} \cos(\phi - \frac{\theta}{2}) \tag{3.1}$$

and

$$z_f = \frac{L \cos(\phi + \frac{\theta}{2})}{2 \sin 2\phi} \sin(\phi - \frac{\theta}{2}) \tag{3.2}$$

where

$$\phi = \tan^{-1}(\frac{d}{2f})$$

is the convergence half angle. We note that in Eq. (3.1) x_f is always negative, while z_f can take negative or positive values depending on the angles θ and ϕ.

The electric field in the recording plane (x=0) is given by the sum of the reference wave and converging one and is given by:

$$E(x=0,z) = Ae^{-ikz\sin(\theta/2)} + \alpha e^{ik\{[(z-z_f)^2+x_f^2]^{1/2}\}} \tag{3.3}$$

where $k = 2\pi/\lambda$ is the wave number for the incident field, A and α the amplitudes of the plane and converging wave respectively. If we assume

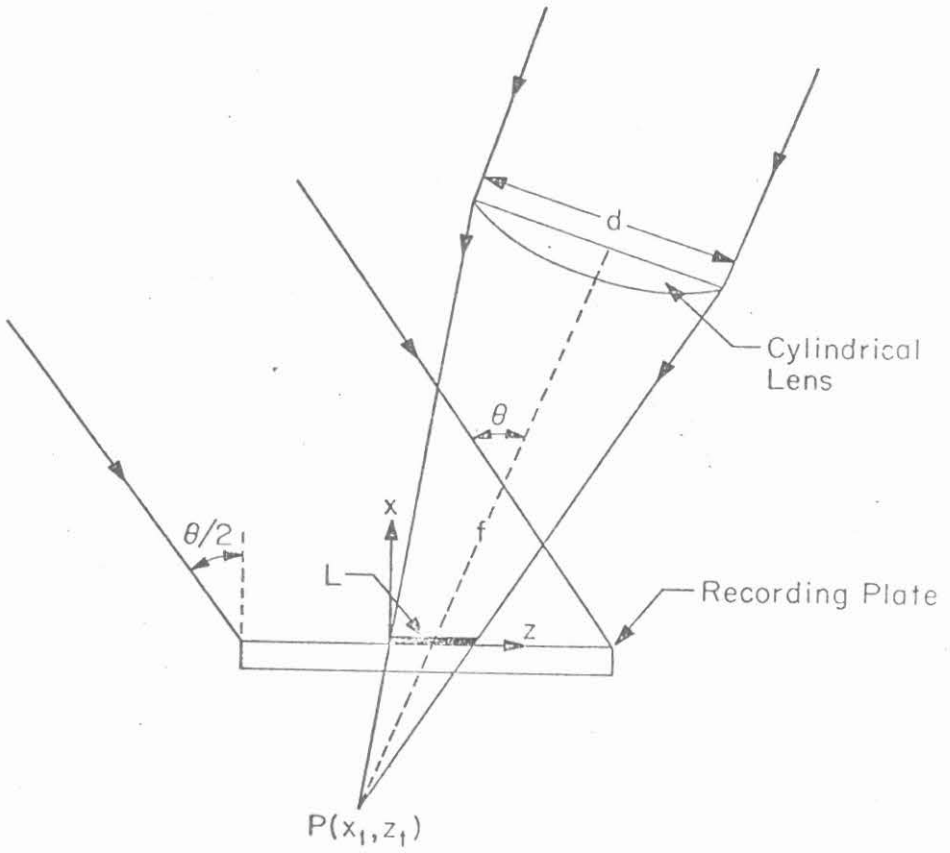

Fig. 3.1 Recording arrangement and geometry for the fabrication of chirped gratings. (After reference 1.)

that the transmission function of the recording medium t is proportional to EE^{*2}, and that $A = \alpha$, then

$$t = \beta[1 + \cos\{kz\sin(\theta/2) + k\sqrt{(z-z_f)^2 + x_f^2}\}] \tag{3.4}$$

where β is a proportionality constant. The period Λ for this particular grating is given by:

$$\Lambda(z) = \frac{\lambda}{\sin(\theta/2) + \dfrac{z-z_f}{\sqrt{(z-z_f)^2+x_f^2}}} \tag{3.5}$$

In the paraxial approximation $(z-z_f)^2 << x_f^2$ Eq.(3.4) and (3.5) reduce to:

$$t = \beta\left[1 + \cos\left\{\frac{k}{2x_f} z^2 + (k\sin(\theta/2) - \frac{kz_f}{x_f})z + kx_f + \frac{kz_f^2}{2x_f}\right\}\right] \tag{3.6}$$

The corresponding expression for Eq. (3.5) is therefore

$$\Lambda(z) = \frac{\lambda}{\sin(\theta/2) + \dfrac{z-z_f}{x_f}} \tag{3.7}$$

It is seen from Eqs. (3.1), (3.2) and (3.5) that the period variation $\Lambda(z)$ depends on the F number of the lens ($F \equiv f/d$), θ the angle subtended by the collimated beam and the bisector of the converging beam angle, λ the wavelength of illumination, and L the length of the grating.

The dependence of the period variation on F is illustrated by 3.2 and 3.3. In Fig. 3.2 the angle is set at 60° and the grating has a total length of 1 cm. For various F numbers period variations from 0.8 μm to 0.4 μm are obtained. The lower the F number the greater the period

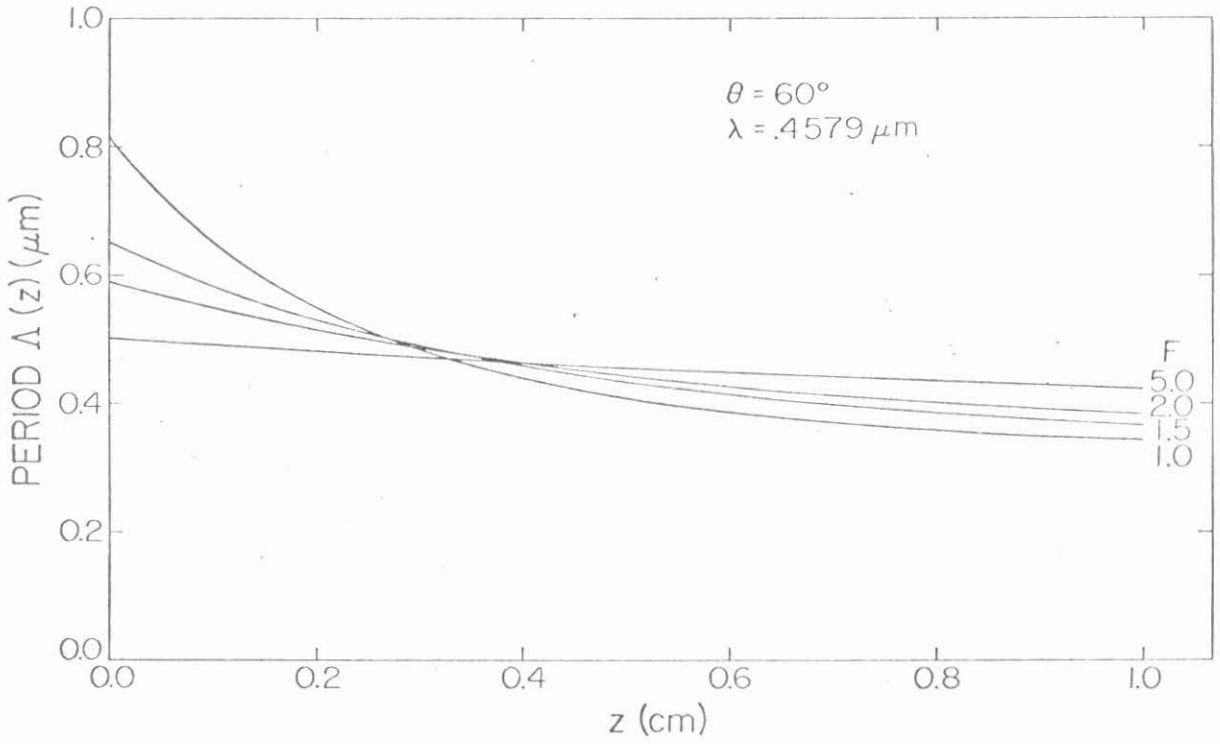

Fig. 3.2 Period variation as a function of the F number of the converging lens (F = f/d). The angle θ = 60° is suitable for variations of 0.8 μm to 0.4 μm over a distance of 1 cm. (After reference 1.)

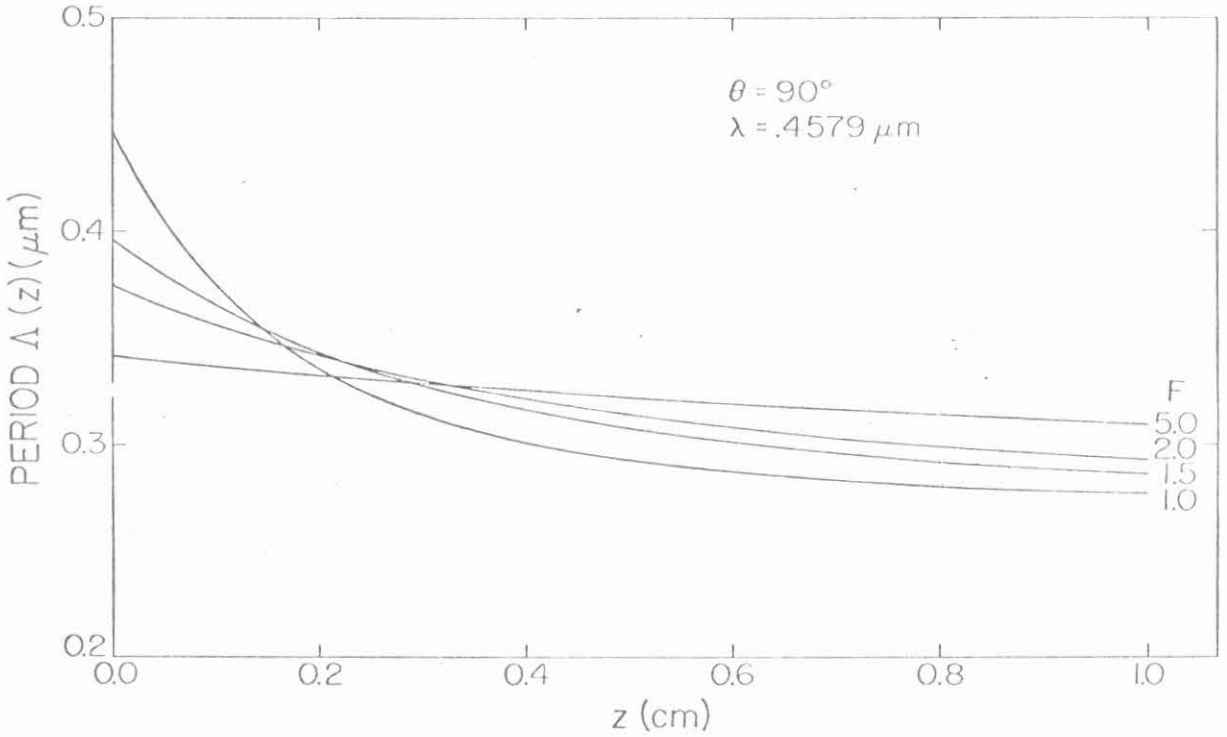

Fig. 3.3 Period variation as a function of F number. The angle θ has a value of 90° and the range of period variation is from .45 to .28 μm, again over a distance of 1 cm. (After reference 1.)

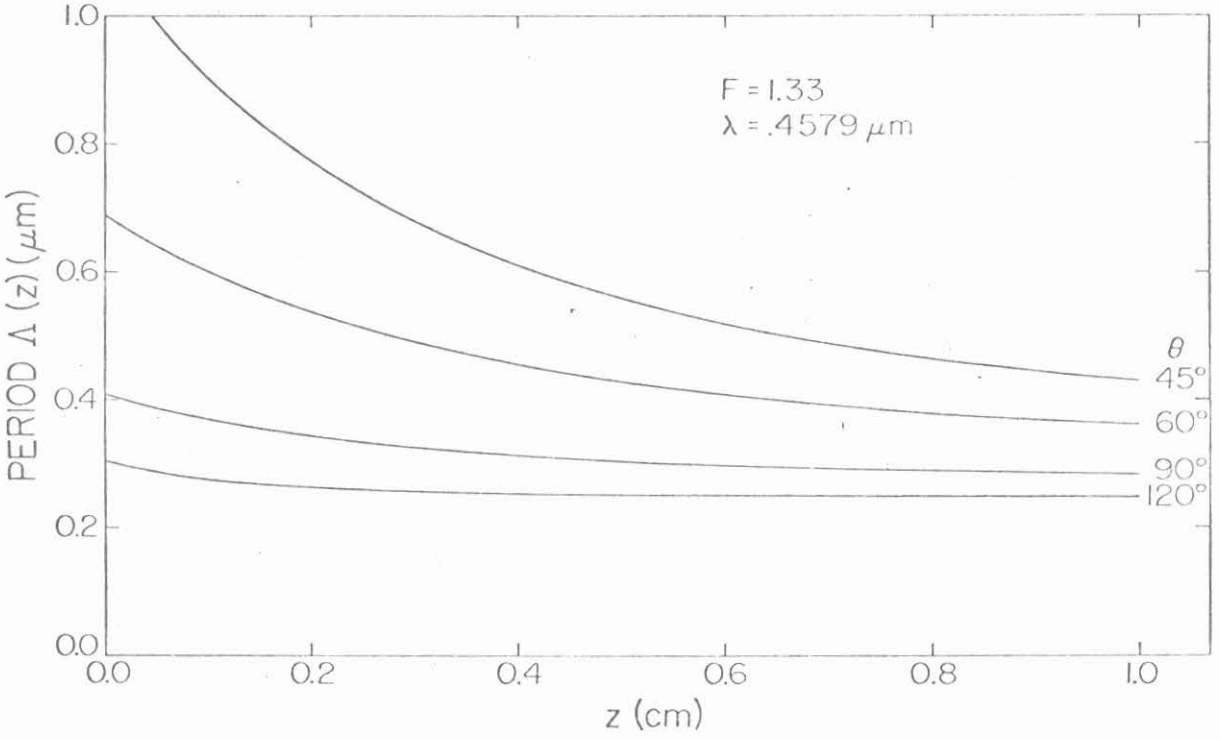

Fig. 3.4 Period variation as a function of θ (the angle between the plane wave and the bisector of the converging wave). The F number of the lens is 1.33 and the illumination wavelength is .4579 μm. The recording distance is kept constant at 1 cm. (After reference 1.)

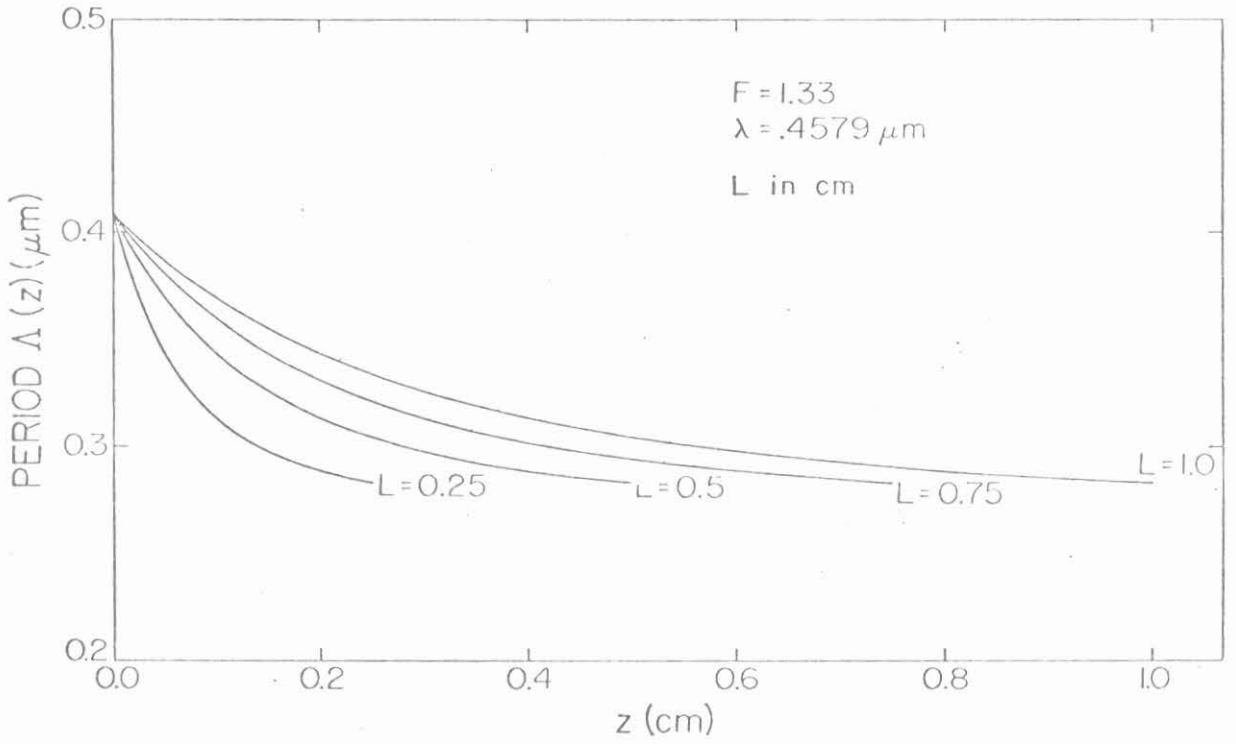

Fig. 3.5 Period variation as a function of recording distance L. The total amount of chirp is the same for all curves; the linearity of variation is seen to improve for large values of L. The angle θ is 90 degrees, the F number is 1.33 and the wavelength is .4579 μm. (After reference 1.)

variation; higher F numbers result in smaller and more linear period variations. In Fig. 3.3 the angle θ has the value of 90°. Here the maximum period variation is for an F=1 lens and it extends from .45μm to .28μm over a distance of 1 cm. It is noted that large values of θ produce smaller period variations.

This particular point is illustrated in Fig. 3.4 where an F = 1.33 lens was chosen and θ was varied from 45° to 120°. Again the grating extends over a distance of 1 cm. It is seen that with θ = 120° the period varies only by 0.05μm, while for θ = 45° the period variation is .5μm.

The linearity of the period variation as a function of grating length L is shown in Fig. 3.5. It should be noted that the beginning and end period is identical for all values of L. Again the F number is 1.33 and the angle θ is 90°.

3.3 Waveguide Coupling

Chirped grating etched onto a dielectric waveguide results in a simultaneous output coupling and focusing to a point $P(x_\lambda, z_\lambda)$ which will vary as a function of the modes supported by the waveguide and the wavelength of the guided modes.

Consider the geometry described by Fig. 3.6. When the guided mode is propagating unperturbed in the waveguide its z dependence is given by $e^{-i\beta z}$, where $\beta = kn_1\cos\theta_1$. When the wave reaches the perturbation the radiated mode will have a z dependence given by $e^{-ik_z z}$. At point z=0, k_z is given by

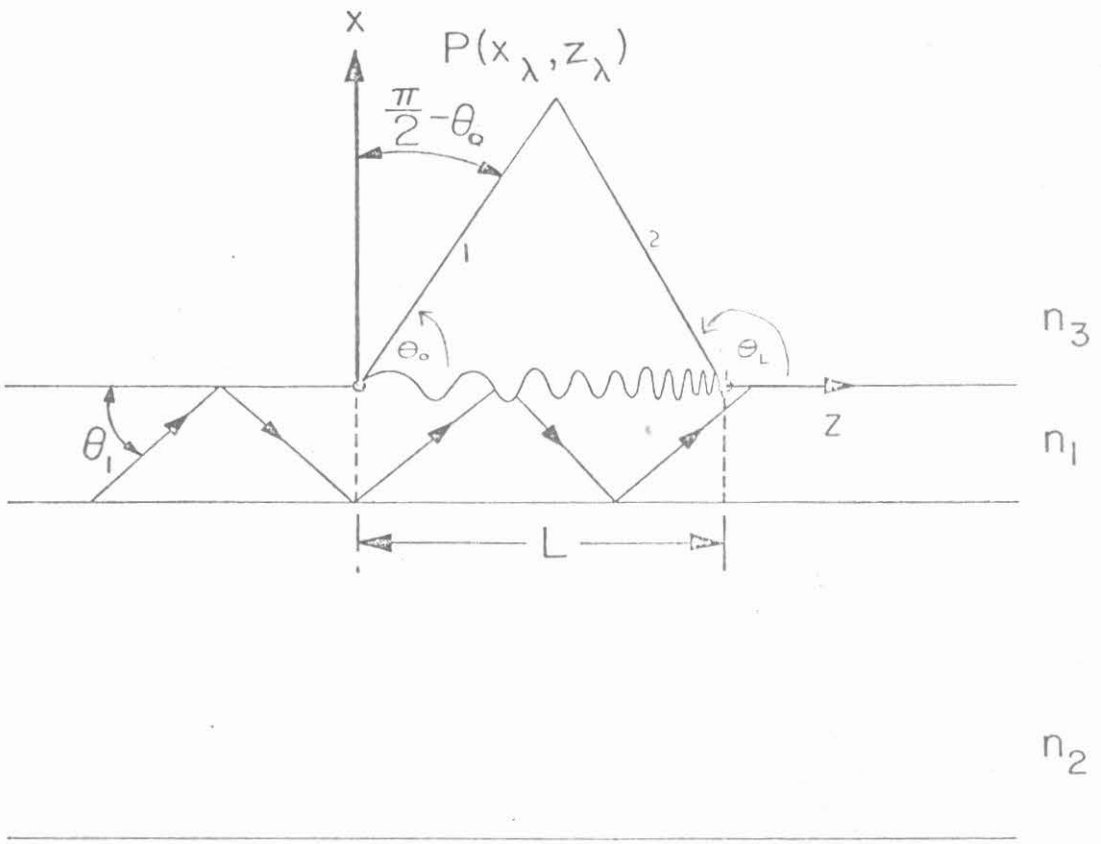

Fig. 3.6 Geometry for a chirped grating etched on the top surface of a waveguide of index n_1. The substrate has an index n_2, and n_3 is the index of refraction of air. A waveguide mode will focus at point $P(x_\lambda, z_\lambda)$ depending on the chirp of the grating and the wavelength. (After reference 1.)

$$k_z(0) = \beta - \frac{2\pi}{\Lambda(0)} \tag{3.8}$$

and at z = L

$$k_z(L) = \beta - \frac{2\pi}{\Lambda(L)} \tag{3.9}$$

Equations (3.8) and (3.9) simply express conservation of momentum for light incident on a periodic medium. Referring to Figure 3.6 we have

$$\tan \theta_o = \frac{k_x(z=0)}{k_z(z=0)} = \frac{\sqrt{k^2 n_3^2 - k_z^2(0)}}{k_z(0)}$$

$$\tan \theta_L = \frac{k_x(z=L)}{k_z(z=L)} = \frac{\sqrt{k^2 n_3^2 - k_z^2(L)}}{k_z(L)}$$

$$k \equiv \frac{\omega}{c}$$

The equations for ray 1 and ray 2 are

$$x = z \tan \theta_o$$

$$x = (z-L) \tan \theta_L$$

The point of focus $P(x_\lambda, z_\lambda)$ is thus found to be

$$z_\lambda = \frac{L \tan \theta_L \omega}{\tan \theta_L - \tan \theta_0} = \frac{k_z(0)\, L \sqrt{k^2 n_3^2 - k_z^2(L)}}{k_z(0) \sqrt{k^2 n_3^2 - k_z^2(L)} - k_z(L) \sqrt{k^2 n_3^2 - k_z^2(0)}} \tag{3.10}$$

and

$$x_\lambda = \frac{\sqrt{k^2 - k_z^2(0)}}{k_z(0)} \, z_\lambda \tag{3.11}$$

The focusing effect and especially the variation of the focus as function of wavelength and period variation is illustrated by Fig. 3.7. Taking $n_1 = 1.565$, $n_2 = 1.51$, $n_3 = 1.0$ and a waveguide thickness of $d = 1.35\mu m$ the eigenvalue equation for β was solved for wavelengths ranging from 4500Å to 6500Å. Having thus determined β for the unperturbed waveguide we calculate $k_z(0)$, $k_z(L)$ for various ranges of period variation. It can be seen from this figure that (a) the larger the period variation the closer to the waveguide the locus of the focal points will be, (b) the smaller the period variation the larger the separation between the different wavelengths and the larger the distance of the locus of the focal points from the waveguide, and (c) if the average period of the chirped grating is increased the focus will shift towards greater values of z.

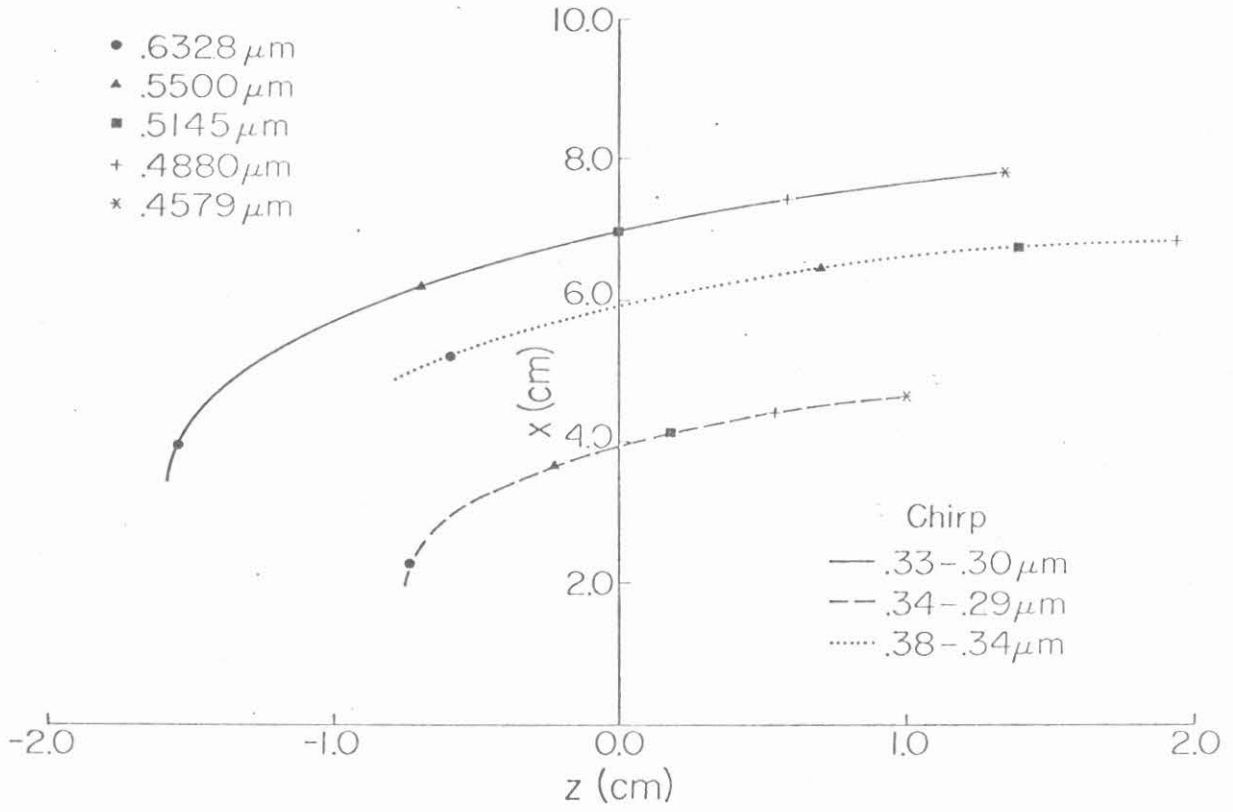

Fig. 3.7 Locus of the foci of various wavelengths for different chirps. The grating is located between z = 0 and z = 1.0 cm at x = 0. $\Lambda(0)$ is the longest period and Λ(1 cm) is the shortest. The waveguide mode is traveling in the positive z direction. (After reference 1.)

3.4 Calculation of Power Output Distribution for Chirped Gratings

In the previous section the characteristics of the chirped gratings and some of their properties were discussed. To complete our theoretical discussion we present a calculation of the actual power radiated into air by a chirped grating.

To analyze this problem we expand the electric field of the perturbed waveguide in terms of the guided modes, the substrate modes and the air modes. This work is essentially an extension of Marcuse's work[3] for which the symmetric case was treated. In our case the waveguide is not symmetric, but the notation and method are similar to Marcuse's.

A closed form solution for the power radiated into air by a chirped grating is presented and the solution is illustrated with examples of gratings where the amount of chirp and the wavelength of the guided radiation is varied.

Consider the geometry and notation as presented in Fig. 3.8a. Using the results from Appendix 1-A, we have for the TE guided modes

$$\mathcal{E}_y = Ae^{-\delta x} \qquad \text{for } x \geq 0 \tag{3.12}$$

$$= A[\cos\kappa x - \frac{\delta}{\kappa}\sin\kappa x] \qquad \text{for } 0 \geq x \geq -d \tag{3.13}$$

$$= A[\cos\kappa d + \frac{\delta}{\kappa}\sin\kappa d]e^{\gamma(x+d)} \qquad \text{for } x \leq -d \tag{3.14}$$

where

$$\kappa \equiv (n_1^2k^2-\beta^2)^{1/2} \tag{3.15}$$

$$\gamma \equiv (\beta^2-n_2^2k^2)^{1/2} \tag{3.16}$$

$$\delta \equiv (\beta^2-n_3^2k^2)^{1/2} \tag{3.17}$$

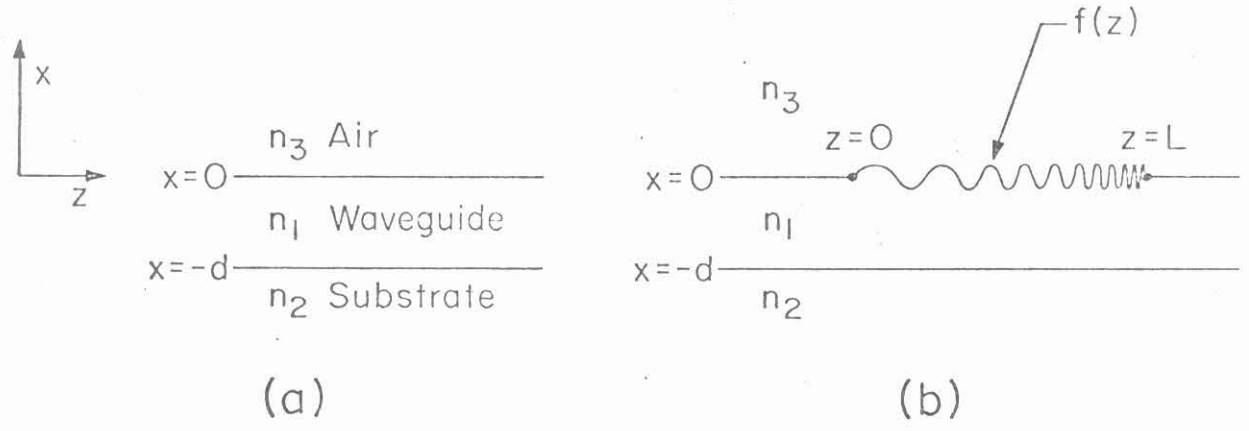

Fig. 3.8a Geometry for a dielectric waveguide.

3.8b Dielectric waveguide with a chirped grating etched on the top surface. (After reference 1.)

where n_1, n_2, n_3 are the indices of refraction of the waveguide, substrate and air, k is the wavenumber in air and β describes the z dependence of the electric field. It should be noted that the factor $e^{i\omega t}\ e^{-i\beta z}$ has been suppressed in Eqs. (3.12)-(3.14). Furthermore, the constants κ, γ, and δ can be determined by the eigenvalue equation:

$$\tan \kappa d = \frac{\kappa(\gamma+\delta)}{\kappa^2-\gamma\delta} \tag{3.18}$$

The amplitude of the electric field A is related to the power carried by the mode, namely:

$$A^2 = \frac{4\kappa^2\omega\mu_o P}{|\beta|[d+1/\gamma+1/\delta](\kappa^2+\delta^2)} \tag{3.19}$$

$$P = \frac{\beta}{2\omega\mu_o}\int_{-\infty}^{\infty} |\mathcal{E}_y|^2 dx$$

where P is the power carried by the mode, d is the thickness of the guide, ω is the radian frequency and μ_o is the magnetic permeability of vacuum.

These guided modes occur for $kn_2 \leq |\beta| \leq kn_1$. For the region $kn_3 \leq |\beta| \leq kn_2$ the substrate modes exist, and finally in the region $0 < |\beta| < kn_3$ the TE air modes of the continuum occur. For the purposes of this discussion we consider the air mode since we want to calculate the power radiated by the waveguide into the air. Appendix 1-A gives the electric field as:

$$\mathcal{E}_y^a = C_r[\cos\Delta x + (\sigma/\Delta)F_i \sin\Delta x] \qquad \text{for } x \geq 0 \qquad (3.20)$$

$$= C_r(\cos\sigma x + F_i \sin\sigma x) \qquad \text{for } 0 \geq x \geq -d \qquad (3.21)$$

$$= C_r[(\cos\sigma d - F_i \sin\sigma d)\cos\rho(x+d) + \frac{\sigma}{\rho}(\sin\sigma d + F_i \cos\sigma d)\sin\rho(x+d)] \qquad \text{for } x \leq -d \qquad (3.22)$$

$$\Delta = (n_3^2 k^2 - \beta^2)^{1/2} \qquad (3.23)$$

$$\sigma = (n_1^2 k^2 - \beta^2)^{1/2} \qquad (3.24)$$

$$\rho = (n_2^2 k^2 - \beta^2)^{1/2} \qquad (3.25)$$

where C_r is again related to the power carried by the mode

$$C_r^2 = \frac{4\omega\mu_o P}{\pi|\beta|}\left[(\cos\sigma d - F_i \sin\sigma d)^2 + \frac{\sigma^2}{\rho^2}(\sin\sigma d + F_i \cos\sigma d)^2 + (1 + \frac{\sigma^2}{\Delta^2}F_i^2)\frac{\Delta}{\rho}\right]^{-1} \qquad (3.26)$$

and F_i can be chosen arbitrarily.

It is instructive to compare the solution for a confined, guided mode with that of the above continuum modes. Matching boundary conditions (E_y and $\frac{\partial E_y}{\partial x}$) at x=0 and x=-d give four constraints on the solution. A fifth constraint is obtained by the normalized power condition. Since Maxwell's equations are second order and the field must be found in three regions, we have to determine six constants using five conditions. This cannot be done for the continuum case, and thus we have one degree of freedom indicated by the F_i coefficient. For the guided

waves, however, the field must decay toward zero as $x \to \pm\infty$. These two added constraints give a total of seven constraints involving six coefficients, with the well-known result being an eigenvalue equation given by equation (3.18).

Since the F_i is arbitrary, it is convenient to choose two fixed values F_1 and F_2. An arbitrary continuum mode can then be given by a linear combination of the F_1 and F_2 type modes. Following the conventional procedure, F_1 and F_2 are chosen so that the two radiation modes are orthogonal to one another

$$F_{1,2} = [(\sigma^2-\rho^2)\sin 2\sigma d]^{-1}\{(\sigma^2-\rho^2)\cos 2\sigma d + (\tfrac{\rho}{\Delta})(\sigma^2-\Delta^2) \pm [(\sigma^2-\rho^2)^2 + 2(\rho/\Delta)(\sigma^2-\rho^2)(\sigma^2-\Delta^2)\cdot\cos 2\sigma d + (\rho^2/\Delta^2)(\sigma^2-\Delta^2)^2]^{1/2}\} \tag{3.27}$$

where

$$P\,\delta(\rho-\rho') = \frac{\beta^*}{2\omega\mu_o}\int_{-\infty}^{\infty} \hat{\mathcal{E}}_y{}^a(\rho)\hat{\mathcal{E}}_y^{a\,*}(\rho')dx$$

Again the factor $e^{i\omega t}e^{-i\beta z}$ has been suppressed in equations (3.20)-(3.22); in this work β is an inherently positive quantity.

Next we expand an arbitrary T E electric field for the perturbed waveguide in terms of the discrete guided modes and the continuum of both substrate and air modes:

$$E_y = \sum_{\text{discrete}} C_n(z)\mathcal{E}_n + \int_0^{k(n_2^2-n_3^2)^{1/2}} g(\rho,z)\mathcal{E}^s(\rho)d\rho + \sum_{\substack{\text{even}\\ \text{odd}}} \int_{k(n_2^2-n_3^2)^{1/2}}^{kn_2} h(\rho,z)\mathcal{E}^a(\rho)d\rho \tag{3.28}$$

where $\mathcal{E}_n$ are the discrete guided modes, given by equations (3.12), (3.13), (3.14) for the n values of β determined from the eigenvalue equation (3.18). Similarly $\mathcal{E}^a$ are the air modes given again by equations (3.20), (3.21) and (3.22), where even and odd refer to the choice of F_2 and F_1 (Eq. 3.27). $\mathcal{E}^s$ are the substrate modes which have not been presented explicitly since they will not affect this calculation. It is to be noted that the above expansion for the total electric field E_y is possible since the set of eigenfunctions is complete. The calculation is simplified due to the orthogonality of the modes as a result of the choice of F_i.

The limits of integration in equation (3.28) were found from equation (3.25) and the requirement that for guided modes $kn_2 \leq \beta \leq kn_1$, for substrate modes $kn_3 \leq \beta \leq kn_2$, and for air modes $0 \leq \beta \leq kn_3$ (β inherently positive)

To determine the value of $h(\rho,z)$, we substitute equation (3.28) into the Helmholtz wave equation, multiply by $\mathcal{E}^{*a}$, integrate over x, and using the orthogonality relations, get a differential equation for $h(\rho,z)$.

$$\frac{\partial^2 h}{\partial z^2} - 2i\beta\frac{\partial h}{\partial z} = H(\rho,z)$$

The above differential equation is easily converted to an integral equation.

$$h(\rho,z) = Q(\rho) + R(\rho)e^{2i\beta z} + \frac{1}{2i\beta}\int_0^z [e^{2i\beta(z-\zeta)} - 1]H(\rho,\zeta)d\zeta \qquad (3.29)$$

where

$$H(\rho,z) = \frac{-\beta k^2}{2\omega\mu P}\left[\sum_n C_n(z)\int_{-\infty}^{\infty}\mathcal{E}_\rho^{*a}(\rho)\Delta n^2\mathcal{E}_{\rho n}\,dx\right.$$
$$+\int_{k(n_2^2-n_3^2)^{1/2}}^{kn_2} d\rho' g(\rho',z)\int_{-\infty}^{\infty}\mathcal{E}_\rho^{*a}(\rho)\Delta n^2\mathcal{E}_\rho^{s}(\rho')dx + \int_{k(n_2^2-n_3^2)^{1/2}}^{kn_2} d\rho' h(\rho',z)\left.\int_{-\infty}^{\infty}\mathcal{E}_\rho^{*a}(\rho)\Delta n^2\mathcal{E}_\rho^{a}(\rho')dx\right] \qquad (3.30)$$

where Δn^2 describes the deviation of the corrugated guide dielectric constant from that of a uniform waveguide.

Note that for $\Delta n^2=0$, $H(\rho,z)=0$, and we have

$$h(\rho,z) = Q(\rho) + R(\rho)e^{2i\beta z}$$

When this is multiplied by $\mathcal{E}_\rho^a$, which contains a z dependence $e^{-i\beta z}$, we get the sum of a forward traveling mode with z dependence $e^{-i\beta z}$ and a backward traveling mode with z dependence $e^{+i\beta z}$ (time dependence $e^{+i\omega t}$). This, of course, was to be expected.

To solve equation (3.29) we use the Born approximation. In other words, we use $C_n(0) = \delta_{on}$, where δ_{on} is the Kronecker delta, instead of $C_n(z)$ and set $g(\rho,z) = h(\rho,z) = 0$ in Eq. (3.30), resulting in

$$H(\rho,z) \simeq \frac{-\beta k^2}{2\omega\mu P}\int_{-\infty}^{\infty}\mathcal{E}_\rho^{*a}(\rho)\Delta n^2\mathcal{E}_{\rho o}\,dx \qquad (3.31)$$

In the next step we assume that the perturbation of the guide from its ideal shape is on the top surface of the guide as shown in Fig. 3.8b. By taking a shallow grating and thus setting $x = 0$ in the above equation we get

$$H(\rho,z) = \frac{-\beta k^2}{2\omega\mu P}(n_1^2-n_3^2)f(z)\underset{\sim}{\xi}^{*a}(0,\rho,z)\underset{\sim}{\xi}_0(0,z) \tag{3.32}$$

Equation (3.29) can then be divided into parts as follows:

$$h^+ = Q - \frac{1}{2i\beta}\int_0^z H(\rho,\zeta)d\zeta \tag{3.33}$$

$$h^- = [R + \frac{1}{2i\beta}\int_0^z e^{-2i\beta\zeta}H(\rho,\zeta)d\zeta]e^{2i\beta z} \tag{3.34}$$

such that

$$h = h^+ + h^-$$

Recalling equation (3.28) we note that the contribution to the total electric field arises from the product of $h(\rho,z)\cdot\underset{\sim}{\xi}^a(\rho,z)$. The z dependence of $\underset{\sim}{\xi}^a(\rho,z)$ is $e^{-i\beta z}$. If we consider the z dependence of the product, then

$$\underset{\text{(z dependence)}}{h(\rho,z)\underset{\sim}{\xi}^a(\rho,z)} = h^+e^{-i\beta z} + [R + \frac{1}{2i\beta}\int_0^z e^{-2i\beta\zeta}H(\rho,\zeta)d\zeta]e^{i\beta z} \tag{3.35}$$

Then we can associate the h^+ part of the wave with the amplitude of the forward traveling radiating mode and the term in brackets with the negative traveling one.

The power radiated into air is given by

$$\left(\frac{\Delta P}{P}\right)_{\substack{\text{radiated}\\ \text{into air}}} = \sum_{\substack{\text{even}\\ \text{odd}}} \int_{k(n_2^2-n_3^2)^{1/2}}^{kn_2} d\rho \left\{ [\,|h^+(\rho,L)|^2 + |h^-(\rho,0)|^2] \frac{\int_0^\infty |\underset{\sim}{\xi}^a|^2\,dx}{\int_{-\infty}^\infty |\underset{\sim}{\xi}^a|^2\,dx} \right\} \tag{3.36}$$

The term involving the integration with respect to x gives the fraction of the air mode radiated into the air. The remainder is, of course, radiated into the substrate. Furthermore, the boundary conditions require that

$$h^+(\rho,z=0) = 0$$

$$\Longrightarrow \quad h^+ = -\frac{1}{2i\beta}\int_0^z H(\rho,\zeta)d\zeta$$

$$h^-(\rho,z=L) = 0 \tag{3.37}$$

$$h^- = \left[\frac{1}{2i\beta}\int_L^z e^{-2i\beta\zeta} H(\rho,\zeta)d\zeta\right] e^{2i\beta z} \tag{3.38}$$

Using the above conditions and equations (3.32), (3.12) and (3.20) we get

$$h^+(\rho,L) = \frac{k^2(n_1^2 - n_3^2)}{4i\omega\mu P}\,\phi_+\,AC_r \tag{3.39}$$

$$h^-(\rho,0) = \frac{k^2(n_1^2 - n_3^2)}{4i\omega\mu P}\,\phi_-\,AC_r \tag{3.40}$$

where

$$\phi_+ = \phi_+(\beta,L) = \int_0^L f(z)\, e^{i(\beta-\beta_o)z}\, dz \tag{3.41}$$

and

$$\phi_- = \phi_-(\beta,L) = \int_0^L f(z)\, e^{-i(\beta+\beta_o)z}\, dz \tag{3.42}$$

Using equations (3.19) and (3.26) we can calculate $h^+(\rho,L)$, namely

$$|h^+(\rho,L)_i|^2 = \frac{k^4(n_1^2-n_3^2)^2|\phi_+|^2\,\kappa_o^2}{|\beta_o|[d+1/\gamma_o+1/\delta_o](\kappa_o^2+\delta_o^2)\pi|\beta|}$$

$$\cdot\ [(\cos\sigma d - F_i\sin\sigma d)^2 + \frac{\sigma^2}{\rho^2}(\sin\sigma d + F_i\cos\sigma d)^2 \qquad (3.43)$$

$$+ (1+\frac{\sigma^2}{\Delta^2}F_i^2)\frac{\Delta}{\rho}]^{-1}$$

where κ_o, γ_o, δ_o refer to the zero order mode solutions for equations (3.15), (3.16), (3.17), and (3.18).

Similarly

$$|h^-(\rho,0)_i|^2 = \frac{|h^+(\rho,L)_i|^2|\phi_-|^2}{|\phi_+|^2} \qquad (3.44)$$

Finally, to calculate the fraction of the air mode radiated into air we use equations (3.20), (3.21) and (3.22)

$$\left(\frac{\int_0^\infty |\xi^a|^2\,dx}{\int_{-\infty}^\infty |\xi^a|^2\,dx}\right)_{\substack{\text{even}\\\text{odd}}} = \frac{1+\frac{\sigma^2}{\Delta^2}F_i^2}{1+v_i^2+w_i^2+\frac{\sigma^2}{\Delta^2}F_i^2} \qquad (3.45)$$

where $v_i = \cos\sigma d - F_i\sin\sigma d$ (3.46)

$$w_i = \frac{\sigma}{c}(\sin\sigma d + F_i\cos\sigma d) \qquad (3.47)$$

Now using (3.45), (3.44), and (3.43), equation (3.36) becomes

$$\left(\frac{\Delta P}{P}\right)_{\substack{\text{radiated into}\\ \text{air per unit } \beta}} = \frac{S}{\rho}\left[|\phi_+|^2 + |\phi_-|^2\right] \cdot \sum_{i=1}^{2} \frac{u_i}{\left[(v_i)^2+(w_i)^2+u_i\right]\cdot\left[(v_i)^2+(w_i)^2+\frac{\Delta}{\rho}u_i\right]} \tag{48}$$

(3.48)

where
$$u_i = 1 + \frac{\sigma^2}{\Delta^2} F_i^2 \tag{3.49}$$

and

$$S = \frac{k^4(n_1^2 - n_3^2)\kappa_o^2}{|\beta_o|(d + 1/\gamma_o + 1/\delta_o)(\kappa_o^2 + \delta_o^2)\pi} \tag{3.50}$$

Equation (3.48) shows the fractional power radiated per unit beta for an arbitrary perturbation on the top surface. Once the perturbation is given, then ϕ_+ and ϕ_- can be calculated.

For the particular case of the chirped grating with a transmission function given by equation (3.4), f(z) can be written as

$$f(z) = a \sin(\alpha z + \gamma z^2) \tag{3.51}$$

Direct substitution into equations (3.41) and (3.42) and using the method of stationary phase results in

$$|\phi_+|^2 = \frac{\pi a^2}{4\gamma} \tag{3.52}$$

if $\gamma > 0$, $\alpha+\beta-\beta_o < 0$, and $\alpha+\beta-\beta_o+2\gamma L > 0$ (a)

or $\gamma < 0$, $\alpha+\beta-\beta_o > 0$, and $\alpha+\beta-\beta_o+2\gamma L < 0$ (b)

or $\gamma < 0$, $\alpha+\beta_o-\beta > 0$, and $\alpha+\beta_o-\beta+2\gamma L < 0$ (c)

otherwise $\phi_+ = 0$.

Similarly,

$$|\phi_-|^2 = \frac{\pi a^2}{4\gamma} \tag{3.53}$$

if $\gamma > 0$, $\alpha-\beta-\beta_o < 0$, and $\alpha-\beta-\beta_o + 2\gamma L > 0$ (a)

or $\gamma < 0$, $\alpha-\beta-\beta_o > 0$, and $\alpha-\beta-\beta_o + 2\gamma L < 0$ (b)

or $\gamma < 0$ $\alpha+\beta+\beta_o > 0$, and $\alpha+\beta+\beta_o + 2\gamma L < 0$ (c)

otherwise $|\phi_-|^2 = 0$

These equations, (3.52a,b,c) and (3.53a,b,c) give the range of β for which the guide radiates. They can be interpreted simply as conservation of momentum equations for Umklapp processes. For forward scattering, an Umklapp process requires

$$\beta = \beta_o \pm \frac{2\pi}{\Lambda(z)} \tag{3.54}$$

where $\Lambda(z)$ is the period of the grating at point z, but

$$\frac{2\pi}{\Lambda(z)} = \frac{\partial}{\partial z}(\alpha z + \gamma z^2) = \alpha + 2\gamma z \tag{3.55}$$

Thus,

$$\beta - \beta_o \mp \alpha = \pm 2\gamma z \tag{3.56}$$

Equation(3.56) must hold somewhere in the grating region $(0 < z < L)$ for scattering to occur. Considering the separate cases $\gamma > 0$ and $\gamma < 0$, as well as the two sign possibilities in equation(3.56) results in the conditions given in equations (3.52a,b,c). Since we have taken β as an inherently positive quantity, the case of backward scattering must be considered separately and the equation governing it is

$$-\beta = \beta_o \pm \frac{2\pi}{\Lambda(z)} \tag{3.57}$$

The above equation results in (3.53a,b,c).

To illustrate equation (3.48) we present Figure 3.9. The guide is 1.0 cm long, its thickness is .6425μm and the index of refraction $n_1 = 1.55$. The substrate index of refraction is $n_2 = 1.52$, and that of air is taken to be $n_3 = 1.0$. The film perturbation is of the form of equation (3.51) and a was chosen to be 100Å. The calculation for the fundamental mode gave $\beta_o = 1.505 \times 10^7 (m^{-1})$ corresponding to a wave number of $9.78 \times 10^6\ m^{-1}$. The figure illustrates the fractional power output in the air per unit β as a function of β for various chirps. We see from the figure that the lower the chirp (curve 4) the narrower the range of β distribution. In the limit of no chirp we expect the familiar delta function. For high chirp we have a wide range of β distribution extending over most of the theoretically possible range (k_z = 0 to k). The total power output radiated into air is the area under the curves. For Figure 3.9 it ranges from 10 to 15 percent of the incident mode power.

The sharp vertical boundaries to the curves are easily interpreted as follows. Consider, for example, curve 4 of Figure 3.9, for which Λ ranges from .35μ to .4 μm.

$$\beta' = \beta_o - \frac{2\pi}{\Lambda} \tag{3.58}$$

where β' = z dependence of field after interaction with the grating. Using $\beta_o = 1.505 \times 10^7/m$ and Λ = .35μ we find $\beta' = -3.0 \times 10^6/m$. Similarly for Λ = .4 , $\beta' = -.66 \times 10^6/m$. These values are simply the

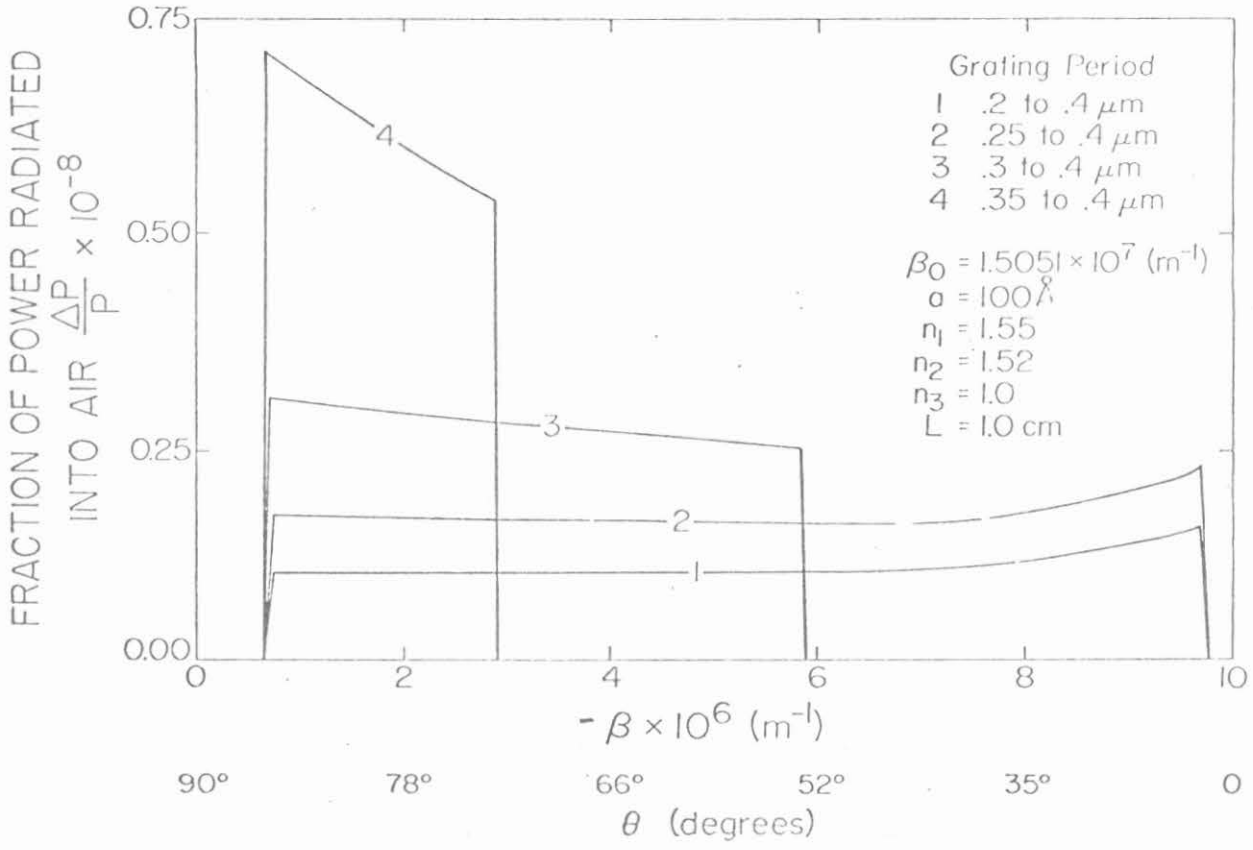

Fig. 3.9 Fraction of mode power radiated into air per unit β as a function of β or θ, where θ is the angle of scattering with respect to the z-axis ($\theta = \pi - \theta_0$, see Fig. 3.6) for various chirps. The area under each curve represents the total power radiated into air for a given chirp. (After reference 1.)

range of permissible β values and mark the two sides of curve 4.

It is important to note that in the actual calculation the waveguide is divided into approximately one hundred sections. $\Delta P/P$ is calculated from the first section and then it is subtracted from the total P. This new value of P is used as input power for the next section, and so on. This enables us to handle large power coupling and not be limited by the first Born approximation. This particular point is illustrated in Fig. 3.10. The total power output radiated into air is greater than 45 percent, due to the larger perturbation. In Figure 3.10 the film thickness is 1.35 μm and its index of refraction $n_1 = 1.565$. The substrate has an index of refraction $n_2 = 1.51$ and air $n_3 = 1.0$. The guide is 1.1 cm long and again the perturbation on the top surface is given by equation (3.51). In this case a is 500Å, and the period varies from .295 to .33 μm. The different curves represent the fractional power output per unit β for various wavelengths. It can be seen from this figure that different wavelengths radiate over different and non-overlapping β ranges.

In addition, we have calculated the fractional power (per unit β) radiated into air and substrate, and found that as predicted by the theory[5], it is twice as large as the one radiated into air.

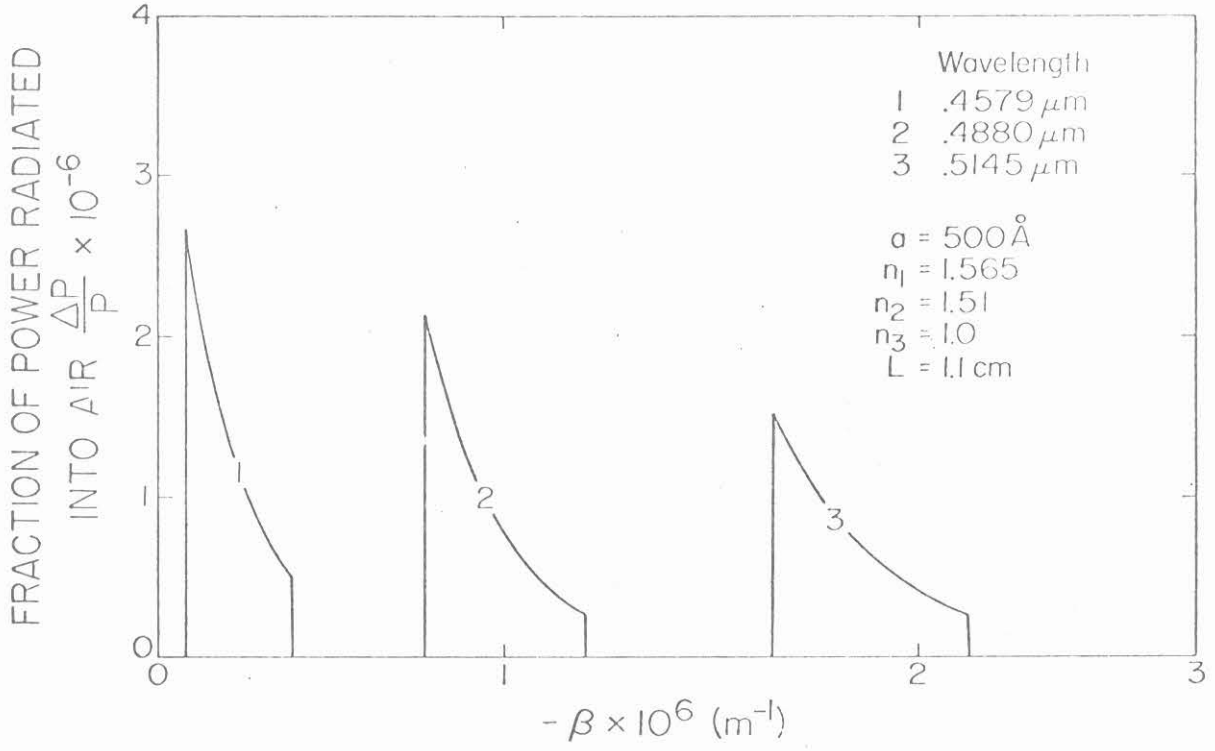

Fig. 3.10 Fraction of mode power radiated into air per unit β as a function of β for a chirp of .33 to .295 μm and various wavelengths. The amplitude of the chirp is set at 500Å, and the corrugation extends over a length L of 1.1 cm. (After reference 1.)

3.5 Experimental Results

The dielectric waveguides were made, as described in the previous chapter, by sputtering Corning 7059 glass with a Technics MIM Model 5.5 ion beam etching machine. The refractive index of the sputtered glass was 1.565 and the film thickness of all samples, as measured with a Sloan Dektak, was 1.35μ.

Chirped gratings were fabricated on the surface of the waveguide as follows: a layer of undiluted Shipley AZ1350B photoresist was spin coated at 6000 rpm on the waveguide. After prebaking, the photoresist was exposed to the interference pattern of a collimated laser beam with a converging beam. As detailed above, such interference pattern gives rise to chirped gratings. The $\lambda = 4579\text{Å}$ line from an Ar^+ laser was used under the following conditions $\theta = 94.5$, $F = 1.33$, $L = 1.2$ cm, resulting in gratings with periods varying from 0.29 to 0.33 μm over a distance of 1.2 cm.

Typically the laser beam intensity was 0.6 mw/cm^2 (in each leg) and the exposure time used was 60 sec. Gratings of high efficiency were obtained using AZ 303 developer, and 10 sec development time.

The photoresist was next post baked under vacuum for 30 min and the waveguide was ion beam etched through the photoresist, at ion current density 0.1 mA/cm^2 and accelerating voltage of 1800V, for 30 min. The sample was kept at an angle of 30° with respect to the ion beam. The gratings thus fabricated in the glass had a peak to trough height of about 500Å.

In the focusing experiment light was coupled from an argon laser into the waveguide using a prism coupler. The light entering the corrugated section was focused outside the waveguide. The position of the focal point (x_f, z_f) was measured experimentally for various lines of the argon laser. The experimental points are shown in Figure 3.11, along with the theoretical predicted curve for this particular waveguide.

An output prism coupler was added at the end of the corrugated region. The light intensity which was coupled out was measured for two cases: a) light going through the corrugated region, and b) light going through a neignboring uncorrugated region. The ratio between the intensities in case (a) and case (b) was found to be 1:10. The fabrication and experimental work was done by Alexis Livanos and A. Katzir.

3.6 Conclusion

In this work the properties of chirped grating output couplers have been studied. Expressions giving the grating period variation for various geometries and recording conditions have been presented. As one important application of this device, the focusing effect in a waveguide incorporating chirped grating was demonstrated. The thickness of this waveguide, and the chirp were chosen so as to focus the light about 6 cm away from the waveguide. The theoretical calculations, which were verified experimentally, show that the focal point moves by about 1-2 cm when the wavelength was changed from 4579Å to 5145Å. The chirped grating structure therefore separates very well between propagating beams of different wavelengths, while focusing them outside the waveguide.

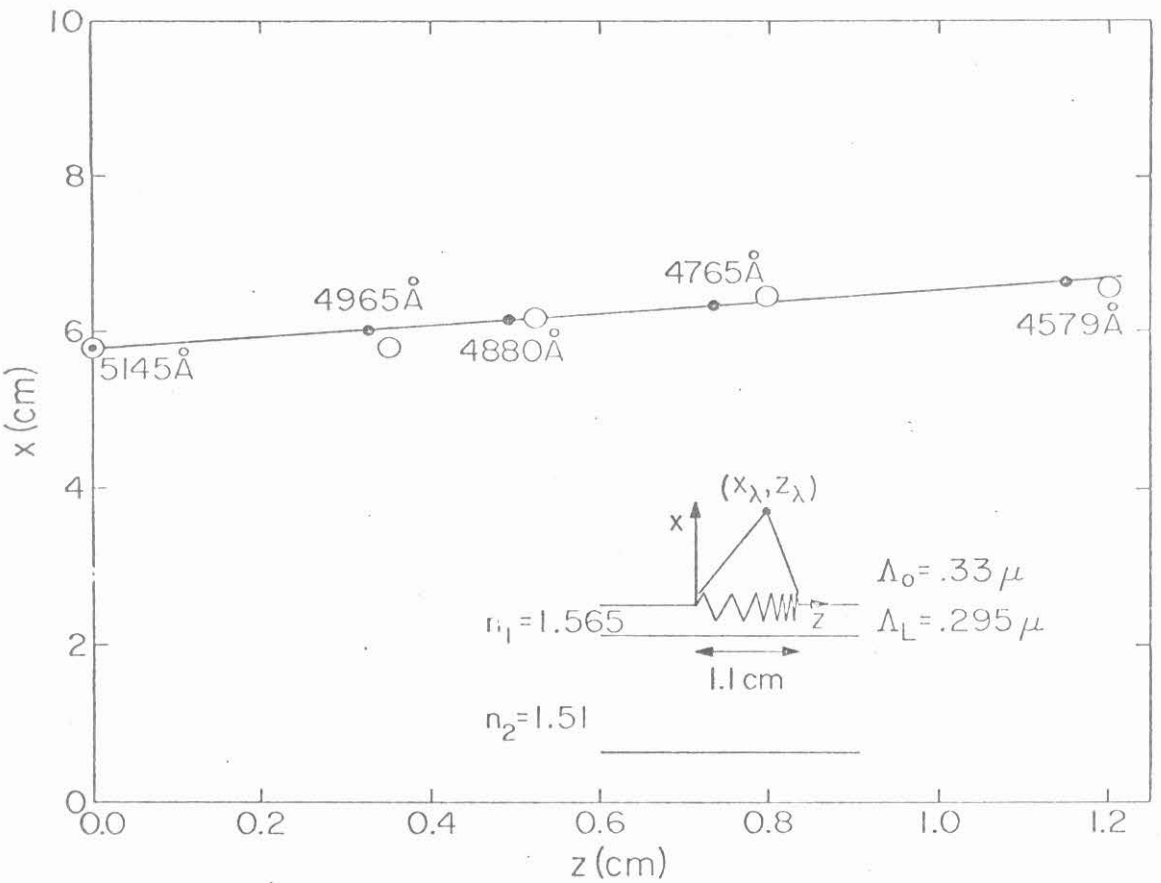

Fig. 3.11 Experimental and theoretical results of the focusing of the corrugated structure used. The solid line represents the theoretical position of the focus as a function of wavelength. The solid dots represent the focus of the prominent lines of the Ar^+ laser. The large circles are the experimental points for these wavelengths as measured with a two-dimensional translation probe. (After reference 1.)

Finally, a coupled mode theory was presented which predicted the amount of light radiated out of the guide at various angles.

Chapter 3 References

1. A. Katzir, A. C. Livanos, J. B. Shellan and A. Yariv, IEEE J. Quantum Elect. QE-13, 296 (1977).

2. R. A. Bartolini, Appl. Opt. 13, 129 (1974).

3. D. Marcuse, Bell Syst. Tech. J. 48, 3187 (1969).

4. D. Marcuse, Theory of Dielectric Optical Waveguides (Academic Press, New York, 1974).

5. N. Streifer, R. D. Burnham and D. R. Scifres, IEEE J. Quantum Elect. 12, 494 (1976).

Chapter 4

STATISTICAL ANALYSIS OF BRAGG REFLECTORS

In previous chapters we considered the effects of introducing a predetermined and controlled aperiodicity in an optical structure. We now turn our attention to studying the effects of a random, statistical aperiodicity in a multilayer reflector. We will no longer be able to predict the reflection properties of any single sample, but only the properties of an ensemble. Analytic expressions are obtained for $\langle\rho\rangle$ and $\langle\rho\rho^*\rangle$, the expected value of the reflection and reflectivity coefficients as a function of σ, the standard deviation in layer thickness. These expressions are then compared with values obtained using a computer routine which "builds" a reflector with the desired parameters and σ value, and then calculates the reflection. The results of the computer experiment are presented in the form of $p(\rho\rho^*)$, the probability distribution function of a statistical Bragg reflector. Finally, simple phenomenological expressions are presented for the reflectivity probability distribution.

4.1 Introduction

Extensive studies have been made of the reflection of light from ideal periodic multilayered media.[1,2] Among the many uses of such structures are coatings for both high reflection and antireflection. Other proposals involve the use of these structures for phase matching in nonlinear optical applications[3,4,5] and for obtaining optical birefringence in stratified media composed of isotropic or cubic materials[6,7].

In practice, however, it is not possible to fabricate perfect structures, and to date the standard deviation in layer thicknesses of commer-

cially made mirrors is typically 2% when monitored optically, and even greater when measured mechanically[8,9]. Great precision in layer thickness can be achieved by using new techniques such as molecular-beam epitaxy, but these techniques are also costlier than the standard electron beam evaporation.

Although there is ample literature on periodic structures, the study of aperiodic structures has been rather limited[10,11,12]. The primary effect of a slight aperiodicity is to decrease the amplitude and broaden the width of the reflectivity spectrum. It is the purpose of this paper to study the effect on reflectivity of a random fluctuation in layer thickness about an ideal thickness. There are many additional causes of a less than ideal reflectance from a mirror. Among them are absorption, index variations, and systematic errors in the manufacturing of reflectors. What follows is simply an analysis of one of the imperfections, namely a statistical fluctuation in layer thickness about some predetermined mean.

The case of a low reflectivity structure is easily handled using the undepleted incident wave approximation. Next a perturbation solution to the coupled mode equations is presented which gives results for arbitrarily large reflectances. Finally, a computer study is presented which uses the formalism of the matrix and translation operator developed by Yeh, Yariv and Hong[2] to predict the expectation value of ρ and $|\rho|^2$ as a function of σ as well as $p(|\rho|^2)$, the probability of manufacturing a sample of given reflection. An analytic expression is then presented for $p(|\rho|^2)$ which agrees well with the results from the computer experiment.

4.2 Low Reflectivity Limit

We start by calculating the reflectivity of a mirror with N cells in the limit of low reflectance. Assuming a constant incident wave of unit amplitude we obtain for the reflected wave:

$$\rho = r_1[1 + e^{2i(k_{1x}a_1 + k_{2x}b_1)} + e^{2i[k_{1x}(a_1+a_2) + k_{2x}(b_1+b_2)]} + \cdots + e^{2i[k_{1x}(a_1+a_2+\cdots a_N) + k_{2x}(b_1+b_2+\cdots+b_N)]}]$$
$$- r_1 e^{2i\,k_{2x}b_1}[1 + e^{2i(k_{1x}a_1 + k_{2x}b_2)} + e^{2i[k_{1x}(a_1+\cdots+a_{N-1}) + k_{2x}(b_2+\cdots+b_N)]} + \cdots + e^{2i[k_{1x}(a_1+\cdots+a_{N-1}) + k_{2x}(b_2+\cdots+b_N)]}] \qquad (4.1)$$

where $k_{ix} = \frac{\omega}{c} n_i \quad i = 1,2, \qquad r_1 = \frac{k_{1x} - k_{2x}}{k_{1x} + k_{2x}}$,

ω is the radian frequency of light, c is the velocity of light, and n_1 is the index of refraction in a layer of material 1, and n_2 is the index in a layer of material 2. N is the number of unit cells and the number of dielectric interfaces is 2N+1, with r_1 representing the magnitude of the reflection from a single layer. a_p is the thickness of the layer of index n_1 in the p^{th} cell, and b_p is the thickness of the layer of index n_2 in the p^{th} cell (see Figure 4.1).

We denote the random deviation of the layers' thickness by parameters u_p, v_p defined by

$$a_p = a^{(o)} + u_p \qquad p = 1,N$$
$$b_p = b^{(o)} + v_p$$
$$a^{(o)}, b^{(o)} = \text{ideal thickness of layers} \qquad (4.2)$$
$$u_p, v_p = \text{random variables with assumed Gaussian distribution and standard deviations } \sigma_a \text{ and } \sigma_b$$

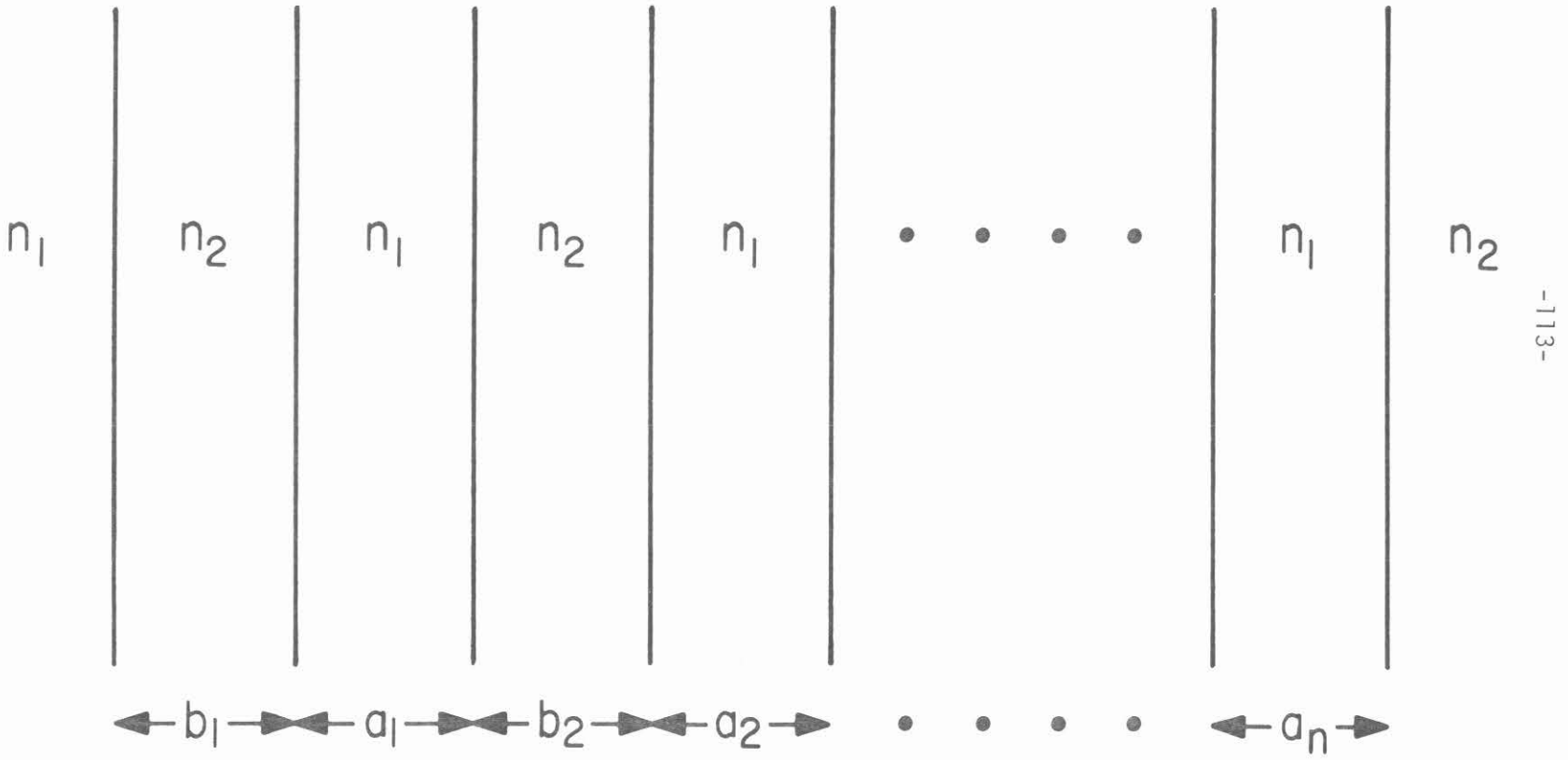

Fig. 4.1 Geometry of reflection with n cells in low reflectivity case

In the process of taking the ensemble average of r we use the following theorem: If G is a random Gaussian variable with average value zero and standard deviation σ_G, then the ensemble average of $e^{iG} \equiv \langle e^{iG} \rangle = e^{-\frac{1}{2}\sigma_G^2}$. This can easily be shown by expanding e^{iG} in a Taylor series and averaging term by term.

A typical term in (4.1) is

$$e^{2i[k_{1x}(a_1+\cdots+a_p) + k_{2x}(b_1+\cdots+b_p)]}$$

$$= e^{2ip[k_{1x}a^{(o)} + k_{2x}b^{(o)}]} \; e^{2i[k_{1x}(u_1+\cdots+u_p) + k_{2x}(v_1+\cdots+v_p)]} \tag{4.3}$$

The ensemble average of this term is

$$e^{2ip[k_{1x}a^{(o)} + k_{2x}b^{(o)}]} \; e^{-2[k_{1x}^2 p\sigma_a^2 + k_{2x}^2 p\sigma_b^2]} = e^{2ip\,k\Lambda} \; e^{-2pk^2\sigma^2}$$

where $k^2\sigma^2 \equiv k_{1x}^2\,\sigma_a^2 + k_{2x}^2\,\sigma_b^2$

$$k\Lambda \equiv k_{1x}a^{(o)} + k_{2x}b^{(o)}$$

We thus find the expectation value of ρ is

$$\langle \rho \rangle = \frac{r_1}{1 - e^{2ik\Lambda}\, e^{-2k^2\sigma^2}} \{1 - e^{2i(N+1)k\Lambda}\, e^{-2(N+1)k^2\sigma^2}$$

$$- e^{2ik_{2x}b^{(o)}}\, e^{-2k_{2x}^2\,\sigma_b^2}\,(1 - e^{2iNk\Lambda}\, e^{-2Nk^2\sigma^2})\} \tag{4.4}$$

The magnitude of this quantity is plotted in Figure 4.2 for the case N = 25 and $r_1 = 1.96 \times 10^{-3}$. We have taken $k_{2x}^2\,\sigma_b^2 = k_{1x}^2\,\sigma_a^2 = \frac{1}{2}k^2\sigma^2$ and $\rho = .1$ for $\sigma = 0$ at the center of the band gap, as well as $k_{2x}b^{(o)} = k_{1x}a^{(o)}$. It can be seen in Figure 4.2 that the nonzero value of σ has the effect of broadening the response as well as lowering

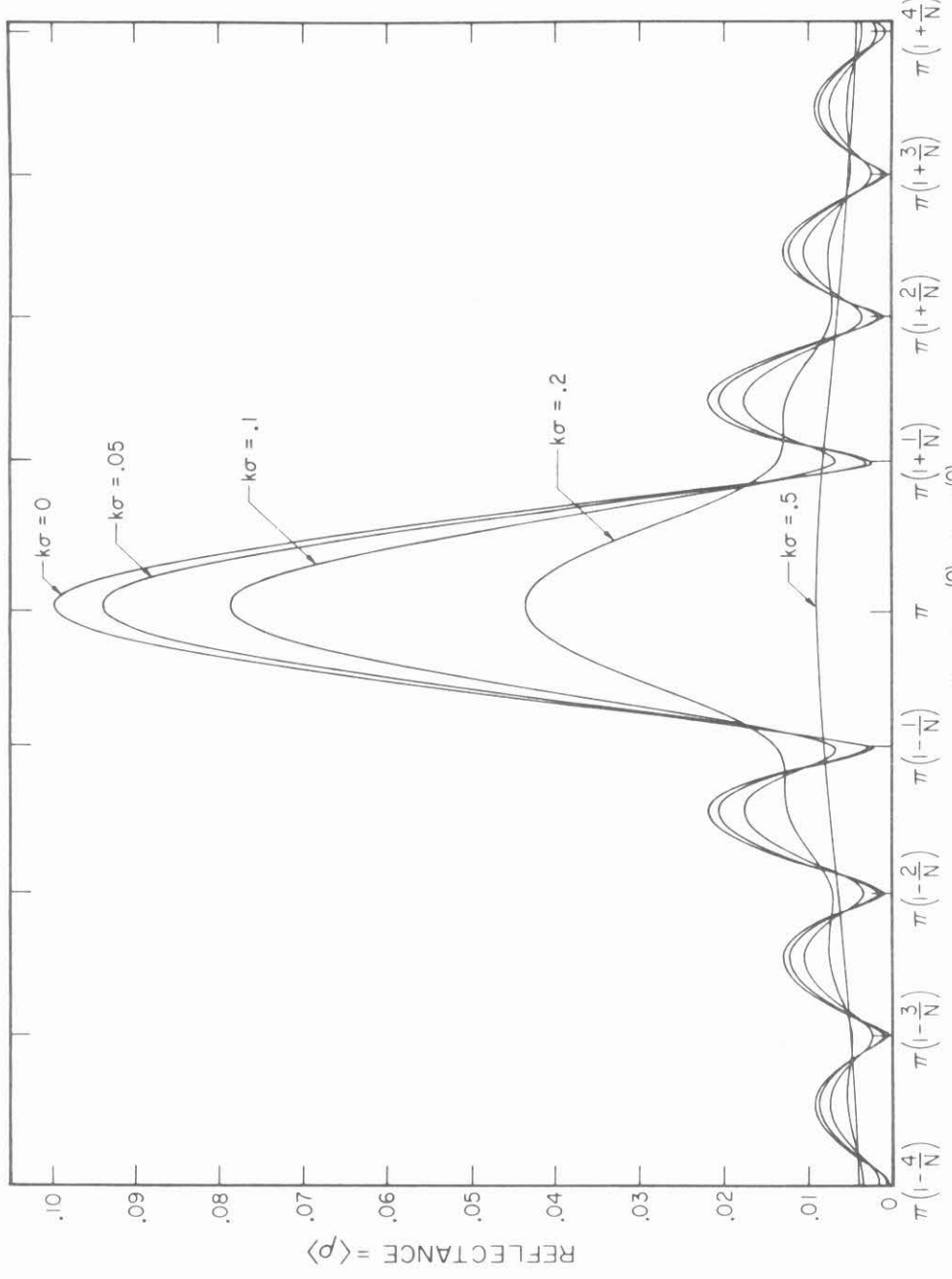

Fig. 4.2 Average reflectance as a function of layer standard deviation and shift from center of the band gap, indicating the broadening and lowering of the response curve for the case of 25 cells.

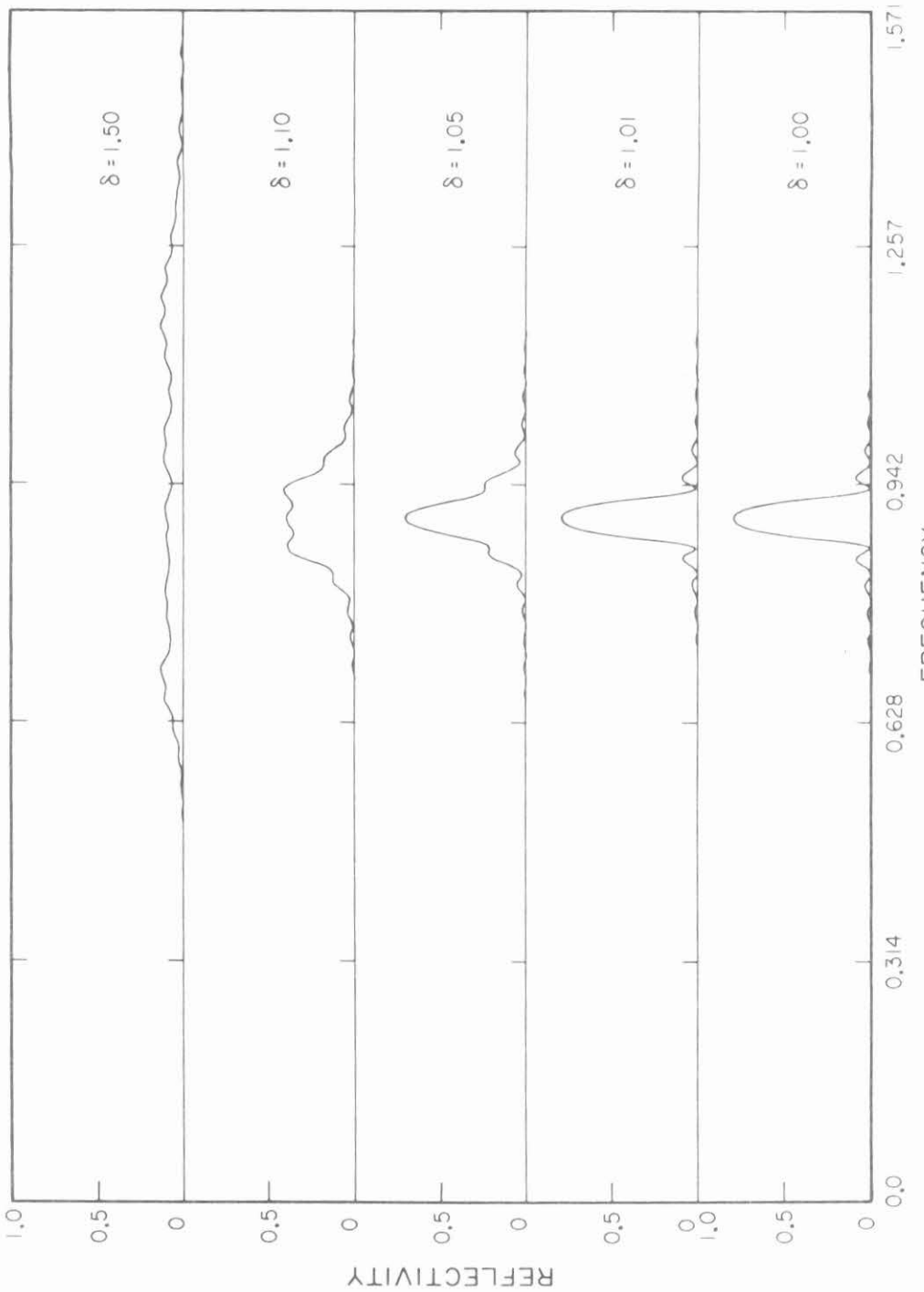

Fig. 4.3 Reflectivity profile for a chirped slab structure

it, as expected. For comparison Figure 4.3 is a plot of a chirped dielectric mirror containing a total of 51 layers of index 3.4 and 3.6. The variable δ gives the chirp of the mirror. The length of the period on the end of the structure nearest the incident light is Λ_o/δ while that on the other end is $\Lambda_o\delta$, with all layers between these varying geometrically from one extreme to the other. The frequency scale is normalized to $\omega\Lambda_o/c$. The qualitative effect of the aperiodicity is quite similar to that of the statistical variation illustrated in Figure 4.2. Figure 4.4 is a plot of $\langle\rho\rangle$ as a function of $k\sigma$ for various values of N at the condition $k\Lambda = \pi$, indicating the increasing sensitivity of $\langle\rho\rangle$ on σ for large N values. The parameters of each structure have been chosen to give a 10% reflectance for a perfect reflector. In the limit of $Nk^2\sigma^2 << 1$, $N >> 1$, and $e^{2ik_{2x}b(o)} = -1$ expression (4.4) reduces to

$$\langle\rho\rangle = (2N+1)r_1\,[1 - Nk^2\sigma^2]$$

$$= r_o[1 - Nk^2\sigma^2] \qquad (4.4a)$$

It is interesting to compare this expression to the well-known Debye-Waller factor for X-ray diffraction from a crystal at a finite temperature for which[13]

$$\langle\rho\rangle = r_o\, e^{\frac{-G^2\sigma^2}{6}} \approx r_o[1 - \frac{G^2}{6}\sigma^2] \qquad (4.5)$$

where $G = k_{in} - k_{out}$

σ = standard deviation in atomic position due to lattice vibration

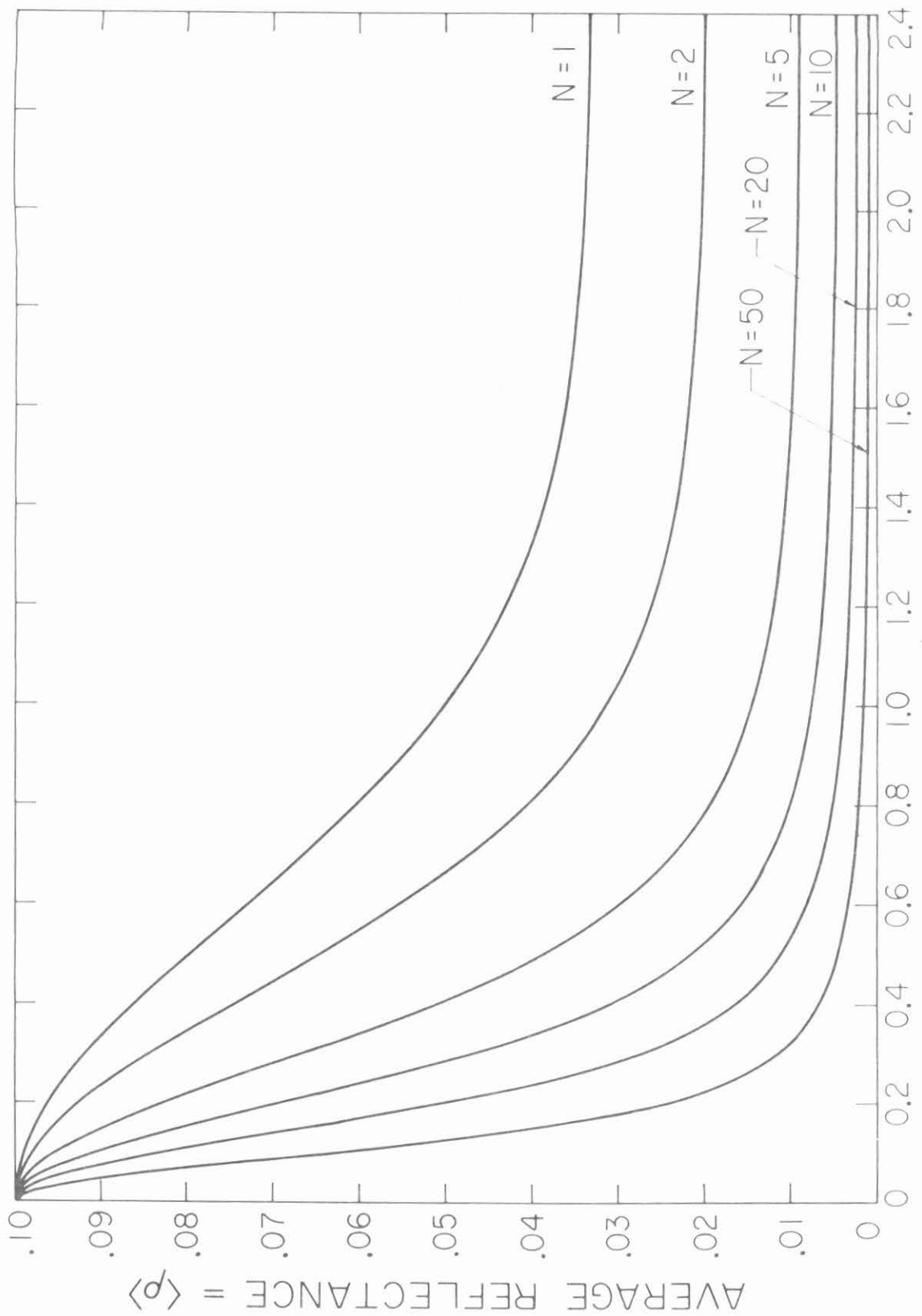

Fig. 4.4 Average amplitude reflectance in low reflectance limit as a function of cell standard deviation and the number of cells. Note that the parameters of each structure have been chosen to give a 10% reflectance for a perfect reflector.

Note that (4.5) does not depend on N, the number of atomic layers, while the correction factor in (4.4a) does depend on N.

The difference between (4.4a) and (4.5) can be reconciled. If we consider a structure for which the thickness of each layer can be controlled precisely, but for which the surface of each layer is not perfect but is rough and uneven, then the reflection from the entire structure is reduced by a term similar to (4.5), that is, independent of N. This can be seen as follows. The reflection from a rough surface is given[14] by $\rho_o \exp[\frac{-8\pi\sigma^2}{\lambda^2} \cos^2\theta]$, where ρ_o is the reflection from a smooth surface, λ is the wavelength of light reflected, σ is the standard deviation of the surface from its average, and θ is the angle of incidence. Again, taking the case where $k_{2x}b^{(o)} = k_{1x}a^{(o)} = \pi/2$ we find that the reflection from each surface of a Bragg reflector is reduced by the factor $\exp[-\frac{\pi}{2}\sigma_{r_i}^2]$, where

σ_{r_i} is the relative standard deviation,

$\sigma_{r_a} = \frac{\sigma_a}{a^{(o)}}$ for layers of index n_1

$\sigma_{r_b} = \frac{\sigma_b}{b^{(o)}}$ for layers of index n_2

Thus for a structure of many layers, we have

$$\langle\rho\rangle = \frac{1}{2} r_o \left[e^{-\frac{\pi}{2}\sigma_{r_a}^2} + e^{-\frac{\pi}{2}\sigma_{r_b}^2}\right] \tag{4.6}$$

$$\approx r_o\left[1 - \frac{\pi}{4}(\sigma_{r_a}^2 + \sigma_{r_b}^2\right]$$

which is independent of N.

The quantity $\langle\rho\rho^*\rangle$ can be calculated in a manner similar to $\langle\rho\rangle$. If we take, for simplicity, the case $k\Lambda = \pi$, we arrive at the rather complicated expression:

$$\langle\rho\rho^*\rangle = |r_1|^2 \left\{ \left[N+1 + \frac{2e^{-2Nk^2\sigma^2}}{(1-e^{2k^2\sigma^2})^2} [1 - (N+1)e^{2k^2\sigma^2 N} + Ne^{2(N+1)k^2\sigma^2}] \right] + \left[N + \frac{2e^{-2(N-1)k^2\sigma^2}}{(1-e^{2k^2\sigma^2})^2} [1 - Ne^{2k^2\sigma^2(N-1)} + (N-1)e^{2Nk^2\sigma^2}] \right] - \left[2\cos(2k_{2x}b_1^{(o)})(e^{-2k_{2x}^2\sigma_b^2} + e^{-2k_{1x}^2\sigma_a^2}) \times \left[\frac{e^{-2(N-1)k^2\sigma^2}}{(1-e^{2k^2\sigma^2})^2} (1 - Ne^{2(N-1)k^2\sigma^2} + (N-1)e^{2Nk^2\sigma^2}) + N \right] \right] \right\} \quad (4.7)$$

In the limit of $Nk^2\sigma^2 \ll 1$, (4.7) reduces to

$$\langle\rho\rho^*\rangle = |r_1|^2 \{[2N^2 + 2N + 1 - 2(N^2+N)\cos(2k_{2x}b^{(o)})] - k^2\sigma^2[(\tfrac{4}{3}N^3 + 2N^2 + \tfrac{2}{3}N) - 2(\tfrac{2}{3}N^3 + N^2 + \tfrac{N}{3})\cos(2k_{2x}b^{(o)})]\} \quad (4.8)$$

Equation (4.7) is plotted in Figure 4.5 for various values of N under the same conditions as Figure 4.4. Although equation (4.7) is quite complicated it reduces to $[(2N+1)r_1]^2$ for $k\sigma \to 0$ and to $(2N+1)(r_1^2)$ as $k\sigma \to \infty$. This is to be expected, since as $\sigma \to 0$, the reflections from each dielectric interface are correlated and thus the amplitudes add. For large $k\sigma$ values, the reflections from each interface are not correlated and the intensities from the 2N+1 interfaces add.

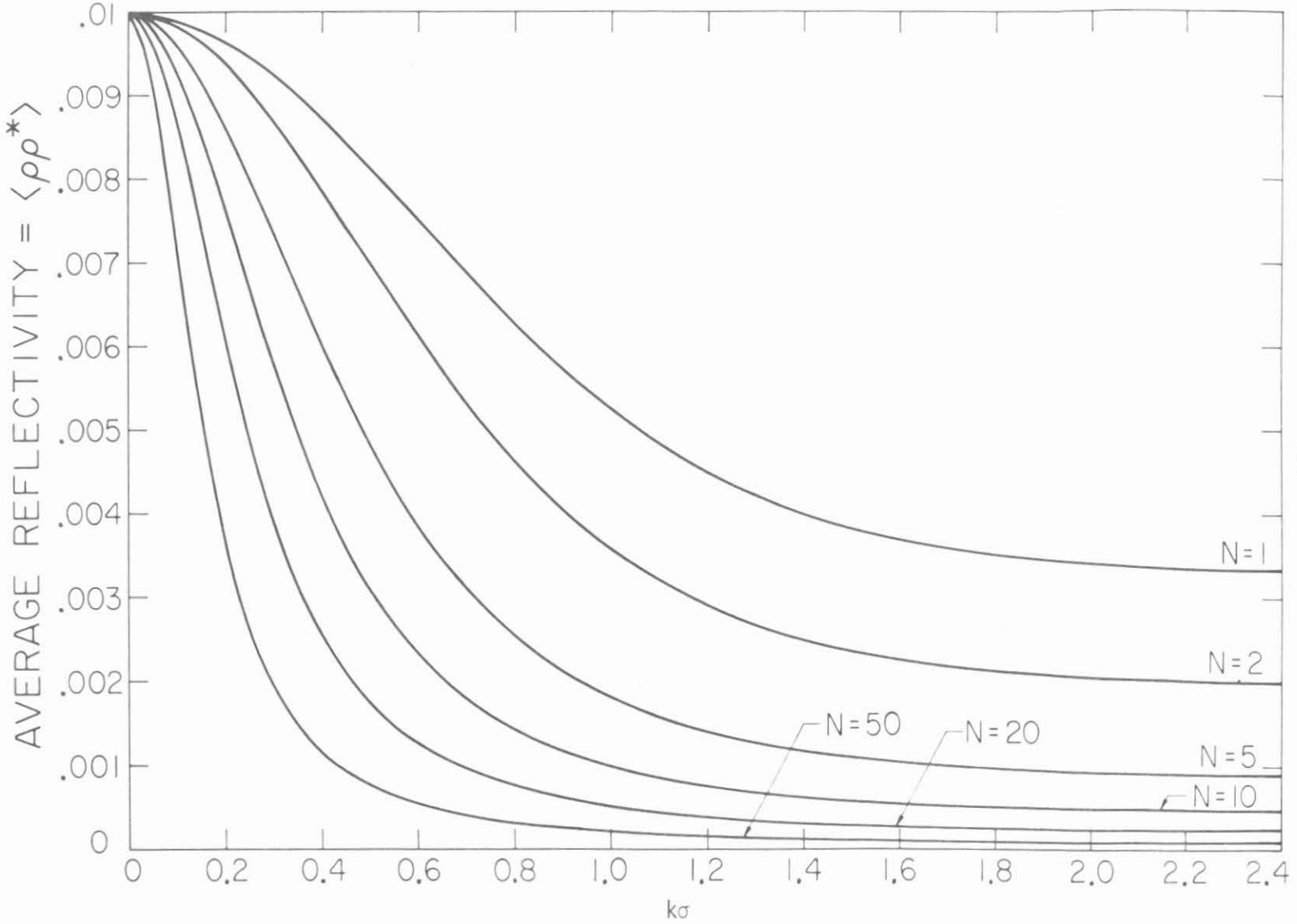

Fig. 4.5 Average intensity reflectivity in low reflectance limit as a function of cell standard deviation and the number of cells. Note how, as kσ becomes large, the asymptotic reflectance becomes .01/(2N+1).

4.3 Coupled Mode Theory

In many cases of practical interest, we deal with high reflectivities and the methods of the previous section are inappropriate. This problem can be overcome by using the coupled mode theory[15,16] and the effects of a random statistical variation in layer thickness can be included by using a perturbation scheme similar to Streifer et al.[17], but carried to a higher order.

Consider a periodic structure which extends from $z = -L/2$ to $z = L/2$. A wave propagating in the z direction, $R(z)e^{i\beta z}$, with time dependence $e^{-i\omega t}$ will generate a contradirectional wave $S(z)\, e^{-i\beta z}$. We take the dielectric constant as varying according to $\cos(\frac{2\pi z}{\Lambda_o} + \varepsilon\phi(z))$ where Λ_o is the ideal period and $\varepsilon\phi(z)$ describes the perturbation or deviation from this ideal period. Although the dielectric constant of a periodic slab guide does not vary sinusoidally, we can decompose the index variation into its Fourier components and allow coherent interaction with the propagating wave and the first Fourier harmonic of the structure.

The coupled mode equations at the Bragg condition $\beta = \pi/\Lambda_o$ are

$$R' = i\kappa\, e^{i\varepsilon\phi}\, S \tag{4.9}$$

$$S' = -i\kappa\, e^{-i\varepsilon\phi}\, R \tag{4.10}$$

where the prime denotes derivative with respect to z. In order to keep the results fairly simple we will solve the problem at the Bragg condition only. In equations (4.9) and (4.10) κ is the coupling constant. It is seen from equation (4.10) that

$$\kappa = \left|\frac{dS/dz}{R}\right| = \left|\frac{\text{amplitude reflected/unit length}}{\text{amplitude incident}}\right|$$

$$= \frac{r_1}{\Lambda_o/2} = \frac{2N\, r_1}{L}$$

The boundary conditions are

$$R(-\tfrac{1}{2}L) = 1 \tag{4.11}$$

$$S(\tfrac{1}{2}L) = 0 \tag{4.12}$$

The filter function or reflection coefficient is defined as

$$\rho(-\tfrac{1}{2}) = S(-\tfrac{L}{2}) / R(-\tfrac{L}{2}) = S(-\tfrac{L}{2})$$

Equations (4.9) and (4.10) can be combined to give

$$R'' - i\varepsilon\phi'R' - \kappa^2 R = 0 \tag{4.13}$$

Next we expand R in a power series in ε

$$R = R_0(z) + \varepsilon R_1(z) + \varepsilon^2 R_2(z) + \cdots \tag{4.14}$$

When this is substituted in equation (4.13) and powers of ε are equated, we get

$$R_0'' - \kappa^2 R_0 = 0 \tag{4.15a}$$

$$R_1'' - \kappa^2 R_1 = i\,\phi'\,R_0' \tag{4.15b}$$

$$R_2'' - \kappa^2 R_2 = i\,\phi'\,R_1' \tag{4.15c}$$

$$R_n'' - \kappa^2 R_n = i\,\phi'\,R_{n-1}' \qquad n \geq 1 \tag{4.15d}$$

These equations, subject to the boundary conditions of equations (4.11) and (4.12) are solved in Appendix 4-A where it is shown

$$R_o = \frac{\cosh(\kappa(\frac{L}{2} - z))}{\cosh \kappa L} \tag{4.16}$$

$$R_n = \frac{1}{\kappa} \int_{-\frac{L}{2}}^{z} i\, \phi'(\xi)\, R'_{n-1}(\xi)\, \sinh[\kappa(z - \xi)]d\xi \tag{4.17}$$

$$- \frac{i}{\kappa C_1} \frac{\sinh[\kappa(\frac{L}{2} + z)]}{\cosh \kappa L} \int_{-L/2}^{L/2} \phi'(\xi)\, R'_{n-1}(\xi)\, \cosh[\kappa(\frac{L}{2} - \xi)]d\xi$$

$n = 1,2,\ldots$

The reflection coefficient $\rho(-\frac{L}{2})$, is given by

$$\rho(-\frac{L}{2}) = \frac{-i}{\kappa} e^{-i\varepsilon\phi(-\frac{L}{2})} R'(-\frac{L}{2}) \tag{4.18}$$

If we consider an ensemble of these structures, each will have a different reflection since $\varepsilon\phi'(z)$ is a random variable for each structure. In order to proceed we must consider the auto-correlation function of $\phi'(z)$ which we will take as

$$R_\phi(z_o) \equiv \langle \phi'(z)\, \phi'(z + z_o) \rangle \equiv \lim_{W\to\infty} \frac{1}{2W} \int_{z=-W}^{W} \phi'(z)\, \phi'(z + z_o)dz \tag{4.19a}$$

$$= \Sigma^2 (1 - \frac{|z_o|}{\ell}) \quad \text{for } |z_o| \leq \ell$$

$$= 0 \quad \text{for } |z_o| \geq \ell \tag{4.19b}$$

Expression (4.19b) is an assumed form for the autocorrelation function. Although other forms can be considered, the final result will not depend on the exact form because of subsequent approximations (Appendix 4-B). Also (4.19b) can be shown to be the unique autocorrelation function for the case of a slab reflector (Appendix 4-D).

The quantity ℓ is a correlation length and $\Sigma^2 = \langle\phi'^2\rangle$ is the standard deviation of the random variable. Also we assume $\langle\phi'\rangle = 0$. This will be discussed further in the next section.

Using the results of Appendices 4-B and 4-C, we arrive at the following results for $\langle\rho(-\frac{L}{2})\rangle$ and $\langle\rho(-\frac{L}{2})\ \rho^*(-\frac{L}{2})\rangle$

$$\langle\rho(-\tfrac{L}{2})\rangle = ie^{-i\varepsilon\phi(-\frac{L}{2})}\left\{\tanh\kappa L - \frac{\varepsilon^2\Sigma^2\ell}{8\kappa C_1^3}[2C_1^5 - \tfrac{1}{4}S_1S_4 - C_1C_2 - C_1 + \kappa LS_1]\right\} \tag{4.20}$$

$$\langle\rho(-\tfrac{L}{2})\ \rho^*(-\tfrac{L}{2})\rangle = \tanh^2\kappa L - \frac{\varepsilon^2\Sigma^2\ell}{2\kappa C_1^4}\left\{\frac{\kappa L}{4} - \frac{1}{16}S_4 - \frac{S_1}{2}(C_1C_2 + C_1 - 2C_1^5 - \kappa LS_1 + \tfrac{1}{4}S_1S_4)\right\} \tag{4.21}$$

Where $S_n \equiv \sinh(n\kappa L)$, $C_n \equiv \cosh(n\kappa L)$. In the low reflection limit (4.20) and (4.21) reduce to

$$\langle\rho(-\tfrac{L}{2})\rangle = ie^{-i\varepsilon\phi(-\frac{L}{2})}\kappa L(1 - \frac{\varepsilon^2\Sigma^2 L\ell}{4}) \tag{4.22}$$

$$\langle\rho(-\tfrac{L}{2})\ \rho^*(-\tfrac{L}{2})\rangle = \kappa^2L^2\ (1 - \frac{\varepsilon^2\Sigma^2 L\ell}{6}) \tag{4.23}$$

In the high reflection limit

$$\langle \rho(-\tfrac{L}{2}) \rangle = i e^{-i\varepsilon\phi(-\frac{L}{2})} \left\{ \tanh \kappa L - \frac{\varepsilon^2 \Sigma^2 \ell}{8\kappa} \right\} \tag{4.24}$$

$$\langle \rho(-\tfrac{L}{2})\ \rho^*(-\tfrac{L}{2}) \rangle = \tanh^2 \kappa L - \frac{\varepsilon^2 \Sigma^2 \ell}{2\kappa} e^{-2\kappa L} (2\kappa L - 1) \tag{4.25}$$

$$\approx 1 - e^{-2\kappa L}\left[4 + \frac{\varepsilon^2 \Sigma^2 \ell}{\kappa} (\kappa L - \tfrac{1}{2})\right]$$

4.4 Connection between $\varepsilon^2\Sigma^2$, and, $a^{(0)}$, $b^{(0)}$, and σ^2 of the slab reflector considered in the low reflectivity limit section.

In order to apply the results of the last section which assumed a sinusoidal variation of the index to the case of multilayered mirrors with abrupt index discontinuities, we establish the connection between the parameters used in characterizing these systems.

We start by defining the local period through the relationship

$$\int^z \frac{2\pi}{\Lambda(z)}\, dz \equiv \int^z \left\{ \frac{2\pi}{\Lambda_o} - \frac{2\pi}{\Lambda_o^2} \delta\Lambda(z) \right\} dz = \frac{2\pi z}{\Lambda_o} + \varepsilon\phi(z) \tag{4.26}$$

$$\varepsilon\phi'(z) = \frac{-2\pi}{\Lambda_o^2} \delta\Lambda(z) \tag{4.27}$$

where $\delta\Lambda(z)$ is the local period variation.

Next we take the auto-correlation function of $\delta\Lambda(z)$ to be

$$R_{\delta\Lambda}(z_o) = \langle \delta\Lambda(z + z_o)\ \delta\Lambda(z) \rangle = S^2 \left(1 - \frac{|z_o|}{\ell'}\right) \qquad |z_o| \le \ell' \tag{4.28}$$

$$= \qquad 0 \qquad \text{otherwise}$$

From equation 27) we obtain

$$\varepsilon^2 \langle \phi'(z)\ \phi'(z + z_o) \rangle = \frac{4\pi^2}{\Lambda_o^4} \langle \delta\Lambda(z)\ \delta\Lambda(z + z_o) \rangle$$

$$\varepsilon^2\ \Sigma^2\ (1 - \frac{|z_o|}{\ell}) = \frac{4\pi^2}{\Lambda_o^4} S^2\ (1 - \frac{|z_o|}{\ell'}) \qquad (4.29)$$

From equation (4.29) we see immediately that

$$\varepsilon^2\ \Sigma^2 = \frac{4\pi^2}{\Lambda_o^4} S^2 \qquad (4.30)$$

$$\ell' = \ell \qquad (4.31)$$

Next we relate ℓ to $\Lambda_o \equiv a^{(0)} + b^{(0)}$ and S^2 to σ^2.

As shown in Appendix 4-D the autocorrelation function for a slab reflector is given by

$$\langle \Delta t(z)\ \Delta t(z + z_o) \rangle = \bar{\sigma}^2\ (1 - \frac{2|z_o|}{\Lambda_o}) \qquad (4.32)$$

$$\bar{\sigma}^2 = \frac{1}{2}(\sigma_a^2 + \sigma_b^2), \quad \frac{\Lambda_o}{2} \approx a^{(0)} \approx b^{(0)}$$

The quantity $\Delta t(z)$ is the deviation in the slab located at z from its ideal thickness of $\frac{\Lambda_o}{2}$. Comparing equations (4.32) and (4.29) we see that the correlation length ℓ is equal to the slab thickness $\Lambda_o/2$. In order to find the connection between $\bar{\sigma}^2$ and Σ^2 (and thus S^2 through equation (4.30), we compare either equation (4.22) to equation (4.5), or alternatively, (4.23) to (4.8) (in limit of large N). In either case for the equations to agree, we must take

$$S^2 = (2\bar{\sigma})^2 \tag{4.33}$$

$$\varepsilon^2 \Sigma^2 = \frac{4\pi^2}{\Lambda_o^4} (2\bar{\sigma})^2 \tag{4.34}$$

Thus we have related the quantities $\bar{\sigma}^2$ and $\Lambda_o/2$ which are assumed known for our slab Bragg reflector to the quantities $\varepsilon^2\Sigma^2$ and ℓ which appear in equations (4.20) through (4.25).

Also by comparing equation (4.5) to (4.22) or equation (4.8) to (4.23) for large N, we again find $\kappa = (2Nr_1)/L$.

After using equation (4.34) and $\ell = \Lambda_o/2$, equations (4.20) and (4.21) become

$$\langle\rho(-\tfrac{L}{2})\rangle = ie^{-i\varepsilon\phi(-\frac{L}{2})}\left\{\tanh \kappa L - \frac{\bar{\sigma}^2 \pi^2}{\Lambda_o^3 \kappa C_1^3}\left[2C_1^5 - \frac{1}{4}S_1S_4 - C_1C_2 - C_1 + \kappa L S_1\right]\right\} \tag{4.35}$$

$$\langle\rho(-\tfrac{L}{2})\ \rho^*(-\tfrac{L}{2})\rangle = \tanh^2\kappa L - \frac{4\bar{\sigma}^2\pi^2}{\Lambda_o^3 \kappa C_1^4}\left\{\frac{\kappa L}{4} - \frac{1}{16}S_4 - \frac{S_1}{2}\left(C_1C_2 + C_1 - 2C_1^5 - \kappa L S_1 + \frac{1}{4}S_1S_4\right)\right\}$$

$$= \tanh^2 x - \frac{2\pi^2\bar{\sigma}^2 L}{\Lambda_o^3} G(x) \tag{4.36a}$$

or

$$\frac{\langle\rho(-\frac{L}{2})\ \rho^*(-\frac{L}{2})\rangle - \tanh^2 x}{\tanh^2 x} = \frac{-2\pi^2\bar{\sigma}^2 L}{\Lambda_o^3}\left(\frac{G(x)}{\tanh^2 x}\right) \qquad x \equiv \kappa L \tag{4.36b}$$

$$G(x) \equiv -\frac{1}{x}\left\{\frac{1}{2\,C_1^4}\left(\frac{1}{4}S_4 - x\right) + \frac{S_1}{C_1^4}\left(C_1C_2 + C_1 - 2\,C_1^5 - xS_1 + \frac{1}{4}S_1S_4\right)\right\}$$

The function G(x) is plotted in Figure 4.6. For small x, $G(x) \approx \frac{2}{3}x^2$ while for large x, $G(x) \approx 2e^{-2x}(2 - \frac{1}{x})$.

Alternative Derivation Using Coupled Mode Theory

If equations (4.9) and (4.10) are used directly and a series expansion is used in both R and S, we can avoid having to use equation (4.13) which involves ϕ' and instead work only with the random variable ϕ. The procedure is outlined below

$$R' = i\kappa e^{i\varepsilon\phi}S \tag{4.37}$$

$$S' = -i\kappa e^{-i\varepsilon\phi}R \tag{4.38}$$

$$R' = i\kappa S + i\kappa(e^{i\varepsilon\phi}-1)S \tag{4.39}$$

$$S' = -i\kappa R - i\kappa(e^{-i\varepsilon\phi}-1)R \tag{4.40}$$

where

$$\varepsilon\phi(z) = \frac{\omega}{c}n_1 \sum_{i=1}^{\frac{z}{\Lambda}} u_i + \frac{\omega}{c}n_2 \sum_{i=1}^{z/\Lambda} v_i \tag{4.41}$$

The boundaries of the reflector are between z = 0 and z = L, and u_i and v_i are given in equation (4.2).

We define the random variable $\chi = i\kappa(e^{i\varepsilon\phi}-1)$, assume it is small and expand R and S in a series, with the $n^{\underline{th}}$ term being of order χ^n

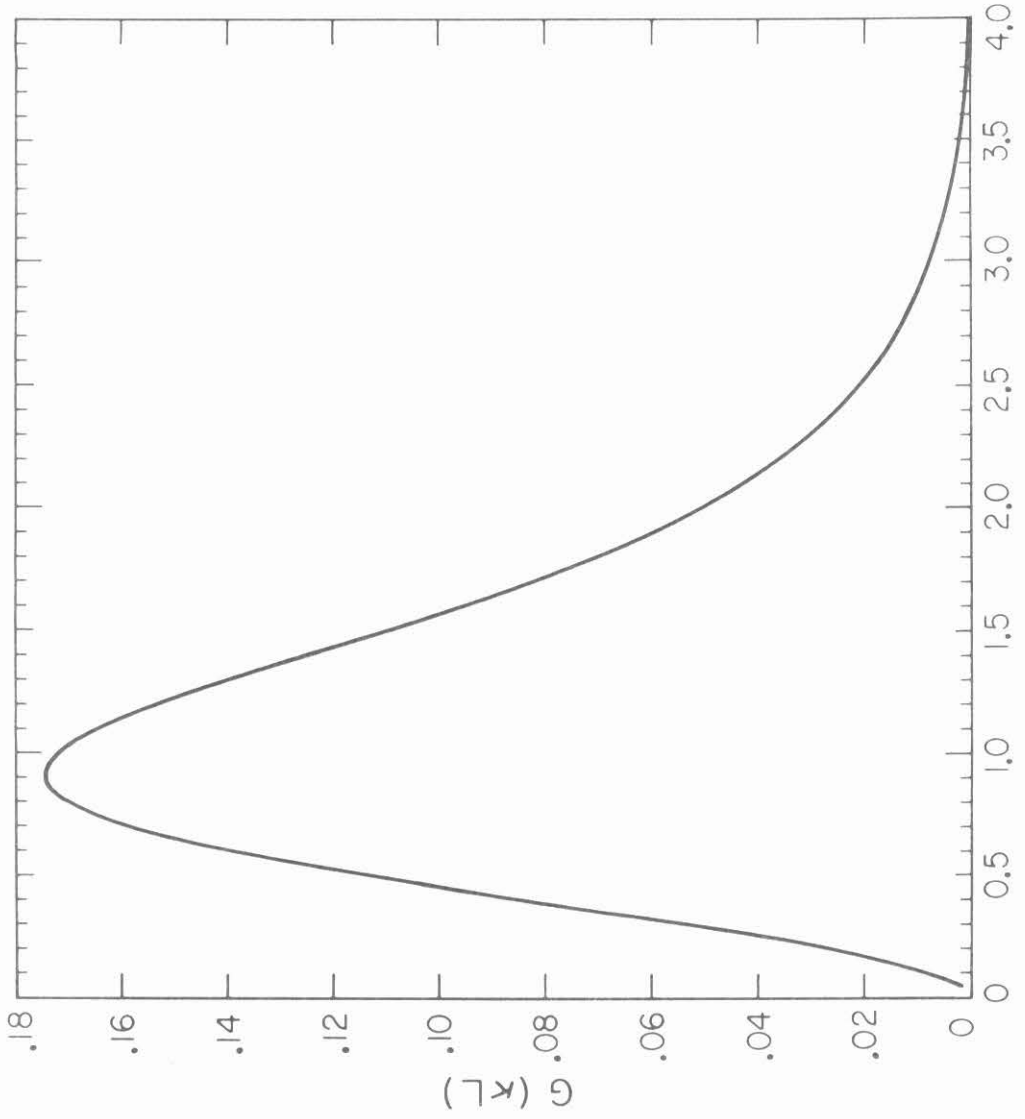

Figure 4.6 Plot of the function G(κL)

$$R = R_o + R_1 + R_2 + \cdots \tag{4.42}$$

$$S = S_o + S_1 + S_2 + \cdots \tag{4.43}$$

with boundary conditions $R_n(0) = \delta_{no}$, $S_n(L) = 0$. After substituting (4.42) and (4.43) into (4.39) and (4.40) and collecting terms of order χ we find

$$R_o' = i\kappa S_o \tag{4.44}$$

$$S_o' = -i\kappa R_o \tag{4.45}$$

$$R_n' = i\kappa S_n + \chi S_{n-1} \qquad n \geq 1 \tag{4.46}$$

$$S_n' = -i\kappa R_n + \chi^* R_{n-1} \qquad n \geq 1 \tag{4.47}$$

This system of equations can be solved iteratively for increasing n. We will only consider first order and take the region of space containing the reflectors between z=0 and z=L.

$$\rho \approx \frac{S_o(0) + S_1(0)}{R_o(0)} = S_o(0) + S_1(0) \tag{4.48}$$

Solving equations (4.44) and (4.45) we find

$$R_0(z) = \frac{\cosh \kappa (L-z)}{C_1} \tag{4.49}$$

$$S_0(z) = \frac{+ i \sinh \kappa (L-z)}{C_1} \tag{4.50}$$

Next we combine equations (4.46) and (4.47) to find an equation for S_1

$$S_1'' - \kappa^2 S_1 = -i\kappa\chi S_o + \chi^{*\prime} R_o + \chi^* R_o' \tag{4.51}$$

Using the boundary conditions on S_1, integrating by parts to get rid of the derivative of χ^* and using equations (4.49) and (4.50) we find

$$S_1(0) = \frac{i\kappa}{C_1^2} \int_0^L \Big[(e^{-i\varepsilon\phi} - 1) \cosh^2\kappa(L-z) - (e^{i\varepsilon\phi} - 1) \sinh^2\kappa(L-z) \Big] dz \tag{4.52}$$

$$\rho\rho^* = |S_o(0) + S_1(0)|^2 \approx |S_o|^2 + S_1 S_o^* + S_1^* S_o \tag{4.53}$$

$$\Delta r^2 \equiv \rho\rho^* - |S_o|^2 = S_o(S_1^* - S_1) \tag{4.54}$$

After using equations (4.50) and (4.52) we arrive at the result

$$\Delta r^2 = \frac{-\kappa \tanh \kappa L}{\cosh^2 \kappa L} \int_0^L (2 - e^{i\varepsilon\phi(z)} - e^{-i\varepsilon\phi(z)}) dz \tag{4.55}$$

Next we average the above equation, recalling (see eq. (4.41)) that

$$\langle \varepsilon^2 \phi^2(z) \rangle = \frac{\omega^2}{c^2} \frac{z}{\Lambda} [n_1^2 \sigma_a^2 + n_2^2 \sigma_b^2]$$

$$= \frac{2z\Psi}{\Lambda} \tag{4.56}$$

$$\Psi \equiv \frac{\omega^2}{2c^2} [n_1^2 \sigma_a^2 + n_2^2 \sigma_b^2] \tag{4.57}$$

$$\langle \Delta r^2 \rangle = \frac{-2\kappa S_1}{C_1^3} \int_0^L (1 - e^{-\Psi \frac{z}{\Lambda}}) dz = - \frac{2\kappa S_1 \Lambda}{C_1^3} \left[\frac{N\Psi + e^{-N\Psi} - 1}{\Psi} \right] \tag{4.58}$$

Finally the fractional decrease in average reflectivity is

$$\frac{\langle \Delta r^2 \rangle}{r_o^2} = \frac{-2\kappa\,\Lambda}{\tanh \kappa L \cosh^2 \kappa L}\left[\frac{N\Psi + e^{-N\Psi} - 1}{\Psi}\right] \qquad (4.59)$$

Although this formula is simpler than equation (4,36b), it is not as accurate as we shall see in the next section. Greater accuracy could be obtained by including higher order terms in S.

4.5 Computer Results

The analytical results of the last section are compared with calculated reflectivity values of a large number of computer simulated stratified media. The multilayer samples were "fabricated" such that the thickness of each layer was a random variable assuming Gaussian distribution about predetermined thicknesses a_o and b_o of the n_1 and n_2 layers respectively. The same relative standard deviation was used for all layers, i.e. $\sigma_a/a^{(o)} = \sigma_b/b^{(o)}$. The reflectivity was calculated using the matrix multiplication method. (For a detailed discussion of the method, the reader is referred to ref. [2]).

Samples of 50 cells each were prepared this way. The reflectivity was calculated for each sample every 5 cells, giving reflectivity values of stratified media of 5, 10, 15, 25, 30, 35, 40, 45 and 50 cells. There were 1500 such samples. The parameters used in the calculations were: $n_1 = 3.6$, $n_2 = 3.4$, $a^{(o)} = \frac{n_2\Lambda_o}{n_1+n_2} = 0.4857\Lambda_o$, $b^{(o)} = \frac{n_1\Lambda_o}{n_1+n_2} = 0.5143\Lambda_o$ ($\Lambda_o \equiv a^{(o)}+b^{(o)}$, $\omega = \frac{\pi c}{2n_1 a^{(o)}}$, and normal incidence.

Each sample structure has a different reflection, but all are less than $R_p \equiv \langle \rho\rho^* \rangle_p$, the reflection from a perfect structure where

$\sigma = 0$. The average reflection $\langle R \rangle \equiv \langle \rho\rho^* \rangle$ is then determined as well as $\sigma_{\langle R \rangle} = \sqrt{\langle R^2 \rangle - \langle R \rangle^2}$, the standard deviation of the reflection. The standard deviation of the computed quantity $\langle R \rangle$ is then determined by $\frac{\sigma_{\langle R \rangle}}{\sqrt{N}}$ where N is the number of structures tested. The value N = 1500 was taken to insure sufficient accuracy in $\langle R \rangle$.

The results of the computer experiment are presented in Table 1. For comparison, results are also given for the two theories. The results are plotted in Figure 4.7. Values of $\sigma_r \equiv \frac{\sigma_a}{a^{(o)}} = \frac{\sigma_b}{b^{(o)}} = .02$ were used.

In Figure 4.8 are the results for a structure with 10 unit cells and various values of σ_r. It can be seen that there is excellent agreement between the computer results and the second order theory using ϕ' for small values of σ_r. The first order theory using ϕ also gives good results.

Finally Figures 4.9 through 4.14 illustrate the probability distribution function for various reflections. The points were determined by the computer routine, while the solid line represents the theoretical prediction which is described in the next section. P(R)dR gives the probability of a structure having reflection between R and R + dR. The vertical axis on the left hand side gives P(R)dR with dR specified. Figures 4.9, 4.10 and 4.11 give the probability distribution for 10, 25, and 50 cells with relative standard deviation of 2%. Notice how the distribution is broader for 25 cells than for 10 or 50 cells.

In Figures 4.12, 4.13, and 4.14 we take a structure of 25 cells and plot the probability distributions for relative standard deviations of 5%, 7.5% and 10%. The same scale is used in these three figures and the broadening of P(R) with standard deviation is readily seen.

The computer routine used in this analysis is presented in Appendix 4-E.

Number of cells	R_P	$\langle R \rangle_{Exper}$	$\frac{R_P - \langle R \rangle_{Exper}}{R_P}$	$\frac{R_P - \langle R \rangle_{Theory\ \phi'}}{R_P}$	$\frac{R_P - \langle R \rangle_{Theory\ \phi}}{R_P}$
5	.07743	.07695	$6.20 \pm .20 \times 10^{-3}$	6.11×10^{-3}	4.67×10^{-3}
10	.26680	.26420	$9.75 \pm .19 \times 10^{-3}$	9.75×10^{-3}	8.00×10^{-3}
15	.48289	.47785	$10.4 \pm .20 \times 10^{-3}$	10.6×10^{-3}	9.41×10^{-3}
20	.66500	.65870	$9.47 \pm .20 \times 10^{-3}$	9.47×10^{-3}	9.22×10^{-3}
25	.79469	.78865	$7.60 \pm .15 \times 10^{-3}$	7.45×10^{-3}	8.07×10^{-3}
30	.87840	.87343	$5.66 \pm .11 \times 10^{-3}$	5.49×10^{-3}	6.53×10^{-3}
35	.92942	.92573	$3.97 \pm .06 \times 10^{-3}$	3.79×10^{-3}	5.01×10^{-3}
40	.95952	.95695	$2.68 \pm .04 \times 10^{-3}$	2.50×10^{-3}	3.69×10^{-3}
45	.97694	.97523	$1.75 \pm .04 \times 10^{-3}$	1.68×10^{-3}	2.63×10^{-3}
50	.98691	.98580	$1.12 \pm .01 \times 10^{-3}$	1.04×10^{-3}	1.83×10^{-3}

$R_P = \rho\rho^*$ for perfect structure

$\langle R \rangle = \langle \rho\rho^* \rangle$

$\sigma_r = .02$

$n_1 = 3.6$

$n_2 = 3.4$

Table 4.1 Comparing results of the computer experiment with the two analytic expressions. Note the close agreement between the second order ϕ' expression and the experiment.

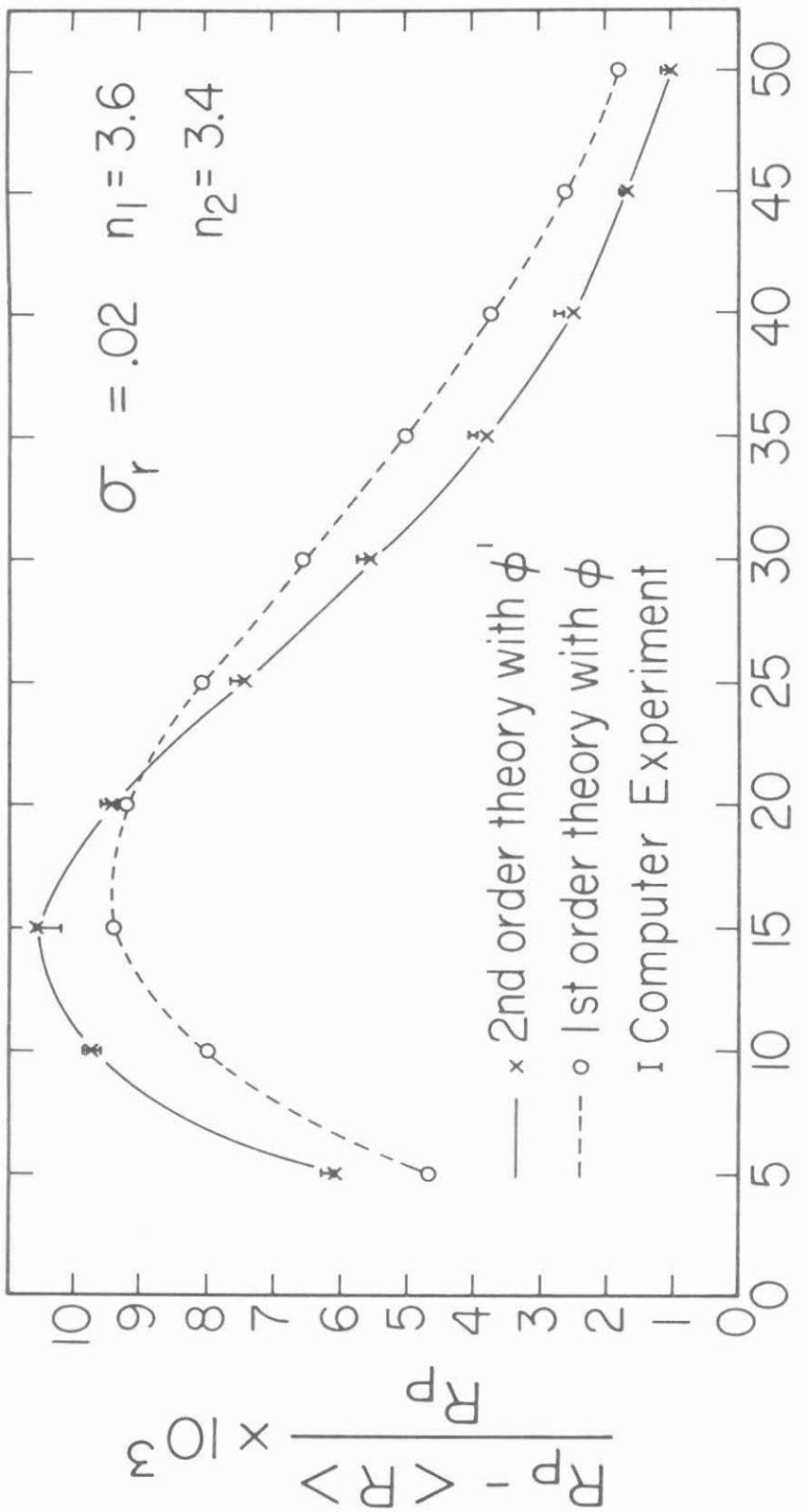

Figure 4.7 Plot of the data given in Table 4.1 (σ_r = 2%)

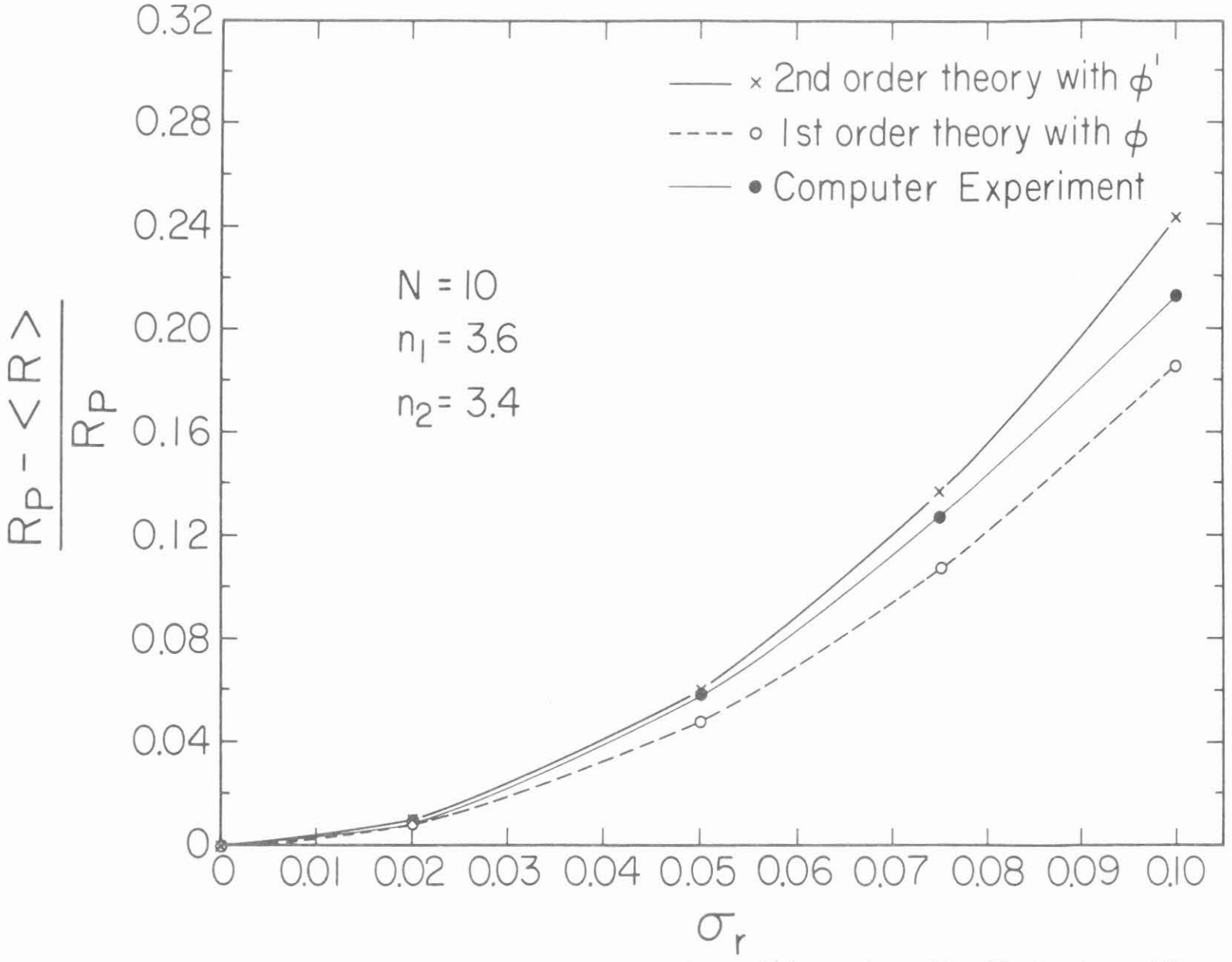

Figure 4.8 Comparison of computer experimental results and theory for a 10-cell structure with various values of σ_r.

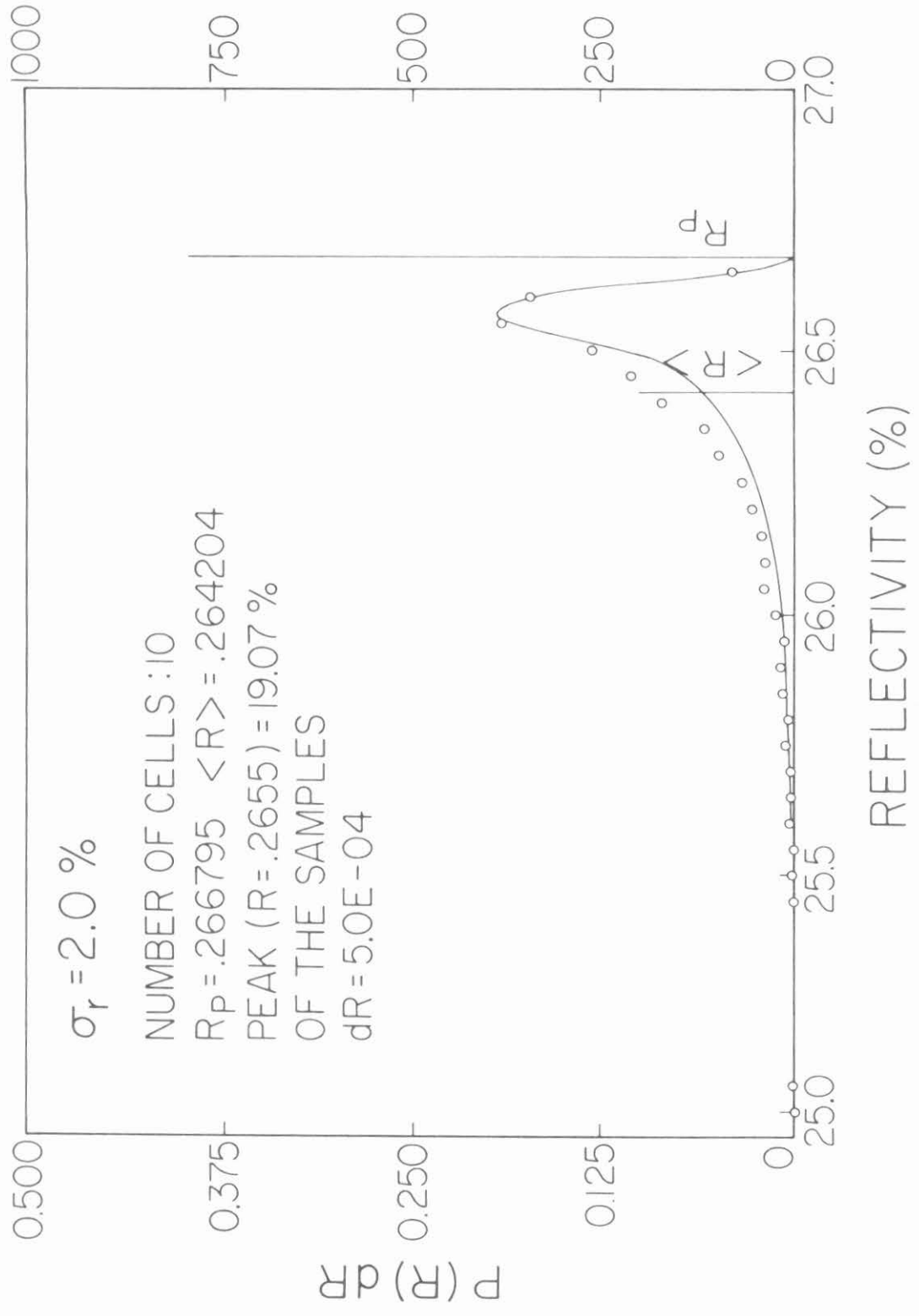
σr = 2.0 %
NUMBER OF CELLS : 10
Rp = .266795 <R> = .264204
PEAK (R = .2655) = 19.07 %
OF THE SAMPLES
dR = 5.0E-04
P (R) dR
P (R)
REFLECTIVITY (%)
0.500
0.375
0.250
0.125
0
1000
750
500
250
0
25.0
25.5
26.0
26.5
27.0
Rp
< R >

Fig. 4.9

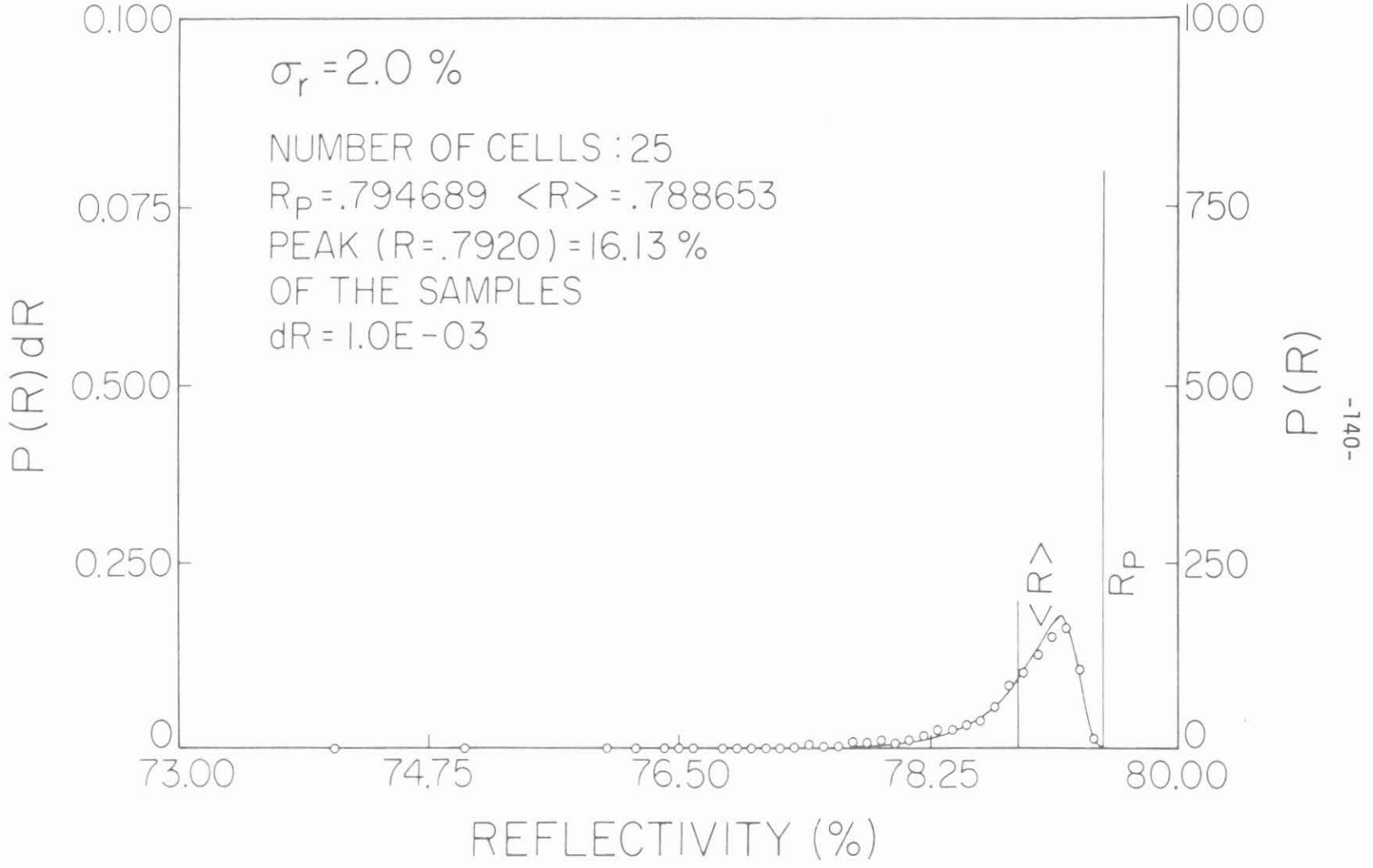
σ_r = 2.0 %
NUMBER OF CELLS : 25
R_P = .794689 <R> = .788653
PEAK (R = .7920) = 16.13 %
OF THE SAMPLES
dR = 1.0E-03
P(R) dR
P(R)
0.100
0.075
0.500
0.250
0
1000
750
500
250
0
<R>
R_P
73.00
74.75
76.50
78.25
80.00
REFLECTIVITY (%)

Fig. 4.10

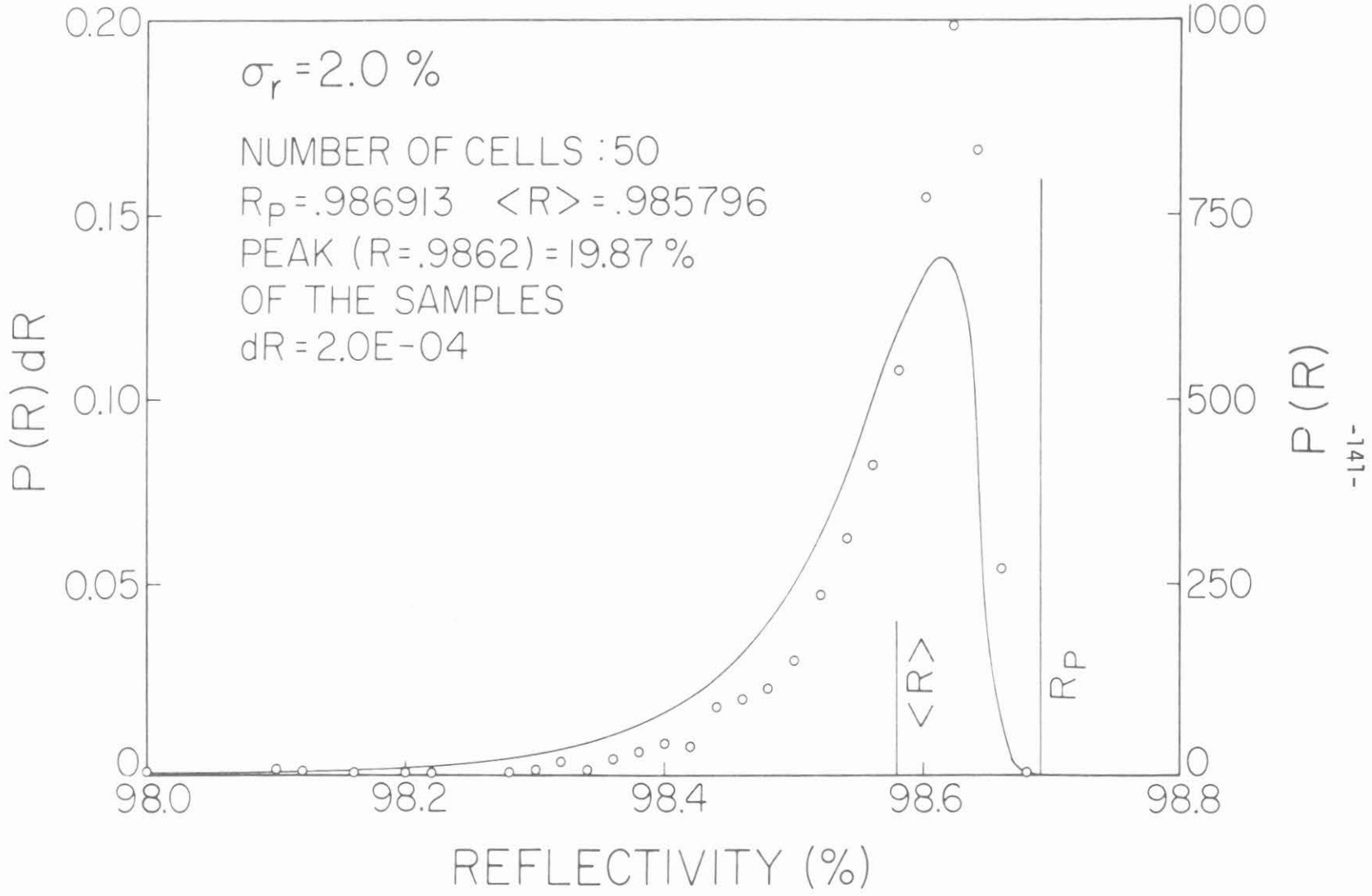
σ_r = 2.0 %
NUMBER OF CELLS : 50
R_P = .986913 <R> = .985796
PEAK (R = .9862) = 19.87 %
OF THE SAMPLES
dR = 2.0E-04
P(R) dR
P(R)
0.20
0.15
0.10
0.05
0
1000
750
500
250
0
98.0
98.2
98.4
98.6
98.8
<R>
R_P
REFLECTIVITY (%)

Fig. 4.11

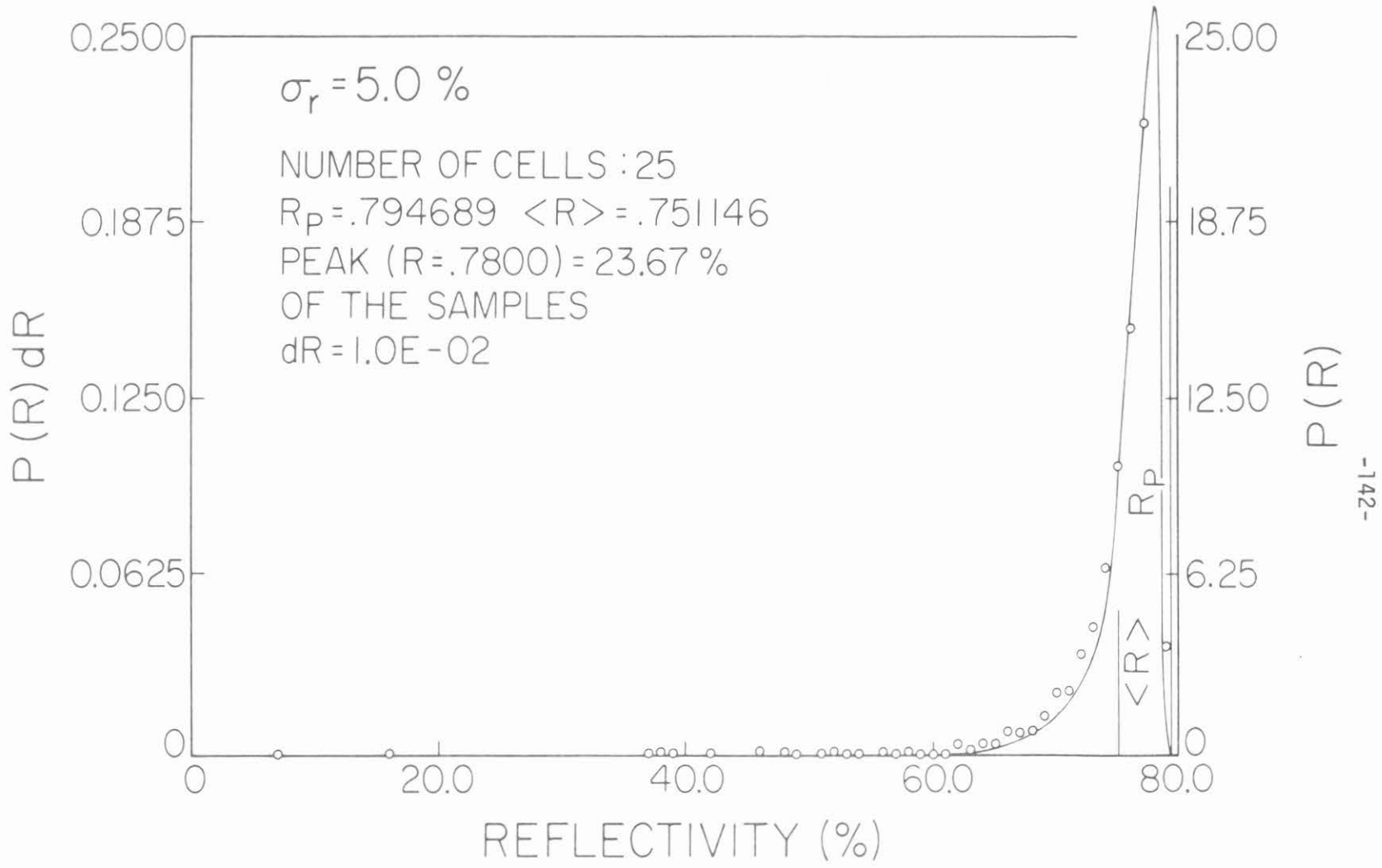
σ_r = 5.0 %
NUMBER OF CELLS : 25
R_P = .794689 <R> = .751146
PEAK (R = .7800) = 23.67 %
OF THE SAMPLES
dR = 1.0E-02
P (R) dR
P (R)
0.2500
0.1875
0.1250
0.0625
0
25.00
18.75
12.50
6.25
0
R_P
<R>
0
20.0
40.0
60.0
80.0
REFLECTIVITY (%)

Fig. 4.12

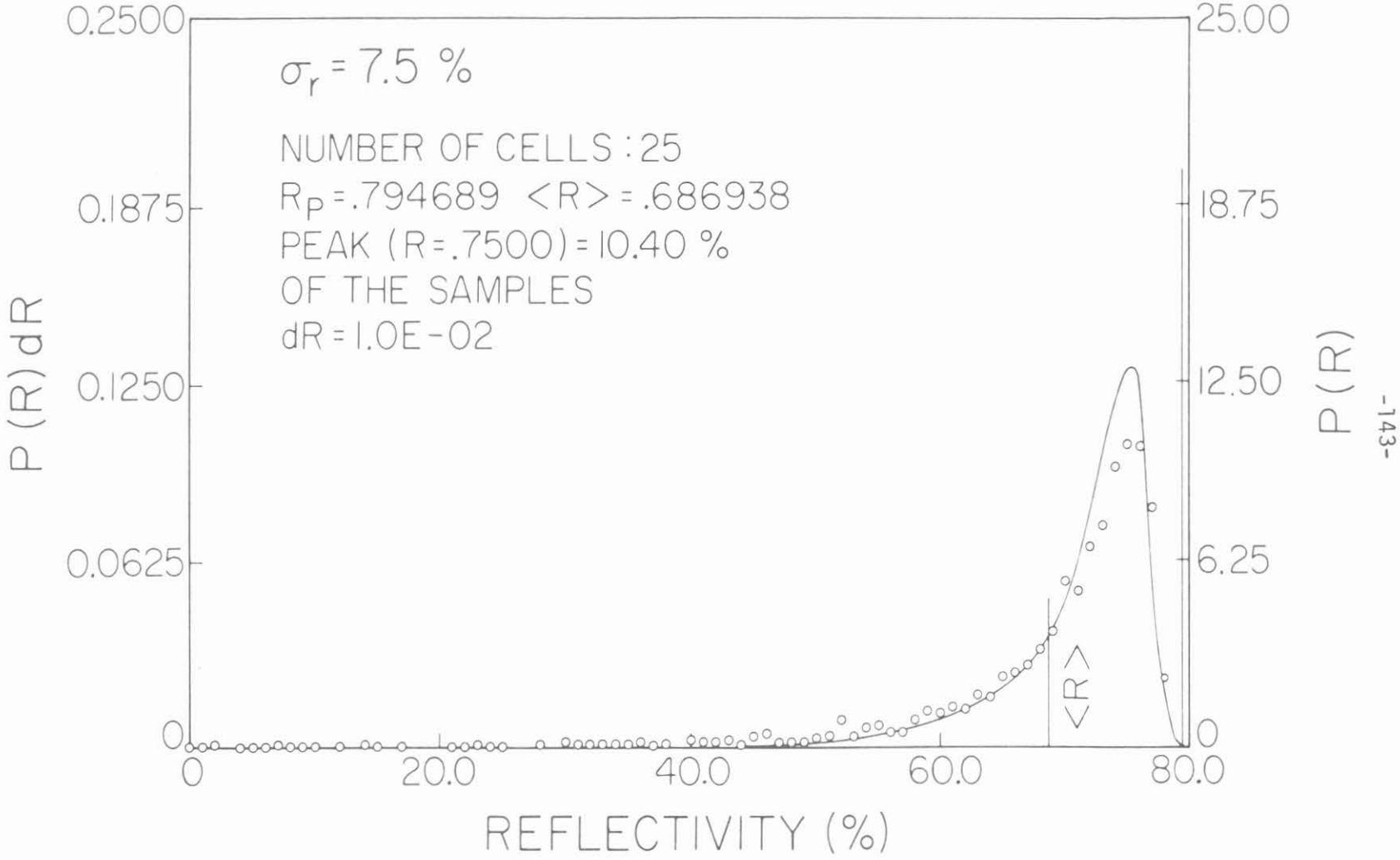
σ_r = 7.5 %
NUMBER OF CELLS : 25
R_P = .794689 <R> = .686938
PEAK (R = .7500) = 10.40 %
OF THE SAMPLES
dR = 1.0E-02
0.2500
0.1875
0.1250
0.0625
0
P(R) dR
25.00
18.75
12.50
6.25
0
P(R)
<R>
0
20.0
40.0
60.0
80.0
REFLECTIVITY (%)

Fig. 4.13

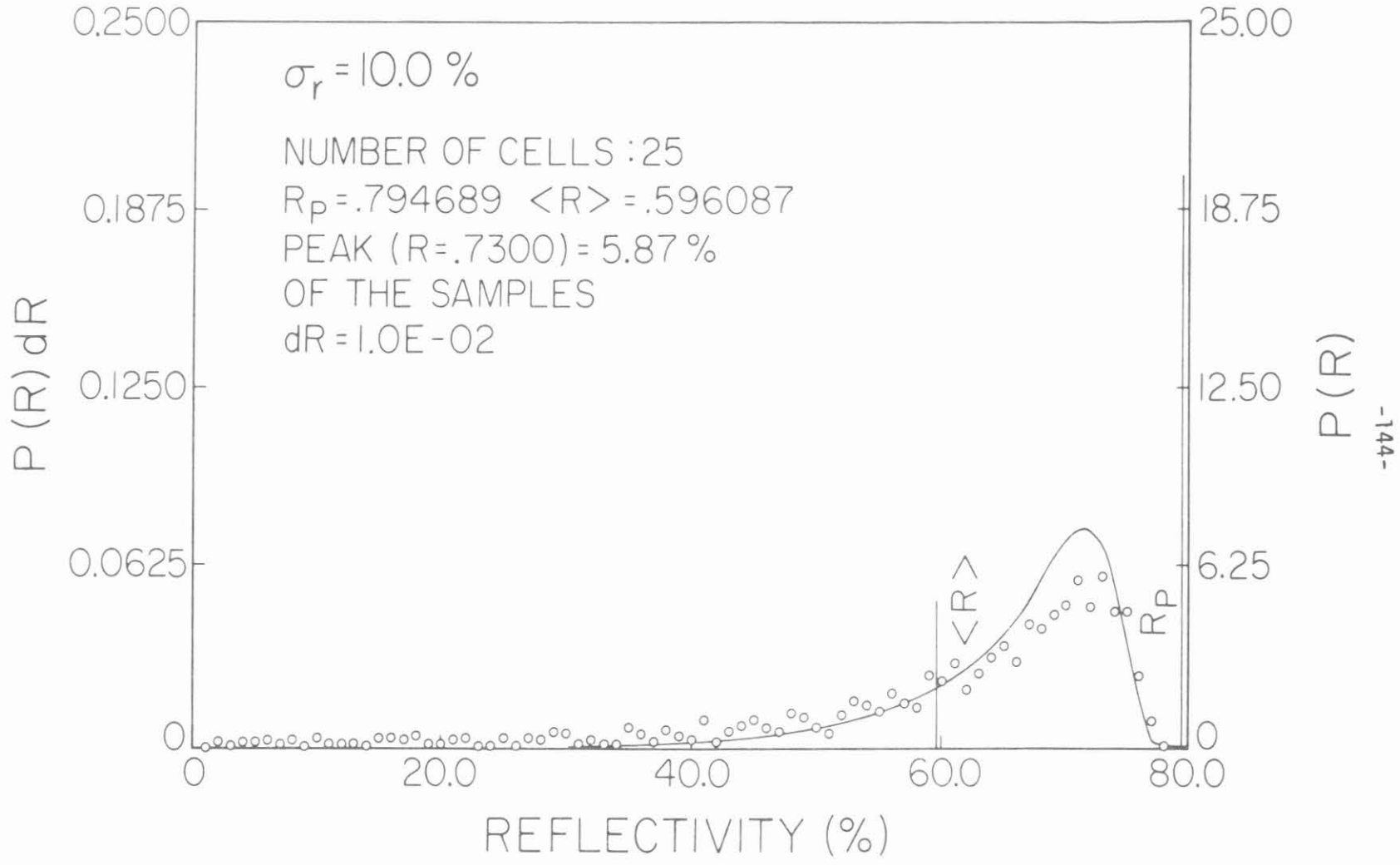
σ_r = 10.0 %
NUMBER OF CELLS : 25
R_P = .794689 <R> = .596087
PEAK (R=.7300) = 5.87 %
OF THE SAMPLES
dR = 1.0E-02
0.2500
0.1875
0.1250
0.0625
0
P(R) dR
25.00
18.75
12.50
6.25
0
P(R)
<R>
R_P
0
20.0
40.0
60.0
80.0
REFLECTIVITY (%)

Fig. 4.14

4.6 A Phenomenological Expression for $p(|\rho|^2)$

As seen from Figures 4.9 - 4.14 the value of $\langle\rho\rho^*\rangle = \langle R\rangle$, while an important parameter of the reflector, does not describe the spread in distribution, or the most likely value of reflectivity. It also does not answer the following important question. If the value of σ is allowed to increase, how many structures will no longer satisfy a given required reflectivity. For example from Figure 4.14 we see that although the reflectivity from a perfect structure is almost 80%, a substantial number of reflectors reflect less than 60%. Also it may be desirable to relax the manufacturing tolerances if this does not lead to a large increase in the number of "bad" mirrors.

Based on Figures 4.9 - 4.14 we will fit these data to the function

$$p(r) = \frac{C^{q-1}}{\Gamma(q-1)} \frac{e^{-\frac{C}{r_p - r}}}{(r_p - r)^q} \tag{4.60}$$

where $r = \rho\rho^*$ is the reflection, Γ is the gamma function, r_p is the reflection from a perfect structure, and the parameters C and q are determined from the average value and standard deviation of the distribution function.

It is easily shown that the parameters C and q are related to the average and standard deviation of p(r) through

$$q = 3 + \frac{(r_p - \langle r\rangle)^2}{\langle r^2\rangle - \langle r\rangle^2} \tag{4.61}$$

$$C = \frac{(r_p - \langle r\rangle)\left[(r_p - \langle r\rangle)^2 + (\langle r^2\rangle - \langle r\rangle^2)\right]}{\langle r^2\rangle - \langle r\rangle^2} \tag{4.62}$$

From equation (4.55) we have

$$\langle r\rangle \equiv \langle \rho\rho^{*}\rangle = r_p - \frac{\kappa S_1}{C_1^3}\langle f\rangle \tag{4.63}$$

$$f \equiv \int_0^L [2 - e^{i\varepsilon\phi(z)} - e^{-i\varepsilon\phi(z)}]dz$$

$$\langle f\rangle = 2\Lambda\left[\frac{N\Psi + e^{-N\Psi} - 1}{\Psi}\right] \tag{4.64}$$

We need only use equation (4.55) to find $\langle r^2\rangle$. Before proceeding, an important point should be made. In the derivation of (4.58) we neglected terms of order $S_n \alpha (e^{i\varepsilon\phi} - 1)^n \sim (i\varepsilon\phi)^n$ where $n > 1$. The solution (4.58) is, however, of order ϕ^2, indicating that terms of S_2 should have been retained.

Nevertheless the results are in good agreement with experiment as well as the more accurate second order results and because of its simplicity expression (4.55) will be used to compute $\langle r^2\rangle$ as well. Equation (4.55) gives us

$$\langle r^2\rangle - \langle r\rangle^2 = \frac{\kappa^2 S_1^2}{C_1^6}\left[\langle f^2\rangle - \langle f\rangle^2\right] \tag{4.65}$$

Using the results of Appendix 4-F we find

$$\sqrt{\langle r^2\rangle - \langle r\rangle^2} = \frac{\kappa S_1}{C_1^3}\frac{2}{\sqrt{3}} NL\left(\frac{\pi}{2}\right)^2 \left(\frac{\bar{\sigma}}{\Lambda/2}\right)^2 \tag{4.66}$$

Combining equation (4.58) and (4.57), using the definition of $\bar{\sigma}$, and keeping only the lowest order term in $\bar{\sigma}$, we find

$$r_p - \langle r \rangle = \frac{\kappa S_1}{C_1^3} NL \left(\frac{\pi}{2}\right)^2 \left(\frac{\bar{\sigma}}{\Lambda/2}\right)^2 \tag{4.67}$$

or the interesting result

$$\frac{\sqrt{\langle r^2 \rangle - \langle r \rangle^2}}{r_p - \langle r \rangle} = \frac{2}{3}\sqrt{3} \approx 1.15$$

We thus arrive at values for the parameters q and C

$$q = \frac{15}{4} \tag{4.68}$$

$$C = \frac{7}{4} \frac{\kappa S_1}{C_1^3} NL \left(\frac{\pi}{2}\right)^2 \left(\frac{\bar{\sigma}}{\Lambda/2}\right)^2 \tag{4.69}$$

which when used in (4.60) give

$$p(r) = \frac{C^{11/4}}{\Gamma(\frac{11}{4})} \frac{e^{-\frac{C}{r_p - r}}}{(r_p - r)^{15/4}}$$

$$\Gamma(\tfrac{11}{4}) = \tfrac{7}{4}! \approx 1.608 \tag{4.70}$$

The function p(r) is indicated in Figures 4.9 - 4.14 by the solid line and agrees well with the computer results.

Finally from equation (4.70) we find that the peak of the function p(r) occurs at the point.

$$r_{peak} = r_p - \frac{C}{q} = r_p - \frac{7}{15} \frac{\kappa S_1}{C_1^3} NL \left(\frac{\pi}{2}\right)^2 \left(\frac{\bar{\sigma}}{\Lambda/2}\right)^2 \tag{4.71}$$

or $$\frac{r_p - r_{peak}}{r_p - \langle r \rangle} = \frac{7}{15} \quad .$$

4.7 Experimental Results

As a final example we consider a multilayered dielectric mirror manufactured by Spectra-Physics. The structure is designated by S, $HL(LH)^4$, Air (S = Substrate, H = High index material, L = low index material) and is depicted in Figure 4.15. It is a quarter wave stack for $\lambda_o = 4500$ Å (except for the double n_L stack) with a reflection (for a perfect structure) of .986.

Twelve such devices were built and tested and the following reflections were measured:

.946
.972
.966
.954
.964
.973
.974
.974
.986
.972
.980
.974

$\langle r \rangle \approx .970$, $\langle \Delta r^2 \rangle = .016$

$$\sqrt{\langle r^2 \rangle - \langle r \rangle^2} = 1.09 \qquad (4.72)$$

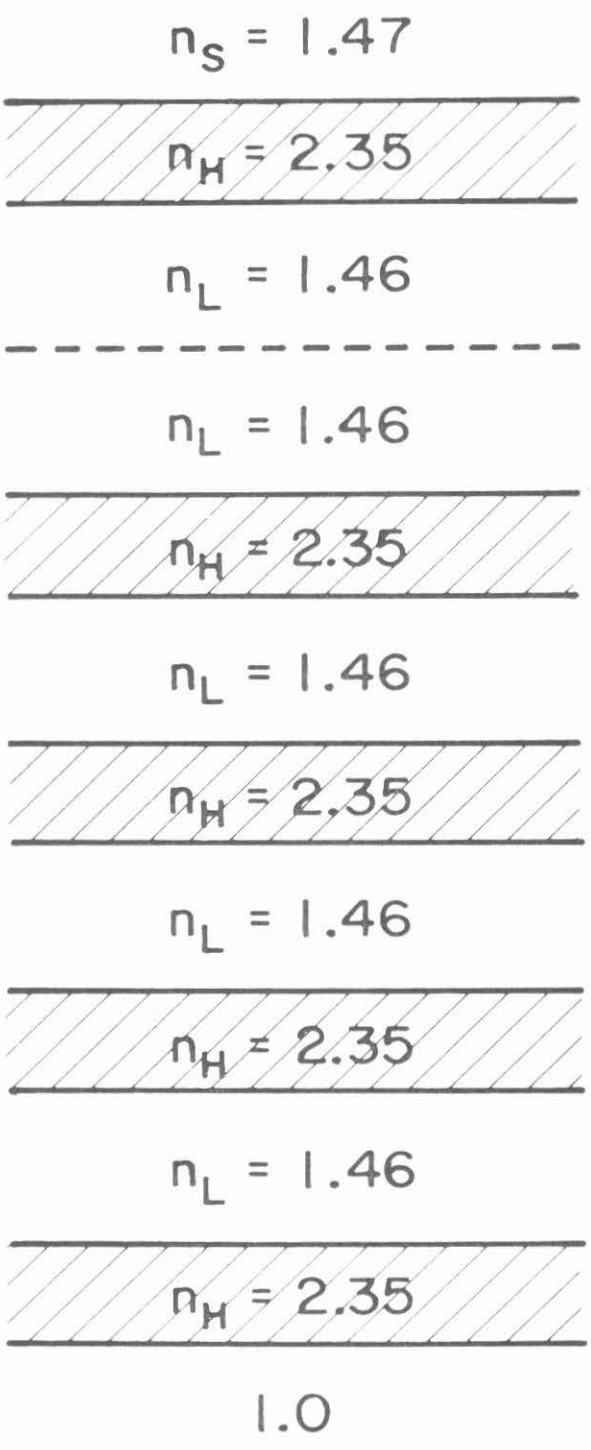

Fig. 4.15 Dielectric mirror tested by Spectra-Physics

Reflectivity measurements are accurate to .003 and the following calculations do not consider any systematic errors. For example, the index of refraction may increase slightly as the sample is grown due to changing temperatures and growing conditions.

Using equation (4.59) with the following variable values

$$\langle \Delta r^2 \rangle = .016$$

$$\kappa L = 2.34$$

$$\psi = \left(\frac{\bar{\sigma}}{\Lambda_{o/2}}\right)^2 \frac{\pi^2}{4}$$

$$N = 5$$

we find

$$\langle \Delta r^2 \rangle \approx \frac{\kappa L \; N}{\sinh \kappa L \cosh \kappa L} \; \frac{\pi^2}{4} \left(\frac{\bar{\sigma}}{\Lambda_{o/2}}\right)^2$$

or

$$\frac{\bar{\sigma}}{\Lambda_{o/2}} \approx .12 \qquad (4.73)$$

We next check to see if this is consistent with equation (4.66) and the experimental value of $\sqrt{\langle r^2 \rangle - \langle r \rangle^2}$ given in equation (4.72). From (4.66) and $\sqrt{\langle r^2 \rangle - \langle r \rangle^2} = 1.09$, we find $\bar{\sigma} / \Lambda_{o/2} \approx .10$, in approximate agreement with (4.73).

4.8 Conclusion

The effect on reflectivity of a statistical variation in the thickness of layers in a Bragg reflector has been studied using the coupled mode equations. Closed form expressions were obtained for the reduction in reflectivity, which agreed with a computer experiment. These expressions are accurate for small values of σ which is typical for most cases. A phenomenological expression for the reflectivity distribution function $p(r)$ was presented which also agreed well with the experiment. Results for arbitrarily large σ values were obtained for low reflectivity reflectors. The formulas were then applied to a structure which was grown and results were found to be consistent.

Appendix 4-A

In this appendix we solve

$$R_o'' - \kappa^2 R_o = 0 \tag{4-A.1}$$

and

$$R_n'' - \kappa^2 R_n = i\,\phi'\,R_{n-1}' \quad , n = 1, 2 \tag{4-A.2}$$

subject to

$$R(-\tfrac{1}{2}L) = 1 \tag{4-A.3}$$

and

$$S(\tfrac{1}{2}L) = 0 \tag{4-A.4}$$

where

$$R = R_o + \varepsilon R_1 + \varepsilon^2 R_2 \tag{4-A.5}$$

and

$$S = -\,ie^{-i\varepsilon\phi}\,(\frac{R'}{\kappa}) \tag{4-A.6}$$

The procedure for determining R_o is straightforward and the solution is

$$R_o(z) = \frac{\cosh[\kappa(\frac{L}{2} - z)]}{\cosh(\kappa L)}$$

The boundary conditions on R' are, from (4-A.4) and (4-A.6) $R'(\frac{L}{2}) = 0$.

Since these must hold for all values of ε we have

$$R_1(-\tfrac{L}{2}) = R_2(-\tfrac{L}{2}) = R_1'(\tfrac{L}{2}) = R_2'(\tfrac{L}{2}) = 0 \tag{4-A.7}$$

A homogeneous solution to (4-A.2) is given by

$$B_n \sinh[\kappa(\tfrac{L}{2} + z)] \tag{4-A.8}$$

where B_n is a constant to be determined. The particular solution is given by

$$\frac{1}{\kappa}\int_{-L/2}^{z} i\,\phi'(\eta)\,R_{n-1}'(\eta)\,\sinh[\kappa(z-\eta)]\,d\eta \tag{4-A.9}$$

This can be confirmed by differentiating (4-A.9) and substituting in (4-A.2).

The total solution is thus

$$R_n(z) = B_n \sinh[\kappa(\frac{L}{2} + z)] + \frac{1}{\kappa} \int_{-L/2}^{z} i\, \phi'(\eta) R'_{n-1}(\eta) \sinh \kappa(z-\eta)]d\eta$$

The boundary solution at $z = -L/2$ is also satisfied and B_n is determined through the boundary condition $R'_n(\frac{L}{2}) = 0$. The result is given by equation (4.17).

Appendix 4-B

We wish to solve for the expectation value of $\rho(-\frac{L}{2}) = \langle\rho(-\frac{L}{2})\rangle$ given that $\langle\phi'(z)\ \phi'(z + z_o)\rangle = \Sigma^2\ (1 - \frac{|z_o|}{\ell})$ and using equations (4.16), (4.17), and (4.18),

$$\langle R'(-\tfrac{L}{2})\rangle = \langle R'_o(-\tfrac{L}{2})\rangle + \varepsilon\langle R'_1(-\tfrac{L}{2})\rangle + \varepsilon^2\langle R'_2(-\tfrac{L}{2})\rangle \qquad (4\text{-B.1})$$

After differentiation we find from equation (4.17)

$$\langle R'_1(-\tfrac{L}{2})\rangle = \frac{-i}{C_1}\int_{-L/2}^{L/2} \langle\phi'(\eta)\rangle\ R'_o(\eta)\ \cosh[\kappa(\tfrac{L}{2} - \eta)]d\eta \ = 0 \qquad (4\text{-B.2})$$

since $\langle\phi(\eta)\rangle = 0$

Equation (4.18) also gives

$$R'_2(-\tfrac{L}{2}) = \frac{-i}{C_1}\int_{-L/2}^{L/2} \phi'(\xi)\ R'_1(\xi)\ \cosh[\kappa(\tfrac{L}{2} - \xi)]d\xi \qquad (4\text{-B.3})$$

We now use equation (4.17) to express R'_1 in terms of R_o and ϕ'. The result is

$$\langle R'_2(-\tfrac{L}{2})\rangle = \frac{-\kappa}{C_1^2}\int_{\xi=-\frac{L}{2}}^{L/2}\int_{\eta=-\frac{L}{2}}^{\xi} \langle\phi'(\xi)\ \ \phi'(\eta)\rangle\cosh[\kappa(\tfrac{L}{2} - \xi)] \qquad (4\text{-B.4})$$

$$\cdot\ \cosh[\kappa(\xi - \eta)]\ \sinh[\kappa(\tfrac{L}{2} - \eta)]d\xi d\eta \ + \frac{\kappa}{C_1^3}\int_{\xi=-\frac{L}{2}}^{L/2}\int_{\eta=-\frac{L}{2}}^{L/2} \langle\phi'(\xi)\phi'(\eta)\rangle\ \cdot$$

$$\cdot\ \cosh[\kappa(\tfrac{L}{2} - \xi)]\ \cosh[\kappa(\tfrac{L}{2} + \xi)]\ \cosh[\kappa(\tfrac{L}{2} - \eta)]\ \sinh[\kappa(\tfrac{L}{2} - \eta)]d\xi d\eta$$

From equation (4.19) we have $R_\phi(\xi-\eta) = \langle\phi'(\xi)\phi'(\eta)\rangle = \Sigma^2\ (1 - \frac{|\xi-\eta|}{\ell})$

The integration is quite involved unless we make the approximation

$$R_\phi(\xi - \eta) \approx \ell\Sigma^2\ \delta(\xi - \eta) \qquad (4\text{-B.5})$$

where $\delta(x)$ is the Dirac delta function.

This is a quite reasonable approximation and is good whenever $\kappa\ell << 1$.

After using

$$\int_a^b \delta(x)\, f(x)\, dx = f(0) \quad \text{for } a < 0 < b \tag{4-B.6}$$

and

$$\int_0^b \delta(x)\, f(x)\, dx = \frac{1}{2} f(0) \quad \text{for } b > 0 \tag{4-B.7}$$

we find

$$\langle R_2'(-\tfrac{L}{2})\rangle = \frac{\Sigma^2 \ell}{8\, C_1^3} \left[- C_1 C_2 - C_1 + 2C_1^5 + \kappa L S_1 - \frac{1}{4} S_1\, S_4\right] \tag{4-B.8}$$

When this is combined with (4-B.1) and equation (4.18) we arrive at equation (4.20).

Appendix 4-C

The expectation value of $\rho(-\frac{L}{2})\ \rho^*(\frac{L}{2})$ is calculated in a fashion similar to $\langle\rho(-\frac{L}{2})\rangle$

$$\rho(-\tfrac{L}{2}) = \frac{-i}{\kappa} e^{-i\varepsilon\phi(-\frac{L}{2})} [R_o'(-\tfrac{1}{2}L) + \varepsilon R_1'(-\tfrac{1}{2}L) + \varepsilon^2 R_2'(-\tfrac{1}{2}L)] \tag{4-C.1}$$

$$\langle\rho(-\tfrac{1}{2}L)\ \rho^*(-\tfrac{1}{2}L)\rangle = \frac{1}{\kappa^2}[R_o' R_o'^* + \varepsilon^2 \langle R_1' R_1'^*\rangle + \tag{4-C.2}$$

$$\varepsilon^2 \langle R_o' R_2'^* + R_o'^* R_2'\rangle]_{z=-\frac{L}{2}}$$

All terms of order ε do not contribute since $\langle\phi'\rangle = 0$ (See Appendix 4.B)

$\langle R_o' R_2'^* + R_o'^* R_2'\rangle = R_o' \langle R_2'^*\rangle + R_o'^* \langle R_2'\rangle$, $\langle R_2'\rangle$, the expectation value of R_2' has been calculated in Appendix 4-B. Thus we need only determine $\langle R_1' R_1'^*\rangle$

$$\langle R_1'(-\tfrac{L}{2})\ R_1'^*(-\tfrac{L}{2})\rangle = \frac{\kappa^2}{C_1^4} \int_{-\frac{L}{2}}^{L/2} \int_{-L/2}^{L/2} \langle\phi'(\eta)\phi'(\xi)\rangle. \tag{4-C.3}$$

$$\sinh[\kappa(\tfrac{L}{2} - \eta)] \sinh[\kappa(\tfrac{L}{2} - \xi)] \cosh[\kappa(\tfrac{L}{2} - \eta)] \cosh[\kappa(\tfrac{L}{2} - \xi)] d\eta d\xi$$

using (4-B.5) this reduces to

$$\langle R_1'(-\tfrac{L}{2})\ R_1'^*(-\tfrac{L}{2})\rangle = \frac{\kappa\ \Sigma^2\ \ell}{C_1^4} (\frac{1}{32} S_4 - \frac{1}{8}\ \kappa) \tag{4-C.4}$$

After combining (4-C.2), (4-C.4) and 4-B.8) we arrive at equation (4.21).

Appendix 4-D

In this appendix we solve $R_t(z_o) = \langle \Delta t(z)\ \Delta t(z + z_o)\rangle =$

$$\lim_{W\to\infty} \frac{1}{2W} \int_{-W}^{W} \Delta t(z)\ \Delta t(z + z_o)dz. \tag{4-D.1}$$

Equation (4-D.1) can be interpreted as

$$\langle \Delta t(z)\ \Delta t(z + z_o)\rangle = \sigma_a^2\ P_{n_1}(z_o) + \sigma_b^2\ P_{n_2}(z_o) \tag{4-D.2}$$

where $P_{n_i}(z_o)$ is the probability that two points separated by a distance z_o will both be in the same cell of index n_i.

From reference 18 we have

$$\begin{aligned} P_{n_1} &= \frac{a_o}{\Lambda_o}\left(1 - \frac{|z_o|}{a_o}\right) \quad \text{for } |z_o| < a_o \\ &= 0 \quad \text{otherwise} \\ P_{n_2} &= \frac{b_o}{\Lambda_o}\left(1 - \frac{|z_o|}{b_o}\right) \quad \text{for } |z_o| < b_o \\ &= 0 \quad \text{otherwise} \end{aligned} \tag{4-D.3}$$

where we have assumed $\frac{\sigma_a}{a_o}$, $\frac{\sigma_b}{b_o} \ll 1$.

If we now combine (4-D.2) and (4-D.3) and take $a_o \sim b_o \sim \frac{\Lambda_o}{2}$, we obtain

$$\begin{aligned} \langle \Delta t(z)\ \Delta t(z + z_o)\rangle &= \bar{\sigma}^2\left(1 - \frac{|z_o|}{\Lambda_{o/2}}\right) \quad |z_o| < \Lambda_{o/2} \\ &= 0 \quad \text{otherwise.} \end{aligned}$$

Appendix 4-E

Computer program used as a check of the analytical expressions

```
 DAY
9-Jan-78 9:21:04

.TY RRA.F4
C PLOTS P(R)DR (DISTRIBUTION) OF THE SAMPLES.
C HAS THE OPTION OF PLOTTING ON THE XEROX AND SCALING
C (PROGRAMMED BY P. AGMON)
        DIMENSION RF(3000),DD(3),SR(10001)
        DIMENSION RAS(1),RPS(1),SNC(4),SRAP(4)
        DIMENSION Y(10001),X(10001),XP(2),YP(2)
        DIMENSION RAX(2 ),RAY(2),SRES(5),PEAK(10),SUP(5)
        REAL N1,N2
        DOUBLE PRECISION NAMF,FL,XNN,RP
        COMMON/NAM001/NAMF
        COMMON/XGP/XGPFLG
        DATA N1,N2/3.6,3.4/
        DATA RAS/'<R>'/,RPS/'RP'/
        DATA DD/3*0./
 998    FORMAT(1X,A4)
 151    WRITE(5,950)
 950    FORMAT(1X,'TY NEW')
        ACCEPT 60,NEW
 60     FORMAT(F5.0)
        IF(NEW.EQ.0)GOTO15
        ACCEPT 50,FL,NSMP,ISY
  50    FORMAT(A8/I4/I2)
        OPEN(UNIT=1,ACCESS='SEQIN',FILE=FL)
        XNN=(N1/N2)**2
        ITEST=1
        SLBL=.21
        STTL=.21
        SSCL=.21
        STICK=.21
        READ(1,101)NC,SD,RP
 101    FORMAT(I3,F5.4,F7.6)
        RP=((1.-XNN**NC)/(1.+XNN**NC))**2
  333   FORMAT(1X,'SD=',F5.3,3X,'NC=',I3,3X,'RP=',F10.6)
        READ(1,100)(RF(I),I=1,NSMP)
 100    FORMAT(10F7.6)
 1      CONTINUE
```

```
15      ACCEPT 48,DIV,RMIN,RMAX,SMAX,XGPFLG,NAME
 48     FORMAT(F10.3/F10.3/F10.3/F10.3/F10.3/A8)
        IF(DIV.LE.0.)STOP
        DRES=1./DIV
        KX=DIV*RMIN+1.5
        MINX=KX
        XMIN=KX
        KX=DIV*RMAX+1.5
        MAXX=KX
        XMAX=KX
        YMAX=SMAX
        RA=0.
        DO 21 I=1,NSMP
21      RA=RA+RF(I)
        XNS=NSMP
        RA=RA/XNS
        WRITE(5,333)SD,NC,RP
        WRITE(5,105)RA,NSMP
 105    FORMAT(1X,'RA=',F6.5,'(# OF SAMPLES=',I4,')')
20      CONTINUE
        ACCEPT 49,D1
49      FORMAT(F10.3)
        DO 5 I=1,10001
 5      SR(I)=0.
        DO 2 I=1,NSMP
        K=DIV*RF(I)+1.5
        SR(K)=SR(K)+1.
 2      CONTINUE
        RPK=0
        DO 22 K=1,10001
        IF(SR(K).LT.RPK)GOTO22
        RPK=SR(K)
        KPK=K
 22     CONTINUE
        RKPK=(KPK-1)/DIV
        XPK=RPK/NSMP*100.
        XMN=RMIN*100.
        XMX=RMAX*100.
        YMN=0.
        YMX=SMAX
        NCC=NC
        SDPR=SD*100.
        ENCODE(10,855,SDP)SDPR
855     FORMAT('S.D.=',F4.1,'%')
        ENCODE(38,710,PEAK)RKPK,XPK
710     FORMAT('PEAK(R=',F7.6,')=',F6.2,'% OF THE SAMPLES')
        ENCODE (15,700,SNC)NCC
700     FORMAT('# OF CELLS :',I3)
```

```
      ERP=RP
      ERA=RA
      ENCODE (24,701,SRAP)ERP,ERA
701   FORMAT('RP=',F7.6,3X,'<R>=',F7.6)
      ENCODE( 11,702,SRES)DRES
702   FORMAT('DR=',1PE8.1)
C  702 FORMAT('RESOLUTION= X',I4)
      RAXI=(RA-RMIN)/(RMAX-RMIN)*15.+.25
      RPX=(RP-RMIN)/(RMAX-RMIN)*15.+.25
      CALL ERASE
      CALL LABEL(0.,0.,XMN,XMX,15.,4,'REFLECTIVITY(%)',15,0)
      PERMX=YMX/NSMP
      CALL LABEL(0.,0.,YMN,PERMX,10.,4,'P(R)DR/# OF SAMPLES',19,1)
      PRM=PERMX*DIV
      CALL LABEL(15.,0.,YMN,PRM,10.,4,'P(R)',-4,1)
      KI=0
      DO 3 I=MINX,MAXX
      YY=SR(I)
      IF(YY.LE.0.)GOTO3
      KI=KI+1
      Y(KI)=YY
      X(KI)=I
3     CONTINUE
300   FORMAT(3I6)
      CALL XYPLT(KI,X,Y,XMIN,XMAX,0.,YMAX,DD,0,ISY)
      RAX(1)=RA
      RAX(2)=RAX(1)
      RAY(1)=0.
      RAY(2)=YMAX/5.
      CALL XYPLOT(2,RAX,RAY,RMIN,RMAX,0.,YMAX,DD,0)
      XP(1)=RP
      XP(2)=XP(1)
      YP(2)=YMAX/5.*4.
      YP(1)=0.
      LAB=-1
      CALL SYSSYM(RPX,1.,.1,RPS,2,90.)
      CALL SYSSYM(RAXI,1.,.1,RAS,3,90.)
      CALL SYSSYM(2.,7.5,.15,SDP,10,0.)
      CALL SYSSYM(2.,7.,.15,SNC,15,0.)
      CALL SYSSYM(2.,6.75,.12,SRAP,24,0.)
      CALL SYSSYM(2.,6.5,.12,PEAK,38,0.)
      CALL SYSSYM(2.,6.25,.12,SRES,11,0.)
44    CALL XYPLOT(2,XP,YP,RMIN,RMAX,0.,YMAX,DD,LAB)
 4    CONTINUE
      GOTO151
      END
```

Appendix 4-F

In this appendix we find an expression for $\langle f^2 \rangle - \langle f \rangle^2$ where

$$f \equiv \int_0^L (2 - e^{i\varepsilon\phi(z)} - e^{-i\varepsilon\phi(z)}) dz \tag{4-F.1}$$

$$\varepsilon\phi(z) = \frac{\omega}{c} n_1 \sum_{i=1}^{\frac{z}{\Lambda}} u_i + \frac{\omega}{c} n_2 \sum_{i=1}^{\frac{z}{\Lambda}} v_i \tag{4-F.2}$$

The variables u_i and v_i are Gaussian distributed as described in the main body of this paper.

$$\begin{aligned} \langle f^2 \rangle = \Big\langle \int_0^L \int_0^L & (2 - e^{i\varepsilon\phi(z)} - e^{-i\varepsilon\phi(z)}) (2 - e^{i\varepsilon\phi(z')} \\ & - e^{-i\varepsilon\phi(z')}) \, dz \, dz' \Big\rangle \\ = 4L^2 & - 8L \int_0^L \langle e^{-i\varepsilon\phi(z)} \rangle dz \\ & + 2 \int_0^L \int_0^L \langle e^{i\varepsilon(\phi(z) + \phi(z'))} \rangle dz \, dz' \\ & + 2 \int_0^L \int_0^L \langle e^{i\varepsilon(\phi(z) - \phi(z'))} \rangle dz \, dz' \end{aligned} \tag{4-F.3}$$

In arriving at (4-F.3) we used the fact that $\langle e^{i\varepsilon(\phi(z) + \phi(z'))} \rangle = \langle e^{-i\varepsilon(\phi(z) + \phi(z'))} \rangle$, etc.

We now examine the second, third and fourth terms on the right side of (4-F.3).

$$-8L \int_0^L \langle e^{-i\varepsilon\phi(z)}\rangle dz = -8L \int_0^L e^{-\frac{\varepsilon^2}{2}\langle\phi^2(z)\rangle} dz$$

$$= -8L \int_0^L e^{-\frac{\Psi}{\Lambda}z} dz = \frac{8L^2}{N\Psi}(e^{-N\Psi}-1) \qquad (4\text{-F.4})$$

We now examine

$$2 \int_0^L \int_0^L \langle e^{i\varepsilon(\phi(z) + \phi(z'))}\rangle dz\, dz'$$

$\phi(z)$ and $\phi(z')$ are not independent. Over the region of integration where $z' > z$ we can write $\phi(z) + \phi(z') = 2\phi(z) + \Omega(z'-z)$ where ϕ and Ω are independent and $\Omega(x)$ has the same probability distribution function as $\phi(x)$. Thus

$$\langle e^{i\varepsilon(\phi(z) + \phi(z'))}\rangle = \langle e^{2i\varepsilon\phi(z)}\rangle \langle e^{i\varepsilon\Omega(z'-z)}\rangle$$

$$= e^{-2\varepsilon^2\langle\phi^2(z)\rangle} e^{-\frac{\varepsilon^2}{2}\langle\Omega^2(z'-z)\rangle} \qquad (4\text{-F.5})$$

$$= e^{-\frac{4z\Psi}{\Lambda}} e^{-\frac{\Psi}{\Lambda}(z'-z)}$$

with a symmetric expression for $z > z'$. After integrating this third term we find

$$2 \int_0^L \int_0^L \langle e^{i\varepsilon(\phi(z) + \phi(z'))}\rangle\, dz\, dz' =$$

$$\frac{4}{3}\,\frac{L^2}{N^2\Psi^2}\left[\frac{3}{4} - e^{-N\Psi} + \frac{1}{4}e^{-4N\Psi}\right]$$

In a similar manner we find

$$2\int_0^L\int_0^L \langle e^{i\epsilon(\phi(z)-\phi(z'))}\rangle dz\, dz'$$

$$= 4\int_{z=0}^{L}\int_{z'=0}^{z} e^{-\frac{\Psi}{\Lambda}(z-z')}\, dz\, dz' = \frac{4L^2}{N\Psi}\left[1+\frac{1}{N\Psi}(e^{-N\Psi}-1)\right]$$

After combining our results and expanding all expressions in a power series in Ψ, retaining terms up to order Ψ^2, we arrive at the desired result

$$\langle f^2\rangle - \langle f\rangle^2 = \frac{4}{3}(NL\Psi)^2 \simeq \frac{4}{3}N^2L^2\left(\frac{\pi}{2}\right)^4\left(\frac{\bar{\sigma}}{\Lambda/2}\right)^4$$

Chapter 4 References

1. M. Born and E. Wolf, Principles of Optics, (MacMillan, N. Y. 1964).
2. P. Yeh, A. Yariv and C. Hong, J. Opt. Soc. Am. 67, 423 (1977).
3. A. Ashkin and A. Yariv, Bell Labs. Tech. Memo MM-61-124-46 (13 November 1961), (unpublished).
4. N. Bloembergen and A. J. Sievers, Appl. Phys. Lett. 17, 483 (1970).
5. C. L. Tang and P.P. Bey, IEEE J. Quantum Electron. QE-9, 9 (1973).
6. S. M. Rytov, Zh. Eksp. Teor. Fiz. 29, 605 (1955). [Sov. Phys. - JETP 2, 466 (1956).]
7. J. P. Vander Ziel, M. Illegems, and R. M. Mikulyak, Appl. Phys. (to be published).
8. Private communication with Wess Icenogle of Spectra Physics, Mountain View, California.
9. Private communication with Steve Silver of OCLI, Santa Rosa, California.
10. K. O. Hill, Appl. Opt. 13, 1853 (1974).
11. A. Katzir, A. C. Livanos, J. B. Shellan, and A. Yariv, IEEE J. Quantum Electron. QE-13, 296 (1977).
12. C. Hong, J. B. Shellan, A. C. Livanos, A. Yariv, and A. Katzir, Appl. Phys. Lett. 31, 276 (1977).
13. C. Kittel, Introduction to Solid State Physics (Wiley, N. Y. 1971), p. 85.
14. Petr Beckmann, The Scattering of Electromagnetic Waves From Rough Surfaces, (MacMillan, N. Y., 1963), p. 81.
15. H. Kogelnik, Bell. Syst. Tech. J. 55, 109-126 (1976).
16. A. Yariv, IEEE J. Quantum Electron. QE-9, 919 (1973).

17. W. Streifer, D. R. Scifres, and R. D. Burnham, J. Opt. Soc. Am. 66, 1359 (1976).

18. H. W. Harman, Principles of the Statistical Theory of Communication, (McGraw-Hill, N. Y., 1963), p. 75.

Chapter 5

ADDITIONAL USES OF APERIODIC STRUCTURES

5.1 Introduction

In this chapter we will study some of the additional properties and uses of aperiodic devices in optics. The use of a tapered grating to suppress the side lobes of the reflectivity spectrum in a broad-band filter is first discussed. The analogy between this device and the method of side-lobe suppression in the Šolc filter is also covered.

Next a perturbation solution to the coupled mode equations is presented, which is used to study active devices such as DFB lasers and the effects of tapering the guiding layer or chirping the feedback corrugations.

Finally, the topics of pulse compression and optical coatings to reduce electric field intensities are discussed.

5.2 Effects of a Tapered Coupling Coefficient

In his 1976 paper Kogelnik[1] uses the coupled mode equations in the form of a Riccati equation (see Appendix 1-B) to obtain numerical results for reflection from chirped gratings and tapered gratings. The gratings are corrugations on the surface of a dielectric waveguide as we considered in previous chapters. Figure 5.1 is a typical result of the broadening of the reflectivity spectrum with increasing chirps.[1] The notation has been modified so as to be consistent with that used in previous chapters. It was shown in Appendix 2-A that the reflectivity for frequencies that reflect from grating regions sufficiently far from the grating

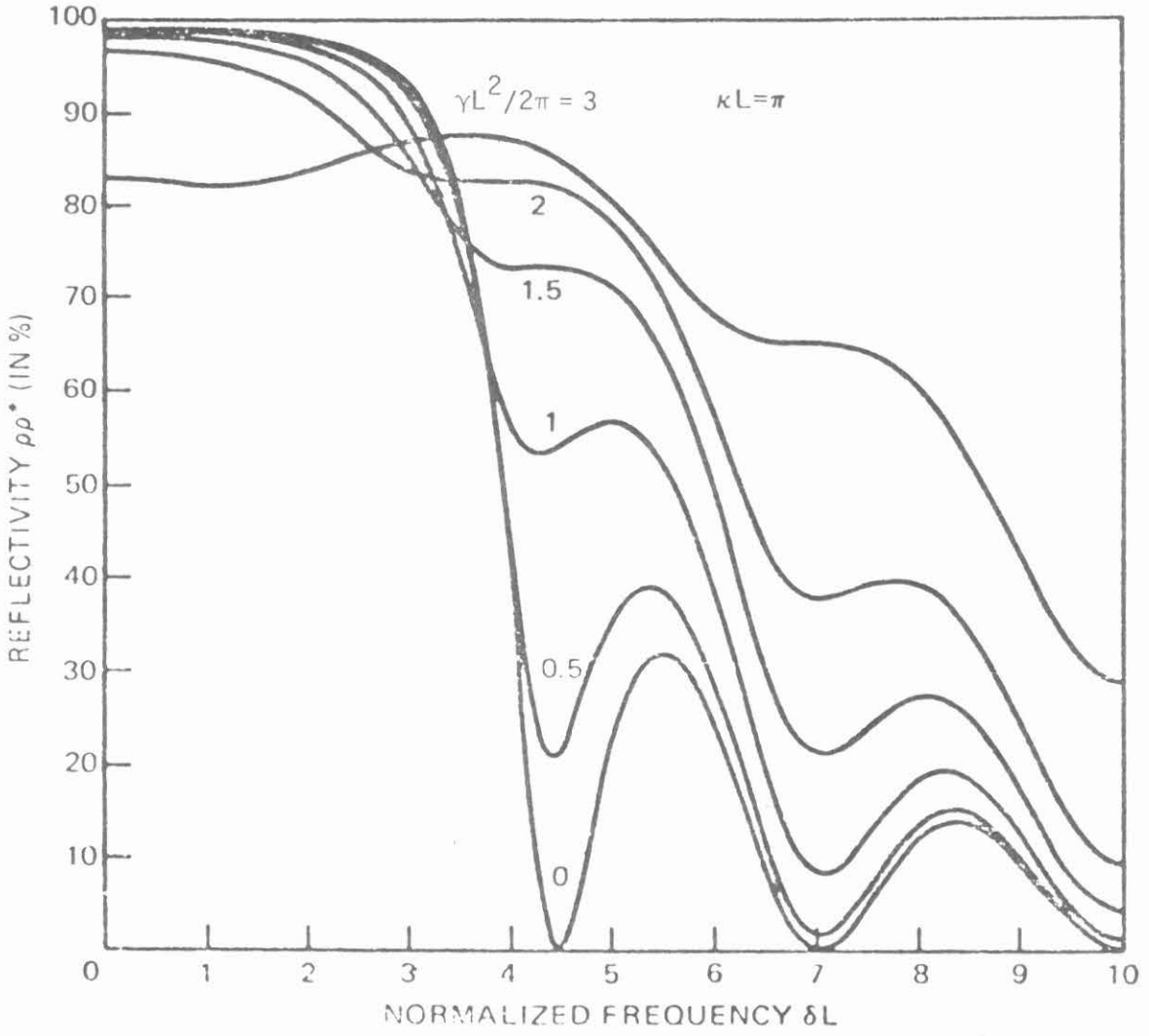

Fig. 5.1 Reflectivity spectrum of a chirped grating used as a broad-band filter. (After reference 1.)

edges is given by $1 - e^{-(\pi\kappa^2)/\gamma}$. The values of the reflectivity in Figure 5.1 for small L are in agreement with the above formula. The plot is also in qualitative agreement with Figure 4.3 which is a plot of the reflectivity spectrum of a chirped slab reflector.

A further interesting effect observed by Kogelnik which has not been covered in this thesis is that of a tapered grating; that is, one in which the period is constant, but the depth of the corrugation varies. Figure 5.2 is a plot of the results. The form of the coupling constant was taken as

$$\kappa = \kappa_0\left(1 - \frac{T}{12} + \frac{T\left(z - \frac{L}{2}\right)^2}{L^2}\right) \qquad (5.1)$$

with T being an adjustable parameter; a positive T value represents a corrugation that is shallower near the center of the grating than near the edges, while a negative T value represents the opposite. The grating region is located between z = 0 and z = L. The key result of Figure 5.2 is that the side-lobe levels of the response characteristics are strongly dependent on the T value. For quadratic tapers the side lobes are strongly suppressed if the incident light first encounters a shallow grating, then a deeper grating, and finally a shallow grating. Thus, while a chirped grating increases the filter bandwidth, a tapered grating serves to suppress the side lobes. Cross, Matsuhara, and Hill[2] also investigated this effect using various tapering functions such as the Hamming function, raised-cosine or Hanning function, the Blackman function, and the Kaiser function. This effect, which results in lowering side-lobe response, occurs in other devices as well. For example,

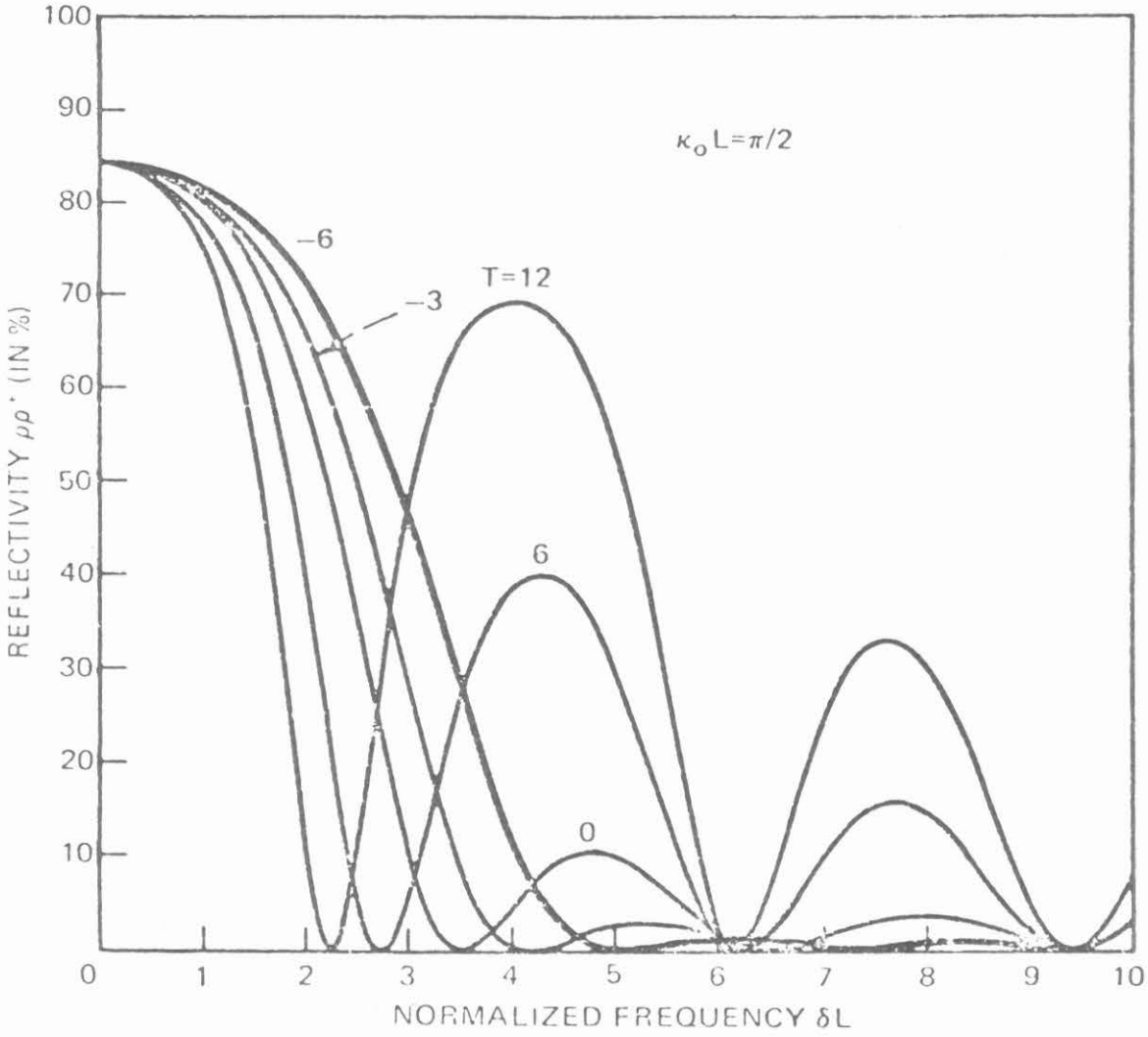

Fig. 5.2 Reflectivity spectrum of a tapered grating used as a reflector in a dielectric waveguide. (After reference 1.)

it is well known that light incident on a slit will produce a far field pattern with side lobes. However, if the slit transmission function is tapered, for example by using a variable transmission filter with maximum transmission near the center and decreasing transmission near the edges, then considerable side-lobe suppression will result.

A further, novel application of this concept was investigated by Šolc in his study of the Šolc filter.[3] The original Šolc filter consisted of a periodic stack of birefringent elements of equal thickness placed between two polarizers. If the optic axis of the n^{th} layer was rotated by an angle $(-1)^n\alpha$ with respect to the $n-1^{st}$ layer, then the device would transmit only one frequency of light. The bandwidth of the filter narrowed as the number of layers was increased, but the response characteristic contained side lobes as in Figure 2. These side lobes were later suppressed by Šolc when he "tapered the angles" through which adjacent elements were rotated. That is, by destroying the periodicity of the filter and rotating the birefringent elements near the center of the filter by more than α and elements near the edge of the filter by less than α, the side lobes were greatly reduced.

If we integrate equation (1-B.9) of Appendix 1-B for the case of low reflectivity ($R'(z) = \text{const} = 1$) and $\phi = 0$ (no chirp), we find

$$|S'(0)| = \int_{-\infty}^{\infty} \kappa(z)\, e^{+i2\delta z}\, dz \qquad (5.2)$$

$|S'(0)|$, which is the reflectance, is simply the Fourier transform of the coupling constant $\kappa(z)$. If $\kappa(z)$ is a constant between $z = 0$ and $z = L$, and zero outside this region, then $|S'(0)|$ will be a sinc function

with side lobes. On the other hand, if $\kappa(z)$ is a Gaussian, then $|S'(0)|$ will be the Fourier transform of a Gaussian which is another Gaussian, and thus $|S'(0)|$ will not contain side lobes. Thus, this interesting effect is readily apparent in the low reflectivity limit. Since the far field pattern resulting from light incident on an aperture is the Fourier transform of the near field pattern, it is also apparent why a "soft" aperture eliminates side lobes.

5.3 Perturbation Solutions to Aperiodic Bragg Reflectors

Although numerical methods must be employed for solutions to problems with the most general chirped or tapered gratings, it is possible to use perturbation techniques for cases of small variations. This was demonstrated in Chapter 4 , where a statistical analysis of Bragg reflectors was presented. Streifer and co-workers[4] have also used this technique. We start with the coupled mode equations given in equation (1-B.5) of Appendix 1-B, but include the possibility of gain or loss for which (1-B.5) must be modified by replacing δ with $\delta + i\alpha \equiv i\mu$ where 2α is the power loss or gain per unit length with $\alpha > 0$ for loss. After combining equations (1-B.5) of Appendix 1-B, we find

$$R'' - (\mu^2 + \kappa^2)R = -\mu' R + \left(\frac{\kappa'}{\kappa} + i\phi'\right)(R' + \mu R) \tag{5.3}$$

where the primes denote differentiation with respect to z. The grating is in the region $0 < z < L$ and the period is assumed to vary according to

$$\cos\left(\frac{2\pi z}{\Lambda} + \phi(z)\right) \tag{5.4}$$

The variables in equation (5.3) are taken to vary as $\kappa = \kappa_o + \kappa_1(z)$, $\mu = \mu_o + \mu_1(z)$, $R = R_o(z) + R_1(z)$, where the terms with the subscript one are assumed small and the R_1 term represents the forward traveling wave correction due to nonzero ϕ', κ_1 and μ_1 values.

It is then straightforward to show[4] that the reflectance is given by

$$\rho(0) = \frac{i \exp(-i\phi(0))}{\kappa(0)} \left(\frac{\kappa_o^2 \sinh \gamma L}{\Omega} + \int_0^L U_1(\xi)\, R_o(\xi)\, d\xi \right) \tag{5.5}$$

where

$$U_1 = 2\kappa_o\kappa_1 R_o + (2\mu_1 + i\phi' + \frac{\kappa_1'}{\kappa_o})(R_o' + \mu_o R_o)$$

$$\gamma^2 \equiv \mu_o^2 + \kappa_o^2$$

$$\Omega \equiv \gamma \cosh \gamma L + \mu_o \sinh \gamma L$$

$$R_o(z) = \frac{1}{\Omega} \{\gamma \cosh[\gamma(L-z)] + \mu_o \sinh[\gamma(L-z)]\}$$

$R_o(z)$ is, of course, the solution for the case $\phi = 0$.

Figure 5.3 is a plot of the filter response for simultaneous linear variations in coupling strength and periodicity.[4] The variations are taken as

$$\kappa(z) = \kappa_o[1 + \varepsilon \frac{2z}{L}]$$

$$\phi = \varepsilon(\frac{2}{L})^2 z^2 \tag{5.6}$$

Notice that for positive ε, there is a larger response for positive δ values (shorter wavelengths). This is easily explained. The grating

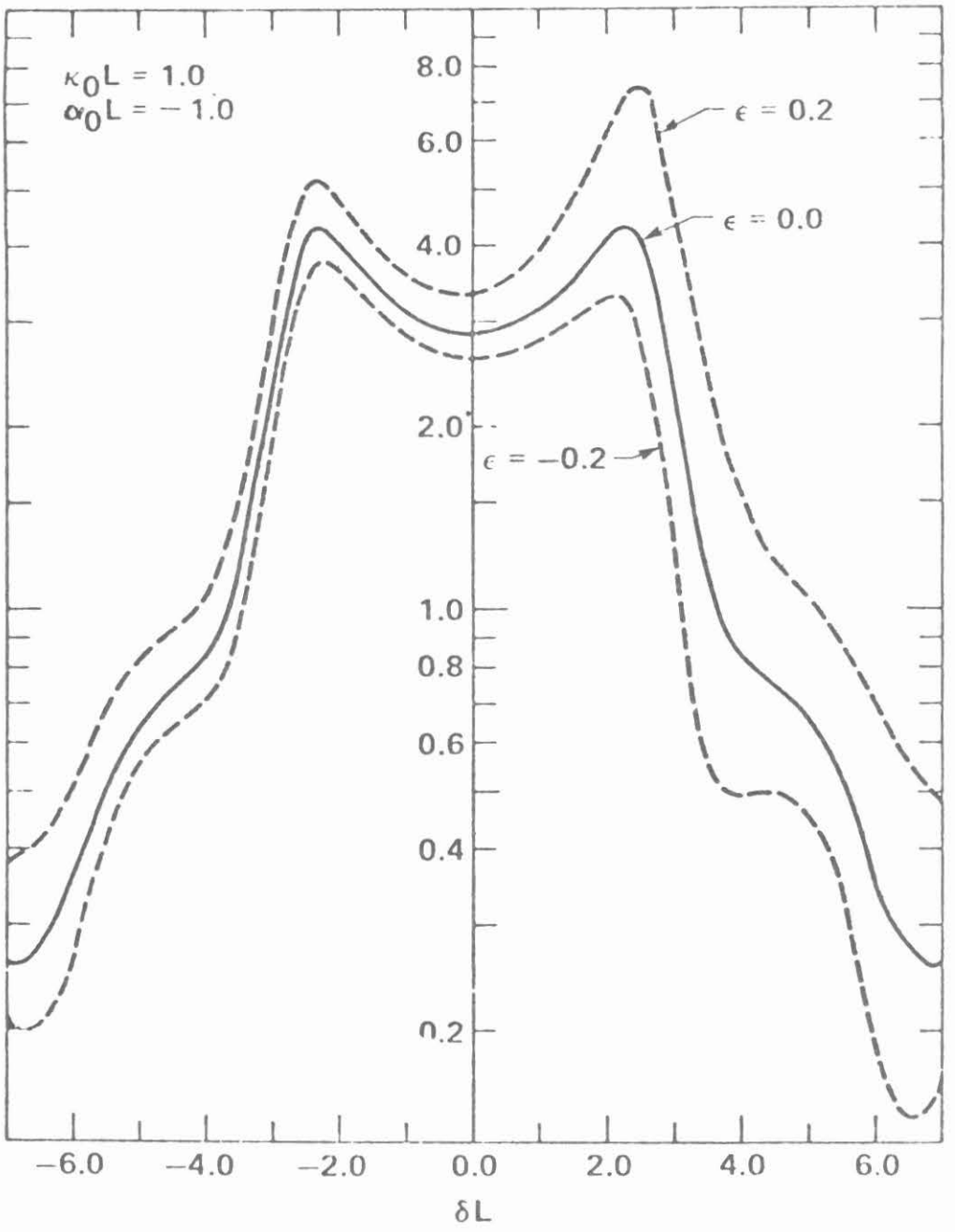

Fig. 5.3 Filter response for simultaneous linear variations in coupling strength and periodicity. (After reference 4.)

depth is larger in regions where the grating period is smaller, and thus these regions interact more strongly with the incident beam. This occurs in regions where z is greater and the light travels a greater distance, resulting in increased gain. The opposite effect occurs for negative ε values.

In Figures 5.4 - 5.6 we have plotted the contours of equal reflectivity (reflectivity = $\left|\frac{S(0)}{R(0)}\right|^2 = \left|\frac{E_r(0)}{E_i(0)}\right|^2$) as a function of various chirp factors. The grating period is taken to vary as $\frac{2\pi}{\Lambda(z)} = \frac{2\pi}{\Lambda(0)} + \frac{8\varepsilon}{L^2} z$. The oscillation condition for a DFB laser is that the reflectivity be infinite (no input and a finite output) and this condition on the gain and frequency is determined by the poles of the contour plots.[5] It is seen that, to first order, the poles do not shift as the chirp is increased. It is readily apparent, however, that the contours are pulled in closer to the poles as the chirp factor ε is increased. This is to be expected, since for a chirped structure the reflectivity will drop. Thus, for example, a contour of reflectivity equal to 600 (contour F) must be drawn closer to the pole as the factor ε is increased.

It should be noted that the gain condition for laser oscillation is changed either as a result of grating aperiodicity or, alternatively, if the grating is uniform, by a tapering in guide thickness. In the latter case, for a guide whose thickness is given by w + gz, the appropriate ε value to use is[6]

$$\varepsilon = \frac{\pi L^2 (n_f^2 - n_{eff}^2)\, g}{2\lambda_o\, w_{eff}\, n_{eff}} \tag{5.7}$$

where n_{eff} is the effective guide index, n_f is the guide index, w_{eff} is

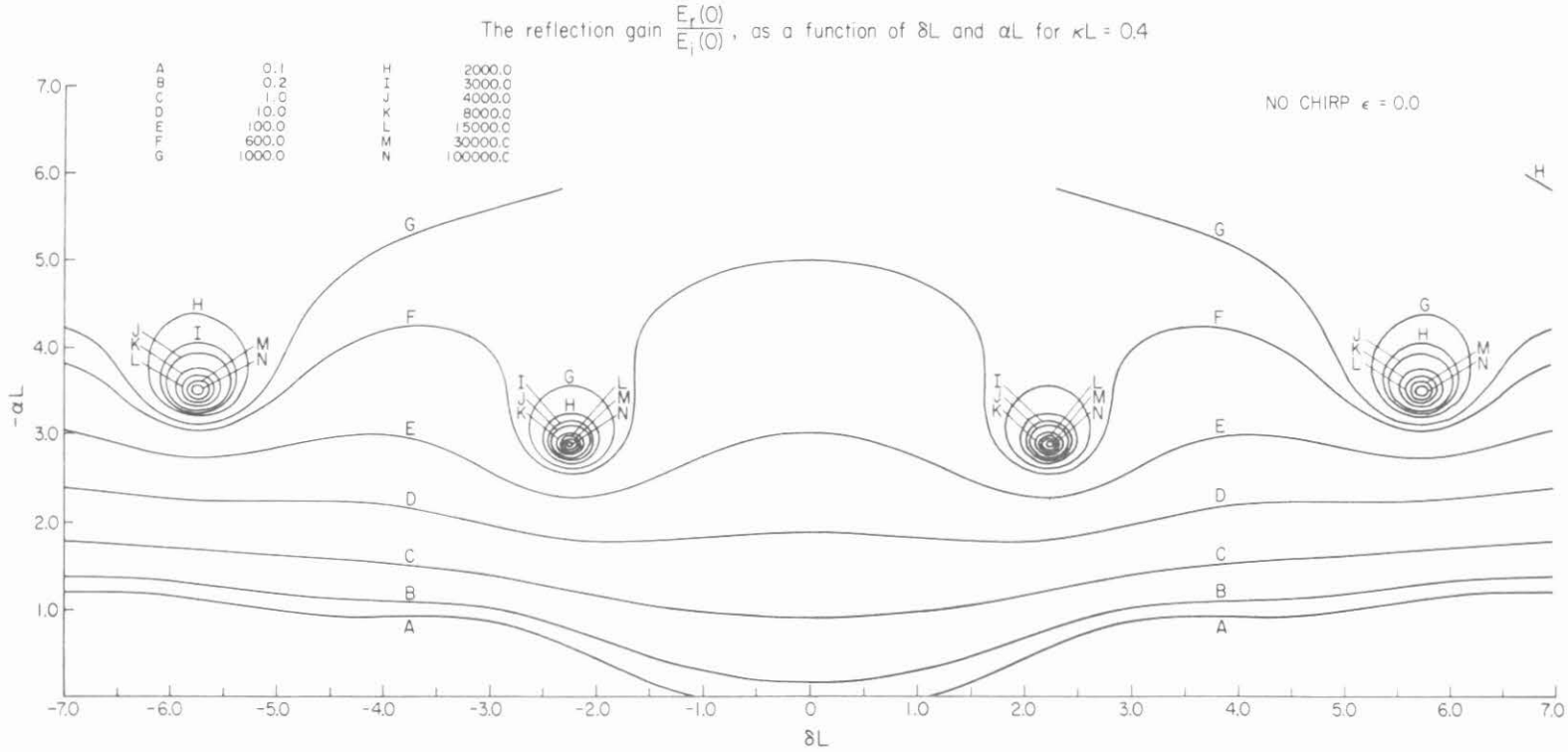

Fig. 5.4 Contour plots of the reflectivity as a function of gain and frequency for uniform grating

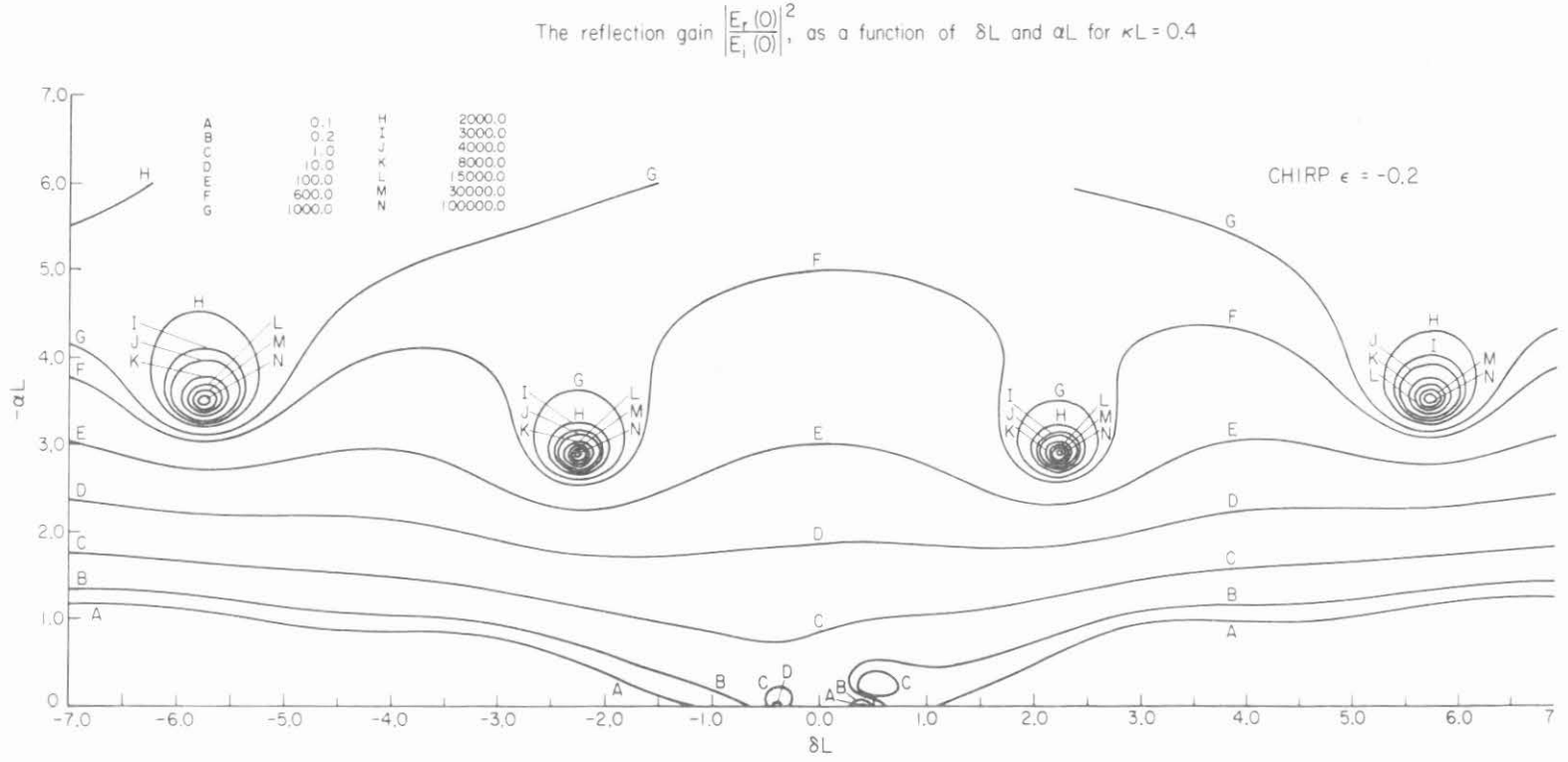

Fig. 5.5 Contour plots of the reflectivity as a function of gain and frequency for grating with $\varepsilon = -.02$.

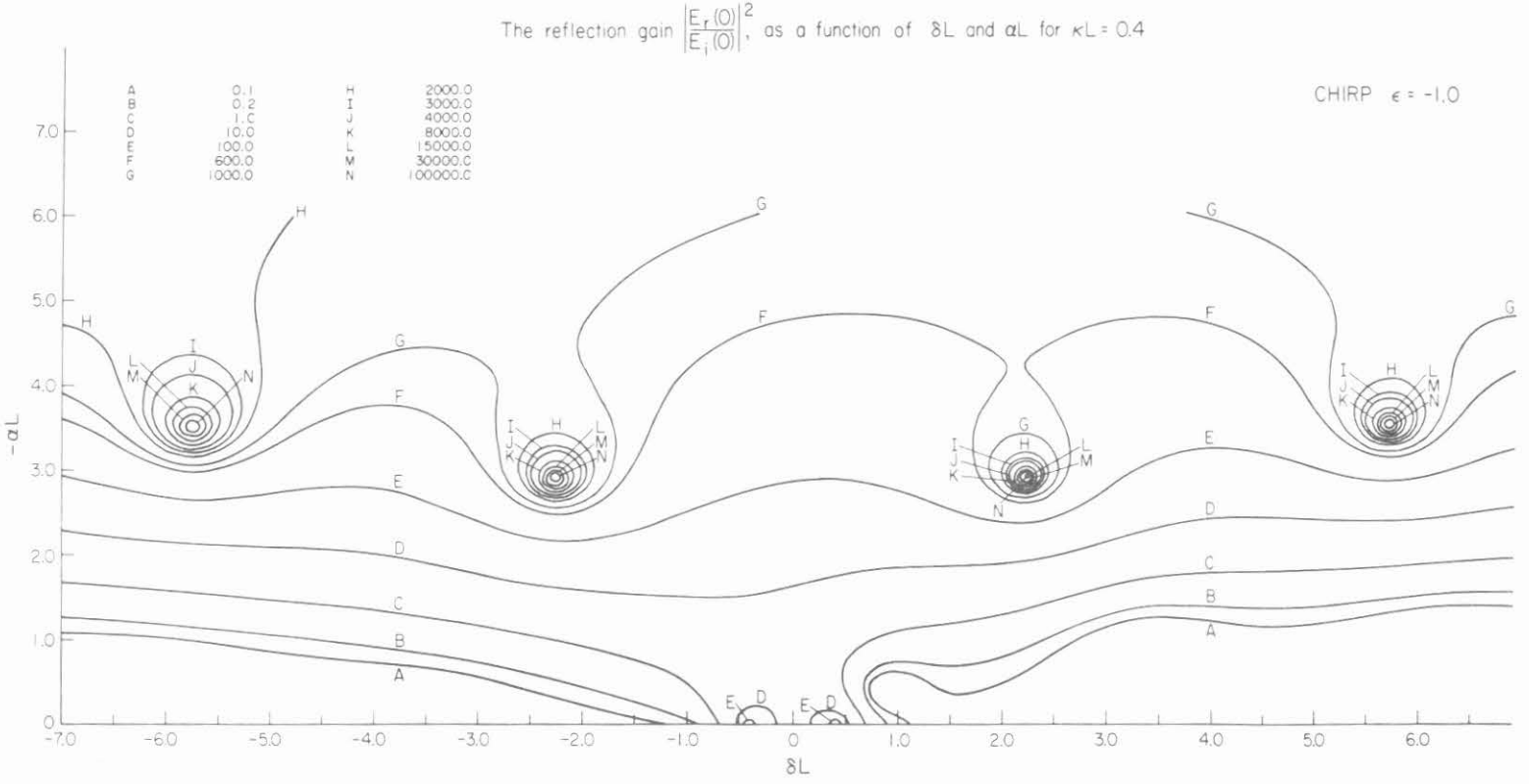

Fig. 5.6 Contour plots of the reflectivity as a function of gain and frequency for grating with ε = -1.0

the effective guide thickness, and λ_o is the wavelength of light in vacuum.

The perturbation analysis presented above is too crude to give results which show how the gain condition for laser oscillation changes as the guide thickness is tapered or the period of the grating is chirped. For a more accurate analysis, we break up the nonuniform region into a series of nine approximately uniform regions. The transmission and reflection properties of each of these nine uniform regions is determined. After the transfer matrix of each region is determined, the matrices are multiplied together, and the oscillation condition thus determined.

In Figures 5.7 and 5.8 the gain required for oscillation of the first four laser modes is plotted for $\kappa L = .4$ and $\kappa L = 2.0$. It is seen that the gain condition for the lowest order mode increases, while the gain required for higher order modes drops slightly as an aperiodicity is introduced. As the chirp is increased, the modes become intermingled. For a DFB laser 500μ long and $\Lambda = 3500\text{Å}$, the right side of the plots in Figures 5.7 and 5.8 represent a change of 1% in the grating period..

5.4 Pulse Compression

A chirped grating or zone plate can also be used to compress a signal. Referring to Figure 5.9, which is simply the broad-band filter discussed in a previous chapter, we see that if a chirped frequency pulse of light is incident on the reflector it may be compressed. For example, if the high frequency part of the signal is leading, it will be delayed upon reflection, since it is reflected from the far right side of the reflector, while the trailing low frequency light is

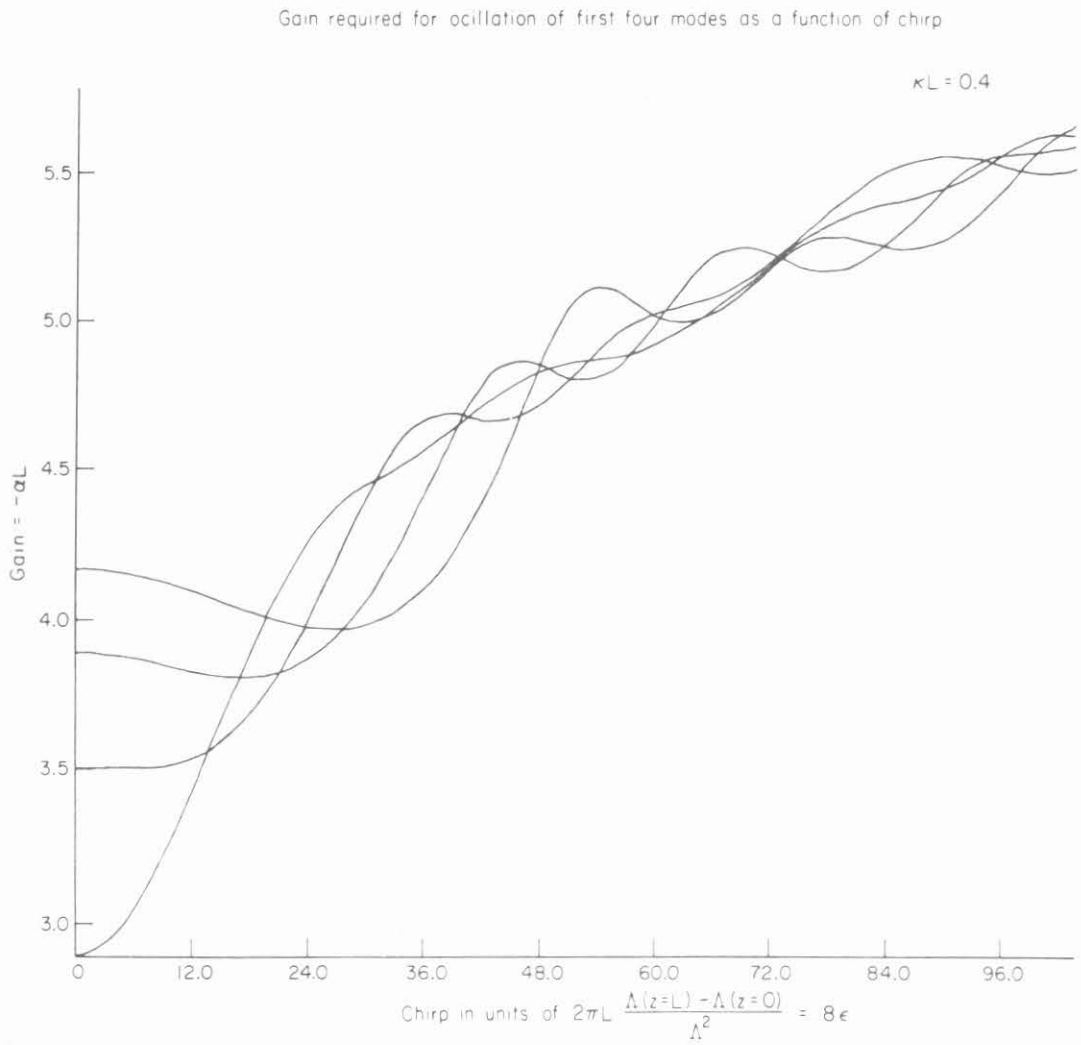

Fig. 5.7 Gain required for oscillation as a function of chirp for $\kappa L = 0.4$

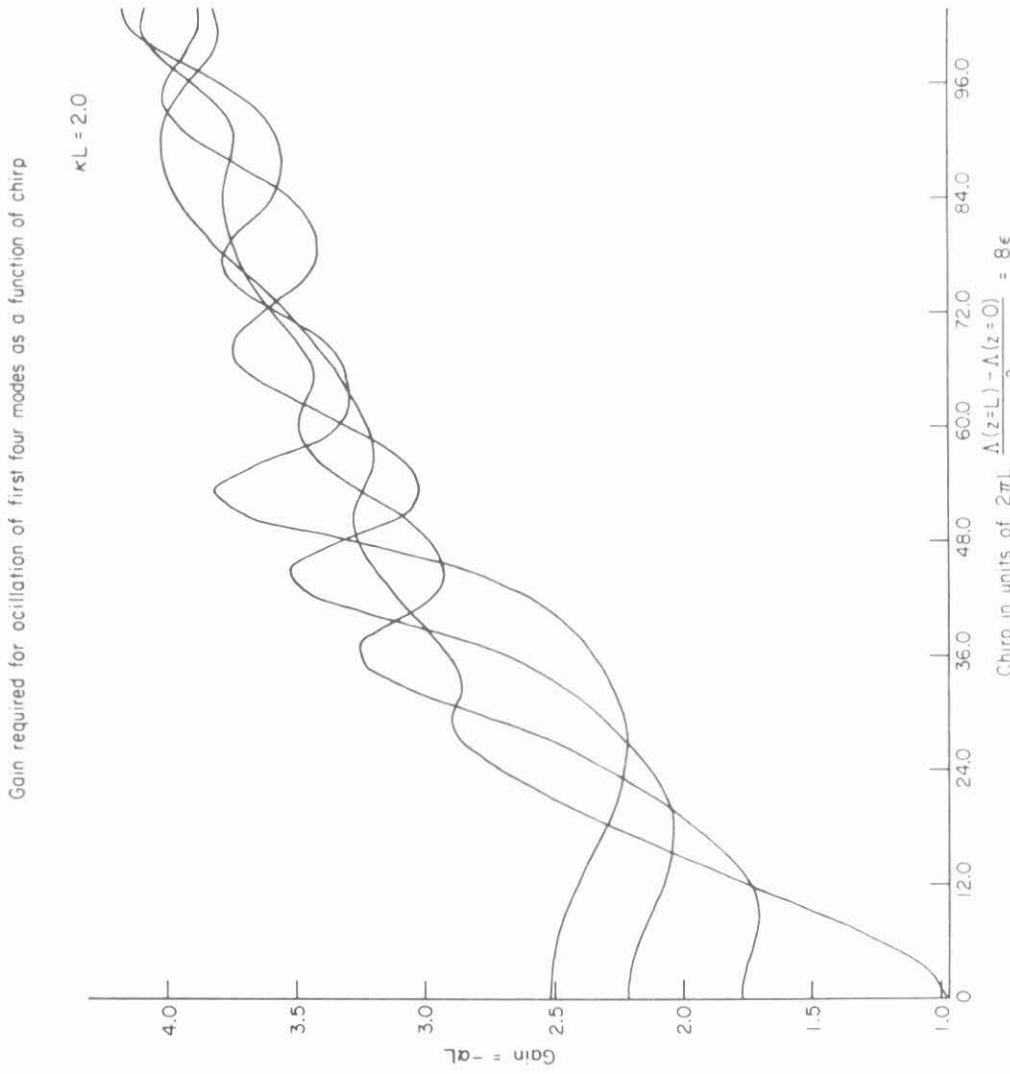

Fig. 5.8 Gain required for oscillation as a function of chirp for κL = 2.0

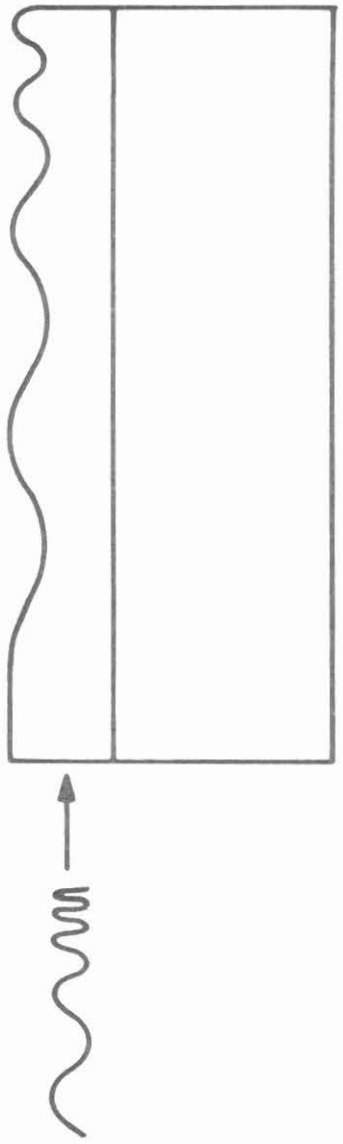

Fig. 5.9 Chirped pulse incident on a chirped grating

reflected from the closer left side of the reflector. A narrow pulse which has been broadened after traveling through a long dispersive single mode fiber may be partially compressed again by this device.

Figure 5.10 is reproduced from Kock's article.[7] A short pulse of light has been directed at the entire zone plate and upon diffraction is focused to a point. Some parts of the incident pulse must travel a greater distance before returning to the point of focus, and thus the short incident pulse is broadened (Fig. 5.10b). This process can also be reversed (Fig. 5.10c); a rapidly rotating plane mirror (marked horn in the figure) first illuminates the more off-axis (more distant) portions of the zone plate; later, through its rotational motion, it illuminates the nearer portions. Since all areas reflect the single-frequency waves back toward the focal point, all parts of the long reflected pulse can be made to arrive at this focal area at approximately the same time by making the rotational motion of the mirror match the travel times of the various portions of the outgoing pulse. A similar effect can be achieved with a uniform grating, but in that case a chirped light signal must be used, rather than a "single frequency" pulse.

5.5 Use of Aperiodic Dielectric Mirrors to Reduce the Electric Field Intensity

High electric fields within dielectric mirrors reflecting intense pulsed laser radiation can damage the mirror.[8] This damage is a result of absorption and the consequent heating of the dielectric layer; the exact mechanism is not understood at this time. Several theories have been proposed, including damage resulting from thermal induced stress

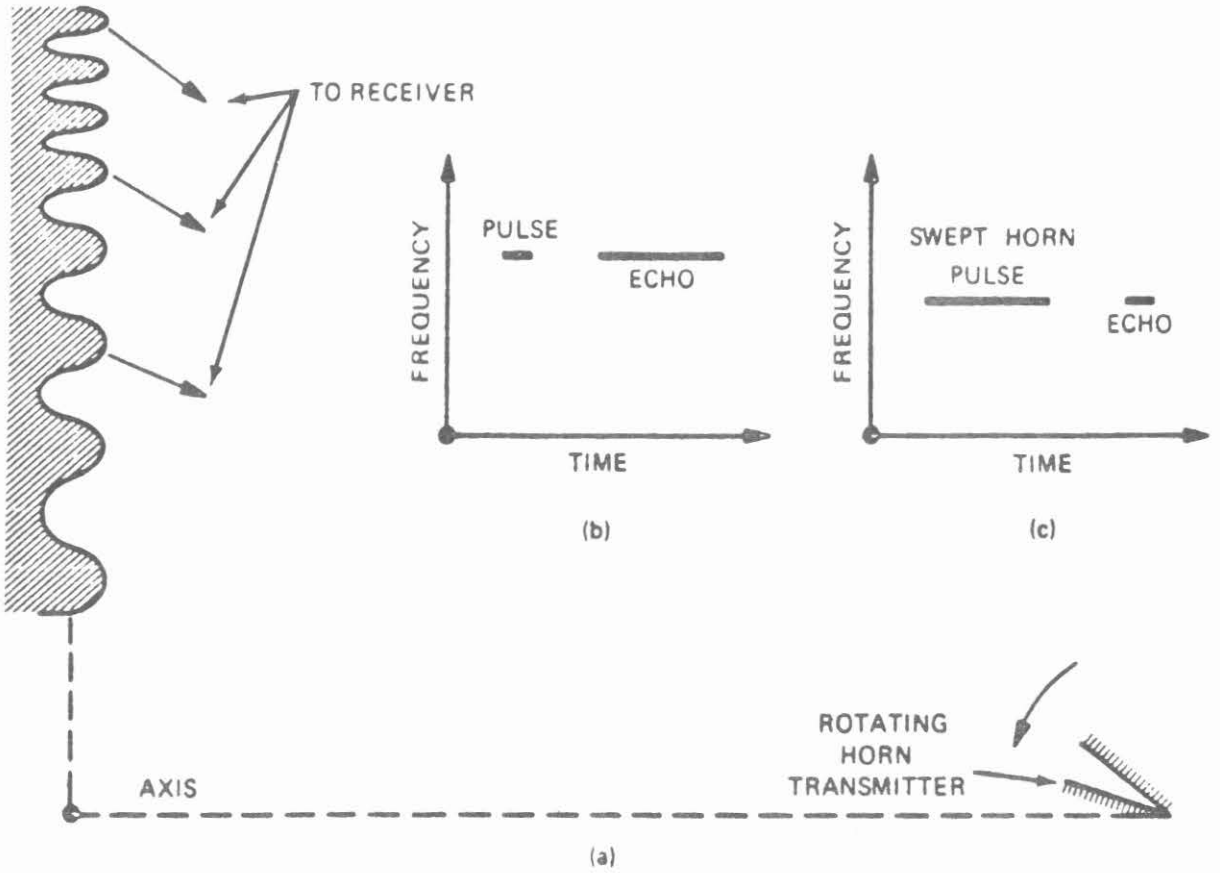

Fig. 5.10 (a) All portions of a grating having a zone plate outline direct reflected single-frequency waves toward its focal area. (b) More distant reflections return later, resulting in a stretched echo. (c) If, however, the areas are illuminated at different times by a rotating horn pulse, pulse compression results. (After reference 7.)

within the film[9] and the heating of the material to the point of melting.[10]

Typically, the damage occurs in only one of the two dielectric materials being used in the mirror. Thus if a method can be found to suppress the peak or maximum value of the electric field intensity within the critical layer, the resistance to laser damage will be increased. Apfel[11] has suggested coating a conventional quarter-wave stack with additional layers of varying thickness, and he has described a method of design so as to minimize the light intensity inside the easily damaged dielectric material (at the expense of the stronger material). In Figure 5.11 the intensity distribution within a conventional quarter-wave stack is shown; it consists of layers of index n_2 and n_1. We assume that the layer with the intensity profile shaded is the easily damaged layer (of index n_2) which must be protected. This is done by adding two additional layers to the stack. The first added layer of index n_1 is slightly thicker than the quarter-wave thickness, while the second added layer of index n_2 is slightly thinner than a quarter-wave thickness. The modified structure with resulting intensity distribution is shown in Figure 5.12.[11] It is evident that the maximum field has been reduced in the critical layer of index n_2. The constraints which Apfel places on the two added layers in order to calculate their thicknesses are that the reflectance of the total multilayer is a maximum and that the peak field intensity within the added n_2 layer equals the peak field in the next high index layer. This second condition is evident in Figure 5.12, where it is seen that the heights of the

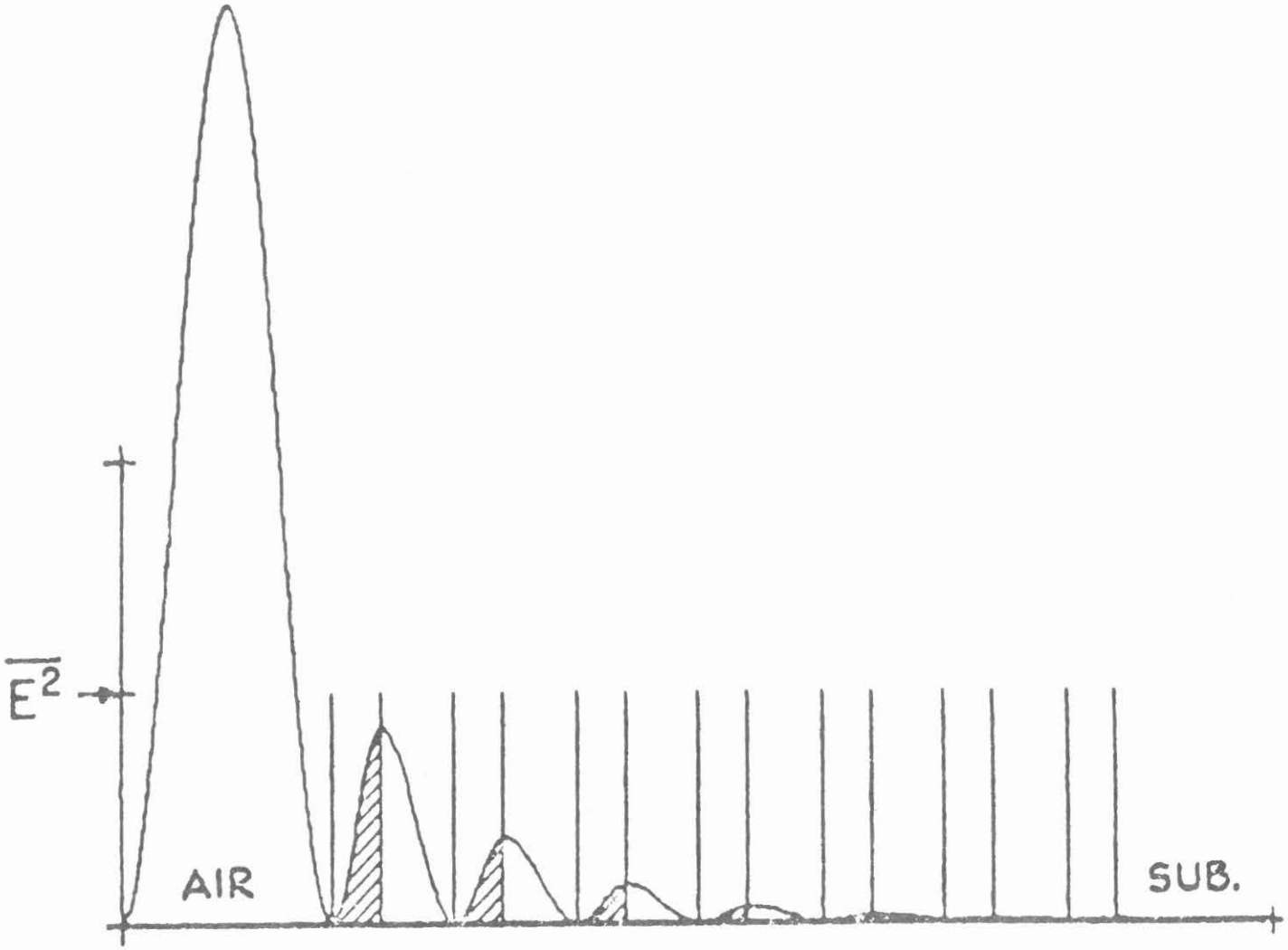

Fig. 5.11 Intensity distribution inside a quarter-wave stack dielectric mirror.

(After reference 11.)

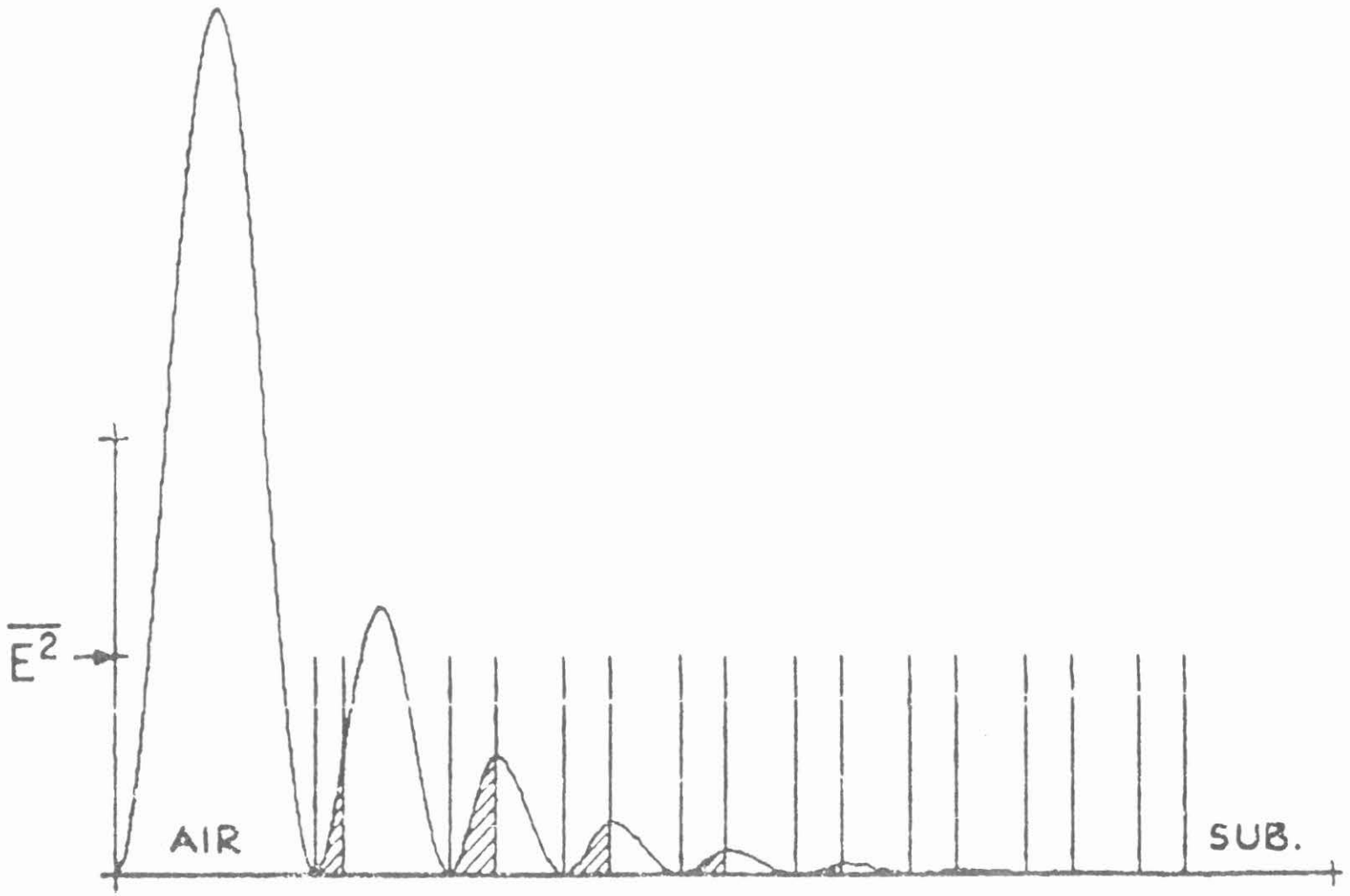

Fig. 5.12 Intensity distribution inside a quarter-wave stack dielectric mirror with two additional layers on the surface. (After reference 11.)

first two shaded regions are identical. For even greater field reduction, additional layers may be added.

5.6 Conclusion

In this chapter additional properties of aperiodic structures were covered. The possibility of using tapered gratings to suppress the side lobes of the reflectivity spectrum in broad-band filters was discussed. Next, in order to study effects of varying the thickness of the active layer in DFB lasers, a perturbation solution to the coupled mode equations was presented. It was found that the gain condition was altered more in some modes than others.

The possibility of coating a quarter-wave reflector with additional layers of varying thicknesses for the purpose of reducing field intensity in the reflector was reviewed. The process may be very useful for mirrors designed to operate with intense laser pulses.

CHAPTER 5 REFERENCES

1. H. Kogelnik, The Bell Syst. Tech. Jour. 55, 109 (1976).
2. M. Matsuhara and K. O. Hill, Appl. Opt. 13, 2886 (1974).
3. I. Solc, J. Opt. Soc. Am. 55, 621 (1965).
4. W. Streifer, D. R. Scifres, and R. D. Burnham, J. Opt. Soc. Am. 66, 1359 (1976).
5. A. Yariv, Quantum Electronics, 2nd Ed. (John Wiley and Sons, Inc., New York, 1975).
6. R. V. Schmidt, D. C. Flanders, C. V. Shank, and R. D. Standley, Appl. Phys. Lett. 25, 651 (1974).
7. W. E. Kock, Proc. IEEE (Lett.) 58, 153 (1970).
8. J. H. Apfel, J. S. Matteucci, B. E. Newnam, and D. H. Gill, The Role of Electric Field Strength in Laser Damage of Dielectric Multilayers (U.S. Government Printing Office, Washington, D.C., 1976), NBS Special Publication #462, p. 301.
9. A. L. Bloom and V. R. Costich, Design for High Power Resistance (U.S. Government Printing Office, Washington, D.C., 1976), NBS Special Publication #435, p. 248.
10. B. E. Newnam, Damage Resistance of Dielectric Reflectors for Picosecond Pulses (U.S. Government Printing Office, Washington, D.C., 1974), NBS Special Publication #414, p. 39.
11. J. H. Apfel, Appl. Opt. 16, 1800 (1977).

PART II

THE TRANSVERSE BRAGG REFLECTOR LASER

CHAPTER 1

INTRODUCTION

It was shown in Appendix 1-A that the guiding of light can occur in a guide whose index of refraction is larger than the surrounding material. Since the medium surrounding the guiding layer is of lower index, the electric field is evanescent in this region and the light is confined to the high index region. It is possible, however, to confine the light within a lower index region if the material adjacent to the low index region is a multilayered reflector medium.

In a conventional guide, the light is confined as a result of total internal reflection with the adjacent lower index material. In the Bragg structure, the light is reflected coherently from successive dielectric interfaces and thus the guiding layer can be of arbitrary index. This mechanism of guiding will be referred to as Bragg waveguiding.

In 1970, E. A. Ash[1] originally suggested the possibility of replacing the conventionally used low index substrate with a layered medium. Four years later A. J. Fox[2] presented a plane-wave theory for this device which he called the integrated optics grating guide. Fox analyzed the problem by finding a transfer matrix relating the field in one layer to that of the adjacent layer. Subsequent to this, Yariv, Yeh and Hong[3,4,5] analyzed in detail, by using a Bloch wave formulation, the problem of electromagnetic propagation in layered media. This general analysis included as a special case the propagation of light in a low index guiding region.

Recently this guiding has been demonstrated[6] in structures grown by Molecular Beam Epitaxy (MBE), a technique of crystal growth which allows

great flexibility and accuracy in the growth of layered media.[7] The successful demonstration of guiding in a passive structure immediately suggested the possibility of growing injection lasers either by MBE or LPE (Liquid Phase Epitaxy) which would contain a periodic layered medium adjacent to the active layer.

Although a thick active layer may support several transverse modes (normal to the junction plane), the Bragg reflector would not reflect, and thus confine, all of these modes to the same extent. Thus it is possible that the Transverse Bragg Reflector Laser (TBRL) would provide a means to discriminate against certain poorly confined and thus high loss modes. It should also be pointed out, that unlike the conventional high index guide, the TBRL structure makes it possible to guide light with arbitrarily low losses in a layer of air surrounded by Bragg reflectors.*

*Actually, lossy (leaky) guiding is possible in a low index (compared to surrounding material) guide, but the losses are usually quite high and the loss constant increases as the third power of the reciprocal thickness of the inner layer.

CHAPTER 1 REFERENCES

1. E. A. Ash, "Grating surface wave waveguides," presented at International Microwave Symp., Newport Beach, CA., May 1970.
2. A. J. Fox, Proc. IEEE 62, 644 (1974).
3. P. Yeh, "Optical Waves in Layered Media," Caltech Ph.D. Thesis (1978).
4. P. Yeh and A. Yariv, Opt. Comm. 19, 427 (1976).
5. P. Yeh, A. Yariv and C. H. Hong, J. Opt. Soc. Amer. 67, 423 (1977).
6. A. Y. Cho, A. Yariv and P. Yeh, Appl. Phys. Lett. 30, 471 (1977).
7. A. Y. Cho and J. R. Arthur, Progress in Solid State Chemistry, Vol. 10, Part 3, pp. 157-191 (Pergamon Press, 1975).

Chapter 2

THEORY OF BRAGG WAVEGUIDES

2.1 Introduction

In this chapter design considerations and the loss constant of a transverse Bragg reflector laser are studied. The condition for maximum confinement of light inside the active region is used in order to minimize radiation losses into the substrate; thus a quarter wave stack is used as the reflector region. The substrate losses are then determined in order to find an expression for the imaginary component of the index of refraction of the active region required for steady state conditions. Finally the loss constant α is calculated.

2.2 Design of Structure

The use of periodic structures in injection lasers is not new. Distributed feedback (DFB)[1,2,3] and distributed Bragg reflector (DBR)[4] structures have been used to provide feedback and longitudinal mode selectivity since the work of Kogelnik and co-workers in 1971.[5,6] A grating is used to provide the feedback, rather than reflection from the cleaved ends of a Fabry-Perot cavity. The use of a periodic structure perpendicular to the junction plane to provide confinement and mode selectivity (transverse) is new.

Figures 2.1 and 2.2 show a typical Bragg waveguide and field distribution for the case $n_g < n_1$. The case of a symmetric Bragg waveguide structure is depicted in Figure 2.3. Figure 2.4 indicates how the field structure changes for the case $n_g > n_1$. It has been shown[7] that, for maximum confinement of light, the electric field or the rate of change of

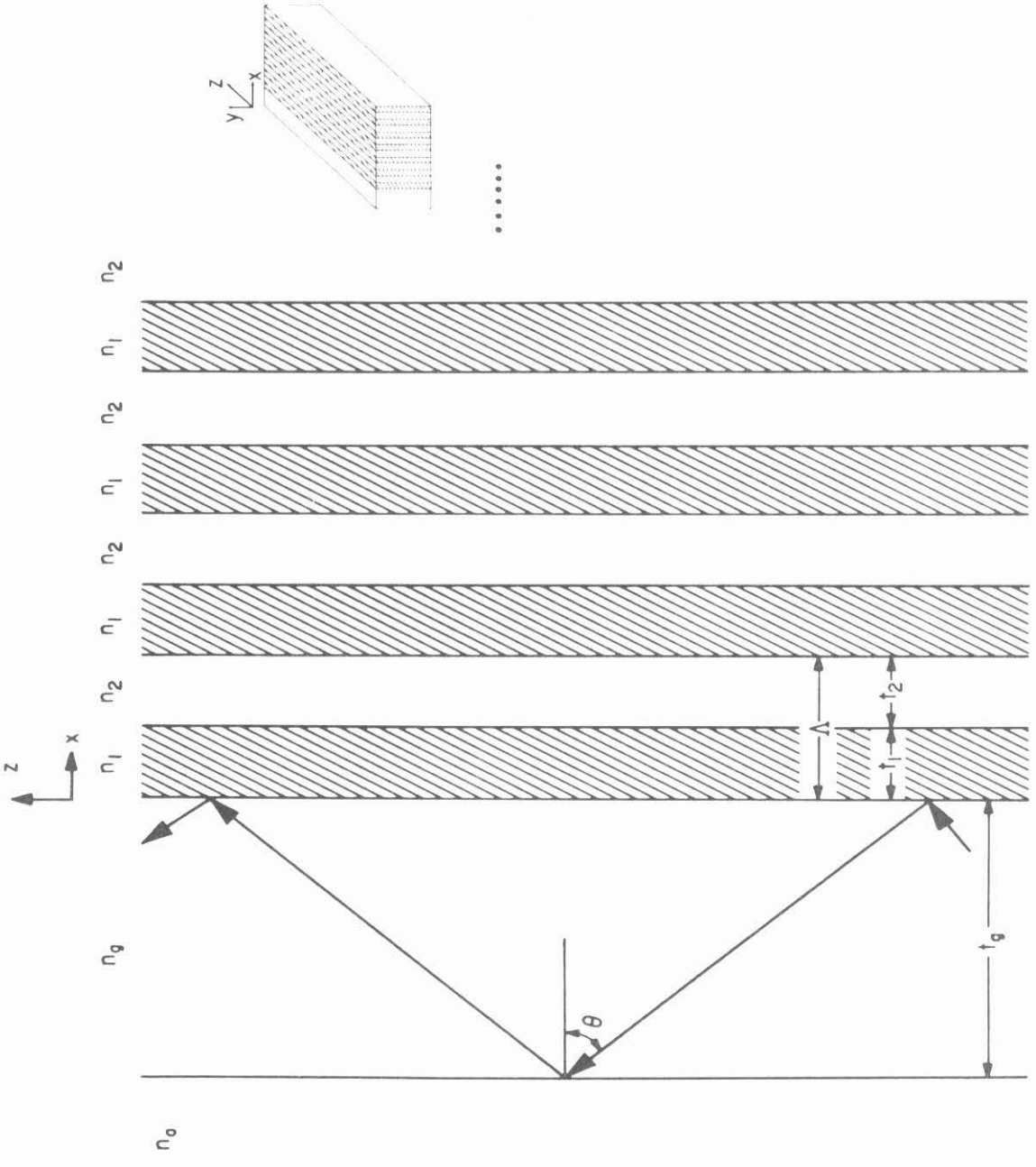

Fig. 2.1 A Bragg reflection (slab) waveguide ($\partial/\partial y = 0$). (After reference 7.)

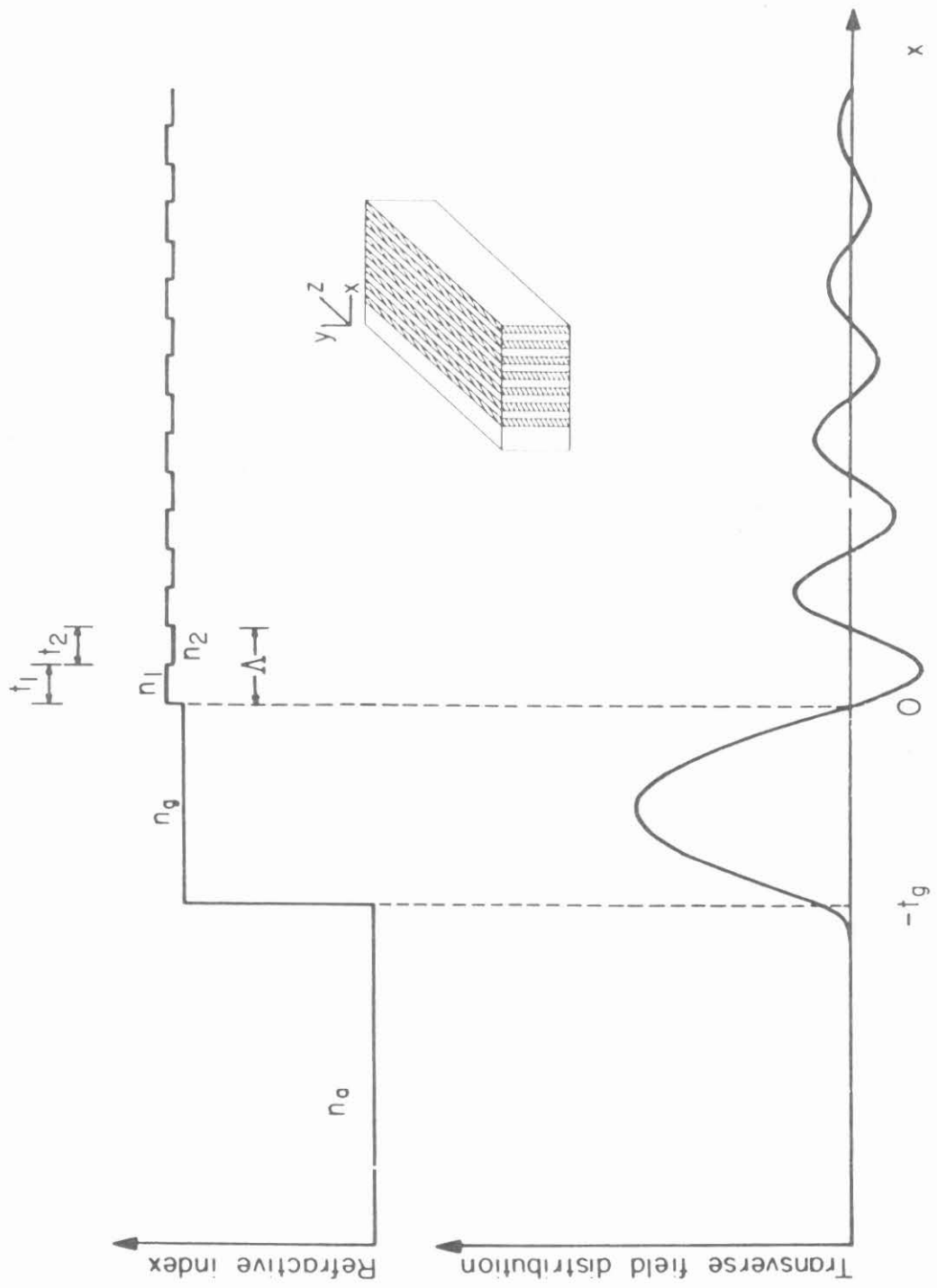

Fig. 2.2 Transverse field distribution of the fundamental modes of a typical Bragg reflection (slab) waveguide for the case $n_g < n_1$. (After reference 7.)

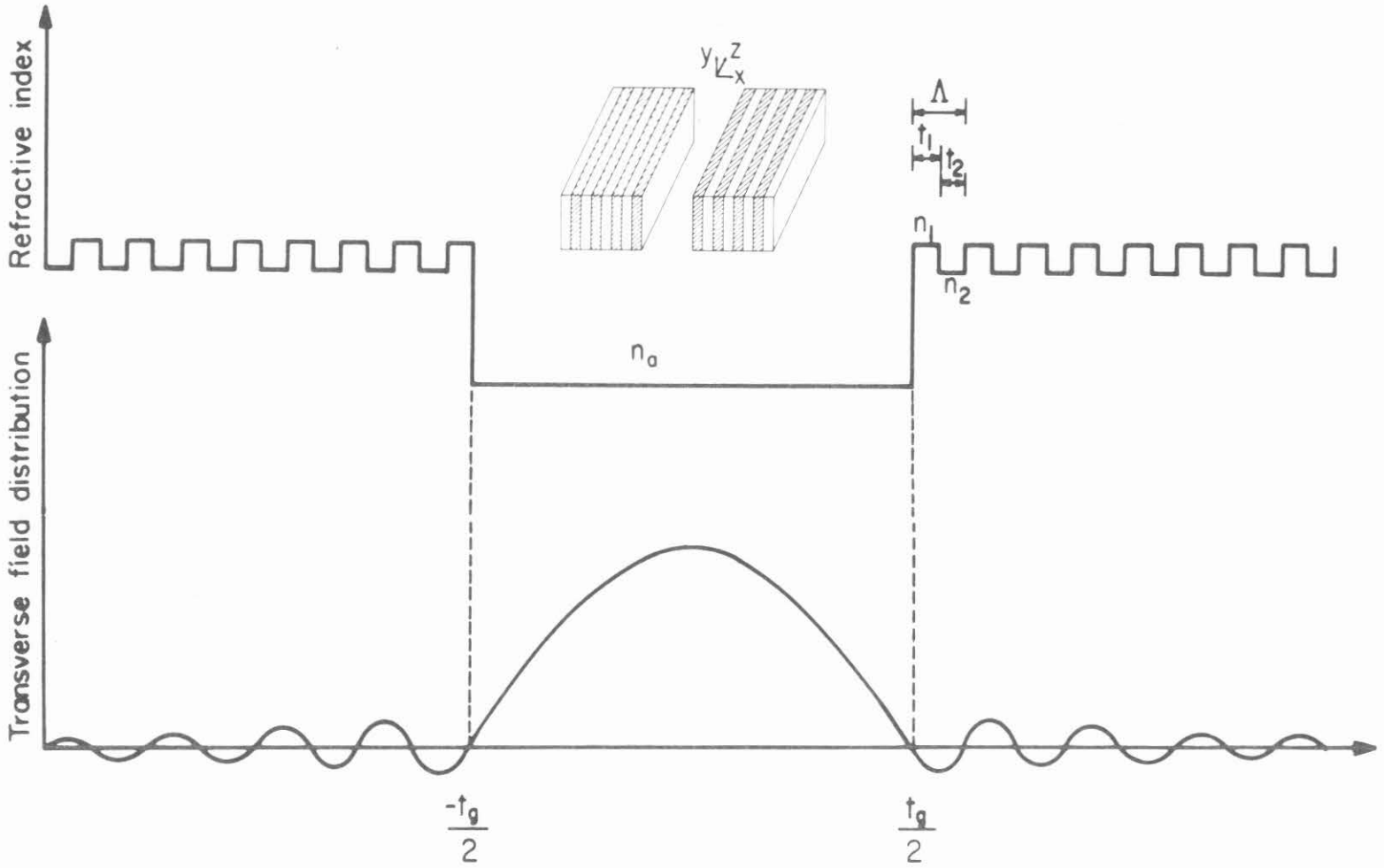

Fig. 2.3 Transverse field distribution of the fundamental mode of a typical Bragg reflection waveguide with air as the guiding channel. (After reference 7.)

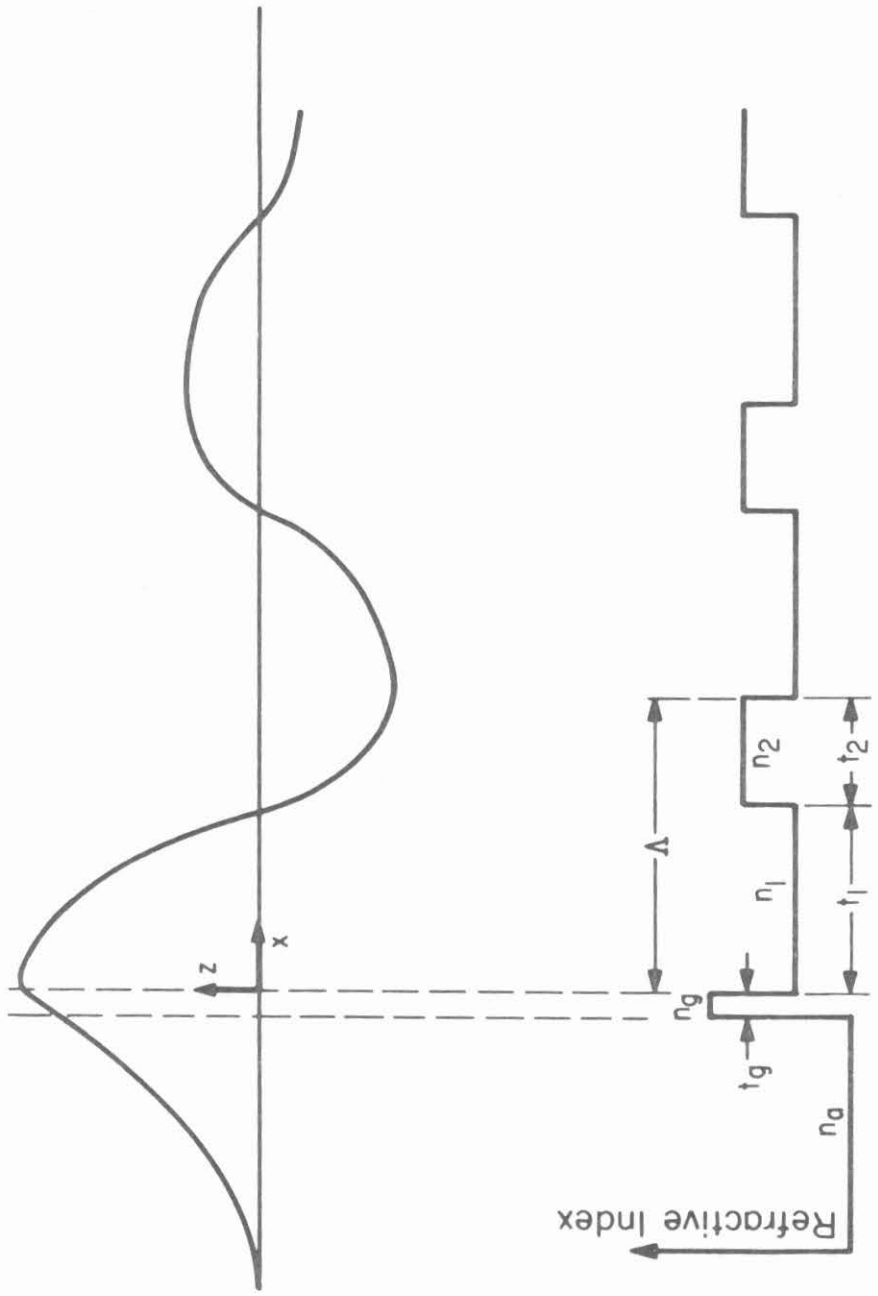

Fig. 2.4 Field Distribution of Transverse Bragg Reflector Laser

the electric field with respect to the x direction must be zero. Referring to Figure 2.5, the conditions for maximum reflection on radiation traveling toward the right are:

$$E_y(x = \text{interface, type A}) = 0 \qquad \text{high index on right}$$

$$\frac{\partial E_y(x = \text{interface, type B})}{\partial x} = 0 \qquad \text{high index on left}$$

Using these conditions and referring to Figure 2.4 , we have for the case $n_g > n_1$

$$E_y(x) = \cos k_{gx}x \qquad -t_a < x < 0 \tag{2.1}$$

$$E_y(x) = A\, e^{k_{ax}x} \qquad -\infty < x < -t_a \tag{2.2}$$

$$k_{gx} = \frac{2\pi}{\lambda_o}\sqrt{n_g^2 - n_{eff}^2} \tag{2.3}$$

$$k_{ax} = \frac{2\pi}{\lambda_o}\sqrt{n_{eff}^2 - n_a^2} \tag{2.4}$$

$$\lambda_o = \frac{2\pi}{k_o} = \text{wavelength in vacuum}$$

We have suppressed the $e^{i\beta z}$ factor and for the moment will concentrate only on the field in the guide and cover (superstrate) regions. Matching the boundary conditions on E_y and $\frac{\partial E_y}{\partial x}$ at $x = -t_g$, we arrive at the following eigenvalue equation

$$\tan(k_{gx}t_g) = \frac{k_{ax}}{k_{gx}} \tag{2.5}$$

If we assume that n_g, n_a and λ_o have been specified, then the easiest way to design an optimum structure is to choose an arbitrary n_{eff},

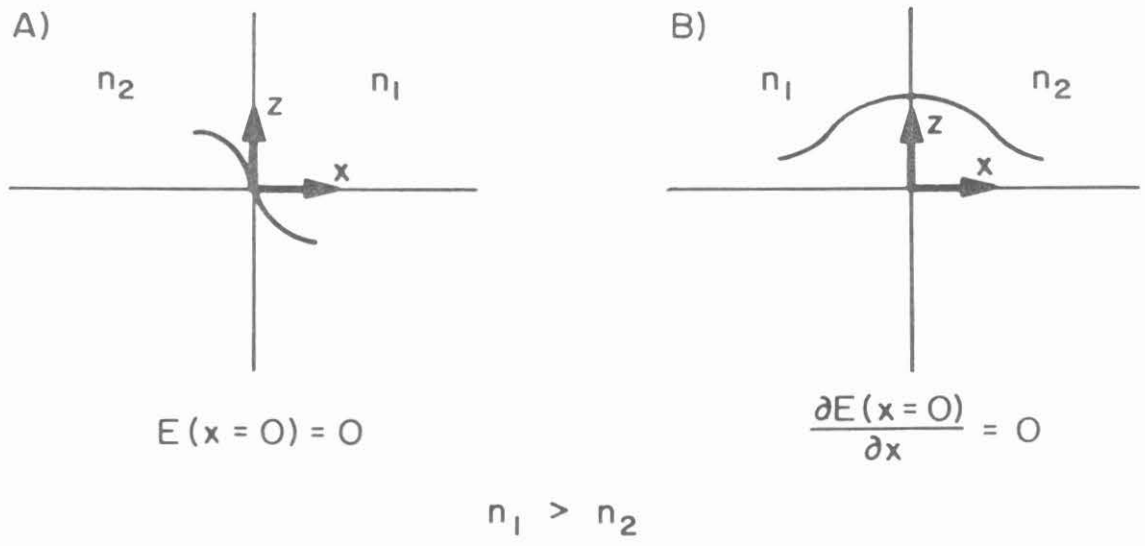

Fig. 2.5 The field condition at dielectric interfaces for maximum confinement. (Field incident from left.)

$n_a < n_{eff} < n_g$, and use equation (2.5) to solve for t_g. Next we must solve for the thicknesses of the layers t_1 and t_2 in the reflector region. It is well known that maximum reflectivity is obtained with a quarter-wave stack, and now that the dynamical variable n_{eff} has been chosen, it is a simple matter to calculate t_1 and t_2

$$t_i = \frac{\pi}{2k_{ix}} \qquad i = 1,2 \tag{2.6}$$

$$k_{ix} = \frac{2\pi}{\lambda_o} \sqrt{n_i^2 - n_{eff}^2} \tag{2.7}$$

Note that eigenvalue equation (2.5) is the result of considering the case $n_g > n_1$. For the case $n_g < n_1$ we must have

$$E_y(x) = \sin k_{gx}x \qquad -t_g < x < 0 \tag{2.8}$$

$$E_y(x) = A\, e^{k_{ax}x} \qquad -\infty \propto x < -t_g \tag{2.9}$$

with resulting eigenvalue equation

$$\cot(k_{gx}t_g) = -\frac{k_{ax}}{k_{gx}} \tag{2.10}$$

The case where $n_g > n_1$ is of greater importance in the work to follow, since the lasers tested were of this design. The steps involved in designing the laser are summarized in Figure 2.6.

2.3 Calculation of the Loss Constant

As is evident from Figure 2.4, the electric field is not evanescent in the reflector region, but is oscillatory under an exponentially decaying envelope. For any real structure with a finite number of periods, some of the field will leak out into the substrate, and in order to

A.

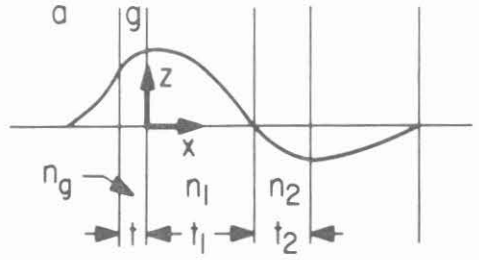

$n_g > n_2 > n_1$

B. Region g: $E = \cos k_{g_x} x$

(Since $\frac{\partial E}{\partial x} = 0$ for maximum reflection)

Region a: $E = Ae^{k_{a_x} x}$

$$k_{g_x} = \frac{2\pi}{\lambda_0} \sqrt{n_g^2 - n_{eff}^2}$$

$$k_{a_x} = \frac{2\pi}{\lambda_0} \sqrt{n_{eff}^2 - n_a^2}$$

C. Match Boundary Conditions at $x = -t$

$$\tan(k_{g_x} t) = \frac{k_{a_x}}{k_{g_x}}$$

D. 1) Choose an arbitrary $n_a < n_{eff} < n_g$

2) Find a t value to satisfy C

3) Find t_1 and t_2 from requirement

$$k_{i_x} t_i = \frac{\pi}{2} \quad i = 1, 2$$

$$k_{i_x} = \frac{2\pi}{\lambda_0} \sqrt{n_i^2 - n_{eff}^2}$$

Fig. 2.6 Design of Laser Structure for Maximum Confinement of Light

satisfy a steady state condition, it is required that enough gain be produced to compensate for these substrate losses. In other words, the index of refraction of the guiding layer must be complex in order to compensate for the substrate losses.

We start with the wave equation and the usual assumed form of the solution for coupled mode calculations:

$$\nabla^2 E_y + (k_o^2 n^2 + k_o^2 \, \delta n'^2) E_y = 0 \tag{2.11}$$

$$E_y = R(x) \, e^{i(\kappa/2)x} \, e^{i\beta z} + S(x) \, e^{-i(\kappa/2)x} \, e^{i\beta z} \tag{2.12}$$

where

ω = radian frequency of light

c = velocity of light in vacuum

$$k_o = \frac{\omega}{c}$$

$$n^2 = \frac{n_1^2 + n_2^2}{2}$$

Λ = period of reflector

$\kappa = 2\pi/\Lambda$

$\delta n'^2$ = index variation = $-(\delta n^2) \sin(\kappa x)$ $\quad (n_g > n_1)$

$R(x)$ = amplitude of incident field (field traveling toward the right)

$S(x)$ = amplitude of reflected field

Note the importance of the proper sign and phase of $\delta n'^2$. $\delta n'^2 = +\delta n^2 \sin \kappa x$ would be the proper choice only if $n_g < n_1$, and in neither case would $\delta n^2 \cos \kappa x$ be correct with a coordinate system chosen for which $x = 0$ is the guide-reflector interface.

If we combine (2.11) and (2.12), make the usual coupled mode approximations (ignore R"(x) and S"(x)) and collect "coherent terms", we find

$$R' - i\delta R = -\eta S \tag{2.13}$$

$$S' + i\delta S = -\eta R \tag{2.14}$$

with

$$\delta = \frac{1}{\kappa}\left(k_o^2\, n^2 - \beta^2 - \frac{\kappa^2}{4}\right) \tag{2.15}$$

$$\eta = \left|\frac{k_{1x} - k_{2x}}{k_{1x} + k_{2x}}\right| \frac{2}{\Lambda} \tag{2.16}$$

L = length of reflector region = $N\Lambda$

N = number of periods

The solutions to (2.13) and (2.14) are

$$S(x) = \sinh\left[\sqrt{\eta^2 - \delta^2}\ (x - L)\right] \tag{2.17}$$

$$R(x) = -\frac{i\delta}{\eta} \sinh\left[\sqrt{\eta^2 - \delta^2}\ (x - L)\right] - \frac{\sqrt{\eta^2 - \delta^2}}{\eta} \cosh\left[\sqrt{\eta^2 - \delta^2}\ (x - L)\right] \tag{2.18}$$

These solutions are valid for $x > 0$. The solution at $x = 0$ is

$$E_y(x = 0) = S_o\, e^{i\beta z} + R_o\, e^{+i\beta z} \tag{2.19}$$

$S_o \equiv S(0)$

$R_o = R(0)$

The solutions in region g (guide) and region a (cover region) are, respectively,

$$E_y(x,z) = \left(S_o\, e^{-ik_{gx}x} + R_o\, e^{+ik_{gx}x}\right) e^{i\beta z},\quad -t_g < x < 0 \tag{2.20}$$

$$E_y(x,z) = (S_o\, e^{ik_{gx}t_g} + R_o\, e^{-ik_{gx}t_g})\, e^{k_{ax}(x+t_g)}\, e^{i\beta z} \qquad (2.21)$$

$$-\infty < x < -t_g$$

After matching $\partial E/\partial x$ at $x = -t_g$, we find

$$\frac{ik_{gx}}{k_{ax}} = \frac{(S_o/R_o)\, e^{2ik_{gx}t_g} + 1}{1 - (S_o/R_o)\, e^{2ik_{gx}t}} \qquad (2.22)$$

where from equations (2.17) and (2.17)

$$\frac{S_o}{R_o} = \frac{\sinh(\sqrt{\eta^2 - \delta^2}\, L)}{\frac{\sqrt{\eta^2 - \delta^2}}{\eta}\cosh(\sqrt{\eta^2-\delta^2}\, L) - \frac{i\delta}{\eta}\sinh(\sqrt{\eta^2 - \delta^2}\, L)} \qquad (2.23)$$

$$\equiv 1 - \varepsilon \qquad (2.24)$$

For most cases of practical interest the reflection from the multilayered medium is quite high and thus $\varepsilon << 1$. For $\varepsilon = 0$, n_g is pure real, and to first order in ε we may take

$$k_{gx} = k_{gr} + is\varepsilon \qquad (2.25)$$

where k_{gr} is a real number and s is to be determined. Combining equations (2.22), (2.24) and (2.25) and equating parts of similar order in ε we find

$$\underline{0^{th}\ \text{order}} \qquad \tan(k_{gr}t_g) = \frac{k_{ax}}{k_{gr}} \simeq \tan(k_{gx}t_g) \qquad (2.26)$$

This is just the eigenvalue equation given by equation (2.5).

Next we equate terms of order ε and arrive at

$$\underline{1^{st}\ \text{order}} \qquad s = \frac{-1}{2\sin^2(k_{gr}t_g)\left(\frac{1}{k_{ax}} + \frac{t_g}{\sin^2 k_{gr}t}\right)} \tag{2.27}$$

$$= \frac{-1}{2t_g + \frac{2k_{ax}}{(k_{gr}^2 + k_{ax}^2)}} \tag{2.28}$$

Equation (2.26) was used in arriving at (2.28) from (2.27). Referring to equation (2.24)

$$1 - \varepsilon \simeq \frac{1}{1+\varepsilon} \simeq \frac{\sinh\left(\sqrt{\eta^2 - \delta^2}\, L\right)}{\frac{\sqrt{\eta^2 - \delta^2}}{\eta}\cosh\left(\sqrt{\eta^2 - \delta^2}\, L\right) - \frac{i\delta}{\eta}\sinh\left(\sqrt{\eta^2 - \delta^2}\, L\right.}$$

$$\varepsilon \simeq \frac{\sqrt{\eta^2 - \delta^2}}{\eta}\coth\left(\sqrt{\eta^2 - \delta^2}\, L\right) - 1\Big] - \frac{i\delta}{\eta} \tag{2.29}$$

Thus after combining (2.25), (2.28) and (2.29), we have

$$k_{gx} \quad k'_{gr} + ik_{gi}$$

$$k'_{gr} = k_{gr} - \frac{\delta/\eta}{2\left[t_g + \frac{k_a}{k_{gr}^2 + k_a^2}\right]} \tag{2.30}$$

$$k_{gi} = \frac{-\left[\frac{\sqrt{\eta^2 - \delta^2}}{\eta}\coth\left(\sqrt{\eta^2 - \delta^2}\, L\right) - 1\right]}{2\left[t_g + \frac{k_{ax}}{k_{gr}^2 + k_{ax}^2}\right]} \tag{2.31}$$

with $\tan(k_{gr}t_g) = k_{ax}/k_{gr}$.

Since $k_{gx}^2 = n_g^2 k_o^2 - \beta^2$, it is easy to show that in order to oscillate, the index of the guide must be complex and

$$n_{gi} = \frac{k_{gr}}{k_o^2 n_{gr}} k_{gi} < 0 \tag{2.32}$$

n_{gi} is the imaginary part of the index in the guide, $k_{gr} \simeq k_{gx}$ is determined by equation (2.26), $n_{gr} \simeq n_g$ is the real part of the index, and k_{gi} is given in equation (2.31).

If we examine (2.31) in the limit of high reflectivity (large ηL) and $\delta = 0$, we find

$$k_{gi} \simeq \frac{e^{-2\eta L}}{t_a + \frac{k_a}{k_{gr}^2 + k_{ax}^2}} \tag{2.33}$$

or

$$n_{gi} \simeq \frac{-k_{gr}}{k_o^2 n_{gr}} \quad \frac{e^{-2\eta L}}{t_g + \frac{k_{ax}}{k_{gr}^2 + k_a^2}} \tag{2.34}$$

In Figure 2.7 the imaginary part of the index of the active region is plotted for various conditions. The guide parameters were those of the laser which was tested, and are given in Figure 2.12 and equation (3.1).

Next we calculate the loss constant α which is defined by $\alpha = (dI/dz)/I$, where I is the light intensity. For the waveguide considered

$$\alpha = \frac{S_x(x = L)}{\int_{-\infty}^{L} S_z(x)\, dx} \tag{2.35}$$

where $\vec{S}$ = Poynting vector = $\frac{1}{2} \mathrm{Re}(\vec{E} \times \vec{H}^*)$. Physically, α is simply the

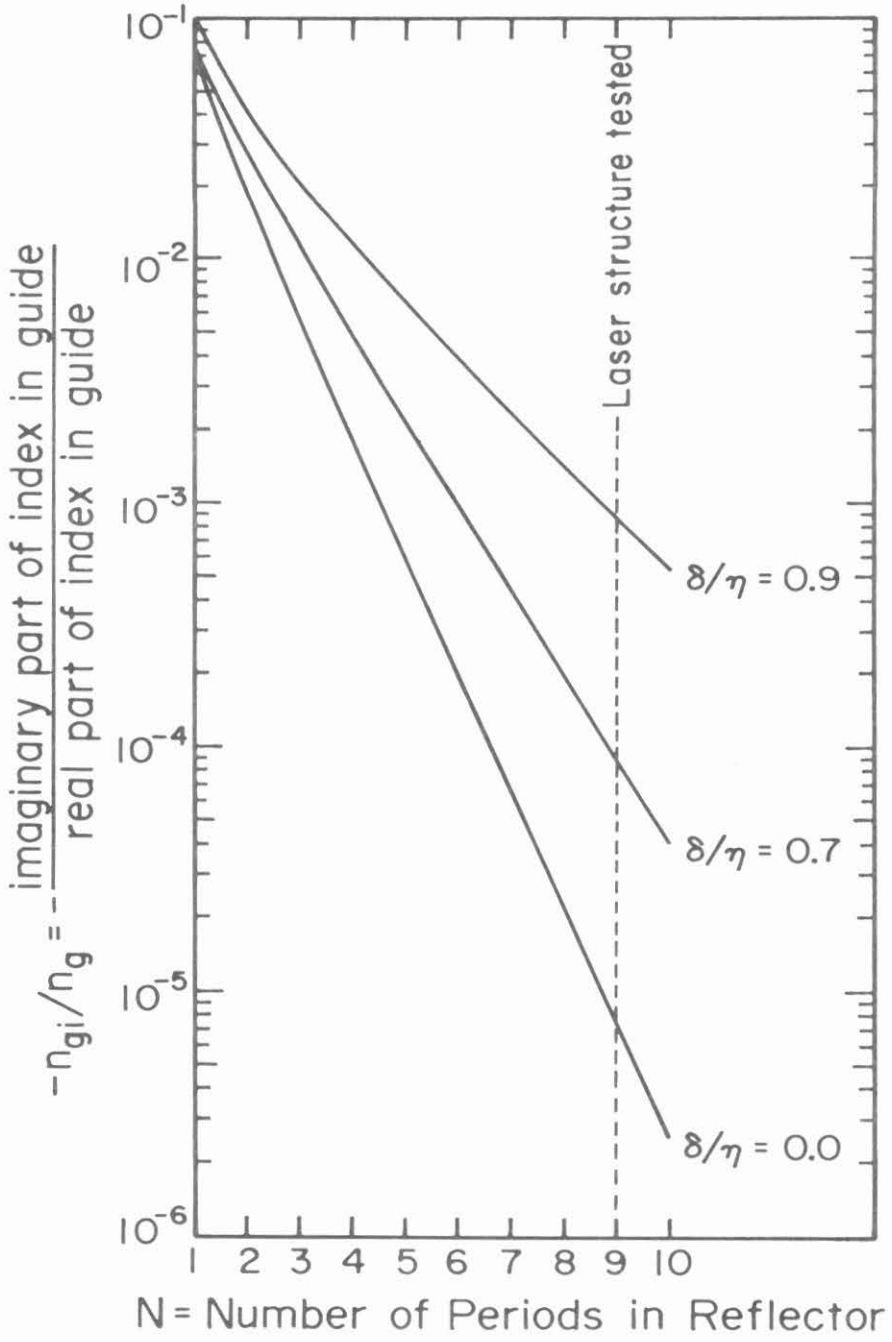

Fig. 2.7 Imaginary part of the index of the active region required for steady state condition as a function of the number of periods in the reflector layer

power loss into the substrate per unit length, divided by the total power flow in the z direction.

From the previous section we have

$$E_x = E_z = 0 \tag{2.36}$$

$$E_y(x,z) = R(x)\, e^{i(\kappa x)/2}\, e^{i\beta z} + S(x)\, e^{-i(\kappa x)/2}\, e^{i\beta z}\,, \qquad 0 < x < L \tag{2.37}$$

$$E_y(x,z) = (S_o\, e^{-ik_{gx}x} + R_o\, e^{ik_{gx}x})\, e^{i\beta z}\,, \quad -t_g < x < 0 \tag{2.38}$$

$$E_y(x,z) = (S_o\, e^{ik_{gx}t_g} + R_o\, e^{-ik_{gx}t_g})\, e^{k_{ax}(x+t_g)}\, e^{i\beta z}\,, \qquad -\infty < x < -t_g \tag{2.39}$$

$$H_x = \frac{+i}{\omega\mu}\frac{\partial}{\partial z} E_y = \frac{-\beta}{\omega\mu} E_y \tag{2.40}$$

$$H_z = \frac{-i}{\omega\mu}\frac{\partial}{\partial x} E_y \tag{2.41}$$

$$S_z = \frac{1}{2}\,\mathrm{Re}(E_y H_x^*) = \frac{-\beta}{2\omega\mu}\,|E_y|^2 \tag{2.42}$$

$$S_x = \frac{1}{2}\,\mathrm{Re}(E_y H_z^*) = \frac{1}{2\omega\mu}\,\mathrm{Im}(E_y \frac{\partial}{\partial x} E_y^*) \tag{2.43}$$

Using(2.36) through (2.43), it is straightforward to show

$$S_x(x=L) = \frac{(\eta^2-\delta^2)\kappa}{4\eta^2\,\omega\mu} \tag{2.44}$$

$$\int_0^L |E_y|^2\, dx = \frac{e^{2\sqrt{\eta^2-\delta^2}\,L}}{4}\left\{\frac{1}{\sqrt{\eta^2-\kappa^2}} + \frac{4(\eta^2-\delta^2) + 2\delta\kappa}{\eta[\kappa^2 + 4(\eta^2-\delta^2)]}\right\} \tag{2.45}$$

$$\int_{-t_g}^{0} |E_y|^2 \, dx = \frac{e^{2\sqrt{\eta^2-\delta^2}\,L}}{4} \left\{ 2t_g + \frac{2\sqrt{\eta^2-\delta^2}}{\eta} \frac{\sin(2k_{gx}t_g)}{2k_{gx}} - \frac{\delta}{\eta k_{gx}} + \frac{\delta \cos(2k_{gx}t_g)}{\eta\, k_{gx}} \right\} \tag{2.46}$$

$$\int_{-\infty}^{-t} |E_y|^2 \, dx = \frac{e^{2\sqrt{\eta^2-\delta^2}\,L}}{8k_{ax}} \left\{ 2 + \frac{2\sqrt{\eta^2-\delta^2}}{\eta} \cos(2k_{gx}t_g) - \frac{2\delta}{\eta} \sin(2k_{gx}t_g) \right\} \tag{2.47}$$

Finally, after combining (2.35), (2.44) through (2.47), and using the eigenvalue equation $\tan(k_{gx}t_g) = k_{ax}/k_{gx}$ to simplify the result, we arrive at the final result for the loss constant α

$$\alpha = [(1 - \frac{\delta^2}{\eta^2}) \frac{\kappa}{\beta} e^{-2\sqrt{\eta^2-\delta^2}\,L}] \div \left\{ t_g + \frac{2\eta - \frac{2\delta^2}{\eta} + \frac{\delta\kappa}{\eta}}{\kappa^2 + 4(\eta^2-\delta^2)} + \frac{1}{2} \left(\frac{1}{\sqrt{\eta^2-\delta^2}} + \frac{\sqrt{\eta^2-\delta^2}}{\eta k_{ax}} - \frac{2\delta}{\eta k_{gx}} + \frac{1}{k_{ax}} \right) \right\} \tag{2.48}$$

This result simplifies somewhat for the case $\delta = 0$,

$$\alpha_o = \frac{\kappa e^{-2\eta L}}{\beta\{t_g + \frac{2\eta}{\kappa^2 + 4\eta^2} + \frac{1}{2\eta} + \frac{1}{k_{ax}}\}} \qquad \text{for } \delta = 0 \, . \tag{2.49}$$

The key steps involved in calculating α are outlined in Figure 2.8, while in Figure 2.9 we have a plot of α as a function of the number of periods. Equation (2.49) was used for this plot and the device parameters are those of the actual laser tested, and are given in the

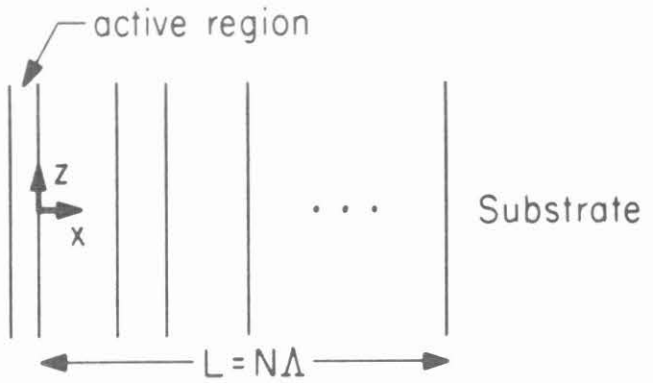

$$E_y = R(x)e^{i\frac{\kappa x}{2}}e^{i\beta z} + S(x)e^{-i\frac{\kappa x}{2}}e^{i\beta z} \qquad \kappa \equiv \frac{2\pi}{\Lambda}$$

1) Find $\beta = \frac{2\pi}{\lambda_0} n_{eff}$ from $\tan k_{g_x} t = \frac{k_{a_x}}{k_{g_x}}$

2) Use coupled mode equations to solve for R(x) and S(x) throughout structure

3) $\alpha = \dfrac{S_x(x=L)}{\int_{-\infty}^{L} S_z(x)dx}$ where $\vec{S}$ is the Poynting vector

Fig. 2.8 Calculation of α

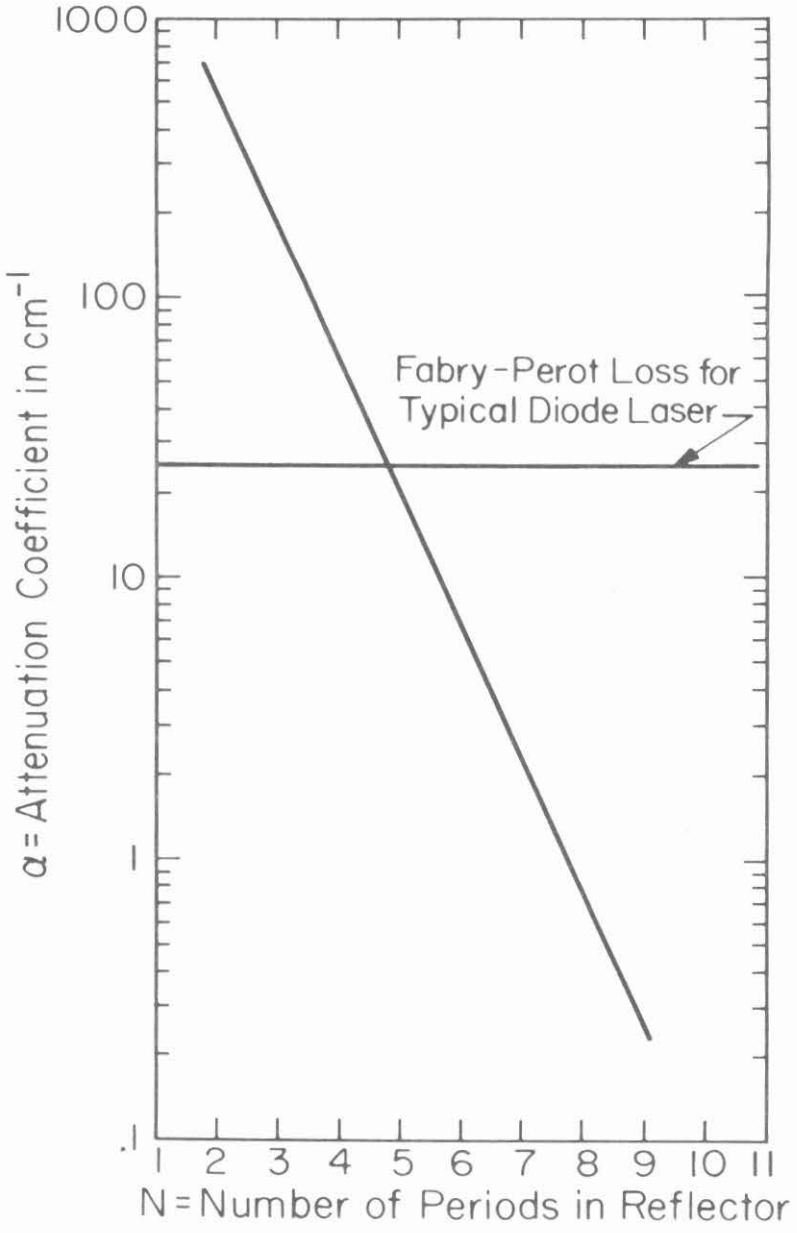

Fig. 2.9 Attenuation Coefficient, α, Due to Losses into Substrate Resulting from Finite Number of Periods

Fabrication and Testing section. Figure 2.10 is a comparison of the effects of other Al concentrations with that of the actual device for which the reflector layers were $Al_{.25}Ga_{.75}As$ and $Al_{.10}Ga_{.90}As$. All other parameters such as guide thickness and Al concentration in the superstrate are the same for the four curves.

It is well known that if k_{1x} and k_{2x} differ substantially, the coupled mode equations still give surprisingly accurate results, despite the fact that they were derived under the assumption $k_{1x} \sim k_{2x}$. Nevertheless, because of the large differences often encountered in k_{1x} and k_{2x}, a modification must be made in expression (2.15). Differentiating equation (2.15) we obtain

$$\Delta\delta = \frac{2\Delta k_o}{\kappa}\left[n^2 k_o - \beta \frac{\partial\beta}{\partial k_o}\right]$$

$$\delta \simeq \delta_o + \frac{2}{\kappa}\left[n^2 k_o - \beta \frac{\partial\beta}{\partial k_o}\right]\Delta k_o \qquad (2.50)$$

If we evaluate δ around the point $\delta = 0$ or, in other words, near the frequency for which $\delta = 0$, we have

$$\delta \simeq \frac{2}{\kappa}\left[n^2 k_o^{(0)} - \left(\beta \frac{\partial\beta}{\partial k_o}\right)_{k_o = k_o^{(0)}}\right]\Delta k_o$$

$$\Delta k_o = k_o - k_o^{(0)}$$

$k_o^{(0)} = k_o$ value for which $\delta = 0$

$\lambda_o^{(0)} = \lambda_o$ value for which $\delta = 0$.

Using the above equations, together with $\lambda_o^{(0)} = 8900\text{Å}$, and guide parameters as given in the section on laser fabrication, we find

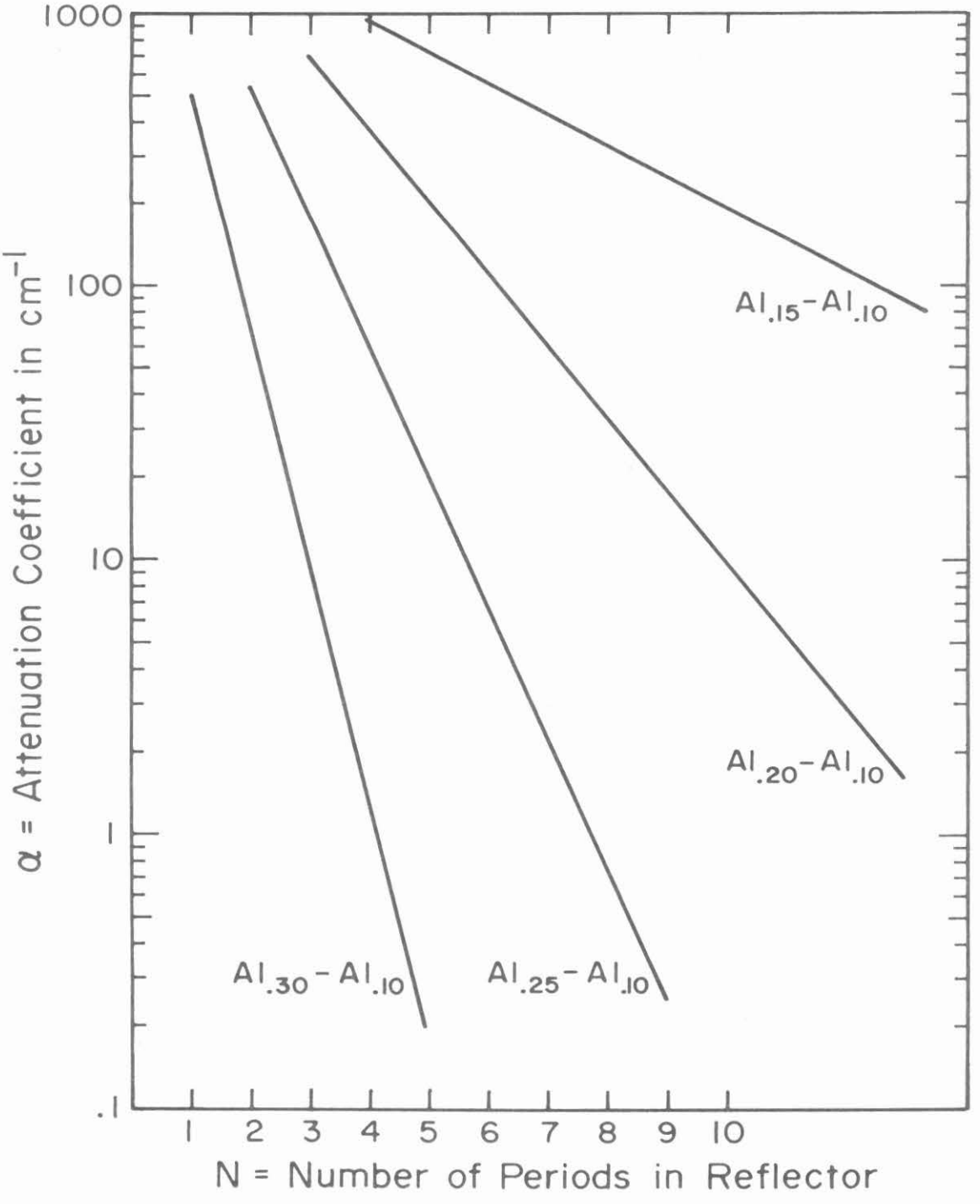

Fig. 2.10 Dependence of loss constant α on laser structure

$$\delta \simeq -693\ \Delta\lambda_o$$

where $\Delta\lambda_o$ is given in $\mathring{A}$.

It is easily verified that the major effect of δ occurs in the exponent of equation (2.48). We thus find

$$\alpha \simeq \alpha_o\ e^{+(\delta^2/\eta)L} \quad , \quad \delta << \eta$$

Figure 2.11 is a plot of the increase of the loss constant α as the lasing wavelength is varied about the central wavelength for which the structure provides maximum confinement. The structure drawn in Figure 2.12 does, in fact, represent the device which was later tested.

Of course the power flow into the substrate is exactly balanced by the power generated in the guide due to the complex index of refraction. This can be shown as follows:

Power generated by complex n_g per unit volume $= \frac{1}{2}\,\mathrm{Re}(\mathring{P}_y^* E_y)$

$$\simeq \varepsilon_o \omega\, n_{gr} n_{gi} |E_y|^2$$

where P_y = polarization $= \varepsilon_o(n_g^2 - 1)E_y$

$$n_g = n_{gr} + i n_{gi} \quad , \quad n_{gi} << n_{gr}$$

In order to find the power generated per unit length of active region, we must integrate along the width of the guide.

$$\text{Power generated/unit length of guide} = \varepsilon_o \omega\, n_{gr} n_{gi} \times \int_{-t_g}^{0} |E_y|^2\, dx = \frac{\varepsilon_o \omega\, n_{gr} n_{gi}}{2}\, e^{2\eta L} \left[t_g + \frac{\sin(2k_{gx} t_g)}{2k_{gx}}\right] \qquad (2.51)$$

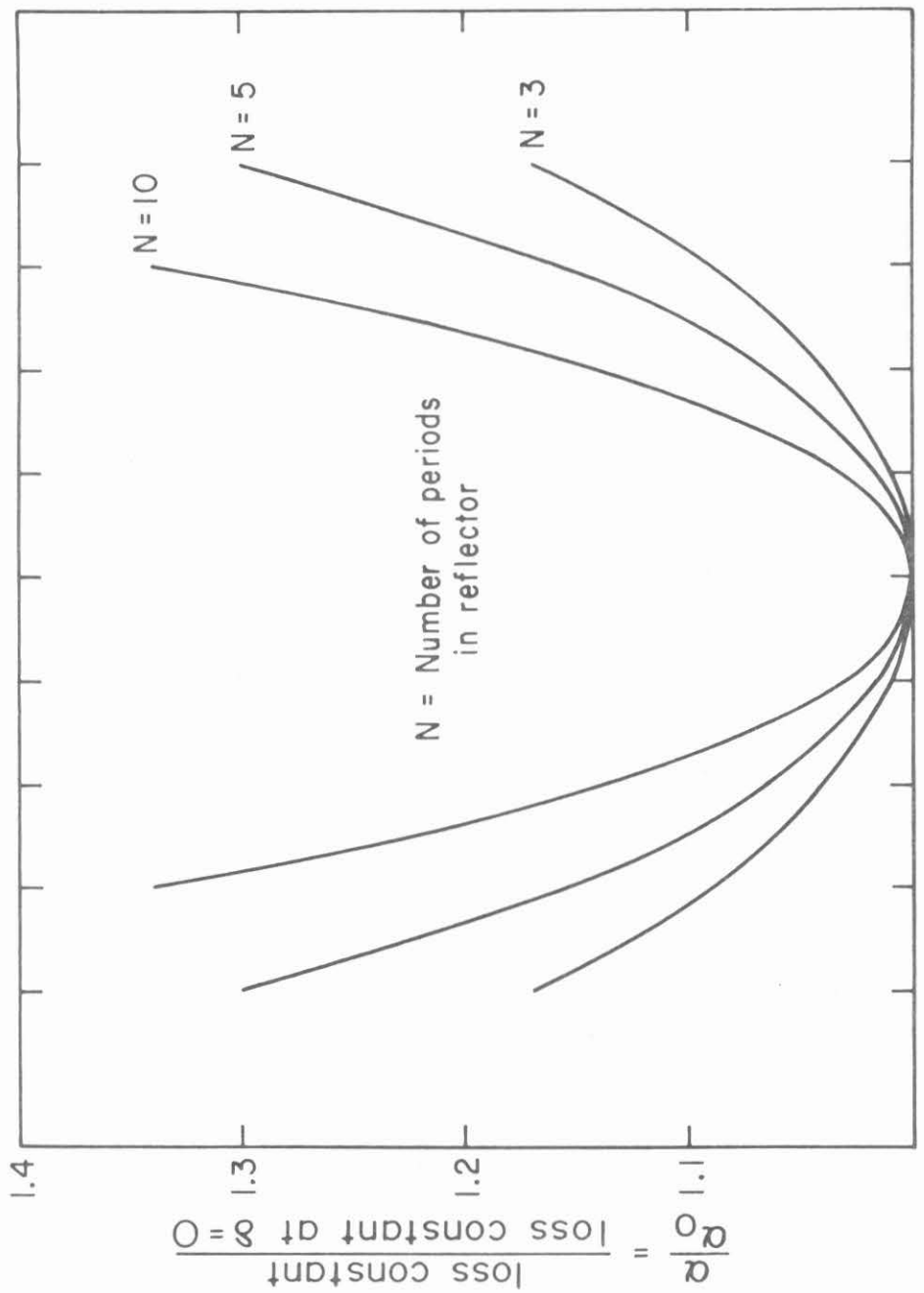

Fig. 2.11 Dependence of loss constant on lasing frequency

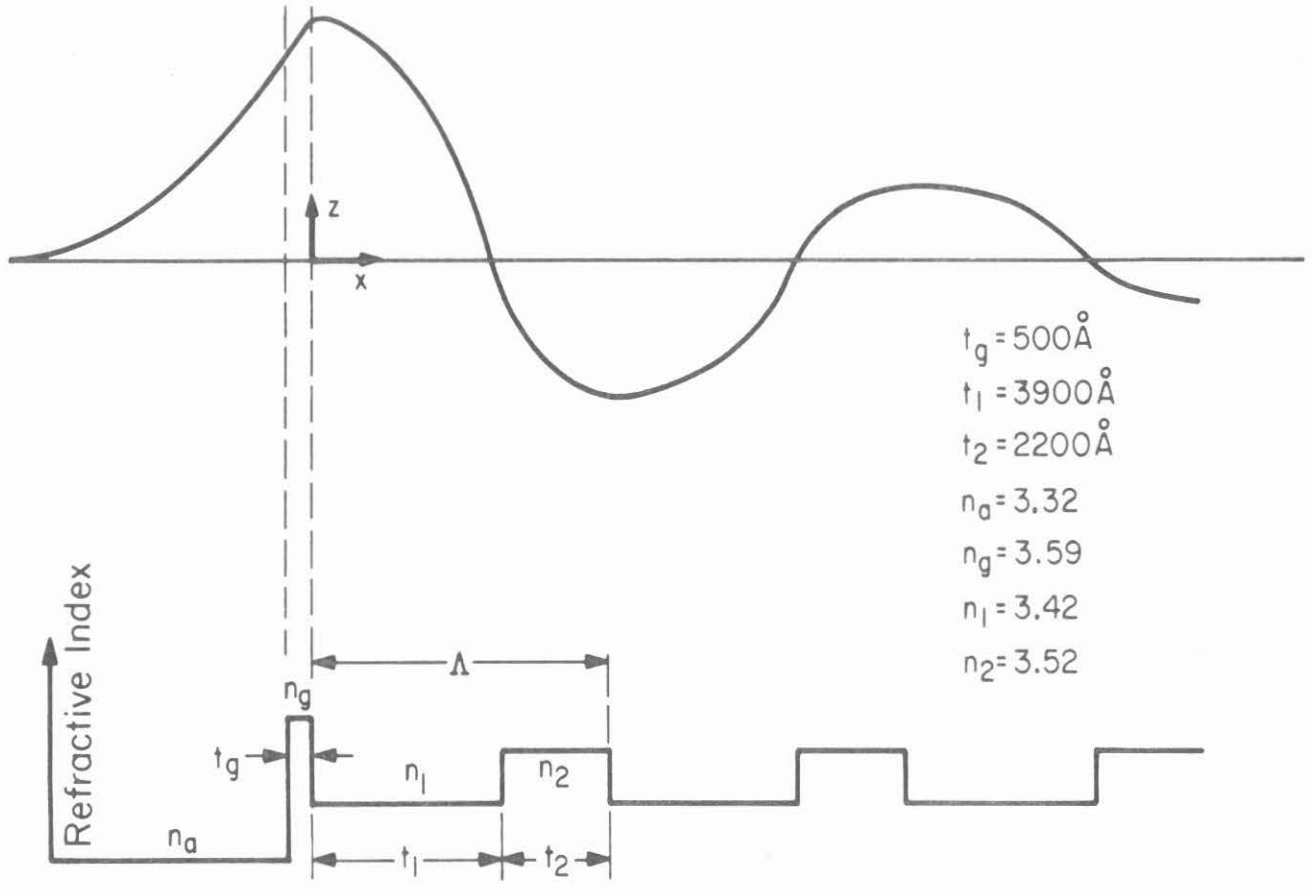

Field Distribution of Transverse Bragg Reflector Laser

Fig. 2.12 Laser structure used in analysis

where $\delta = 0$ has been used for simplicity. If we equate (2.51) to the power flow into the substrate, $S_x(x=L) = \frac{\kappa}{4\omega\mu}$, we find

$$\eta_{gi} = \frac{-\kappa\, e^{-2\eta L}}{2\omega^2\mu\varepsilon_o n_g\left(t_g + \frac{\sin(2k_{gx}t_g)}{2k_{gx}}\right)} \tag{2.52}$$

If we now use $[\sin(2k_{gx}t_g)] / 2k_{gx} = k_{ax}/(k_{gr}^2 + k_{ax}^2)$ which is a result of eigenvalue equation (2.26), as well as $k_{gr} \simeq k_{gx}$, $n_{gr} \simeq n_g$, we find that (2.52) and (2.34) are in agreement, provided

$$\frac{\kappa}{2} = k_{gx} \tag{2.53}$$

or $k_{gx}\,\Lambda = \pi$.

In order for the coupled mode equations to be valid, $k_{1x} \sim k_{2x} \sim k_{gx}$, thus (2.53) is just an expression of the Bragg condition.

Fox[3] obtains a simple expression for the loss coefficient α of a symmetric Bragg guide as shown in Figure 2.3.

$$\alpha = \frac{-8.686\, k_{gx}\, \log_e \rho}{\beta t_g} \tag{2.54}$$

where ρ = reflection coefficient.

Using the coupled mode theory, $\delta = 0$, $\rho = S_o/R_o$, and equations (2.23) and (2.24) we find

$$\log_e \rho \simeq \log_e(1 - 2e^{-2\eta L}) \simeq -2e^{-2\eta L}$$

$$\alpha = \frac{17.372\, k_{gx}}{\beta t_g}\, e^{-2\eta L} \tag{2.55}$$

2.4 Conclusion

In this chapter a simple method for the design of a transverse Bragg reflector laser has been presented. This method was based on the requirement that maximum confinement of light be provided for the radiation within the active region. The imaginary component of the index of refraction of the active region was then calculated, assuming steady state oscillation and the loss constant α determined. It was found that a device with 4 to 5 periods would reduce losses into the substrate to the point where they were comparable to losses due to light coupled out the cleaved ends of the laser cavity.

CHAPTER 2 REFERENCES

1. Shyh Wang, IEEE J. Quant. Electr. QE-10, 413 (1974).

2. K. Aiki, M. Nakamura, J. Umeda, A. Yariv, A. Katzir, H. W. Yeh, Appl. Phys. Lett. 27, 145 (1975).

3. H. C. Casey, Jr., S. Somekh, and M. Ilegems, Appl. Phys. Lett. 27, 142 (1975).

4. F. K. Reinhart, R. A. Logan, and C. V. Shank, Appl. Phys. Lett. 27, 45 (1975).

5. H. Kogelnik and C. V. Shank, Appl. Phys. Lett. 18, 152 (1971).

6. C. V. Shank, J. E. Bjorkholm, and H. Kogelnik, Appl. Phys. Lett. 18, 395 (1971).

7. P. Yeh, Optical Waves in Layered Media, Caltech Ph.D. Thesis, 1978.

Chapter 3

FABRICATION AND EXPERIMENTAL RESULTS

3.1 Introduction

This chapter describes the fabrication and testing of the first transverse Bragg reflector laser. The device, which was grown using liquid phase epitaxy, was designed so as to support only a Bragg reflector type mode. A thin active layer and asymmetric structure makes conventional guiding impossible. The laser was then tested and the longitudinal mode spectrum and transverse mode profile measured.

3.2 Fabrication and Testing

The design of the first transverse Bragg reflector waveguide is shown in Figures 2.12 and 3.1. It was grown by Willie Ng and P. C. Chen using liquid phase epitaxy, and consists of a GaAs substrate, followed by nine layers of $Al_{.10}Ga_{.90}Ar$-$Al_{.25}Ga_{.75}Ar$, the active region of pure GaAs, a superstrate of $Al_{.4}Ga_{.6}Ar$, and a GaAs cap. The $Al_{.4}Ga_{.6}Ar$ is p^+ doped with Ge to a concentration of $10^{18}cm^3$. The substrate is n^+ doped with S_n to a concentration of $10^{18}/cm^3$ and the entire region is n doped to a concentration of $10^{17}/cm^3$. The index of refraction profile is shown in Figure 2.12 along with the expected field distribution. Important design parameters are indicated in this figure and in addition, at λ_o = 8900 Å we have

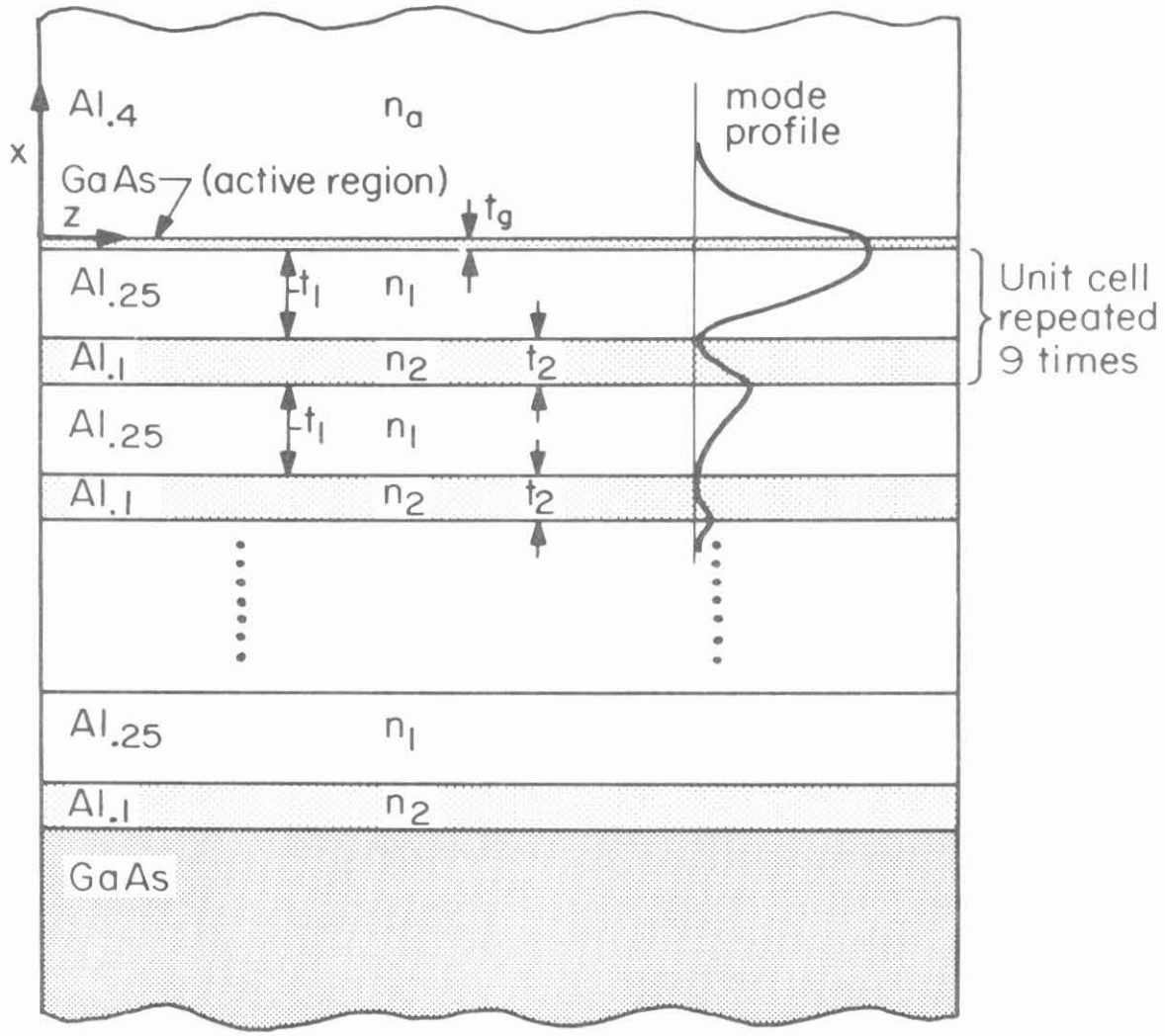

Fig. 3.1 Transverse Bragg Reflector Laser and Intensity Profile

$$
\begin{aligned}
k_o &= 7.06 \times 10^6/m \\
n_{eff} &= 3.371 \\
k_{ax} &= 3.96 \times 10^6/m \\
k_{gx} &= 8.72 \times 10^6/m \\
k_{1x} &= 4.07 \times 10^6/m \\
k_{2x} &= 7.15 \times 10^6/m
\end{aligned}
\qquad (3.1)
$$

Figure 3.2[1] is a plot of refractive index of $Al_xGa_{1-x}As$ at 1.38 eV and is very useful in the design of the laser structures. A thin layer of Au-Zn was evaporated on the p^+ side of the device to form a contact, after which the laser was lapped down to a thickness of about 100 μ. The substrate side was then coated with Au-Ge and the sample was annealed in flowing hydrogen at 400° C for approximately 5 minutes, or until a color change was observed. The sample was then cleaved into lasers with dimensions of 250 μ × 500 μ on the average.

Before growing the sample by LPE, several lasers were grown using MBE, but because of restrictions on the MBE apparatus only samples with pure GaAs (rather than $Al_{.1}Ga_{.9}As$) and $Al_{.25}Ga_{.75}As$ could be grown. As the Al concentration in GaAs is increased, the bandgap increases and the index of refraction drops. Thus light generated inside the GaAs active layer is strongly absorbed in the MBE structure, but is not absorbed in the LPE structure which contains only layers with Al outside the guiding region. Since the majority of the radiation is outside of the active gain region it is impossible for a device to lase if the material out-

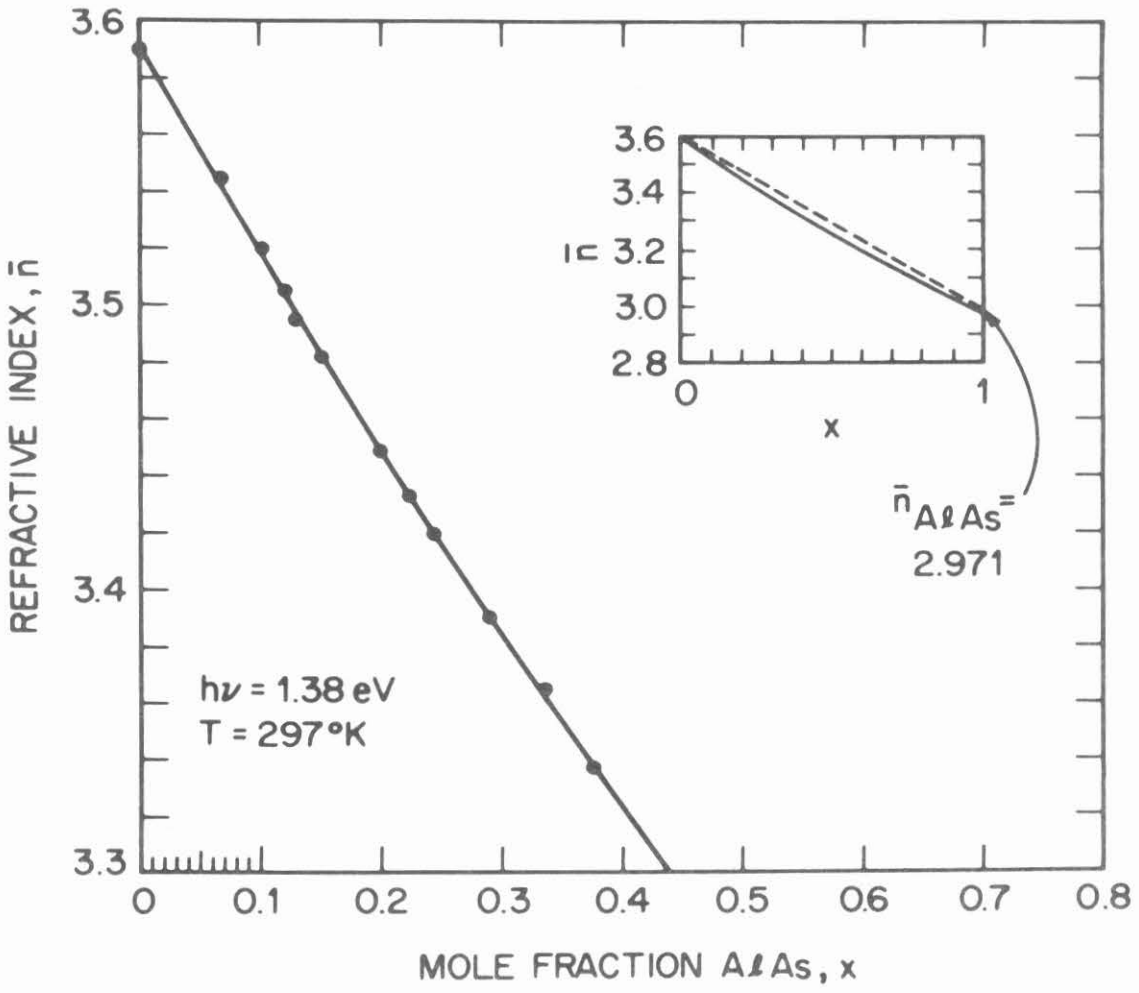

Fig. 3.2 Refractive index as a function of Al concentration in $Al_xGa_{1-x}As$. (After reference 1.)

side the pumped region contains highly absorbent GaAs. Figure 3.3 (courtesy of Al Cho of Bell Laboratories) is an SEM of the MBE sample containing pure GaAs in the reflector region, while Figure 3.4 is an SEM of the LPE growth. The great precision in MBE growth is evident from Figure 3.3.

It should be noted that although the guiding of light in a guiding region of index lower than that of the surrounding material is possible with Bragg waveguiding, it was not demonstrated in the laser tested. Because of the problems with absorption, pure GaAs (high index) must be used in the active region, while lower index $Al_xGa_{1-x}As$ is used in the other regions. It is well known that for an asymmetric dielectric guide, a cut-off thickness exists for guiding. That is, for guiding layers of thickness below a certain cut-off t_c, no propagation is possible. For symmetric structures, the guiding layer can be arbitrarily thin and guiding is still possible. For the asymmetric laser design shown in Figure 2.12 the cut-off thickness is approximately 900 Å at the lasing frequency. Thus guiding in the conventional sense is not possible and any modes must be of the Bragg Waveguide type with field profile as shown in Figure 2.12.

The samples were pulsed at a rate of 140 hz with a pulse width of 10 μsec. Figure 3.5 is a plot of light output as a function of current, indicating a threshold of about 4 amps or 5 ka/cm^2.

Figure 3.6 is a plot of light intensity as a function of wavelength. It is evident that approximately ten longitudinal modes are lasing. The mode spacing is approximately 2.8 Å and agrees well with what is expected for mode spacing in a Fabry-Perot cavity

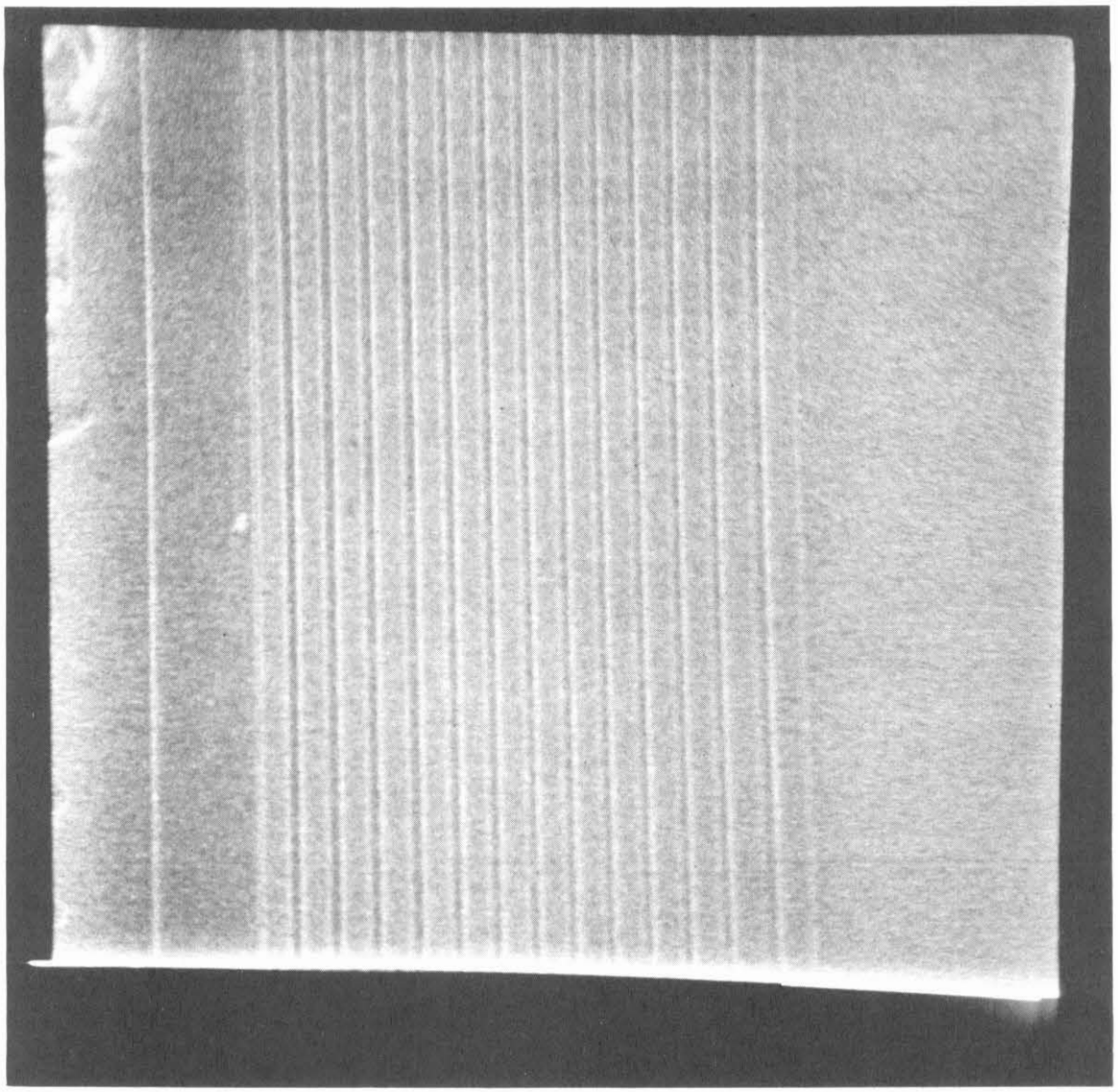

Fig.3.3 SEM of a Molecular Beam Epitaxy structure.

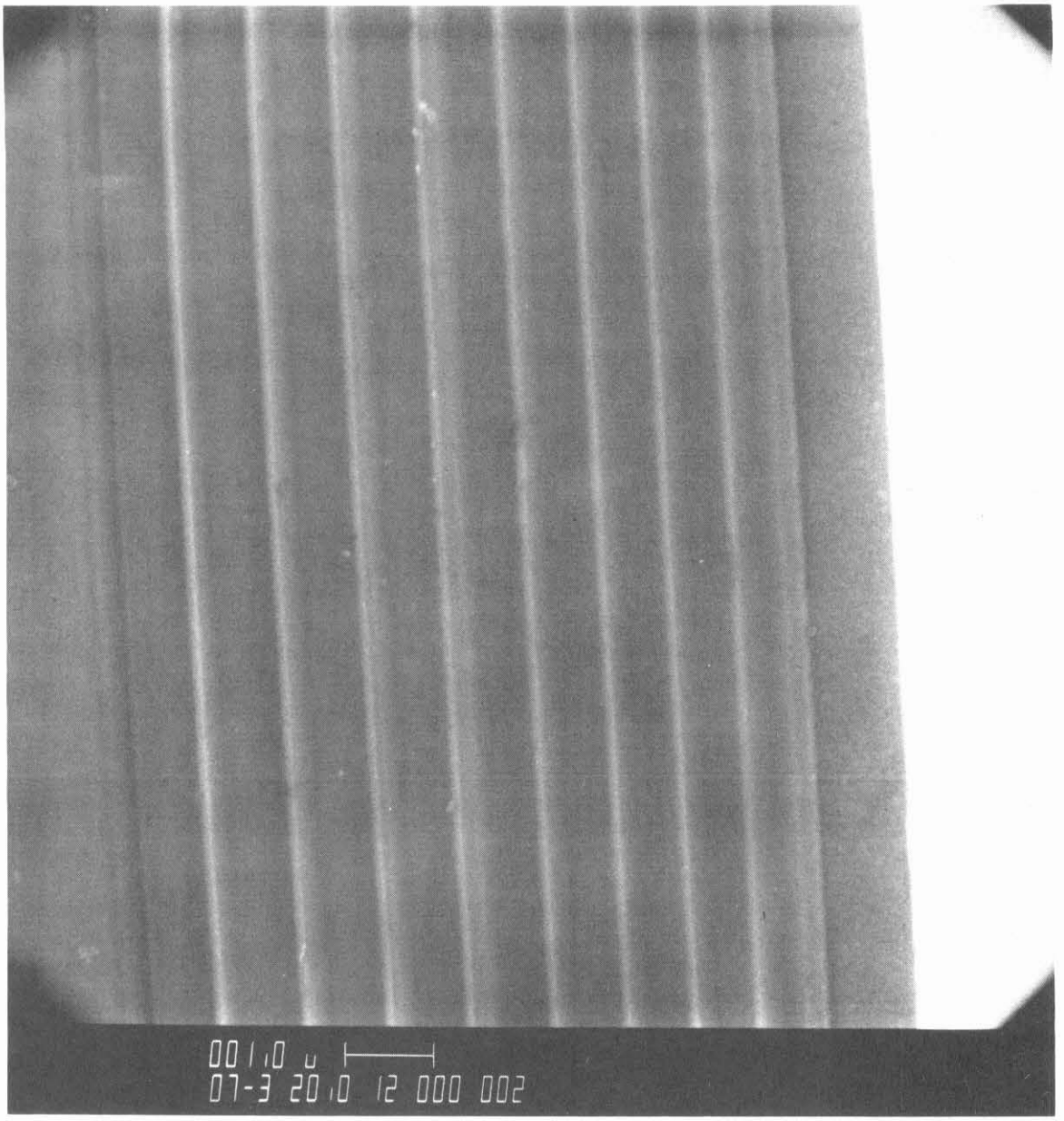

Fig.3.4 SEM of a Liquid Phase Epitaxy structure.

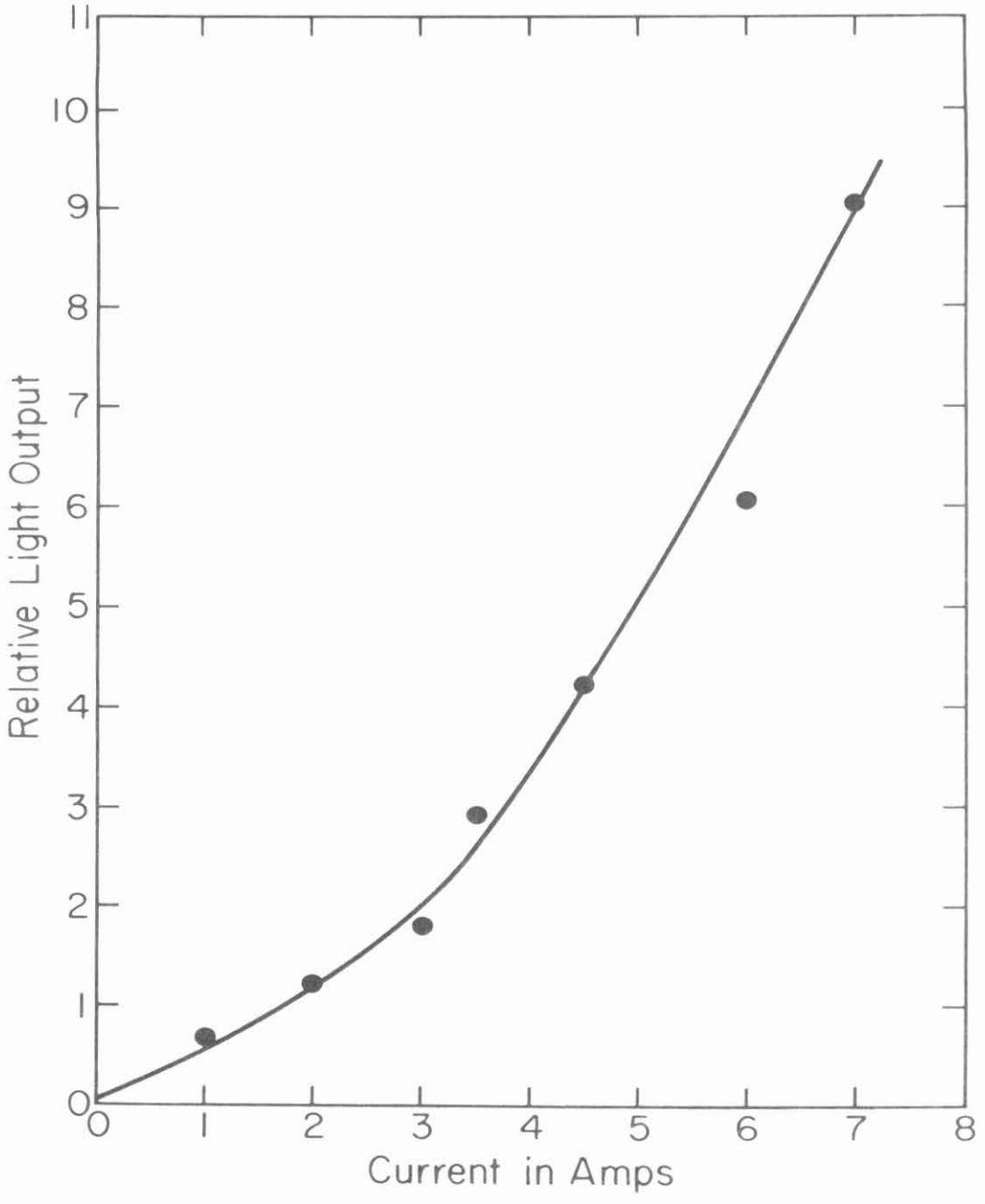

Fig. 3.5 Relative light output as a function of current

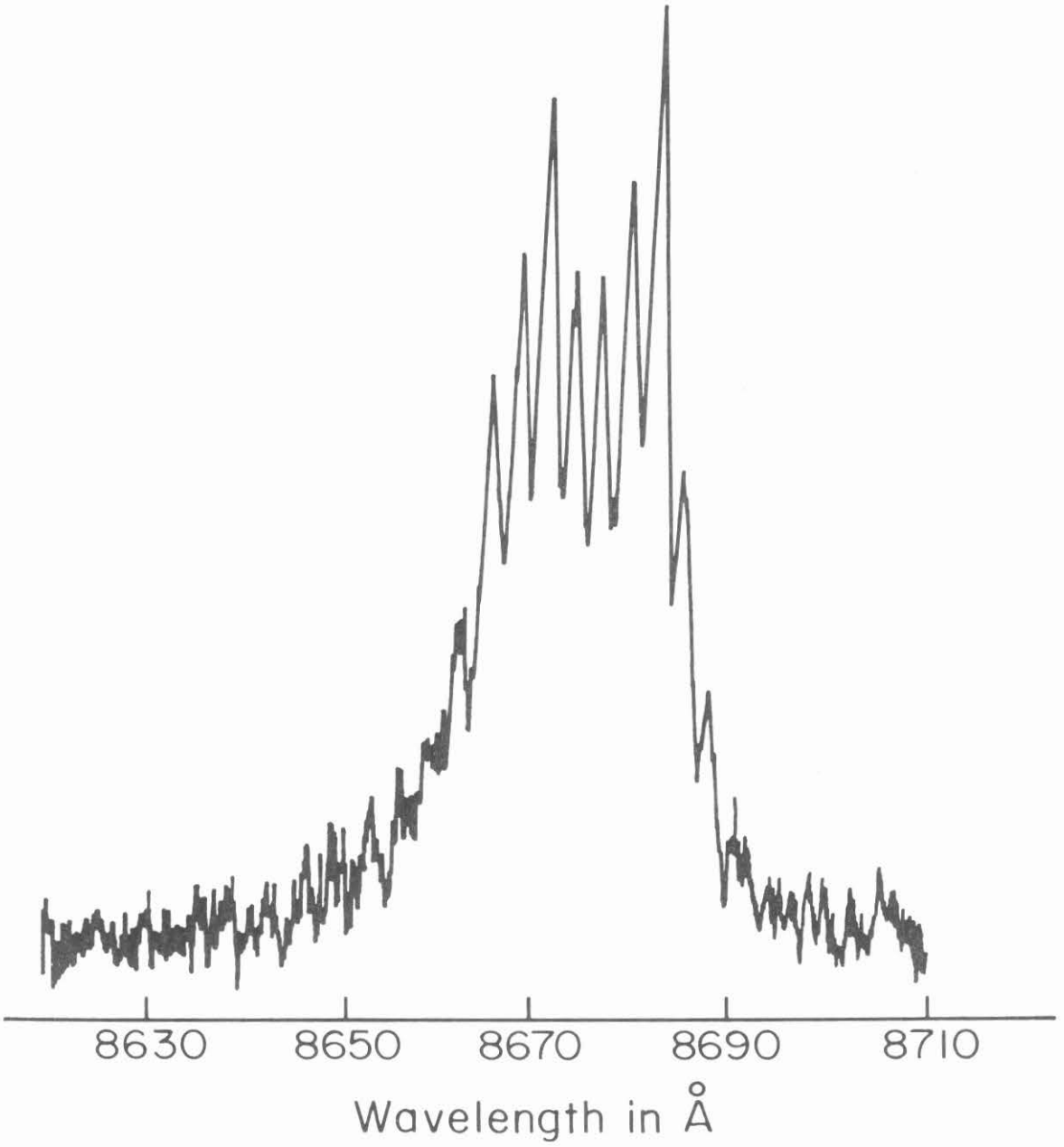

Fig. 3.6 Light output as a function of wavelength

$$\beta\ell = n_{eff}\, k_o\, \ell = n_{eff}\, \frac{2\pi}{\lambda_o}\, \ell = p\pi \qquad (3.2)$$

$$p = \text{integer}$$

after differentiating equation 3.2 we find

$$\Delta\lambda = \frac{\lambda_o^2}{2\ell\left[n_{eff} - \lambda_o \frac{\partial n_{eff}}{\partial\lambda}\right]} \qquad (3.3)$$

For $\lambda_o \frac{\partial n_{eff}}{\partial\lambda} \approx -0.25$, $n_{eff} = 3.37$, $\lambda_o \approx 8670$, and $\ell = 350\ \mu$ (the measured length), we obtain $\Delta\lambda = 3.0$ Å. This is in agreement with Figure 3.6, thus verifying that the measured modes are longitudinal modes.

A final important measurement is that of the transverse mode profile. This is shown in Figure 3.7, where three oscillations under a decaying envelope are apparent, thus indicating Bragg Waveguiding. It is expected that each peak of the intensity profile decreases by a factor of $\frac{1}{3}\left(\left(\frac{k_{1x}}{k_{2x}}\right)^2\right)$ from that of the adjacent peak. This is verified in Figure 3.7.

The apparatus for measuring the mode profile consists of a x43 microscope objective which images the near field onto a galvanometer mirror which reflects the light through a 30 μ slit and into a photomultiplier. The D.C. voltage which is used to rotate the mirrors is measured by the x-input of an x-y recorder, while the output of the photomultiplier is measured by the y-input of the plotter. The schematic of the apparatus is shown in Figure 3.8.

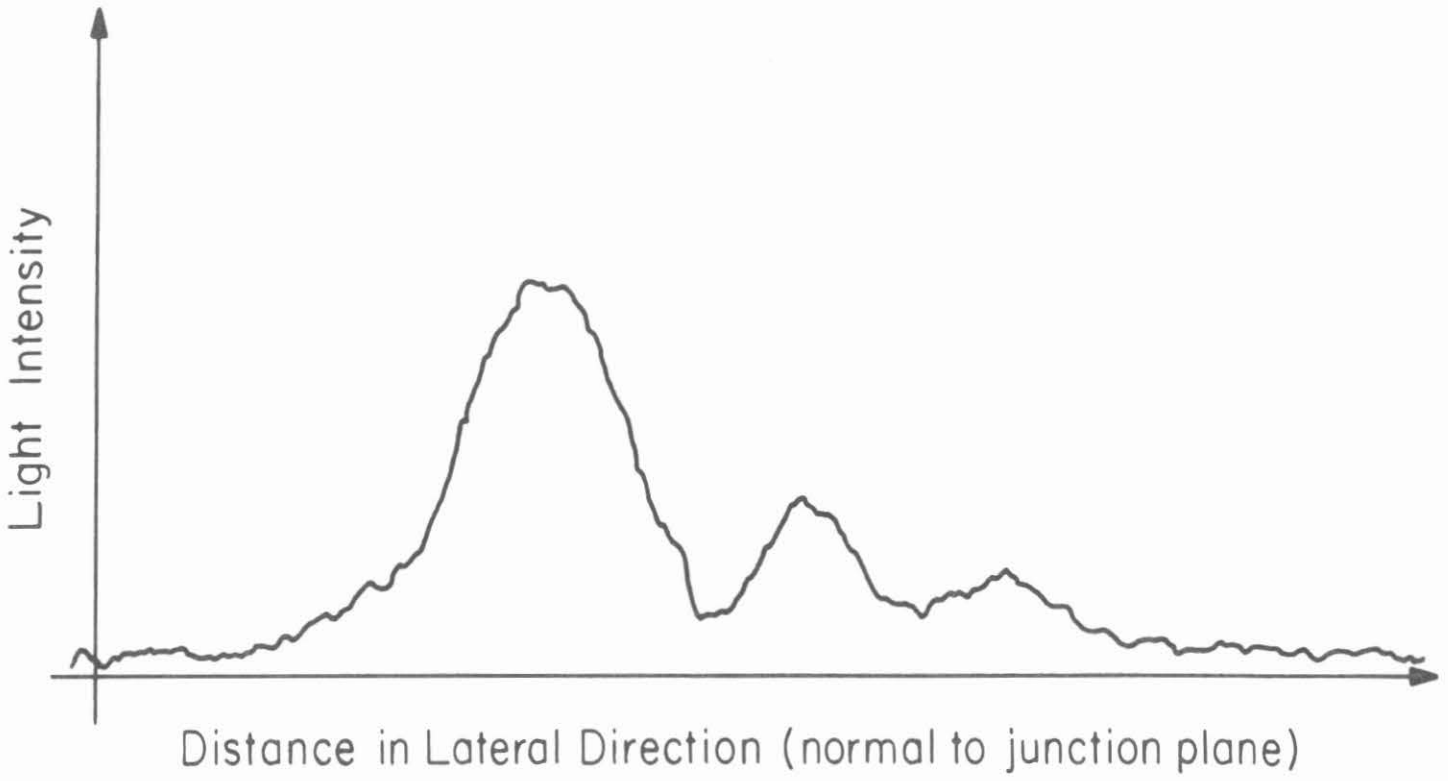

Fig. 3.7 Mode Profile--Light intensity distribution inside Bragg laser

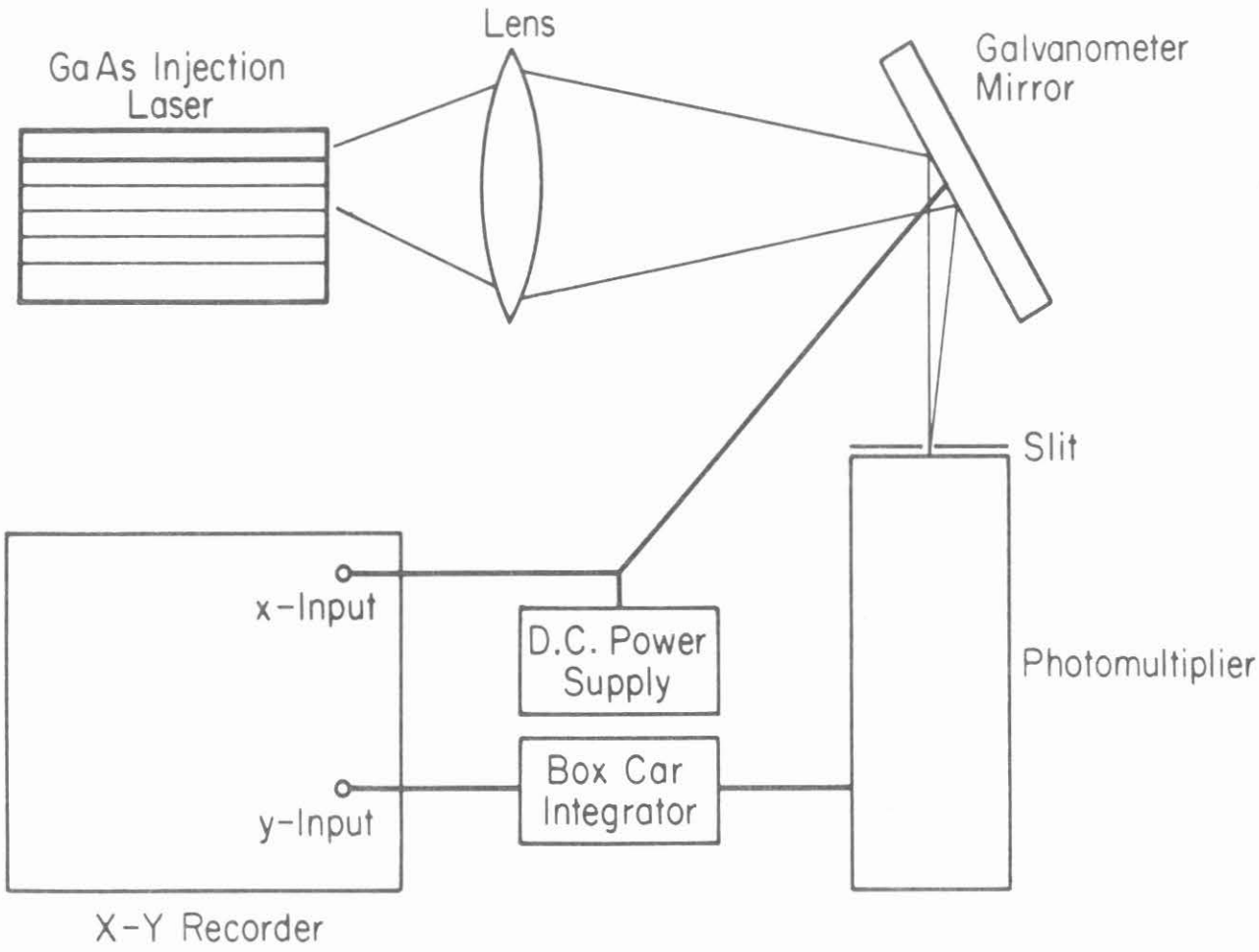

Fig. 3.8 Experimental Apparatus for Measuring Mode Profile

3.3 Conclusion

An analysis of Bragg waveguiding has been presented and expressions for α, the loss constant, as well as the imaginary part of the index of the guiding layer have been derived. It appears that very little light leaks into the substrate compared with Fabry-Perot losses out the ends of the cavity for structures with more than half a dozen or so periods.

A structure was grown by liquid phase epitaxy and successfully tested. The sample was designed so as to support only a Bragg type mode, and transverse mode profile measurements have confirmed this.

CHAPTER 3 REFERENCES

1. Casey, Sell and Panish, Appl. Phys. Lett. 24, 63 (1974).